Structures Research Report 2006/26868

University of Florida
Civil and Coastal Engineering

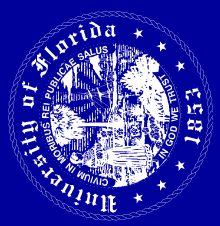

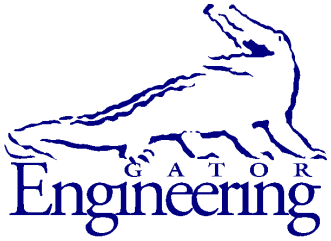

University of Florida
Civil and Coastal Engineering

Final Report **March 2006**

Barge Impact Testing of the St. George Island Causeway Bridge

Phase III : Physical Testing and Data Interpretation

Principal investigators:
Gary R. Consolazio, Ph.D.
Ronald A. Cook, Ph.D., P.E.
Michael C. McVay, Ph.D.

Graduate research assistants:
David Cowan
Alex Biggs
Long Bui

Department of Civil and Coastal Engineering
University of Florida
P.O. Box 116580
Gainesville, Florida 32611

Sponsor:
Florida Department of Transportation (FDOT)
Henry T. Bollmann, P.E. – Project manager

Contract:
UF Project No. 00026868 (4504961)
FDOT Contract No. BC-354 RPWO 76

DISCLAIMER

The opinions, findings, and conclusions expressed in this publication are those of the authors and not necessarily those of the State of Florida Department of Transportation.

Technical Report Documentation Page

1. Report No.	2. Government Accession No.	3. Recipient's Catalog No.
BC-354 RPWO-76		

4. Title and Subtitle	5. Report Date
Barge Impact Testing of the St. George Island Causeway Bridge Phase III : Physical Testing and Data Interpretation	March 2006
	6. Performing Organization Code
	8. Performing Organization Report No.
7. Author(s) G. R. Consolazio, R. A. Cook, M.C. McVay	2006/26868
9. Performing Organization Name and Address University of Florida Department of Civil & Coastal Engineering P.O. Box 116580 Gainesville, FL 32611-6580	10. Work Unit No. (TRAIS)
	11. Contract or Grant No. BC-354 RPWO-76
12. Sponsoring Agency Name and Address Florida Department of Transportation Research Management Center 605 Suwannee Street, MS 30 Tallahassee, FL 32301-8064	13. Type of Report and Period Covered Final Report
	14. Sponsoring Agency Code

15. Supplementary Notes

16. Abstract

This report describes a research study undertaken to quantify and characterize impact loads that are imparted to bridge piers during barge-pier collision events. Because bridges that span over navigable waterways are at risk for such collisions, they must be designed to successfully resist potential barge impact loads. However, few experimental studies have ever been conducted to quantify the magnitude or dynamic nature of such loads. Barge-impact provisions included in the current AASHTO bridge design specifications are based on limited experimental data that were generated using reduced scale (~1:5) pendulum hammer impact tests. The study described in this report utilized a combination of full-scale experimental barge impact testing and state-of-the-art numerical analysis to quantify impact loads, pier responses, and soil responses during barge-pier collisions. Specifically, in April 2004, a series of fifteen full-scale experimental barge impact tests were conducted on the old—now replaced and demolished—St. George Island Causeway Bridge (Bryant Patton Bridge). During each impact test, instrumentation (sensor arrays) and high-speed data acquisition systems were used to directly quantify dynamic impact loads and the resulting structure, soil, and barge responses. This report describes in detail the experimental test procedures that were employed and presents the resultant collected data. To compliment the physical testing, numerical finite element analysis (FEA) techniques were also employed to aid in interpretation of experimental test data. Comparisons of measured experimental data to FEA results substantiated the validity of the experimental data, and furthermore, provided additional insights into the nature of pier response to barge impact loading. Comparisons between experimentally measured data, analytically predicted data, and the AASHTO bridge design provisions are also presented in this report and recommendations are given with regard to the development of improved barge impact design provisions.

17. Key Words	18. Distribution Statement
Vessel, barge, impact, collision, bridge pier, experimental testing, finite element analysis, soil-structure interaction, bridge design specifications	No restrictions.

19. Security Classif. (of this report)	20. Security Classif. (of this page)	21. No. of Pages	22. Price
Unclassified	Unclassified	240	

Form DOT F 1700.7 (8-72). Reproduction of completed page authorized

ACKNOWLEDGEMENTS

The authors would like to acknowledge and thank the Florida Department of Transportation (FDOT) for providing the funding that made this research project possible. The authors are also pleased to acknowledge and thank a significant number of individuals, agencies, and companies that contributed suggestions, assistance, and materials toward the successful execution of this project. FDOT Structures Research Laboratory personnel (Marc Ansley, David Allen, Frank Cobb, Steve Eudy, Tony Johnston, Paul Tighe) provided expertise and suggestions regarding instrumentation and data acquisition systems; fabricated, tested, and transported load-measurement impact blocks; provided a snooper truck to facilitate field installation of sensors; performed field extraction of concrete core samples; and made numerous additional contributions. Boh Bros. Construction Co. (in particular, Al Flettrich, Sonny Henley, and Scott Gros) of Baton Rouge, Louisiana provided logistical expertise, insight, and advice as well as a host of physical services (push-boat operation, crane operation, barge rental, etc.) that were critically important to the successful execution of this project. The contributions of both the FDOT Structures Research Laboratory and Boh Bros. Construction are gratefully acknowledged.

The authors wish to thank Henry Bollmann (FDOT) for initiating—jointly with Marc Ansley—the concept that became this project; providing valuable insights and suggestions, particularly from the point of view of an experienced bridge designer; and carefully reviewing the research findings. The authors thank Benjamin Lehr for important contributions made during an earlier research project that eventually led to the present project. The authors thank the U.S. Army Corps of Engineers for contributing valuable suggestions regarding instrumentation strategies for full-scale barge impact testing (Robert Patev and Bruce Barker) and discussions of barge impact analysis and design practices (Dr. Robert Ebeling). Donations of welded wire fabric sheets by Ivy Steel and Wire of Jacksonville, Florida, are gratefully acknowledged. Finally, the authors thank Chris Ferraro (University of Florida) for conducting material tests on concrete core samples.

TABLE OF CONTENTS

CHAPTER 1
INTRODUCTION

1.1 Introduction

Bridges spanning over waterways that are used by commercial vessel traffic are, by virtue of their location, inherently at risk for possible collisions by errant transport vessels such as barges and ships. In the state of Florida, the combination of a lengthy coastline, several major ports, and an extensive intracoastal waterway system requires that careful attention be given to the vessel-collision-resistance of highway bridges that span over navigable waterways. While large cargo ships are generally restricted to operation in deep water ports, shallow draft barge flotillas operate on a much wider variety of shallower waterways. Indeed, in Florida, several hundred of the roughly ten-thousand bridges in the state span over waterways that are deep enough to carry barge traffic. As a result, heavily laden barge flotillas carrying coal, fertilizer, petroleum, and other commodities routinely pass beneath highway bridges that carry vehicular traffic.

Florida, however, is not unique in this respect. In fact, any geographic region encompassing coastal zones, large inland rivers, or intracoastal waterways is likely to support barge traffic. With such traffic comes the potential for barge collisions with bridges, and the possibility of structural collapse if sufficient impact resistance has not been designed into the respective structures. The study described in this report addresses this issue by developing an improved understanding of barge-bridge collision loads as well as the associated structure and soil responses to such loads. Data experimentally measured during this study will facilitate future development of improved methods of calculating barge impact loads for the purpose of designing collision resistant bridge structures.

1.2 Motivation and research need

It has been noted in the literature (Larsen 1993) that worldwide, vessel impacts (barge and ship impacts combined) occur frequently enough that, on average, approximately one serious vessel-bridge collision incident occurs per year. When designing new bridges, or assessing the structural adequacy of older bridges, lateral impact loads corresponding to possible vessel-bridge collisions constitute a critically important loading scenario that must be taken into account. Despite this fact, as recently as a few decades ago, nationally adopted criteria for designing bridges to resist vessel collision loads did not exist in the United States. This began to change, however, during the 1980s.

In 1980, the cargo ship *Summit Venture* collided with one of the anchor piers of the Sunshine Skyway Bridge over Tampa Bay, causing the collapse of approximately 1300 ft. of bridge deck and the loss of thirty-five lives. Following this incident, investigations were carried out to assess the risks and consequences of vessel-bridge collisions in the United States. Later, in 1988, a formal research study was initiated to develop specifications for the design of highway bridges that span over navigable waterways. In 1991, the product of this research effort was published as the *American Association of State Highway and Transportation Officials (AASHTO) Guide Specification and Commentary for Vessel Collision Design of Highway Bridges* (AASHTO 1991). A few years later, a related set of provisions were included in the then-newly-published *AASHTO Load and Resistance Factor*

Design (LRFD) Specifications (AASHTO 1994). Publication of the AASHTO vessel-collision design provisions (Figure 1.1) in the 1990s—which address both ship-bridge collisions and barge-bridge collisions—represented a major step forward in terms of improving the safety of highway bridges.

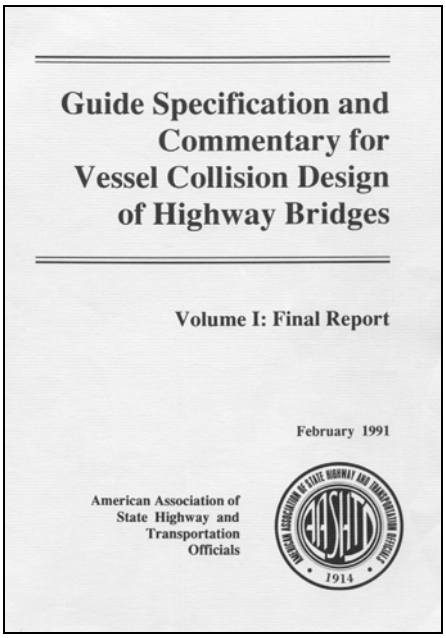

a) Guide Specification and Commentary for Vessel Collision Design of Highway Bridges (1991)

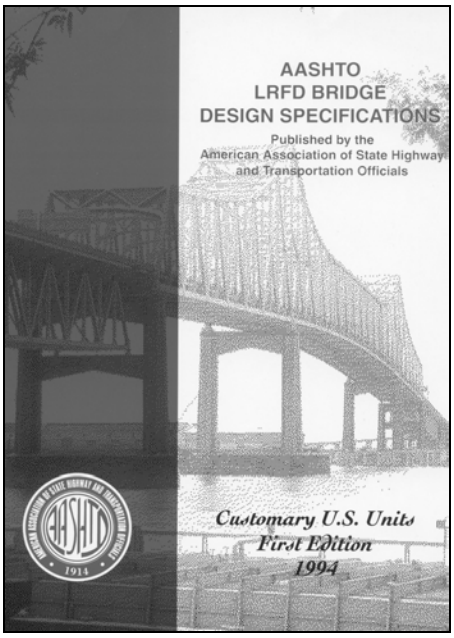

b) Load and Resistance Factor Design (LRFD) Bridge Design Specifications (1994)

Figure 1.1 AASHTO publications containing vessel-collision bridge design provisions

As noted earlier, in Florida, a significant number of bridges span over barge-navigable waterways. To design such structures, lateral loads associated with potential collisions are computed in accordance with the AASHTO barge impact provisions. In many situations, the loads associated with barge impact exceed all other design loads—hurricane wind loads, dead loads, vehicle loads, etc.—and ultimately, control the design of major bridge components. In regard to which bridge components are most vulnerable to barge impact loads, it is noted that barges posses relatively shallow vertical-profiles, generally extending less than 5 to 10 ft. above the waterline when fully loaded, and less than 10 to 15 ft when empty. This is true even in multi-barge flotillas that may span several hundred feet in length. As a result, the bridge components most vulnerable to barge collision loads are those located near water level—typically bridge piers and the underlying foundations.

Despite the risks posed by barges colliding with bridge piers, very few experimental studies have ever been conducted to directly quantify the loads that are transmitted to pier and foundation elements during barge collision events. At the time during which AASHTO barge impact provisions were being developed, full-scale experimental test data for barge impact loads on bridge piers were not available in the literature. As a consequence, the

AASHTO barge impact provisions were, instead, developed from the results of reduced-scale barge bow crushing experiments that were performed in Germany during the early 1980s (Meier-Dörnberg 1983). In these experiments, a pendulum impact hammer was used to dynamically impart energy to the bow sections of reduced-scale (1:4.5) models of European hopper barges. Supplementary static tests were also conducted, at similar scale (1:6). However, this particular study found no significant differences between the measured dynamic and static forces. As a result, data collected from the tests were used to develop relationships between kinetic impact energy, barge deformation, and static—not dynamic—impact force. Fundamentally, it was assumed that static forces were adequate predictors of structural demand, even in dynamic loading conditions.

In developing the AASHTO barge impact provisions, the relationships developed by Meier-Dörnberg were adopted with only minor modifications. Therefore, the AASHTO provisions implicitly incorporate the assumption that a static approach to load prediction (and structural demand assessment) is a sufficiently accurate means of designing highway bridge piers to resist dynamic barge collision loads. While publication of the AASHTO provisions has very clearly elevated the level of safety that is incorporated into vessel-collision bridge design practice in the United States, limitations of the Meier-Dörnberg study, in conjunction with additional factors, have motivated a re-examination of the AASHTO provisions.

While reduced-scale models are often employed in laboratory testing, extrapolating results from such models to full-scale response can introduce uncertainties in terms of accuracy. This is particularly true when full-scale data are unavailable to confirm the validity of the scaling processes used. Given the 1:4.5 and 1:6 scales used in the Meier-Dörnberg tests, and the lack of available full-scale test data, the relationships adopted in the AASHTO provisions necessarily contain some level of uncertainty. Moreover, the impact energy delivery method used in the Meier-Dörnberg tests, specifically, the use of stationary barge models being struck by a swinging pendulum hammer, omits significant dynamic interaction effects that occur between barges and bridge piers during real collision events. Stiffness, inertia, and damping characteristics of the pier, soil, and bridge superstructure all combine to influence the characteristics of the collision loads generated and the resulting responses (deformations and stresses) of the combined structure-soil system. Analysis and design procedures based on static behavior fail to include inertia-related (mass-related) forces, damping resistance, and increases in soil stiffness that can occur under rapid impact loading conditions. Omission of these dynamic phenomena can lead to design provisions that are non-uniform in the level of safety that is provided against dynamic—e.g., collision-induced—structural collapse.

Technological advances in computing hardware and structural analysis/design software over the past two decades further motivate the need to re-examine the static procedures contained in the AASHTO provisions. During the 1980s, linear static structural analysis represented the state-of-the-practice in the design of highway bridge structures. At the time, nonlinear and dynamic analyses required expensive computing hardware and were therefore primarily the domain of research, not design practice. However, the situation has changed dramatically as low-cost, high-speed computers have proliferated. Nonlinear structural analysis procedures are now frequently used in the structural design of bridge elements such as piers and foundations. Similarly, dynamic structural analysis techniques, such as time-domain (time-history) analysis and response spectrum analysis, have become established tools in seismic bridge design.

Applying nonlinear dynamic structural analysis to the practice of pier design for barge collision loading is now realistically feasible. One advantage of taking such an approach, rather than following the traditional static analysis approach, is that a dynamic analysis can account for inertia (mass) resistance, damping resistance, as well as stiffness characteristics of the pier, soil, and superstructure (as noted earlier). Accordingly, improved predictions of impact load and structural response are available for use in the design process. In turn, this holds the potential to produce increased uniformity of safety across a spectrum of differing bridge pier configurations and increased economy of design through improved structural demand assessment.

1.3 Objectives

Given the recognized limitations of the Meier-Dörnberg tests, there is a need for full-scale experimentally-measured barge-pier collision test data. In 2000, steps were taken to address this need by initiating the full-scale test program that is described in this report. This study was made possible by the replacement of the old (now demolished) St. George Island Causeway Bridge (Bryant Patton Bridge). Located in the panhandle region of Florida, approximately 5 miles east of Apalachicola, the 4 mile long bridge spanned over Apalachicola Bay connecting St. George Island to mainland Florida. In 2000, construction began on a new (wider) replacement bridge. Due to the environmentally sensitive nature of Apalachicola Bay, the alignment of the new bridge deviated from that of the old structure by more than 1500 ft. at some locations. This deviation produced a unique opportunity to conduct full-scale barge collision tests on two piers of the old structure without endangering the new structure. After traffic was rerouted to the newly opened bridge in February 2004, demolition of the old structure began. In March and April 2004, full-scale barge collision experiments were performed on two piers of the old bridge. Both piers were subsequently destroyed in May 2004 as part of the normal demolition process.

Given the uniqueness of this testing opportunity, efforts were made to ensure that the tests were as comprehensive in scope as possible, within budget constraints. Two parallel research studies were conducted. A structural investigation, described in this report, dealt with instrumentation and data collection on the barge, two test piers, and bridge superstructure, as well as overall logistical issues related to conducting the tests. A supplementary geotechnical investigation was also carried out, in parallel, to collect insitu soil properties near the test piers and to collect soil response data during the collision tests. (For additional details regarding this latter study, see McVay et al. 2005). During each impact test, sensor networks and high-speed data acquisition systems were used to directly quantify dynamic impact loads and the resulting structure, soil, and barge responses. Moreover, the tests were conducted at full-scale (the test barge was approximately 600 tons in weight, 50 ft. wide, and 151 ft. long) and were fully dynamic in nature; i.e., interactions between the vessel, pier, soil, and superstructure were completely included.

Within the scope of the structural investigation described in this report, the most important project objectives were:

1. To comprehensively instrument the test piers, superstructure, and test barge to permit the direct measurement of loads, displacements, accelerations, deformations, and pressures.

2. To redundantly instrument the test piers and test barge in a manner that permitted indirect ("back-calculated") determination of loads and displacements. Indirectly determined load and displacement data were then used to supplement the corresponding directly measured data.

3. To experimentally quantify the dynamic impact loads that were imparted to the test piers during barge collisions, and to compare measured values to loads calculated using the AASHTO barge impact provisions.

4. To quantify pier and superstructure responses to the barge collision loads.

5. To quantify load-deformation (force-crush) relationships for the test barge and to compare the measured relationship with the AASHTO barge impact provisions.

6. To develop nonlinear dynamic finite element analysis (FEA) models that represent the test piers, superstructure, and soil conditions at the test site.

7. To quantify—through comparison of experimental data and nonlinear dynamic FEA results—the relative magnitudes of displacement, velocity, and acceleration proportional sources of resistance (i.e., stiffness, damping, and inertia) that were mobilized during dynamic barge collision tests.

8. To determine whether soil response to vessel impact loading is sufficiently described using static load-deformation relationships or whether dynamic (rate-dependent) sources of soil resistance should also be incorporated.

9. To compare structural demand indices produced from static (AASHTO) and nonlinear dynamic analyses of piers subjected to corresponding loading conditions.

10. To recommend appropriate procedures for using the data collected during this study to assess the validity of the current AASHTO barge impact provisions.

11. To recommend parameters that should be taken into consideration in the future development of new barge impact design provisions.

12. To identify sources of impact load resistance that should be included in structural analysis software employed in the vessel-collision design of bridge piers.

In general, data collected during this study will enable assessment of the accuracy of the AASHTO barge impact provisions and future development of improved design provisions. The full-scale experimental test data will also permit validation of pier analysis software packages already in use by the bridge design industry and will permit future development of improved-accuracy dynamic analysis procedures suitable for use in bridge design practice.

1.4 Scope of work

The scope of the work encompassed by this study included full-scale field instrumentation and testing, finite element modeling and analysis, and interpretation of results in relation to the applicable AASHTO design provisions. All field activities (instrumentation and collision testing) were carried out at the St. George Island Causeway Bridge on two piers, identified as Pier-1 and Pier-3. Both of these piers were located on the southern side of the navigation channel where, prior to its demolition, the bridge spanned over the Florida intracoastal waterway. Pier-1 was located adjacent to the navigation channel and Pier-3 was located third from the channel. Prior to conducting the collision tests, high-speed data acquisition systems and networks of sensors were installed on Pier-1, Pier-3, the bridge superstructure, and the test barge. Three separate series of collision tests were conducted on the bridge piers, each one on a uniquely different structural configuration (described in detail later). During each of the fifteen total tests that were conducted, the data acquisition systems recorded data from the sensor networks for a total of 60 seconds at a rate of 2000 samples per second per sensor. Upon completion of the field testing activities, recorded test data were reduced and processed into engineering quantities such as force, acceleration, displacement, strain, and pressure.

Supplementing the experimental testing activities, nonlinear dynamic finite element modeling and analysis tasks were also carried out within the scope of this study. Numerical models of Pier-1, Pier-3, and the respective soil conditions were created and then dynamically analyzed using the LS-DYNA (LS-DYNA 2003) and FB-MultiPier (FB-MultiPier 2005) finite element codes. Such analyses were used to plan the physical test program, interpret the experimentally collected data, quantify sources of impact resistance (structure, soil, stiffness, damping, inertia), and assess the suitability of the static load approach prescribed by AASHTO barge impact provisions.

CHAPTER 2
BACKGROUND

2.1 Vessel-bridge collision incidents

Designing bridge structures that span over vessel-navigable bodies of water requires that careful consideration be given to the fact that cargo vessels may inadvertently collide with piers that support the bridge superstructure. Causes of such collisions often involve poor weather conditions, limited visibility, strong cross-currents, poor navigational aids, failure of mechanical equipment, or operator error. Worldwide, vessel impacts occur frequently enough that, on average, at least one serious collision occurs each year (Larsen 1993). Within the United States, a succession of incidents involving ships and barges impacting bridge structures clearly demonstrates that the potential for structural failure and loss of life exist.

One of the most catastrophic incidents of vessel-bridge collision in the United States was the 1980 collapse of the Sunshine Skyway Bridge, which spanned over Tampa Bay in Florida. Navigating in poor weather conditions and limited visibility, the cargo ship *Summit Venture* collided with one of the anchor piers of the bridge causing the collapse of almost 1300 ft. of bridge deck (Figure 2.1) and the loss of thirty-five lives. Due in large part to this incident, comprehensive guidelines for designing bridge structures to resist ship and barge collision loads were later published, in 1991, as the *AASHTO Guide Specification and Commentary for Vessel Collision Design of Highway Bridges* (AASHTO 1991).

Figure 2.1 Collapse of the Sunshine Skyway Bridge in Florida (1980)
after being struck by the cargo ship *Summit Venture*

While massive cargo ships clearly pose a significant threat to bridge structures, they are also limited in operation to relatively deep waterways. Consequently, ships pose significant risks primarily to bridges near major shipping ports. In contrast, multi-barge flotillas are able to operate in much shallower waterways and thus pose a risk to a greater number of structures. Considering that each individual barge within a flotilla might weigh as

much as fifty fully-loaded tractor-trailers, the potential damage that can be caused by barges striking bridge piers is evident.

In September 1993, a multi-barge tow navigating at night and in dense fog collided with the Big Bayou Canot railroad bridge near Mobile, Alabama resulting in a significant lateral displacement of the structure. Moments later, a passenger train attempted to cross the structure at 70 mph, resulting in catastrophic structural failure (Figure 2.2) and forty-seven fatalities. In September 2001 a barge tow navigating near South Padre, Texas veered off course in strong currents and collided with piers supporting the Queen Isabella Causeway Bridge. As a result of this impact, three spans of the structure collapsed (Figure 2.3) and several people lost their lives. In May 2002, an errant barge tow struck a bridge on interstate I-40 near Webbers Falls, Oklahoma. On an average day, this structure carried approximately 20,000 vehicles across the Arkansas River. As a result of the impact, 580 ft. of superstructure collapsed (Figure 2.4), fourteen people died, and traffic had to be rerouted for approximately two months.

Figure 2.2 Failure of the Big Bayou Canot railroad bridge in Alabama (1993) after being struck by a barge flotilla

Figure 2.3 Collapse of the Queen Isabella Causeway Bridge in Texas (2001) after being struck by a barge flotilla

Figure 2.4 Collapse of an Interstate I-40 bridge in Oklahoma (2002)
after being struck by a barge flotilla
(Source: Oklahoma DOT)

2.2 Review of experimental vessel impact tests

Despite the significant number of vessel-bridge collisions that have occurred in recent decades, only a small number of instrumented experimental tests have ever been performed to quantify vessel impact loading characteristics. Generally, ship collision events have been studied to a much greater extent than have barge collisions. Two key ship collision studies form the basis for most current theories relating to ship impact loading. The first was conducted by Minorsky (1959) to analyze collisions with reference to protection of nuclear powered ships, and focused on predicting the extent of vessel damage sustained during a collision. A semi-analytical approach was employed using data from twenty-six actual collisions. From this data a relationship between the deformed steel volume and the absorbed impact energy was formulated. A second key ship collision study was that of Woisin (1976) which also focused on deformation of nuclear powered ships during collisions. Data were collected from twenty-four collision tests (Figure 2.5) of reduced-scale (1:7.5 to 1:12) ship-bow models colliding with ship-side-hull models. Relationships between impact energy, deformation, and force developed during this study were later used in the development of the AASHTO equations for calculating equivalent static ship impact forces (AASHTO 1991).

In terms of quantifying the characteristics of barge impact loads, one of the most significant experimental studies conducted to date is that of Meier-Dörnberg (1983). This research included both static and dynamic loading of reduced-scale (1:4.5 to 1:6) models of European Type IIa barges. In overall dimensions, European Type IIa barges are similar to the jumbo hopper barges that are commonly found in the U.S. barge fleet. All tests in the Meier-Dörnberg study were conducted on *partial* vessel models that consisted only of nose sections of barges. In conducting the dynamic tests in this study, the partial barge models were mounted in a stationary (fixed-boundary-condition) configuration and then struck by a falling impact pendulum hammer. The amount of impact energy imparted to the barge model during each test was dictated by the weight of the hammer and its drop height. Due to limitations of hammer drop height, repeated impacts were carried out on each partial barge model to accumulate both impact energy and impact damage (crushing deformation).

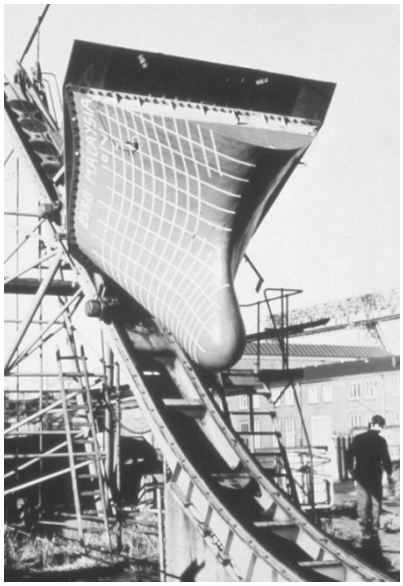

a) Ship bow model on inclined ramp prior to test

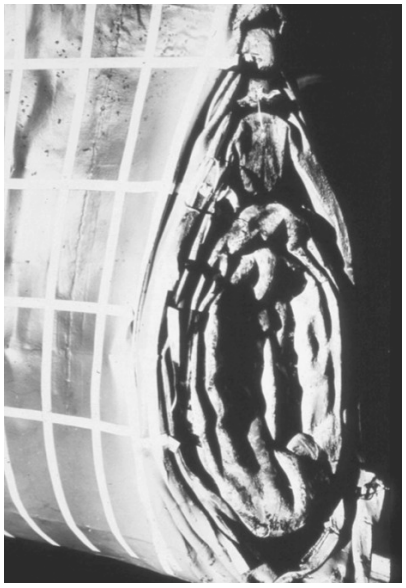

b) Permanent deformation of ship bow model after test

Figure 2.5 Reduced scale ship-to-ship collision tests conducted by Woisin (1976)

From the experimental data collected, Meier-Dörnberg developed relationships (Figure 2.6) between kinetic impact energy E_B, inelastic barge deformation (a_B), and force (dynamic P_B, as well as static $\overline{P}_B$). Importantly, no major differences were found between the magnitudes of static and dynamic impact force measured. However, this is very likely due to the fixed-boundary-condition nature of the test configurations used in the study. By omitting barge-pier interactions from the test setup, dynamic amplification (or attenuation) effects would necessarily be lacking in the results obtained.

Inelastic barge deformations—also called "crushing" deformations—were, however, included in the study. Such deformations have two important effects on observed impact loads. First, once yielding (and/or fracturing) of steel plates in the barge begins, the stiffness of the barge reduces dramatically. This phenomenon is clearly evident in the Meier-Dörnberg results, as shown in Figure 2.6, where the P_B-vs-a_B and $\overline{P}_B$-vs-a_B curves transition from initially steep elastic slopes to less-steep inelastic slopes. Second, inelastic deformation is a form of energy dissipation, and as such, the forces produced during the impact will be dependent upon the amount of energy dissipated.

In developing the AASHTO barge impact provisions, the relationships between impact energy, barge deformation, and impact force developed by Meier-Dörnberg were adopted with only minor modifications. With the exception of a new factor added to take into consideration variations in barge width, fundamentally, the AASHTO provisions rely on the results obtained by Meier-Dörnberg.

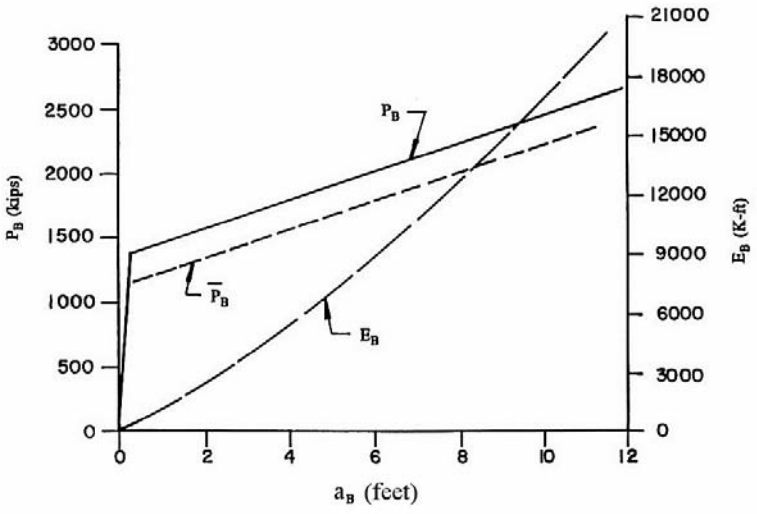

Figure 2.6 Relationships developed from experimental barge impact tests conducted by Meier-Dörnberg (1976) (Source: AASHTO 1991)

More recently, experimental studies have been conducted that overcome one of the key limitations of the Meier-Dörnberg study—i.e., the use of reduced-scale models. In 1989, Bridge Diagnostics, Inc. completed a series of *full-scale* tests for the U.S. Army Corps of Engineers that involved a nine-barge flotilla impacting lock gates at Lock and Dam 26 on the Mississippi river near Alton, Illinois (Goble 1990). Each of the impacts was performed at approximately 0.4 knots. Force, acceleration, and velocity time histories for the impacting barge were recorded using commercially available sensors such as strain gages and accelerometers. In addition, custom manufactured and calibrated load cells, developed by Bridge Diagnostics, were used to measure impact forces (Figure 2.7). Unfortunately, data obtained from this study are not directly applicable to bridge pier design because the system struck by the barge in the tests was a lock gate, not a bridge pier. Lock gates and bridge piers posses different structural characteristics which produce dissimilar impact loads. More importantly, the energy levels used during these tests were insufficient to cause significant inelastic barge deformation. Because inelastic barge deformations are common in head-on barge-pier collisions, and given that such deformations affect both barge stiffness and impact energy dissipation, data obtained from this set of tests are not directly applicable to bridge design.

Several years later, full-scale barge impact tests on concrete lock *walls* were conducted by the U.S. Army Corps of Engineers. In 1997, a 4-barge flotilla was used to ram a lock wall at Old Lock and Dam 2, located north of Pittsburgh, Pennsylvania (Patev and Barker 2003). These experiments (Figure 2.8) were conducted to measure the structural response of the lock wall at the point of impact and to quantify barge-to-barge lashing forces during impact. Strain gages were installed on the barge to record steel plate deformations at the point of impact. An accelerometer was used to capture the overall acceleration history of the flotilla, and clevis pin load cells quantified lashing forces generated during impact. A total of thirty-six impact tests were successfully carried out on the lock wall.

a) Barge bow approaching lock gate

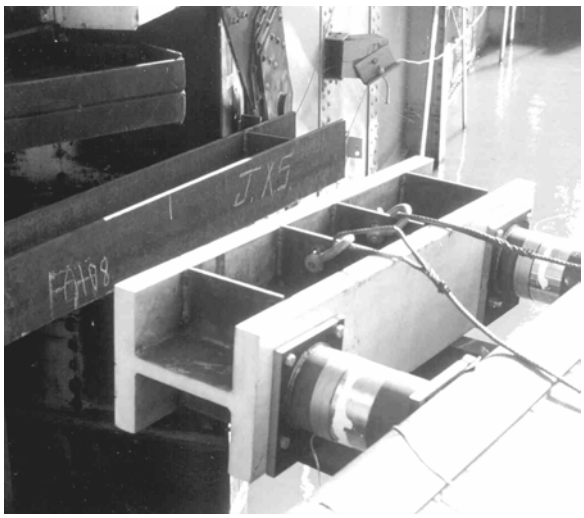

b) Load cells attached to barge bow

Figure 2.7 Instrumented full-scale barge-lock-gate collision tests
(Source: Bridge Diagnostics, Inc.)

a) Push boat and 4-barge flotilla

b) Sensors at impact corner of barge

Figure 2.8 Instrumented 4-barge lock-wall collision tests
(Source: U.S. Army Corps of Engineers)

Following the 4-barge tests, larger impact experiments involving a 15-barge flotilla were initiated in December of 1998 at the decommissioned Gallipolis Lock at Robert C. Byrd Lock and Dam in West Virginia (Arroyo et al. 2003). In contrast to the 4-barge tests, one of the primary goals of the 15-barge tests was to recover time-histories of impact force generated between the barge flotilla and the lock wall. To accomplish this goal, a load-measurement impact beam was affixed to the impact corner of the barge flotilla using two uniaxial high-capacity clevis-pin load cells (Figure 2.9). Additional instrumentation used

during these tests included accelerometers, strain gages, water pressure transducers, and smaller capacity clevis-pin load cells that were installed in-line with the barge-to-barge cable lashings. In total, forty-four impact tests were successfully carried out on the lock wall.

In bridge pier design for barge collision loading, maximum impact forces are generally associated with head-on impact conditions, not oblique glancing blows of the type tested in the 4-barge and 15-barge tests performed by the Army Corps. Therefore, while the data collected during these tests could be useful in developing load prediction models for oblique side impacts on piers, the same data cannot be used to improve the AASHTO expressions for head-on impacts (those derived from results of the Meier-Dörnberg study). Additionally, neither of the Army Corps test series involved dynamic vessel-pier-soil interactions or significant crushing deformation of the impacting barges.

a) Push boat and 15-barge flotilla

b) Force measurement beam attached to barge with clevis-pin load cells

Figure 2.9 Instrumented 15-barge lock-wall collision tests
(Source: U.S. Army Corps of Engineers)

2.3 Design of bridges according to the AASHTO barge impact provisions

A pooled fund research program sponsored by eleven states and the Federal Highway Administration (FHWA) was initiated in 1988 to develop methods of safeguarding bridges against collapse when impacted by ships or barges. The findings of the research were adopted by AASHTO and published in the *Guide Specification and Commentary for Vessel Collision Design of Highway Bridges* and the *Load and Resistance Factor Design (LRFD) Specifications*. Provisions included in these publications serve as a nationally adopted basis for bridge design with respect to vessel collision loads. The provisions allow two approaches to collision resistant bridge design. Either the structure can be designed to withstand the vessel impact loads alone, or a secondary protection system can be designed that will absorb the vessel impact loads and prevent the bridge structure itself from being struck. In addition to providing design guidelines, the AASHTO provisions recommend methodologies for placement of the bridge structure relative to the waterway as well as specifications for navigational aids. Both are intended to reduce the potential risk of a vessel collision with the bridge. Nonetheless, for a wide ranging set of reasons—windy high-current waterways; adverse weather conditions; narrow or curved waterway geometry—most bridges that are

accessible to barge impact will likely be struck at some point during their lifetime (Knott and Prucz 2000). With this in mind, all bridges that span navigable waterways need to be designed with due consideration being given to vessel impact loading.

The AASHTO provisions use a kinetic energy based methodology to determine the design force imparted to a bridge pier during a vessel collision event. Load calculations begin with selection of the "design" impact condition (barge type and impact speed). Factors such as the characteristics of the waterway, expected types of barge traffic, and the importance of the bridge (critical or regular) enter into this selection process. Once the impact conditions have been identified, the kinetic energy of the barge is computed as (AASHTO 1991):

$$KE = \frac{C_H W V^2}{29.2} \tag{2.1}$$

where is KE is the barge kinetic energy (kip-ft), C_H is the hydrodynamic mass coefficient, W is the vessel weight (in tonnes where 1 tonne = 2205 lbs.), and V is the impact speed (ft/sec). It is noted that Eq. 2.1 is simply an empirical version (derived for a specific set of units) of the more common relationship:

$$KE = C_H \left(\tfrac{1}{2} M V^2 \right) \tag{2.2}$$

where KE, M (the vessel mass), and V are all dimensionally consistent. The hydrodynamic mass coefficient, C_H, included in the AASHTO equation for kinetic energy, is present to account for additional inertia forces caused by the mass of the water surrounding and moving with the vessel. Several variables may be accounted for in the determination of C_H: water depth, underkeel clearances, shape of the vessel, speed, currents, position and location of the vessel in relation to the pier, direction of travel, stiffness of the barge, and the cleanliness of the hull underwater. A simplified expression has been adopted by AASHTO in the case of a vessel moving in a forward direction at high velocity (the worst-case scenario). Under such conditions, the recommended procedure depends only on the underkeel clearances (AASHTO 1991) :

- For large underkeel clearances $(\geq 0.5 \cdot Draft)$: $C_H = 1.05$
- For small underkeel clearances $(\leq 0.1 \cdot Draft)$: $C_H = 1.25$

where the draft is the distance between the bottom of the vessel and the floor of the waterway. For underkeel clearances between the two limits cited above, C_H is estimated by interpolation.

Once the kinetic energy of the barge flotilla has been determined, a two-part empirical load prediction model is used to determine the static-equivalent impact load. The first component of the model consists of an empirical relationship that predicts barge crush deformation (inelastic deformation) as a function of kinetic energy:

$$a_B = \left(\sqrt{1 + \frac{KE}{5672}} - 1 \right) \cdot \left(\frac{10.2}{R_B} \right) \tag{2.3}$$

In this expression, a_B is the depth (ft.) of barge crush deformation (depth of penetration of the bridge pier into the bow of the barge), KE is the barge kinetic energy (kip-ft), and $R_B = \left(B_B / 35 \right)$ where B_B is the width of the barge (ft). Figure 2.10 graphically illustrates Eq. 2.3.

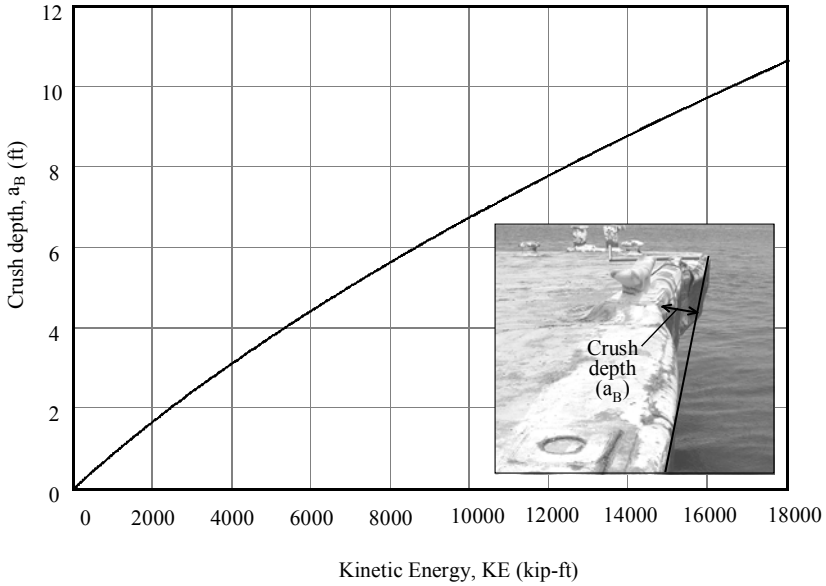

Figure 2.10 AASHTO relationship between kinetic energy and barge crush depth

The second component of the load prediction model consists of an empirical barge crush model that predicts impact loads as a function of crush depth :

$$P_B = \begin{cases} 4112\, a_B\, R_B & a_B < 0.34 \text{ ft.} \\ \left(1349 + 110\, a_B \right) R_B & a_B \geq 0.34 \text{ ft} \end{cases} \tag{2.4}$$

where P_B is the equivalent static barge impact load (kips) and a_B is the barge crush depth (ft). The AASHTO barge crush model represented by Eq. 2.4 is illustrated graphically in Figure 2.11. By substituting Eq. 2.3 into Eq. 2.4, a direct prediction of static impact load P_B may be obtained as a function of kinetic impact energy KE. The resulting relationship is illustrated in Figure 2.12. While AASHTO Eqs. 2.3 and 2.4 utilize the R_B term to reflect the influence of barge width, no such factor has been included to account for variations in either the size (width) or geometric shape of the bridge pier being impacted.

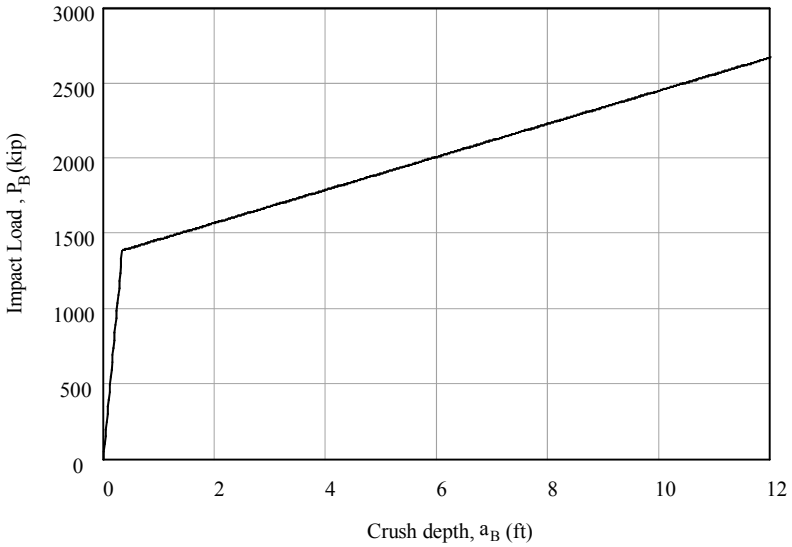

Figure 2.11 AASHTO relationship between barge crush depth and impact force

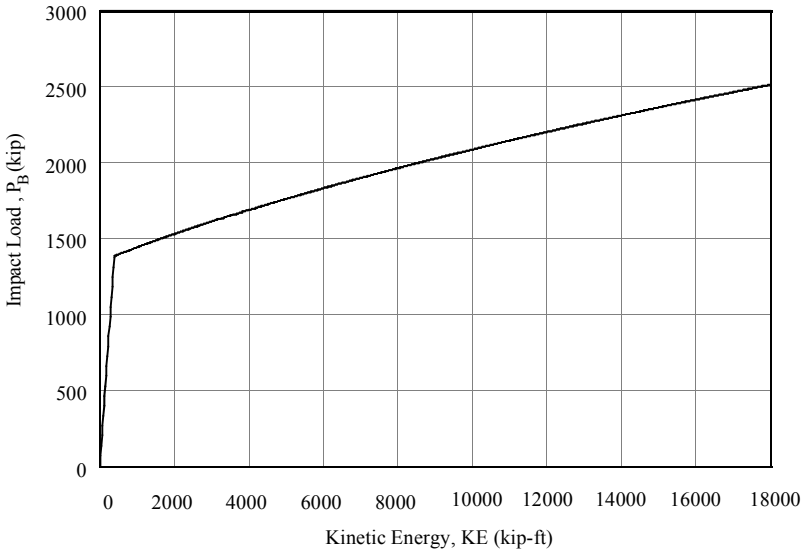

Figure 2.12 Relationship between kinetic energy and impact load

CHAPTER 3
TEST SITE DESCRIPTION

3.1 Introduction

All barge-pier collision tests described in this report were conducted at the old St. George Island Causeway bridge (also known as the Bryant Patton Bridge). Located in the Northwest panhandle region of Florida (Figure 3.1), and extending approximately 4 miles in length, the bridge spanned across Apalachicola Bay to connect St. George Island at the south end to the mainland of Florida at the north end (Figure 3.2). Because it was constructed during the 1960s, a time when national vessel collision design criteria were not in place, by the late 1990s the bridge had become structurally inadequate in terms of modern vessel collision resistance standards. To address this issue, the Florida Department of Transportation (FDOT) initiated construction of a replacement bridge in 2000.

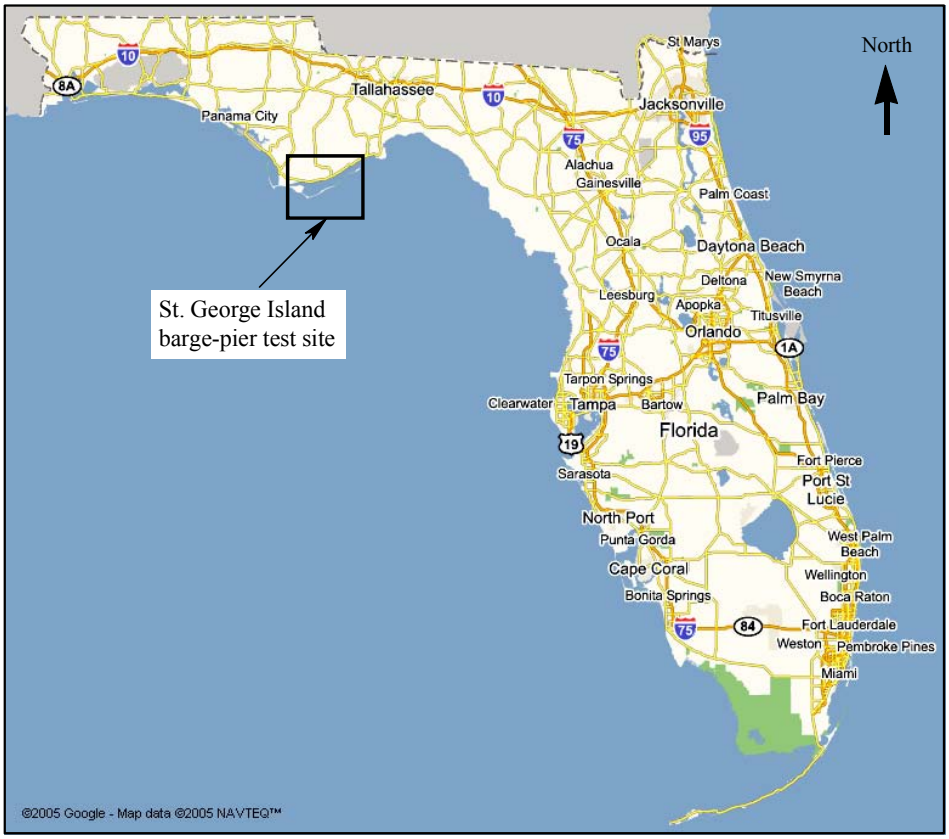

Figure 3.1 Location of the test site within the state of Florida

Both St. George Island bridges—new and old—cross (or crossed before demolition) the Florida intracoastal waterway that lies in the southern half of Apalachicola Bay (Figure 3.3). Barges routinely pass along this waterway to move materials between local ports, the Apalachicola River, and the Gulf of Mexico. Due to the environmentally sensitive nature of Apalachicola Bay, the alignment of the replacement bridge was deviated to the

West of the old structure (Figure 3.4) by more than 1500 ft. at locations near the intracoastal waterway. This deviation prevented construction-related disturbances of prime oyster harvesting areas located near the alignment of the old bridge. The deviation also produced a unique opportunity to conduct full-scale barge collision tests on the old structure without endangering the new replacement bridge.

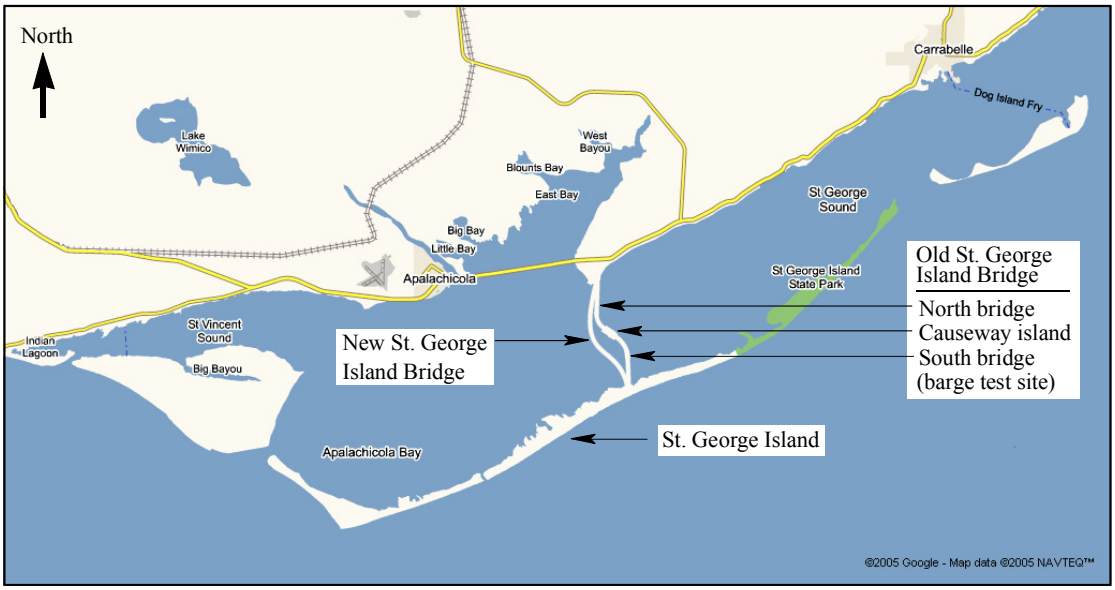

Figure 3.2 St. George Island, Florida and surrounding area

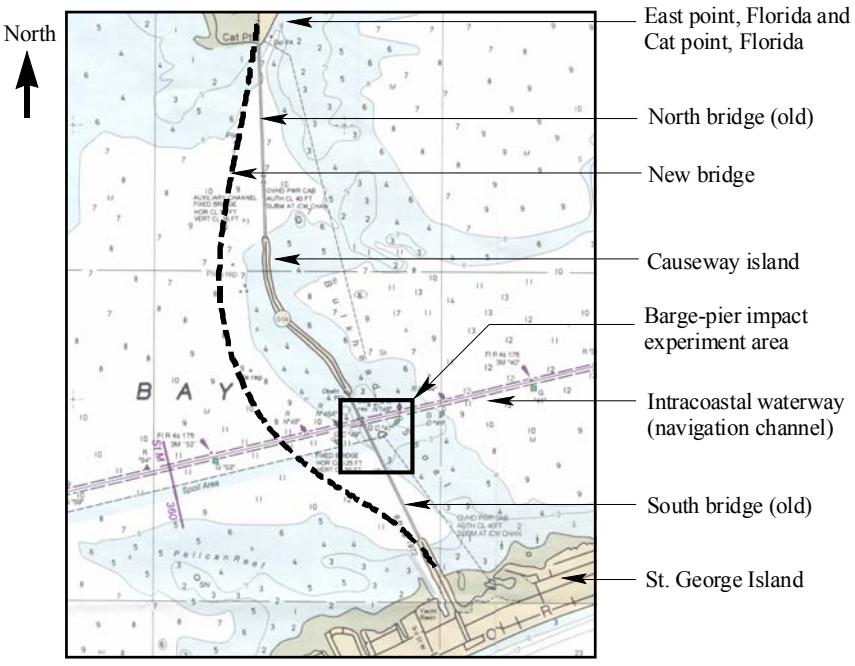

Figure 3.3 Nautical map of area surrounding the St. George Island Causeway Bridges

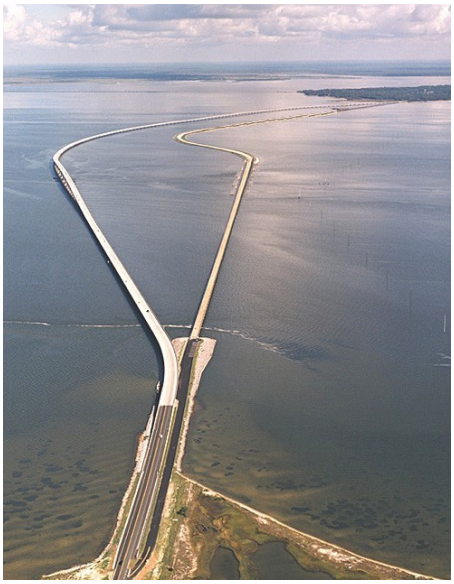

Figure 3.4 Aerial view, looking north, of St. George Island Causeway Bridges
(Barge impact tests were conducted on the old bridge, at right)

In reality, the old St. George Island bridge was actually two separate structures—northern and southern spans—that met at a causeway island near the central region of Apalachicola Bay (Figure 3.3). The tests conducted in this study were performed on portions of the southern bridge, located near the navigation channel. Two separate bathymetric surveys were conducted—one in 2001 and another in 2003—to survey bay bottom depths (water depths) in areas north and south of the navigation channel, and east and west of the old bridge alignment. Based on results obtained from these surveys, it was found that water depths in the area Southwest of the intersection of the navigation channel and the old bridge alignment were sufficient to support full-scale barge impact testing activities.

Construction of the new St. George Island bridge was completed in February 2004, after which time vehicular traffic was routed onto the new structure. Immediately thereafter, demolition of portions of the old bridge began. Simultaneously, and in close coordination with the bridge demolition contractors, researchers from the University of Florida (UF) completed installation of a variety of sensors on piers south of the navigation channel† (Figure 3.5). Pier-1 and Pier-3 were specifically chosen for direct barge collision testing because these piers were accessible from the navigation channel and represented a significant range of structural stiffness, Pier-1 being impact resistant and Pier-3 being much less so. However, instrumentation was also placed on Pier-2 and Pier-4—again, both on the south side of the navigation channel (Figure 3.6)—because a portion of the planned tests involved striking Pier-3 with a barge while leaving the bridge superstructure in-place. For this series of tests, Pier-2 and Pier-4 were linked to Pier-3 through the bridge superstructure.

† All piers studied in this research project were located on the southern side of the navigation channel. Piers are identified in this report as Pier-#, where # indicates position relative to the navigation channel. In McVay et al. (2005), these same piers are identified instead as Pier-#S where "S" is used to emphasize that the piers were located on the southern side of the navigation channel.

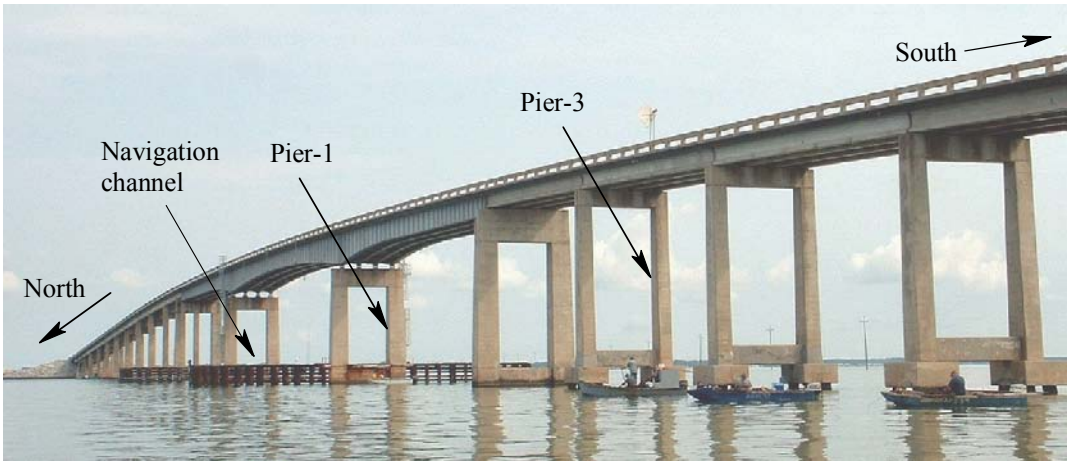

Figure 3.5 Location of Pier-1 and Pier-3

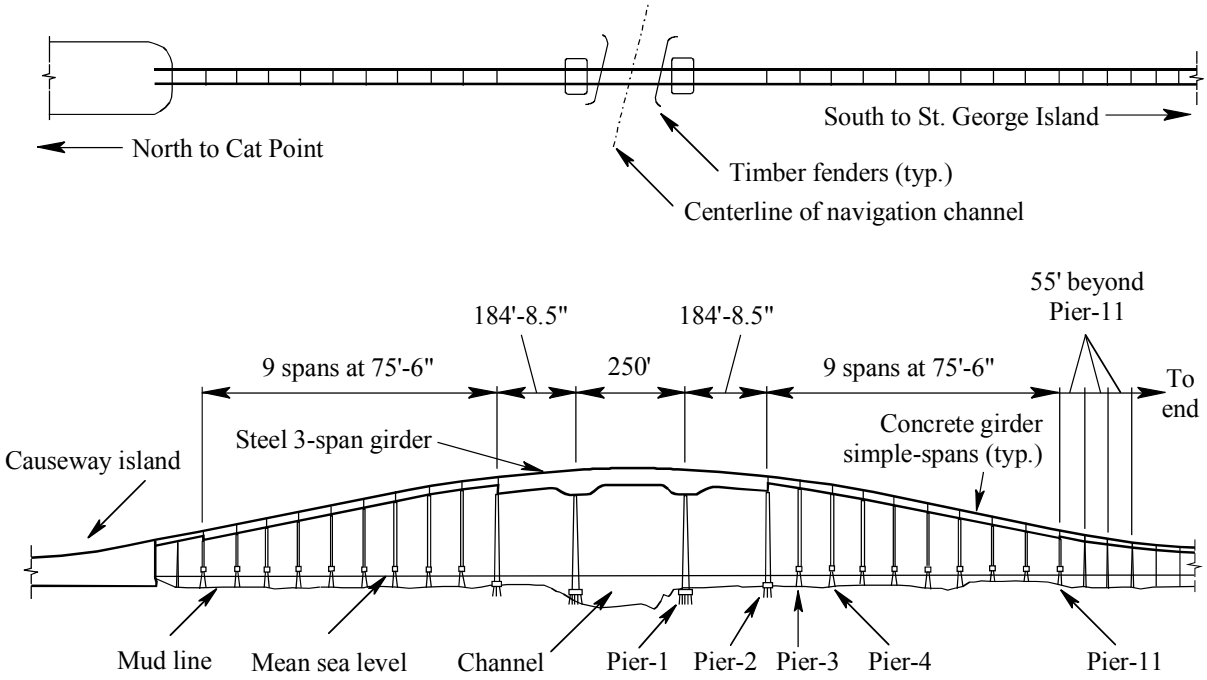

Figure 3.6 Plan and elevation views of the bridge in the vicinity of the navigation channel

A majority of the old St. George Island bridge consisted of 55 ft. long, simple span concrete girder-and-slab bridge sections supported on pile bents. Nearer to the intracoastal waterway, however, portions of the bridge consisted of 75 ft. – 6 in. concrete girder-and-slab bridge segments (Figure 3.6) supported on concrete piers that had waterline footings, which were founded on square prestressed concrete piles. Directly above, and on either side of the intracoastal waterway, a continuous 619 ft. – 5 in. three-span steel girder and concrete slab bridge segment rested atop impact resistant piers with mudline footings founded on steel H-piles. Although it was deemed highly unlikely that the three-span steel bridge section could be dislodged from the support piers as a result of impact tests planned for Pier-1, as a safety

precaution, this portion of the bridge deck was removed prior to testing. The risk of dislodging the steel structure and having it fall and block the intracoastal waterway was considered to be outside the acceptable range of risk. Additionally, the ability of Pier-1 to resist impact loads fully on its own, without the aid of superstructure stiffness, was of primary interest.

3.2 Descriptions of instrumented piers

Given that the old St. George Island bridge was constructed during the 1960s, at a time well in advance of the 1991 publication of the AASHTO vessel collision design provisions, it is not surprising that piers supporting the bridge failed to measure up to current standards for vessel collision resistance. However, designers in the 1960s were aware of the risks associated with barges striking bridge piers, particularly those located close to the navigation channel. As a result, in the old St. George Island bridge, the four piers located nearest the navigation channel—Pier-1 and Pier-2 on the south, and the counterparts on the north—were designed to possess significant impact resistance per the standards of the day. At greater distances away from the channel, piers supporting the approach spans—e.g., Pier-3, Pier-4, etc. south of the channel—were perceived to be at less risk, and were therefore designed with significantly less impact resistance. As a result of these differences, the structure and foundation configurations selected for Pier-1 and Pier-2 differed from that of Pier-3, Pier-4, and beyond.

As indicated in Figure 3.7a, the reinforced concrete (R/C) Pier-1 structure consisted of two pier columns, a pier cap, and a shear wall. Supporting the pier was a massive mudline footing comprised of a pile cap, tremie seal, and forty HP 14x73 steel piles. An underwater inspection of the foundation of Pier-1 indicated that neither the pile cap nor the tremie seal were structurally compromised, and that the bay bottom mudline was located approximately at the top of the pile cap. Consequently, none of the steel H-piles were directly exposed to saltwater.

Similar in configuration to Pier-1 but possessing less lateral load carrying capacity was Pier-2. This R/C structure was comprised of two pier columns, a pier cap, and shear wall (Figure 3.7b) supported on a mudline foundation consisting of a pile cap, tremie seal, and twenty-one HP 14x73 steel piles. Visual inspection of the foundation indicated that both the pile cap and tremie seal were in good condition. Additionally, the mudline was observed to be at the top of the tremie seal, and as such, the steel H-piles were fully embedded in soil and not directly exposed to salt water.

In contrast to Pier-1 and Pier-2, Pier-3 consisted of two smaller concrete columns, a pier cap, and a relatively slender shear strut (Figure 3.8a). Additionally, rather than utilizing a mudline footing, Pier-3 employed a waterline footing system consisting of two separate R/C pile caps, each founded on four battered 20 in. square prestressed concrete piles. A free pile length of approximately 12 ft. extended from the bottom of the pile caps to the mudline at the bay bottom. As a result, Pier-3 possessed considerably more flexibility than either Pier-1 or Pier-2 and possessed much less lateral load carrying capacity. Pier-4 was similar to Pier-3 structurally, the major exception being the overall height of the pier columns, as indicated in Figure 3.8b. The foundation of Pier-4 was identical to that of Pier-3. As was the case for Pier-1 and Pier-2, underwater visual inspection of Pier-3 and Pier-4 indicated that the integrity of the piles supporting the piers was not compromised.

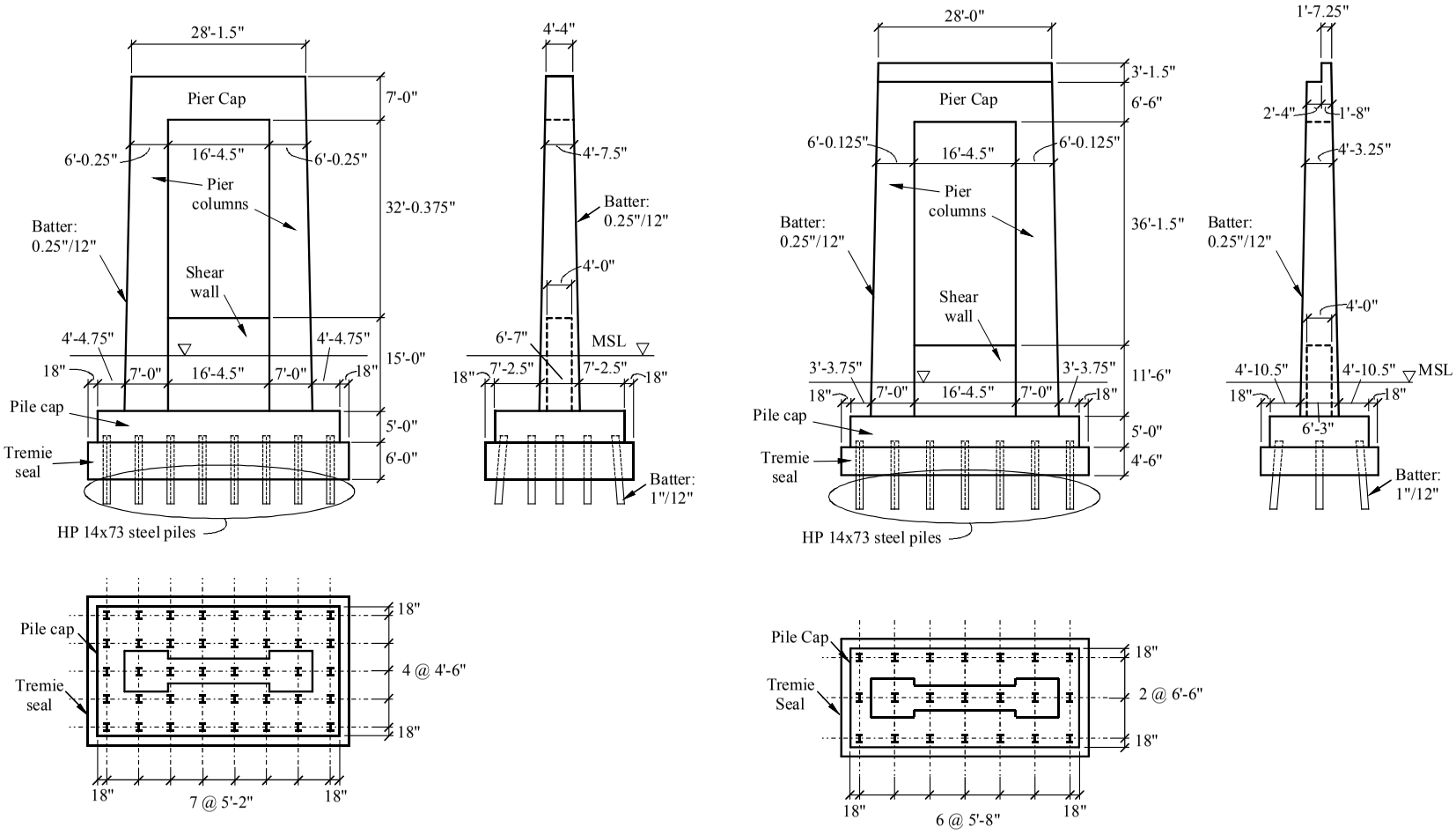

a) Pier-1 b) Pier-2

Figure 3.7 Schematic diagrams of piers with mudline footings

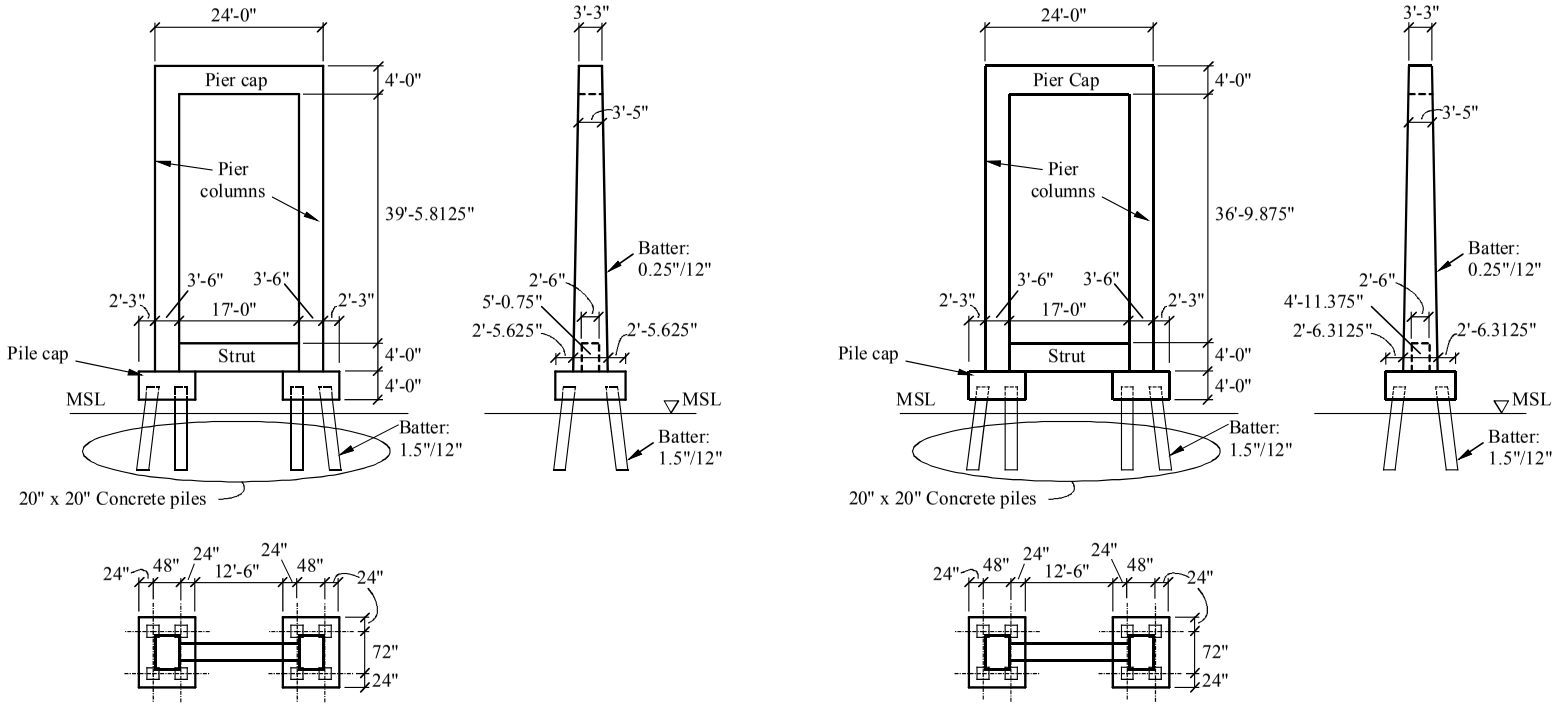

a) Pier-3

b) Pier-4

Figure 3.8 Schematic diagrams of piers with waterline footings

3.3 Description of bridge superstructure

As previously noted, for one series of tests conducted on Pier-3, segments of the superstructure (bridge deck) linking Pier-2, Pier-3, Pier-4, and beyond were left intact. Spanning 75 ft – 6 in. between piers, each of these simple span bridge superstructure segments was composed of a 7.5 in. thick concrete deck compositely cast in-place with four AASHTO Type II prestressed concrete girders (Figure 3.9). At both ends and the midpoint of each span, diaphragms spanning transversely between the girders were also cast. Running longitudinally, concrete barrier railings were cast along each side of the bridge.

Beyond Pier-11 on the south side of the channel, the bridge deck span lengths decreased from 75 ft – 6 in. to 55 ft. Some of these spans—as discussed later in this report—were used as payload to increase the mass of the test barge during selected tests. The cross-section of the shorter 55 ft. spans was identical to that of the longer 75 ft. – 6 in. spans, and diaphragms were once again cast at both ends and at midspan of these shorter segments. Based on the geometry of the superstructure spans, their approximate weights were computed as: 190 tons (380 kips) per 75 ft. – 6 in. span and 141 tons (282 kips) per 55 ft. span.

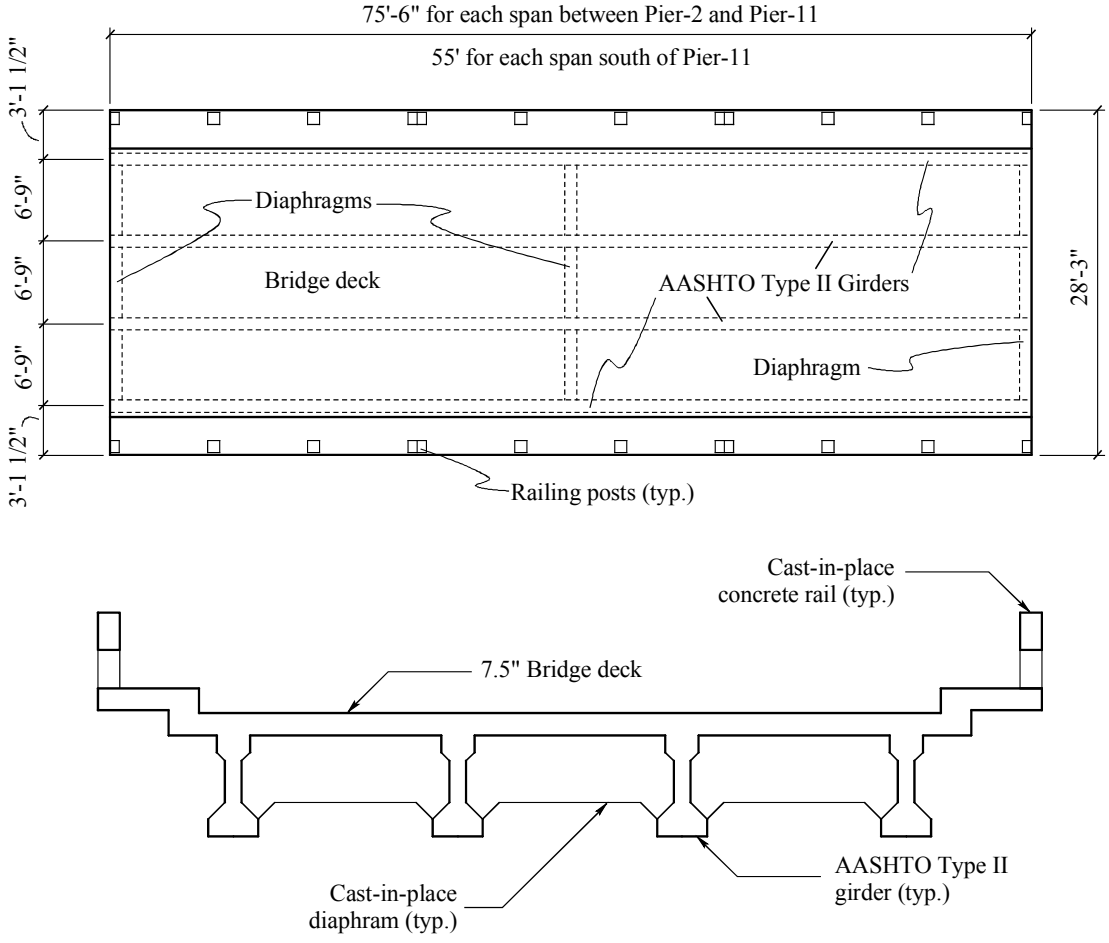

Figure 3.9 Plan and cross-sectional views of bridge superstructure

3.4 Structural material properties

Material properties for the cast-in-place concrete piers, pile caps, and bridge superstructure were determined by taking three core samples from the shear wall area of Pier-1. (The assistance provided by the FDOT Structures Research Laboratory in obtaining these core samples is gratefully acknowledged.) Subsequent laboratory testing of the samples—conducted by the University of Florida (UF) Civil and Coastal Engineering (CCE) materials research group—produced the data listed in Table 3.1. Averaging these values, the mean modulus of elasticity was determined to be $E_c = 4442$ ksi, while the mean Poisson ratio was determined to be $\nu = 0.167$. These material properties were assumed to be representative of all concrete structural components of the piers. The unit weight of the concrete was assumed to be approximately 150 pcf. For purposes of later finite element analysis, the HP 14x73 steel piles supporting Pier-1 and Pier-2 were assumed to have a modulus of elasticity of 29,000 ksi, a Poisson ratio of 0.3, and a unit weight of 490 pcf.

Table 3.1 Elastic modulus and Poisson ratio data from concrete cores

Core number	Elastic modulus (ksi)	Poisson ratio
1	4110	0.229
2	4938	0.140
3	4277	0.132

3.5 Soil conditions at Pier-1 and Pier-3

Determination of insitu properties of the soil surrounding Pier-1 and Pier-3—the two piers subjected to direct barge impact testing—was accomplished via a geotechnical investigation carried out in parallel to the study described in this report. Only summary information regarding soil data is provided here. For additional details regarding test methods used and computation of soil properties, the reader is referred to McVay et al. (2005).

Based on data obtained from the geotechnical insitu field tests (SPT, CPT, etc.), soil profiles were developed for Pier-1 (Figure 3.10) and for Pier-3 (Figure 3.11). Soil properties for each layer within these profiles were computed through a combination of insitu tests as well as data obtained during dynamic barge impact testing. The resulting property values are summarized Table 3.2 and Table 3.3.

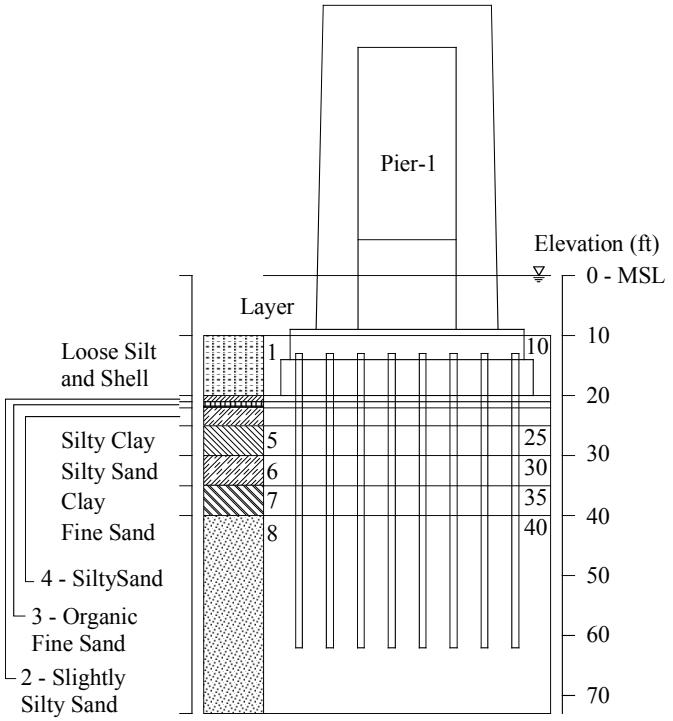

Figure 3.10 Soil profile at Pier-1

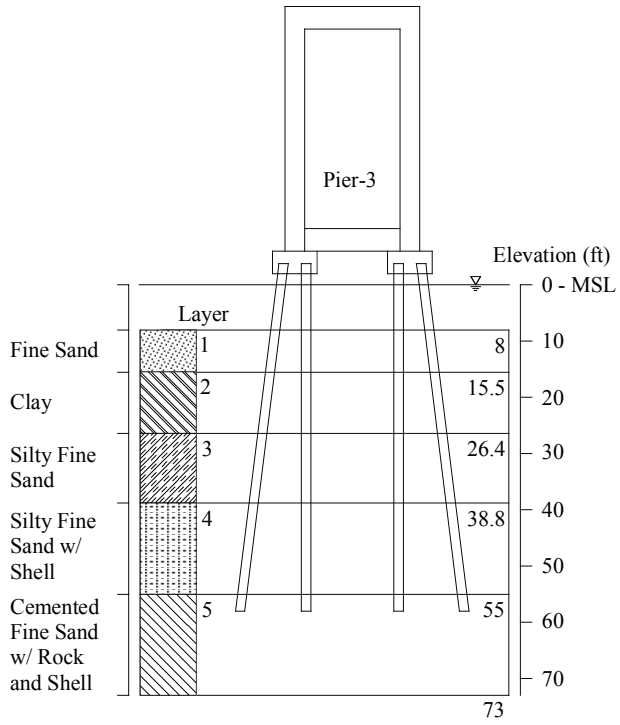

Figure 3.11 Pier-3 soil profile

Table 3.2 Soil properties from in-situ tests at Pier-1

Layer	Soil type	SPT	Depth (ft)	Unit weight (pcf)	Friction angle (deg)	Subgrade (kcf)	Undr. strength (psf)	Strain at 50%	Shear mod. (ksi)	Poisson's ratio	Vert. shear fail. (psf)
1	Loose silt and shell	3	9-20	97	27	43	104	0.02	0.632	0.3	280.1
2	Slightly silty sand	2	20-21	106.33	27	35	NA	NA	1.075	0.3	188.5
3	Organic fine sand	2	21-22	104.33	NA	NA	574	0.02	0.145	0.37	161.9
4	Silty sand	2	22-25	109.67	27	51	NA	NA	2.043	0.3	188.5
5	Silty clay to clayey silt	3	25-30	97	NA	NA	331.33	0.02	0.096	0.2	280.1
6	Silty sand	5	30-35	109	28	77	NA	NA	4.73	0.3	458.2
7	Clay	10	35-40	99.5	NA	NA	370.67	0.07	0.095	0.35	543.2
8	Fine sand	30	40-63	125.33	33	224	NA	NA	23.277	0.37	423.4

Table 3.3 Soil properties from in-situ tests at Pier-3

Layer	Soil type	SPT	Depth (ft)	Unit weight (pcf)	Friction angle (deg)	Subgrade (kcf)	Undr. strength (psf)	Strain at 50%	Shear mod. (ksi)	Poisson's ratio	Vert. shear fail. (psf)
1	Fine sand	3	8-15.5	110	27	35	NA	NA	0.375	0.2	1200
2	Clay	2	15.5-26.4	100	NA	NA	1500	0.02	0.139	0.25	488
3	Silty fine sand	5	26.4-38.8	119	28	67	NA	NA	0.675	0.3	400
4	Silty fine sand	10	38.8-55	124	31	78	NA	NA	3	0.35	2260
5	Cmt. fine sand	39	55-73	124	40	147	NA	NA	8	0.4	2300

CHAPTER 4
BARGE AND PUSHBOAT DESCRIPTIONS

4.1 Introduction

Barge impact tests described in this report were carried out using a construction deck barge (Figure 4.1) that was rented from Boh Bros. Construction Co., L.L.C. of Baton Rouge, Louisiana. Boh Bros. had been contracted by the FDOT to construct the new St. George Island bridge—as well as to demolish the old structure—and therefore, had a significant number of construction vessels already mobilized on-site at St. George Island. Therefore, it was logical from logistical, scheduling, and economic points of view to rent a barge from Boh Bros. for use in this study. After completion of all collision tests, Boh Bros. repaired the damage caused to the barge by the collision tests, and was reimbursed for the repair costs.

Figure 4.1 Construction deck barge used to conduct impact tests

In addition to providing a barge, Boh. Bros. also provided several additional vessels (for a fee) on an as needed basis. In particular, two pushboats (tug boats), a barge with high-capacity winches, and several smaller helper boats—used to guide the test barge during impact testing—were employed during the tests. Beyond providing vessels and corresponding crews, however, it must also be noted that Boh Bros. personnel also offered numerous valuable insights and suggestions that unquestionably contributed to the successful execution of the test program. These contributions are gratefully acknowledged.

4.2 Description of the test barge

Overall dimensions of the construction deck barge are given in Figure 4.2. Based on fabrication drawings provided by Boh Bros., as well as direct physical inspection and measurements, it was determined that the outer hull of the barge was composed of steel plates with thicknesses varying from 1/4 in. to 3/8 in. Internal stiffening of the hull in the raked bow section was provided by a system of cross-braced frames (Figure 4.3). The frames were fabricated in several different structural configurations (Figure 4.4), which were alternately staggered across the width of the barge to distribute internal stiffness. Each frame was constructed from steel angles and channels, and tapered with respect to depth. At the barge bow, steel angles and channels were used to further stiffen the headlog.

It was determined, based on discussions with Boh Bros. personnel, that all steel used in fabrication of the barge was A36 steel having an approximate yield stress equal to $F_y = 36$ ksi. Visual inspections, conducted prior to impact testing, did not reveal any significant damage (either external or internal) that might compromise the structural integrity of the barge during impact testing. Furthermore, no significant corrosion of the steel hull plates or internal frames was found.

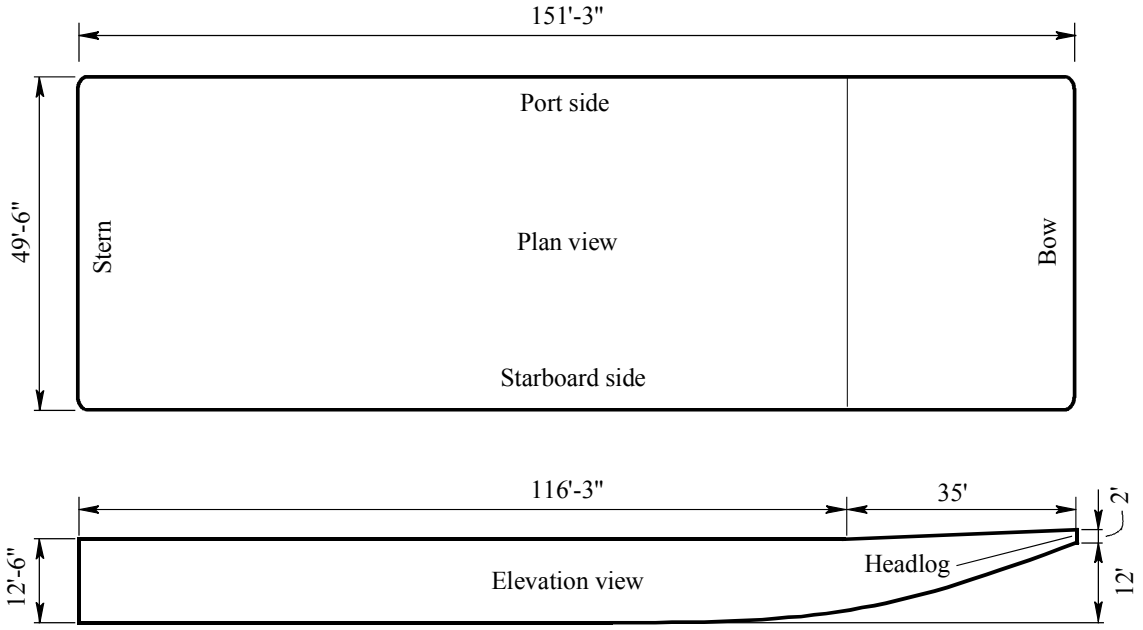

Figure 4.2 Overall dimensions of test barge

4.3 Descriptions of pushboats

Two pushboats (also referred to as "tugboats") were used to propel the barge during the test program: a 24 ton pushboat (Figure 4.6a) and a 20 ton pushboat (Figure 4.6b). Both vessels were shallow-draft and powered by twin Detroit 671 diesel engines (each engine rated at approximately 200 horsepower). During most of the tests, only one of the two pushboats was used. However, during selected tests on Pier-1, both boats were used simultaneously (i.e., in tandem) to generate higher levels of thrust and thus higher levels of barge acceleration and impact speed.

4.4 Barge payload conditions

As noted in the previous chapter, the impact resistances of Pier-1 and Pier-3 differed significantly due to differences in pier size and foundation type. Control of kinetic energy at impact during each test, $KE = (1/2)\,m\,v^2$, was achieved through selection of both the target impact speed and barge mass. In conducting tests on Pier-3, the mass of an empty barge (Figure 4.7), coupled together with selected target impact speeds, was sufficient to generate

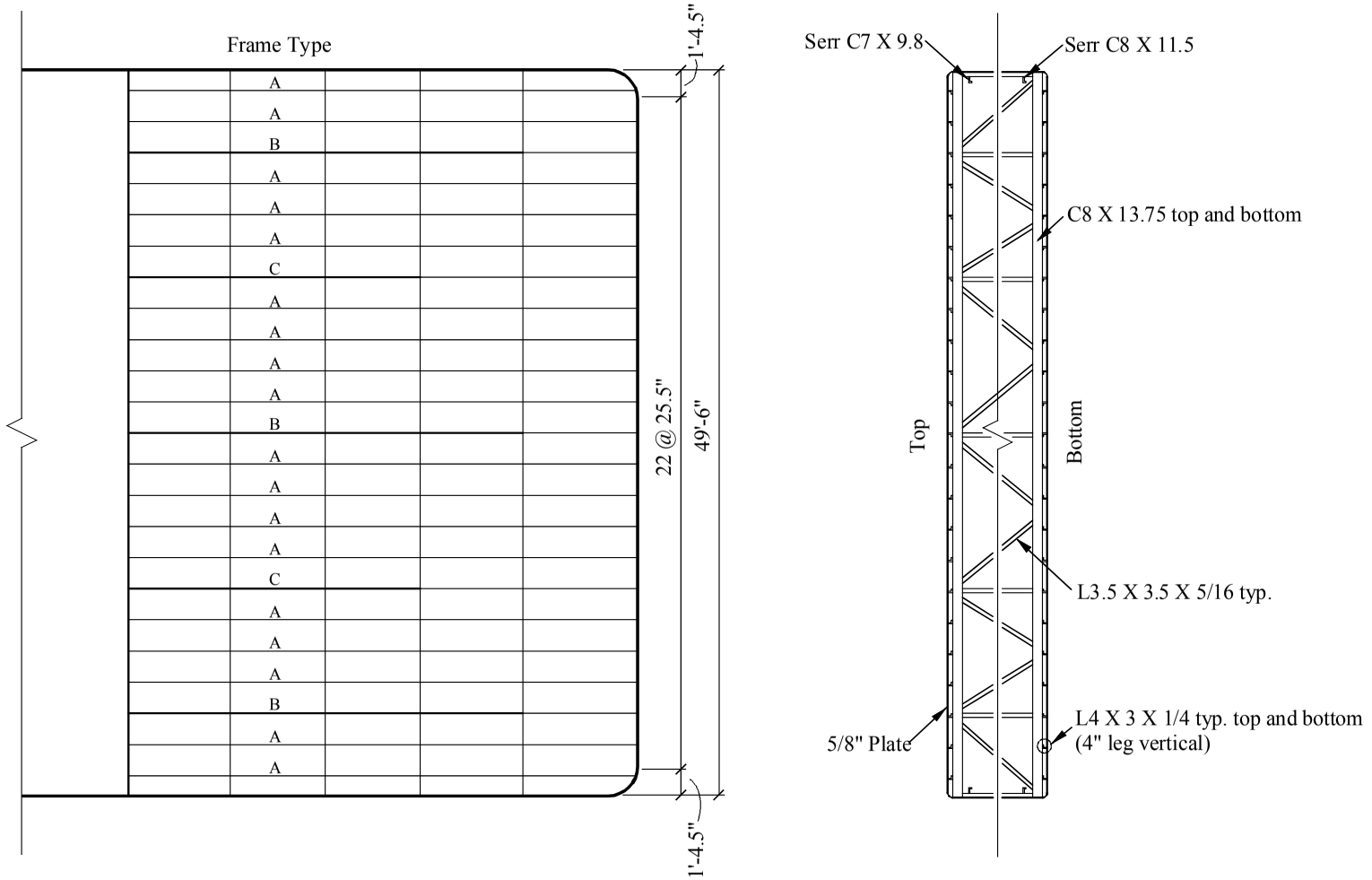

a) Hull framing plan (N.T.S.)

b) Typical cross section (N.T.S.)

Figure 4.3 Framing plan and cross-section of raked barge bow

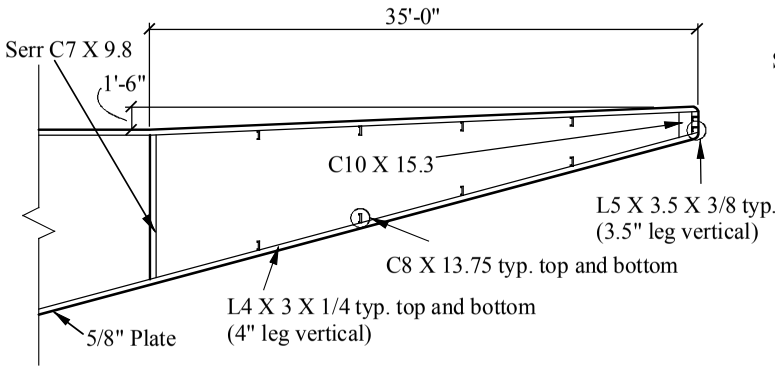

Hull frame type A
N.T.S.

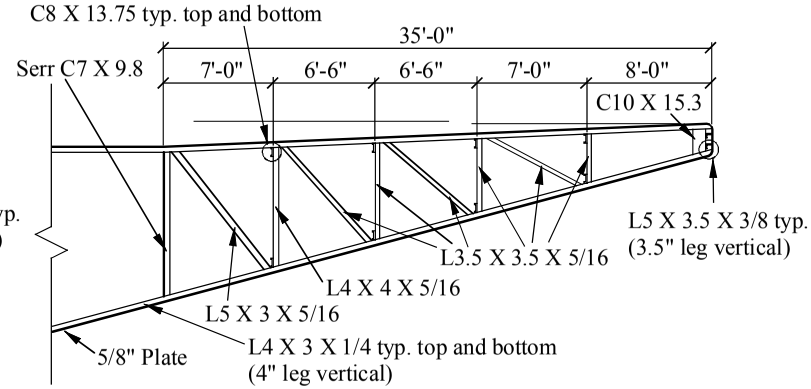

Hull frame type B
N.T.S.

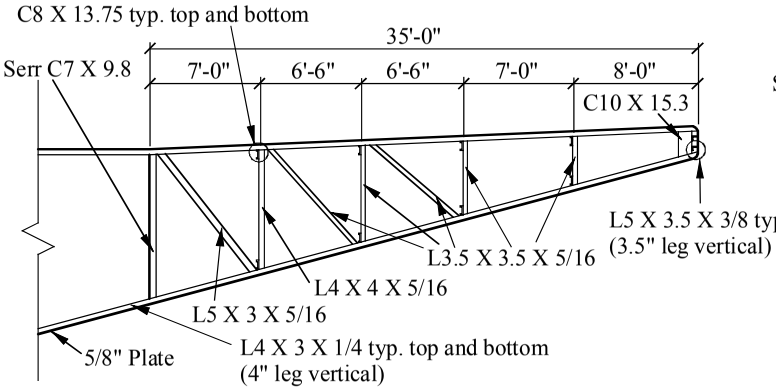

Hull frame type C
N.T.S.

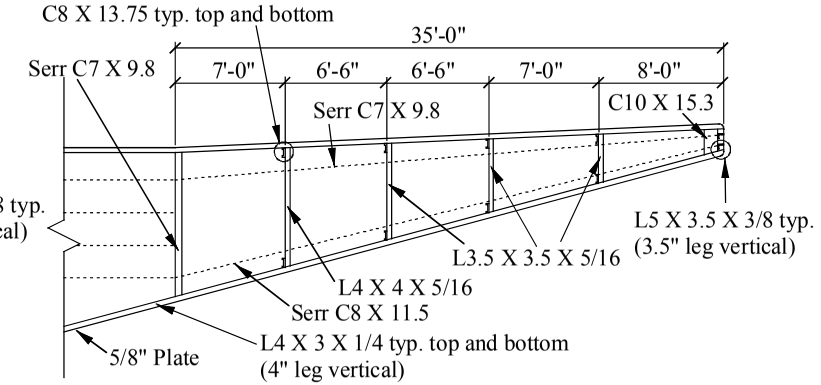

Side wall profile
N.T.S.

Figure 4.4 Structural configuration of raked frames

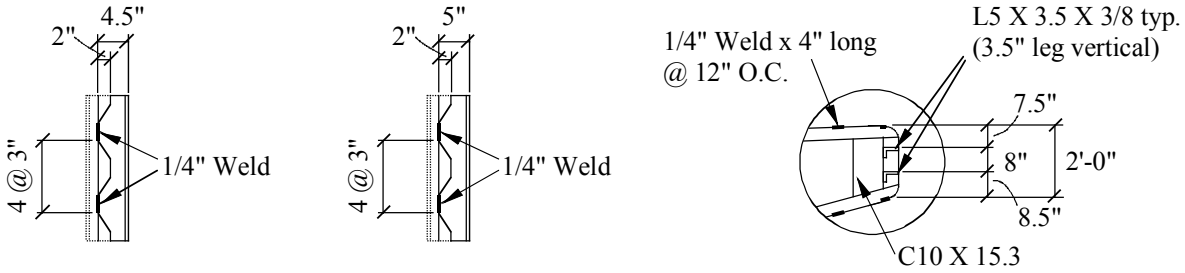

a) Serrated C7x9.8 channel detail (N.T.S.)

b) Serrated C8x11.5 channel detail (N.T.S.)

c) Barge headlog detail (N.T.S.)

Figure 4.5 Structural details for raked bow portion of barge

a) 24 ton pushboat

b) 20 ton pushboat

Figure 4.6 Pushboats used during impact testing

Figure 4.7 Empty-barge condition used during tests on Pier-3

the desired impact energies. In contrast, for Pier-1, it was anticipated that much larger impact loads could be successfully sustained by the pier. Consequently, impact loads and pier response at higher impact energies could be studied, including—importantly—the influence of barge bow crushing deformation. To achieve these higher energies, while staying within impact speeds that could be safely carried out, the mass of the test barge was increased. To accomplish this, a payload consisting of two 55 ft. long concrete bridge deck spans was loaded onto the barge for all Pier-1 impact tests (Figure 4.8).

a) Test barge with payload consisting of two 55 ft. long bridge spans

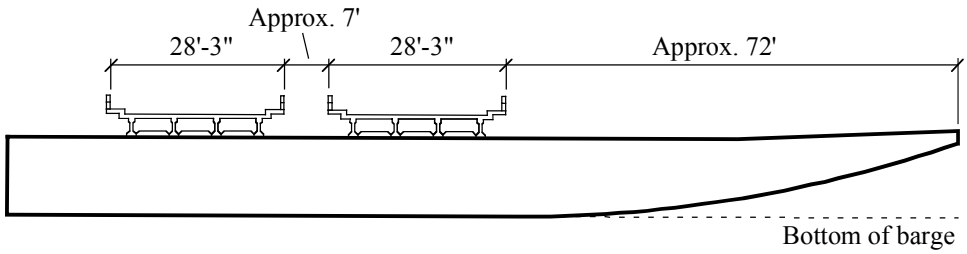

b) Positions of payload spans on test barge

Figure 4.8 Loaded-barge condition used during tests on Pier-1

4.5 Barge draft conditions and weight determination

As will be discussed in more detail later in this report, impact tests on Pier-1 occurred chronologically before the tests on Pier-3. In preparation for the Pier-1 tests, the payload of two 55 ft. bridge spans was loaded onto the barge. Subsequently, the draft profile of the loaded barge was determined by measuring the position of the water line relative to the bottom surface of the barge. Measurements of draft depth were made at 5 ft. intervals along the entire length of the barge using a rigid aluminum square affixed to a ruled aluminum pole (Figure 4.9). Hooking the end of the square under the barge bottom, draft measurements were then recorded from the rule marks. In Figure 4.10, the draft positions of the barge in the loaded (Pier-1) and empty (Pier-3) conditions are illustrated. Note that in the empty (unloaded) condition, due to the length of the raked bow, the barge tended to pitch forward. That is, the barge sloped in a mildly downward direction from stern (back) to bow (front).

Given that the water surface did not remain absolutely stationary during the draft measurement process, the recorded depth values varied slightly. A least squares curve fitting process was therefore applied to the measured data to determine the best-fit draft line, i.e. the line defining the top of the submerged portion of the barge. The weight of the barge was then computed using this best-fit draft line and Archimedes' principle, which states: the weight of water displaced by a floating object is equal to the weight of the object. The total submerged barge volume (the volume of displaced water) was computed using the best-fit draft line and the known geometry of the barge hull. By multiplying this volume by the unit weight of saltwater (64 pcf), the barge weight was established.

Figure 4.9 Measurement of barge draft

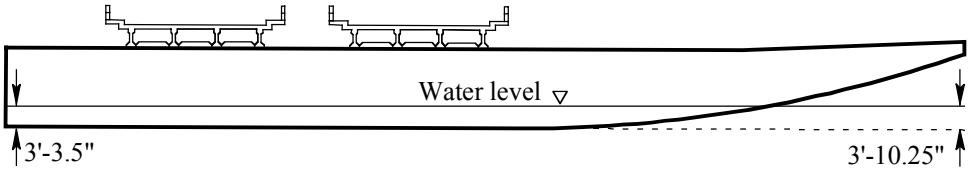

a) Loaded-barge draft condition

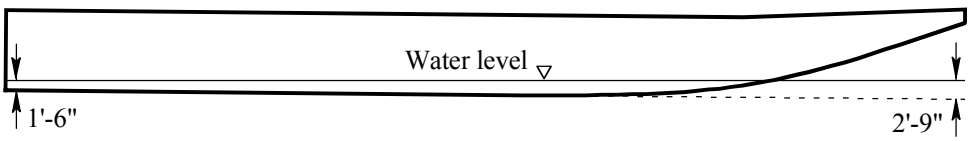

b) Empty-barge draft condition

Figure 4.10 Barge draft conditions

When the draft measurements were made, the barge was anchored in place using two steel spuds (Figure 4.11) approximately 60 ft. long and 26 in. in diameter. To anchor the barge, the spuds were passed vertically through spud-wells in the barge deck and then "speared" into the bay bottom. Weight load from the spuds, therefore, neither acted on the barge nor contributed to displacement of water during the draft measurement process. However, during each of the impact tests, the spuds were raised off the bay bottom and either placed on the barge deck (Figure 4.11) or suspended in the spud wells (Figure 4.8a). As a result, their mass contributed to the total impact energy delivered to the piers. Based on measured dimensions and an assumed unit weight of steel of 490 pcf, each spud was determined to weigh approximately 5 tons, thus producing a total additional weight of 10 tons for both spuds.

During each Pier-1 test, *except* an initial diagnostic impact test, the pushboats were connected to the test barge via a soft line that permitted the pushboats to back off from the barge just prior to impact. Hence, for all Pier-1 tests except the first, the pushboat mass did not contribute energy to the impact. However, for all Pier-3 tests—as well as the initial Pier-1 diagnostic test—the pushboats were connected to the barge via hard rigging, and therefore, the pushboat mass contributed additional kinetic energy during impact. An average value of pushboat weight, 22 tons = ½ (20 tons + 24 tons), was then added to the barge and spud weights for these tests when computing kinetic impact energy. A summary of the component and total weights for each test condition is given in Table 4.1.

a) Lifting posts at top of spud b) Pointed tip at bottom of spud

Figure 4.11 Steel anchor spuds

4.6 Measurement of inelastic barge deformation (pre- and post-test)

Following each of the Pier-1 impact tests—excluding the initial diagnostic test—the level of permanent (inelastic) deformation (also called "crush") caused to the barge bow was non-negligible. Deformation of this type occurs when steel plates, angles, and channels in the barge bow yield, fracture, or tear. Because such processes are non-reversible, they constitute a form a energy dissipation which is capable of consuming part of the kinetic impact energy of the barge. It was therefore desirable to quantify the extent of permanent barge crush

produced by each Pier-1 impact test. During the Pier-3 tests, no measurable permanent barge deformations were observed, therefore crush measurements were not made.

Table 4.1 Summary of impact weights

Impact tests performed	Barge weight (tons)	Payload weight: (tons)	Avg. push boat weight (tons)	Spud weight (tons)	Total impact weight (tons)
Pier-1: Initial diagnostic test	312	282 *	22	10	626
Pier-1: All remaining tests	312	282 *	0 +	10	604
Pier-3: All tests	312	0 #	22	10	344

* Weight of two 55 ft. long bridge deck spans

+ Pushboat separated (backed-off) from barge prior to impact

Payload not present on empty barge

Barge crush deformations for the Pier-1 tests were quantified by measuring damage depths at multiple lateral positions across the width of barge following each test (Figure 4.12). Each set of recorded crush measurements then constituted a "profile" of barge bow damage. Crush depth measurements were carried out using two parallel reference lines: a datum line and an alignment line. At distances of 23 ft. and 15 ft. astern of the headlog, both were well outside of the zone of significant deformation, and therefore, remained stationary during each test. Physically, the reference lines were fabricated from two 8 ft. - 3 in. long, thick-walled square aluminum tubes that were ruled with tick marks every 3 in. along their lengths. The tubes were affixed to the barge by connecting them to steel brackets welded to the deck of the barge. Brackets were installed every 8 ft. transversely across the barge along both of the reference lines. Using a tape rule that was accurate to within 0.04 in. (1 mm), measurements from the barge bow (Figure 4.13a) to the datum line (Figure 4.13b) were made. By ensuring that the tape rule passed directly over matching tick marks on both reference beams, barge crush depths were recorded at specific locations across the width of the barge.

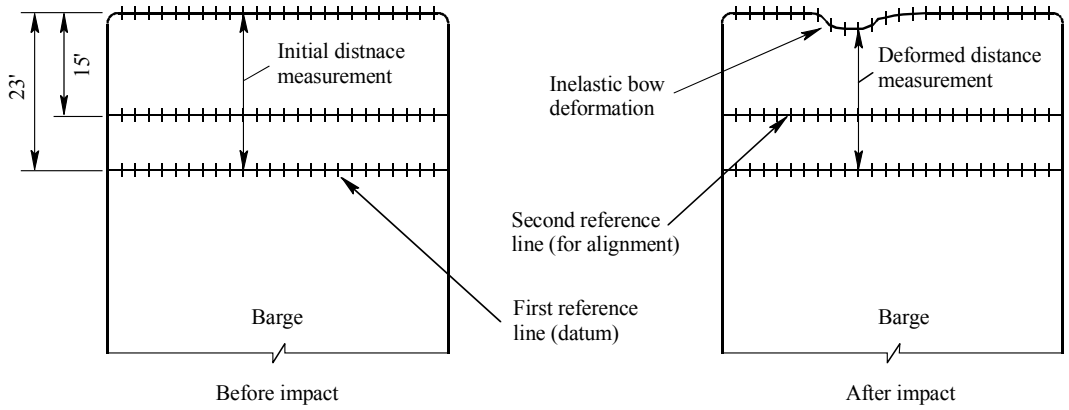

Figure 4.12 Process used to measure inelastic barge deformation

Prior to impact testing, this procedure was performed to measure and establish the undamaged profile of the entire barge bow width. Later, after completing each impact test, the barge profile was again re-measured using the same procedure. Measurements were nominally taken at 6 in. transverse spacings, but smaller spacings were used in locations where the damage profile changed rapidly. Several of the Pier-1 collision tests involved impacts at previously damaged areas of the barge bow. Thus, in general, the damage profiles measured after each test were cumulative in nature including both damage from the test just conducted as well as damage associated with earlier impacts. Incremental damage profiles, representing the increment of damage caused by a particular impact test and its associated energy, were then computed by taking differences between measured damage profiles from successive tests.

a) Positioning tape rule and rigid square at bow

b) Recording distance measurements at datum beam

Figure 4.13 Measurement of inelastic barge deformation

CHAPTER 5
TEST PROGRAM OVERVIEW

5.1 Introduction

The complete set of barge impact experiments conducted on Pier-1 and Pier-3 were performed in three separate and distinct series of tests, each involving impacts on a unique structural configuration. The differences in structural configuration, in turn, led to differences in instrumentation (data collection) systems, as well as barge mass. In this chapter, overall characteristics of each test series are described. Details relating to the instrumentation networks employed during each test series are given in the following chapter.

5.2 Series P1 : Pier-1 impacted by test barge

All tests in series P1 were conducted on Pier-1 in isolation (Figure 5.1), i.e., on the pier alone, with the 3-span continuous steel girder superstructure section removed. Primary goals in conducting this test series were to generate maximal impact loads, generate maximal inelastic barge deformations, and record dynamic pier and soil response during impact. In order to achieve the desired impact energy levels, the weight of the test barge was supplemented by loading two 55 ft. concrete bridge superstructure spans onto the deck of the barge (Figure 5.2).

An initial diagnostic impact test, denoted P1T1 (series P1, test 1), was performed at low speed (0.75 knots) for the purpose of verifying proper triggering and operation of the data acquisition systems. Following successful completion of this test, impact speeds for subsequent tests were increased to the fastest speed that could safely be achieved by the test equipment (3.45 knots). Due to the presence of strong cross-currents at the test site, it was necessary to minimize the barge acceleration distance, i.e. the distance between the barge starting point and the test pier. While starting the barge greater distances from the test pier would generally permit higher speeds to be attained at the time of impact, doing so also increased the likelihood that the barge trajectory would not result in an impact at the desired location on the barge bow. Thus, all acceleration distances were minimized to less than approximately 200 ft.

Barge acceleration was achieved (in part) by pushing at the stern using a pushboat. The pushboat was attached to the barge with soft lines, so that prior to impact, the pushboat could back off to avoid riding through the impact and thereby avoid sustaining motor-mount damage. To supplement the pushboats in accelerating the impact barge, a stationary barge was positioned (and spudded down) to the east of Pier-1, opposite side of the pier being impacted (Figure 5.3). Cables from two winches on this stationary barge were attached at the corners of the bow of the test barge. Acceleration of the test barge (Figure 5.4) was achieved both by pushing at the stern with a pushboat, and pulling at the bow with winch cables.

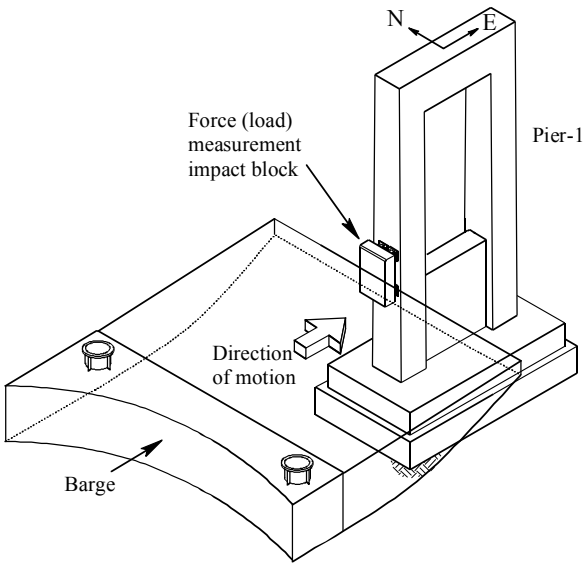

Figure 5.1 Structural configuration of Pier-1 during test series P1

Figure 5.2 Test barge with payload as used in series P1 tests

Figure 5.3 Stationary barge with winches spudded down on east side of Pier-1

Figure 5.4 Test barge propelled by pushboat and winch cables, and guided by helper boat during test series P1

Just prior to the time of impact, the pushboat would back off from the barge and tension in the winch cables would be released so that the barge was in a free-floating condition at impact. Since the pushboat was connected to the barge via soft lines, it was not able to completely control the trajectory of the barge during each test run. Hence, two additional helper boats were also employed to guide the barge by applying transverse thrust at locations near the barge bow. As noted in the previous chapter, the test barge, pushboats, stationary barge, winches, and helper boats used in this study were owned and operated by Boh Bros. Construction. During each test, the task of coordinating (in real-time) the forces that were being applied to the barge by the pushboat, winches, and helper boats was competently carried out by Mr. Scott Gros of Boh Bros Construction.

5.3 Series B3 : Bridge impacted by test barge at Pier-3

Test series B3, the second set of impact tests conducted, involved the test barge striking the "bridge"—i.e., multiple piers connected together via superstructure spans—at Pier-3. During this series, the 75 ft. – 6 in. simply supported concrete girder superstructure spans connecting Pier-2 through Pier-11 were left intact (Figure 5.5). Tests in series B3 were conducted at lower energy levels than in series P1, therefore an empty barge (Figure 5.6), rather than a loaded barge was employed. Impact speeds in series B3 ranged from 0.86 knots to 1.53 knots. Achieving these speeds did not require the use of the stationary barge or winches described earlier. Instead, a single pushboat sufficed to accelerate the barge into Pier-3 during each B3 test (Figure 5.7). Also, in contrast to series P1, hard rigging (tensioned steel cable) was used in series B3 to connect the pushboat to the stern of the test barge. As a result, the pushboat rode through each impact test tightly linked to the barge. The weight of the pushboat then added to the weight of the empty barge in terms of total kinetic energy at the time of impact.

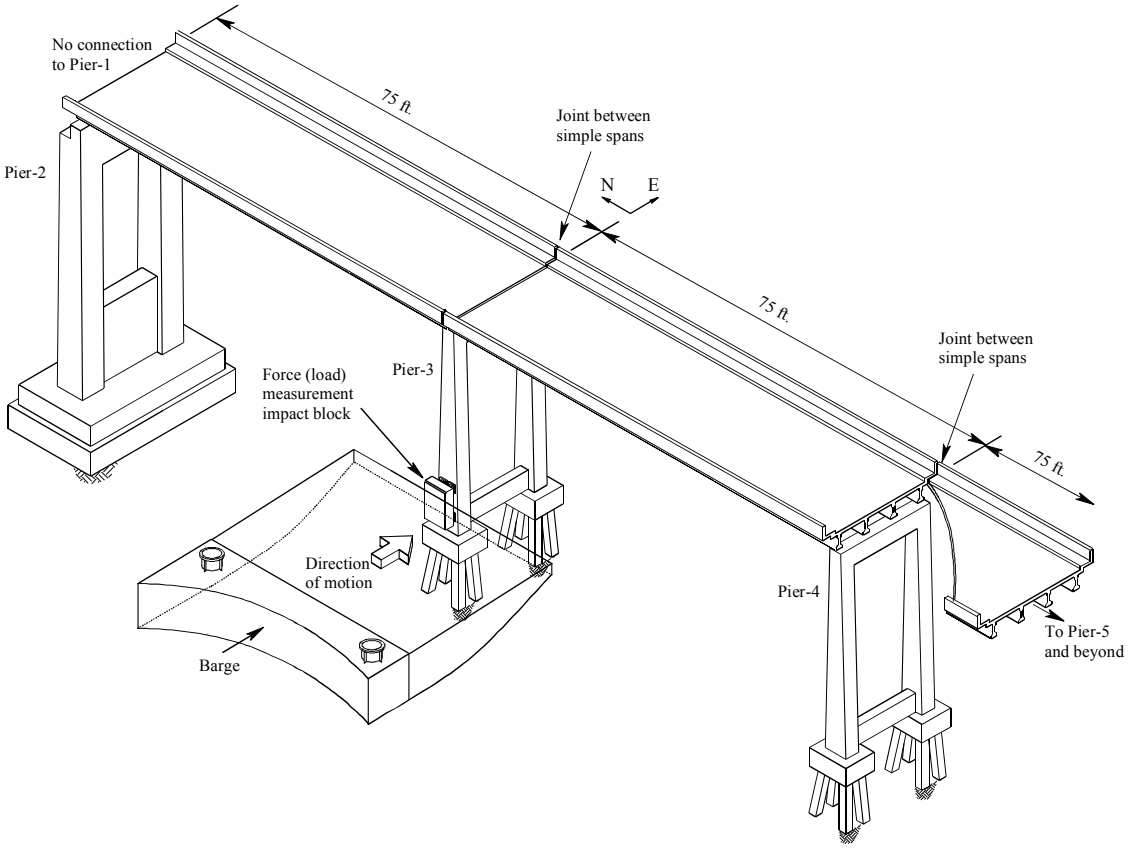

Figure 5.5 Structural configuration of bridge during test series B3

Figure 5.6 Empty test barge as used in series B3 tests

Figure 5.7 Test barge propelled into the bridge at Pier-3 during test series B3

5.4 Series P3 : Pier-3 impacted by test barge

The final series of impact tests conducted, denoted P3, consisted of empty barge collisions with Pier-3 in isolation (Figure 5.8). These tests occurred after the 75 ft. - 6 in. superstructure spans connecting Pier-2, Pier-3, and Pier-4 had been removed (Figure 5.9). Aside from removal of the superstructure spans, tests in series P3 were similar to those in series B3 in terms of impact speeds, barge weight, pushboat rigging, and absence of the stationary barge. Impact speeds achieved during series P3 ranged from 0.4 knots to 1.84 knots.

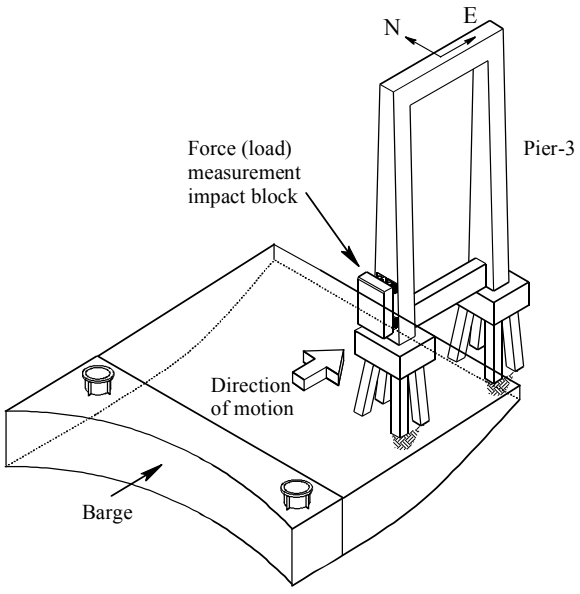

Figure 5.8 Structural configuration of Pier-3 during test series P3

Figure 5.9 Pier-3 isolated for series P3 tests

CHAPTER 6
DATA ACQUISITION AND INSTRUMENTATION

6.1 Introduction

High speed, portable data acquisition systems were developed for this study to collect data from a network of different sensors and sensor-types during each barge impact test. In the sections that follow, instrumentation network configurations, data acquisition systems, and sensor specifications are described in detail.

6.2 Instrumentation networks

In the present context, the phrase "instrumentation network" refers to a collection of sensors that are connected to a data acquisition system through a series of hard-wired connections. Four distinct instrumentation networks were employed in this study: *i*) instrumentation on Pier-1 for test series P1, *ii*) instrumentation on Pier-3 for test series P3, *iii*) instrumentation on Pier-3 and the bridge superstructure for test series B3, and *iv*) instrumentation on the test barge.

6.2.1 Instrumentation network for test series P1

Sensors used in the instrumentation network for test series P1 consisted of accelerometers, displacement transducers, optical break beams, load cells, and a pressure transducer (Figure 6.1). Also located on the pier were a high-speed data acquisition (DAQ) system, signal conditioning equipment, and a 12-volt direct current power supply.

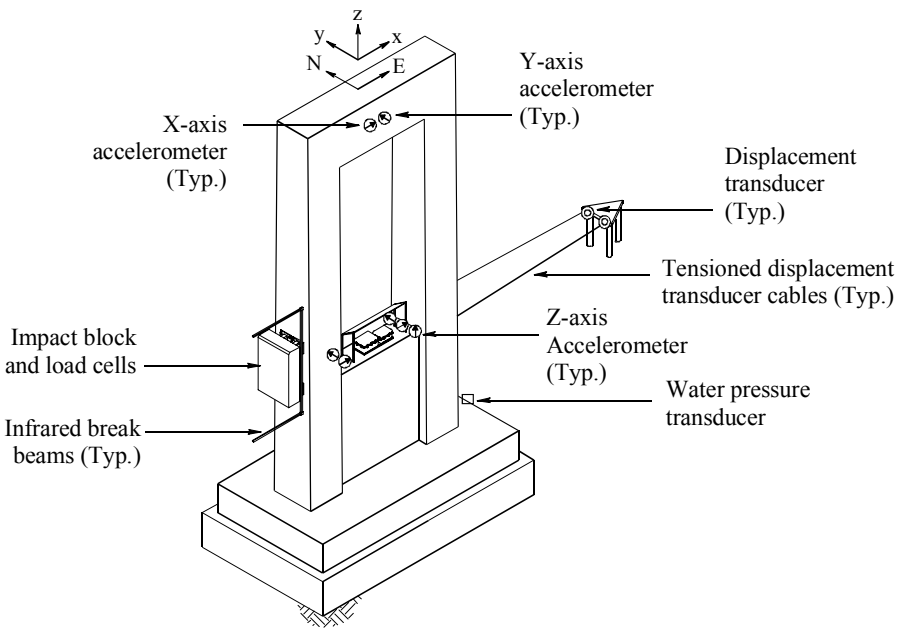

Figure 6.1 Instrumentation network for test series P1

A total of seven uniaxial accelerometers were mounted at two different elevations on the pier: one set at the elevation of the pier cap, and a second set at the elevation of the top of the shear wall (Figure 6.1). Two displacement transducers were attached to pretensioned light gage cables that extended from the east face of Pier-1 to a stationary timber platform (Figure 6.1) approximately 30 ft. east of the pier. Recording displacements at two locations on the pier, rather than simply at the pier centerline, allowed for an examination of possible overall pier rotations about the z-axis during impact. Water pressures on the east side of the pier were also monitored during each P1 test using a submerged pressure transducer. The transducer was suspended at a position approximately 8 ft. below mean sea level on the east face of the Pier-1 pile cap.

Dynamic impact loads imparted to the pier were measured with four biaxial, clevis-pin load cells (additional details are given later) which connected a concrete impact block to the west face of Pier-1 (Figure 6.2). The role of the impact block was to distribute the barge impact load to all four load cells. To ensure that introduction of the impact block between the barge and pier did not influence the collision loads that were generated, the geometry (width) and the material type (concrete) of the impact block were chosen to match those of the west column of the pier. Thus, crushing and sliding interactions between the barge headlog and the concrete impact surface were not altered by introduction of the impact-block-and-load-cell assembly. Biaxial load cells were used, rather than simpler uniaxial load cells, so that impact loads could be independently quantified in the lateral (x) and vertical (z) directions.

Determination of barge impact speed and triggering of the data acquisition system were achieved using two sets of infrared optical break beam sensors mounted in front of the impact block (Figure 6.2). Each set consisted of an infrared transmitter and receiver which were mounted on a 16 ft. tall aluminum alignment bracket. When the barge headlog passed between the transmitter and receiver, the infrared beam spanning between them would be broken, thus causing a clearly identifiable change in the output voltage from the receiver. By aligning the two sets of optical sensors in parallel but offset laterally by 2 ft. (Figure 6.2), and by knowing the duration of time that elapsed between interruption of the first beam and interruption of the second beam, the speed of the barge just prior to impact could be accurately determined.

Also mounted to the aluminum bracket was a light-gage pre-tensioned steel trip wire, which was used to electrically (rather than optically) trigger the data acquisition system on the barge (additional details are provided later).

Self-contained data acquisition (DAQ) and direct current (DC) power supply systems installed on the pier provided excitation power for each sensor; monitored all sensor outputs; provided signal conditioning (high frequency noise reduction); performed analog to digital conversion; and stored the recorded data. Physically, the systems were contained within two weather-tight cases (see Figure 6.3). The DAQ case housed a shock-resistant notebook computer, an analog-to-digital conversion card, and multiple signal conditioner cards (together with associated battery packs). A separate DC battery case contained two deep-cycle 12-volt marine batteries. To protect the data acquisition electronics from shock induced damage, both the DAQ and DC cases were mounted on a custom fabricated shock isolation sled. Additional protection of the DAQ and DC cases included the installation of a steel shelter to deflect spalled concrete debris that might be dislodged from the top of the pier during impact testing.

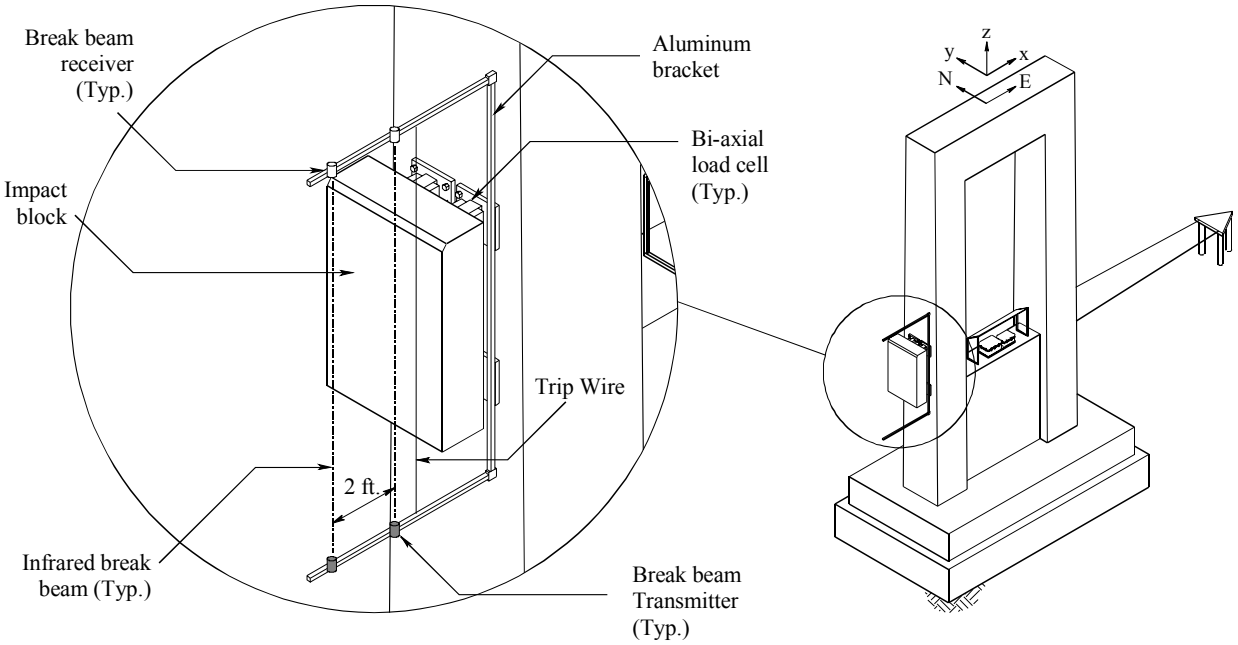

Figure 6.2 Break beams and load cells on Pier-1

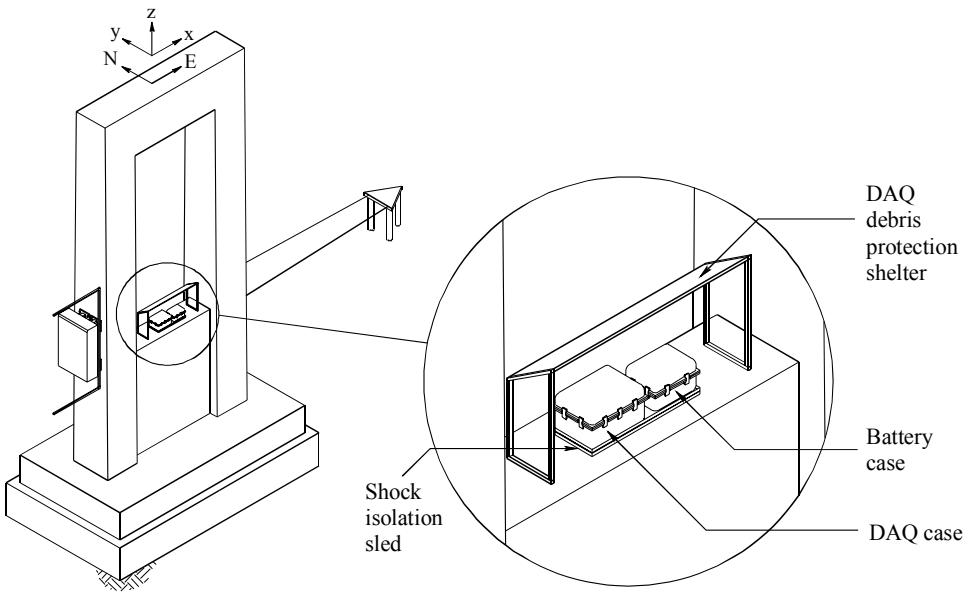

Figure 6.3 Data acquisition system on Pier-1

In the series P1 tests, the data acquisition system collected data from twenty sensor channels: eight from the load cells, seven from the accelerometers, two from the displacement transducers, two from the optical break beams, and one from the pressure transducer.

6.2.2 Instrumentation network for test series P3

The instrumentation network used during the series P3 tests was similar in many ways to that used during the series P1 tests. Seven accelerometers, four biaxial clevis-pin load cells, two displacement transducers, two sets of infrared optical break beams, and a DAQ system were installed on Pier-3 for the series P3 tests (Figure 6.4). Because the pile caps in Pier-3 were above the waterline, the only submerged structural elements were the individual piles. Because the piles had relatively small surface areas (compared to the much larger surface area of the Pier-1 pile cap), significant changes in water pressure at locations adjacent to the piles were not expected. For this reason, water pressure transducers were not used in test series P3 (or B3). However, because the piles of Pier-3 were physically accessible—unlike those of Pier-1—instrumentation for test series P3 also included 32 strain rings (strain measurement devices) that were attached to the eight concrete piles supporting Pier-3. The strain sensors were attached to both the west and east faces of each pile at two different elevations for a total of four strain rings per pile (see Figure 6.5).

In the series P3 tests, the data acquisition system collected data from fifty-one sensor channels: eight from the load cells, seven from the accelerometers, two from the displacement transducers, two from the optical break beams, and thirty-two from the strain rings.

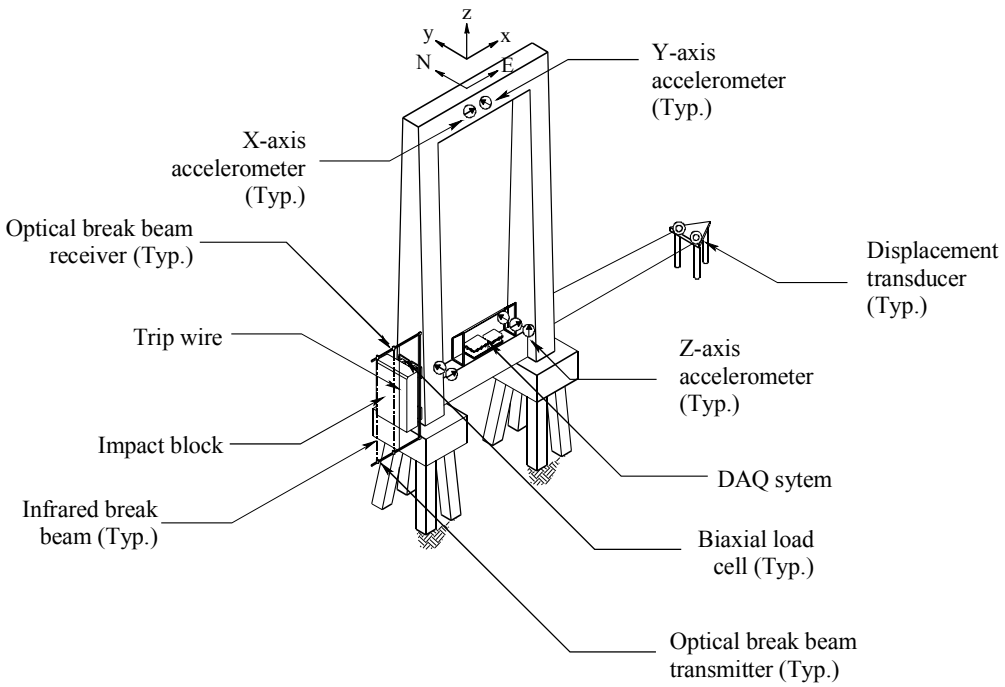

Figure 6.4 Instrumentation network for series P3

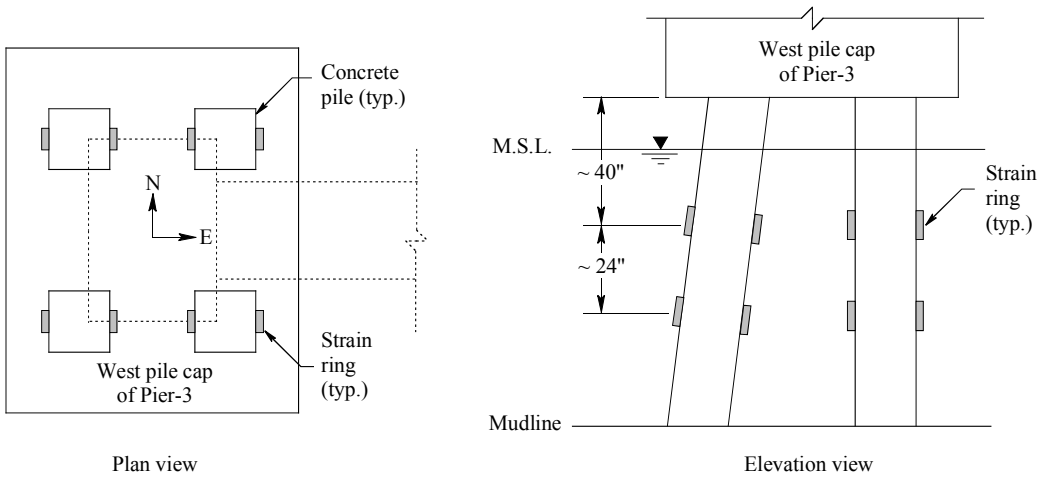

Figure 6.5 Locations of strain rings on Pier-3

6.2.3 Instrumentation network for test series B3

Test series B3 was identical to series P3 except that portions of the bridge superstructure were left intact during series B3. Consequently, the sensor network for series B3 was identical to that of P3 with the exception that nine additional accelerometers were added. These accelerometers were attached both to the bridge superstructure as well as to Pier-2 and Pier-4 (see Figure 6.6).

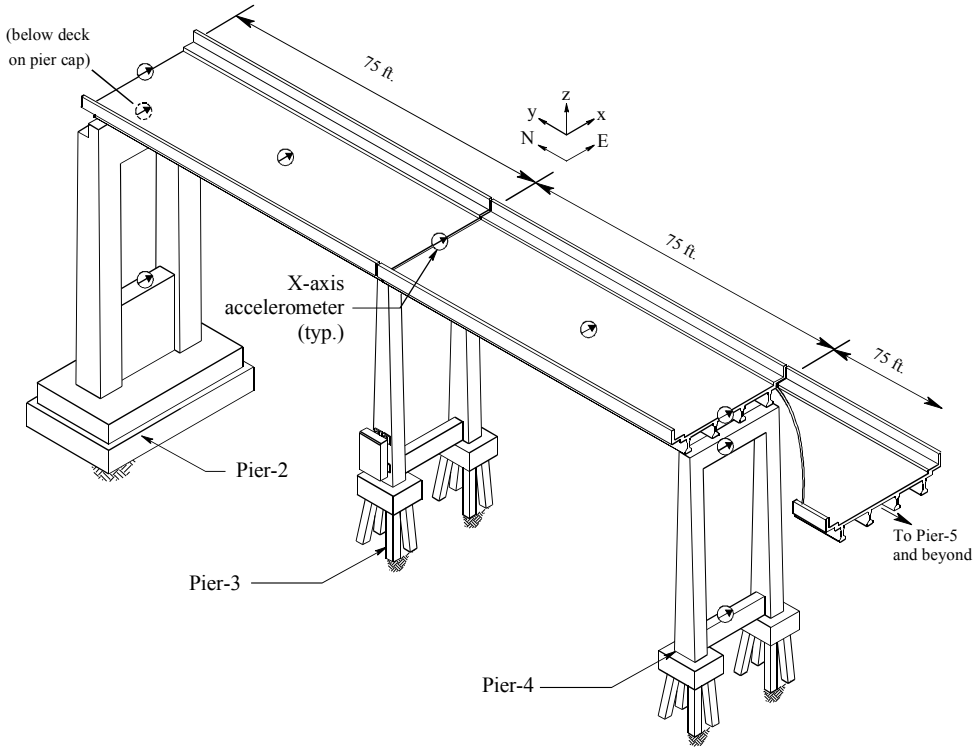

Figure 6.6. Locations of accelerometers on the superstructure, Pier-2, and Pier-4

In the series B3 tests, the data acquisition system collected data from sixty sensor channels: eight from the load cells, sixteen from the accelerometers, two from the displacement transducers, two from the infrared break beams, and thirty-two from the strain rings.

6.2.4 Instrumentation network for the barge

Sensors included in the barge instrumentation network (Figure 6.7) consisted of accelerometers, electrical trip wires, and a global position system (GPS) data logger. The GPS data logger consisted of a handheld GPS unit (a Garmin model GPSMap76S), an external antenna, a serial communication cable, and a notebook computer. Similar to the test piers, the barge was outfitted with a self-contained data acquisition (DAQ) system and direct current (DC) power supply system. These provided sensor excitation, monitoring of sensor outputs, signal conditioning, analog to digital conversion, data capture, and data storage. A shock isolation sled similar to that used on the piers was fabricated and welded to the surface of the test barge to protect the DAQ case, DC case, and GPS case from sustaining shock induced damage.

Seven accelerometers, oriented in three orthogonal directions (x, y, z), were mounted to the top deck of the barge (Figure 6.7) to permit recovery of deceleration-induced inertial forces. Triggering of the DAQ system on the barge was accomplished via an electrical trip wire apparatus (Figure 6.7) that contacted a single complimentary trip wire on the test pier (Figure 6.2). The trip wire apparatus on the barge consisted of retractable steel extension arms mounted to the barge bow (Figure 6.8) and two horizontal, 0.032 in. diameter stainless steel wires that spanned the width of the barge bow and were tensioned between the extension arms. When these horizontal barge trip wires contacted the vertical trip wire mounted on the pier (Figures 6.9), an electrical circuit connected to the barge DAQ system

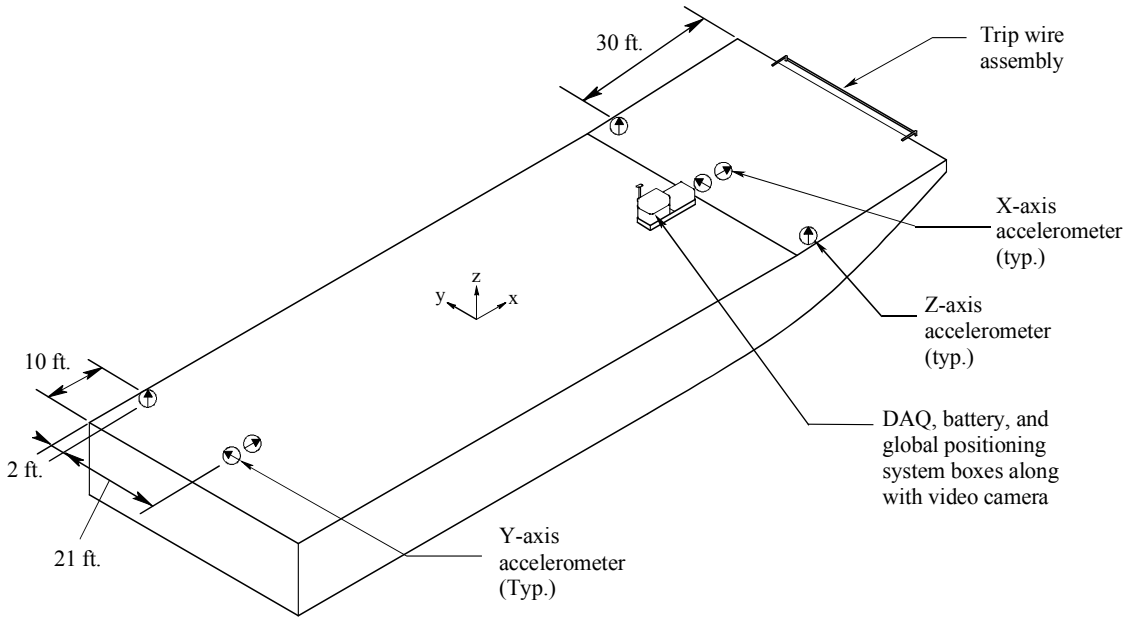

Figure 6.7 Barge instrumentation network

would close, thus, triggering the start of high speed data collection. In total, the barge data acquisition system collected data from eight sensor channels: seven accelerometers and one electrical tripwire circuit.

Figure 6.8 Retractable extension arms and tripwires mounted to barge bow

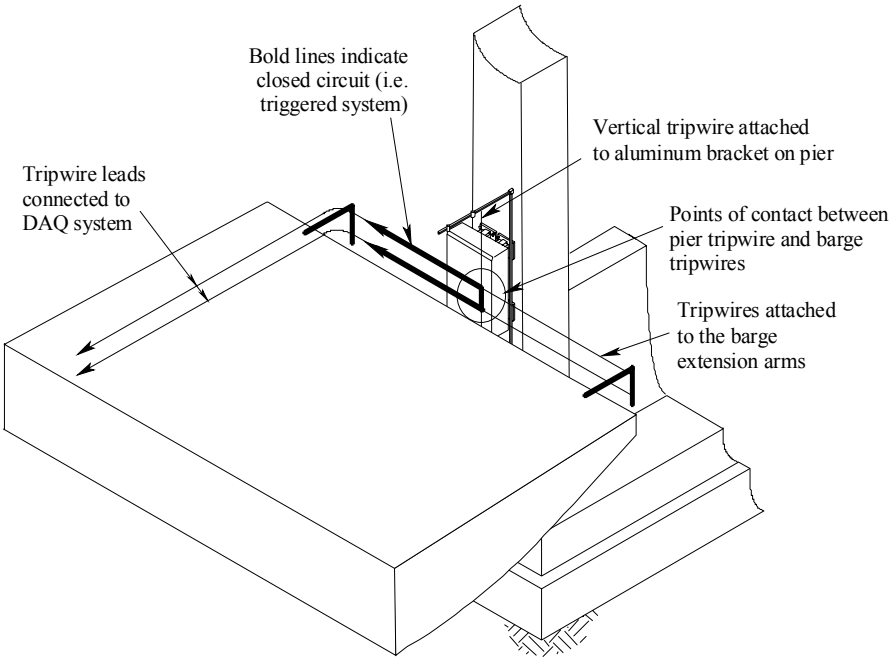

Figure 6.9 Contact between barge tripwires and pier tripwire

6.3 Data acquisition systems

Collection of data from sensors on the bridge piers and barge, both of which were subjected to abrupt impact loading, required the use of data acquisition systems that were portable, self-powered, tolerant of adverse environmental conditions (moisture, dust), and capable of surviving shocks of 2 g or more. In addition, the sampling rate of the DAQ systems needed to be high enough to capture the dynamic responses of the pier and barge for sensor arrays that included as many as sixty channels. Based on results obtained from dynamic finite element barge impact simulations of the anticipated testing conditions for each pier, it was determined that a sampling rate of 2000 samples/second/channel (2000 samples per second per sensor channel) was desirable from the view points of capturing dynamic response as well as facilitating subsequent digital signal processing (e.g., frequency filtering). Capturing data from sixty sensor channels at 2000 samples/second/channel required a *minimum* overall DAQ sampling speed of 120,000 samples/second.

Based on these criteria, two National Instruments Inc. (NI) data acquisition (DAQ) systems were configured for installation on the test piers and barge. Each DAQ system (Figures 6.10 and 6.11) contained an analog-to-digital (A/D) converter, signal conditioning chassis, signal conditioning modules, and a battery pack (DC power source).

As Tables 6.1 and 6.2 indicate, each of the DAQ systems utilized at least one NI SCXI-1000 DC signal conditioning chassis and matching 12 V DC battery pack. Each chassis of this type can accommodate up to four individual signal conditioning modules (cards). In the case of the pier DAQ system, two chassis were daisy-chained (linked) together to increase the maximum number of signal conditioning modules to eight.

Figure 6.10 Data acquisition chassis configuration used on piers

Figure 6.11 Data acquisition chassis configuration used on barge

Table 6.1 Specifications for pier data acquisition system

Analog-to-Digital Conversion Card

Manufacturer	National Instruments
Model number	NI DAQCard-6036E
Sampling Rate (kHz)	200
Signal Ranges (V)	+/- 5
Resolution	16 Bit

Battery Pack (DC Power Supply)

12 VDC Battery	NI SCXI-1382

Signal Conditioning

Chassis (Model)	NI SCXI-1000DC
Shock (g)	30
Num of Slots	4
Card1 (Model)	NI SCXI-1102C
Card Type	Analog Input
Channels	32
Filter (kHz)	10
Card2 (Model)	NI SCXI-1520
Card Type	Strain Gage
Channels	8
Filter (Hz)	10-10,000

Configuration

Analog-to-digital Card	NI DAQCard-6036E
Chassis (1)	NI SCXI-1000DC
Slot 1	NI SCXI-1520
Slot 2	NI SCXI-1520
Slot 3	NI SCXI-1520
Slot 4	NI SCXI-1520
DC Battery	NI SCXI-1382
Chassis (2)	NI SCXI-1000DC
Slot 1	NI SCXI-1520
Slot 2	NI SCXI-1102C
Slot 3	(empty)
Slot 4	(empty)
DC Battery	NI SCXI-1382

Table 6.2 Specifications for barge data acquisition system

Analog-to-Digital Conversion Card

Manufacturer	National Instruments
Model number	NI DAQCard-6036E
Sampling Rate (kHz)	200
Signal Ranges (V)	+/- 5
Resolution	16 Bit

Battery Pack (DC Power Supply)

12 VDC Battery	NI SCXI-1382

Signal Conditioning

Chassis (Model)	NI SCXI-1000DC
Shock (g)	30
Num of Slots	4
Card (Model)	NI SCXI-1102C
Card Type	Analog Input
Channels	32
Filter (kHz)	10

Configuration

Analog-to-digital Card	NI DAQCard-6036E
Chassis (1)	NI SCXI-1000DC
Slot 1	NI SCXI-1102C
Slot 2	(empty)
Slot 3	(empty)
Slot 4	(empty)
DC Battery	NI SCXI-1382

Two types of signal conditioning cards were used in the DAQ systems assembled for this study: NI SCXI-1520 and SCXI-1102C. The eight-channel NI SCXI-1520 modules, intended for use with low output sensor types such as strain gages, provide sensor excitation, programmable gain levels from 1 to 1000, and programmable frequency based filtering. In contrast, the 32-channel NI SCXI-1102C modules are intended for use with higher output (0.1 V to 10 V) analog sensors, and as such, offer more limited gain and signal conditioning features. NI SCXI-1520 cards were used to provide sensor excitation and channel monitoring for all load cells and strain rings. For the accelerometers, optical break beams, displacement transducers, and pressure transducers, NI SCXI-1102C cards were used for channel monitoring, while sensor excitation was provided by separate DC power supplies.

Analog to digital conversion of the conditioned signals generated by the SCXI chassis was performed using a NI-6036E data acquisition card (a PCMCIA-based card intended for use with notebook computers). The NI-6036E DAQ card (Figure 6.12) is capable of a maximum sampling rate of 200,000 samples/second, which exceeded the minimum 120,000 samples/second requirement of this study.

Figure 6.12 NI-6036E PCMCIA data acquisition card

Capture and storage of digitized channel data generated by the DAQ card were accomplished using a notebook computer. Due to the adverse environmental conditions and impact loading that the computer was subjected to, a moisture-tolerant and shock-resistant system capable of meeting military durability standard MIL-STD-810F was selected. Specifically, two Panasonic Toughbook 28 computers (Figure 6.13) were used, one on the pier and one on the test barge. The Toughbook 28 is tolerant to moisture, dust, and shock levels up to 2 g.

National Instruments LabVIEW software (Version 6.1), was installed on each Toughbook 28 computer and used to control the data acquisition systems. A LabVIEW virtual instrument (VI) program was developed to allow control of sampling rate, data storage location, and trigger settings. After integrating the VI, notebook computer, DAQ card, and signal conditioning chassis, tests were conducted at the University of Florida (UF) Structures Research Laboratory (Gainesville, Florida) to confirm that the minimum required sampling rate could be achieved, and to determine the length of time over which data could reliably be captured at this rate. Based on results from these tests, it was determined that the system could safely and reliably capture and store data at the required sampling rate for much more than the desired 60-second data capture window.

Power for the notebook computer, DAQ card, and sensors was provided by two 12-volt deep-cycle marine batteries. Each battery had in excess of 80 amp-hours of capacity when fully charged, allowing the DAQ system, which pulled approximately 6 amps, to run

for at least 13 hours continuously from a single marine battery. A constant charge on the internal battery in the notebook computer was maintained by connecting the computer to a DC power inverter, which was in turn connected to one of the 12-volt marine batteries.

Figure 6.13 Panasonic Toughbook 28 ruggedized notebook computer

Protection against environmental hazards such as water and dust was provided by placing all DAQ equipment—laptop computer, DAQ card, SCXI chassis, and power inverter—inside a single, shock resistant, weather tight case (manufactured by Pelican Products). This case is referred to as the DAQ case (Figure 6.14). Similarly, the two marine batteries were mounted inside a second case, referred to as the DC (direct current) battery case (Figure 6.15). Waterproof connectors were then used to connect the two cases together side-by-side, allowing them function as a single unit (Figure 6.16).

Figure 6.14 Data acquisition (DAQ) case

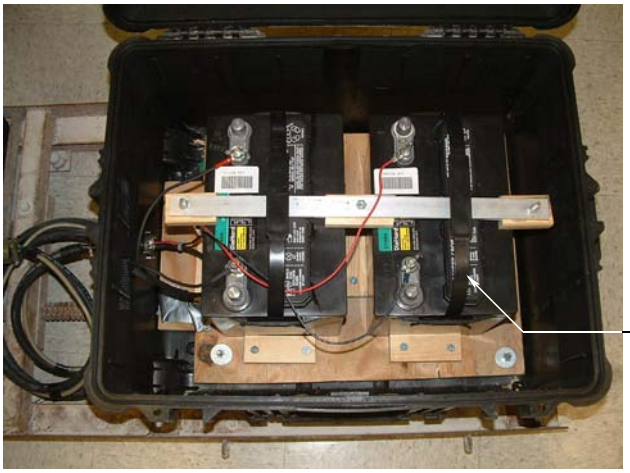

Figure 6.15 Direct current (DC) battery case

Figure 6.16 DAQ and DC cases connected together and placed on shock isolation sled

To protect against the possibility of shock damage, the DAQ and DC battery cases used on the piers and barge were mounted on shock isolation sleds. Each shock isolation sled consisted of two steel frames connected together through a sliding track system and a set of linear compression coil springs. Spring stiffness and the presence of friction between the sliders and guide tracks isolated and damped the shock loading experienced by supported instrumentation. On the test piers, the sliding track system was bolted to the concrete pier (Figure 6.17) using expansion anchors to protect the DAQ and DC cases. In addition, a debris deflection shelter was installed over the shock sled to further protect the DAQ and DC cases. On the barge, the shock isolation sled was welded directly to the top steel deck plate of the barge to protect the DAQ, DC, and GPS cases, as well as a video camera (Figure 6.18).

Figure 6.17 Shock isolation sled and debris shelter for DAQ and DC cases installed on Pier-1

Figure 6.18 DAQ/DC/GPS cases and video camera mounted to the barge deck through a shock isolation sled

6.4 Sensor descriptions

In the sections that follow, detailed descriptions are given for each type of sensor employed during impact testing. Information presented covers sensor specifications, sensor testing, and attachment (installation) procedures.

6.4.1 Optical break beams

Because barge impact energy is a function of vessel speed (velocity), as well as mass, it was necessary to determine the barge impact speed just prior to impact during each test. This speed measurement was accurately achieved using two sets of infrared optical break beam sensors that were positioned above and below the impact face of the concrete impact block (Figure 6.19). Each set of sensors consisted of a transmitter and a receiver, which were mounted to an aluminum bracket and axially aligned (Figure 6.20). Sensor specifications for the break beam sensors are given in Table 6.3. The break beam channels of the DAQ system were set to a range of –10 V to +10 V.

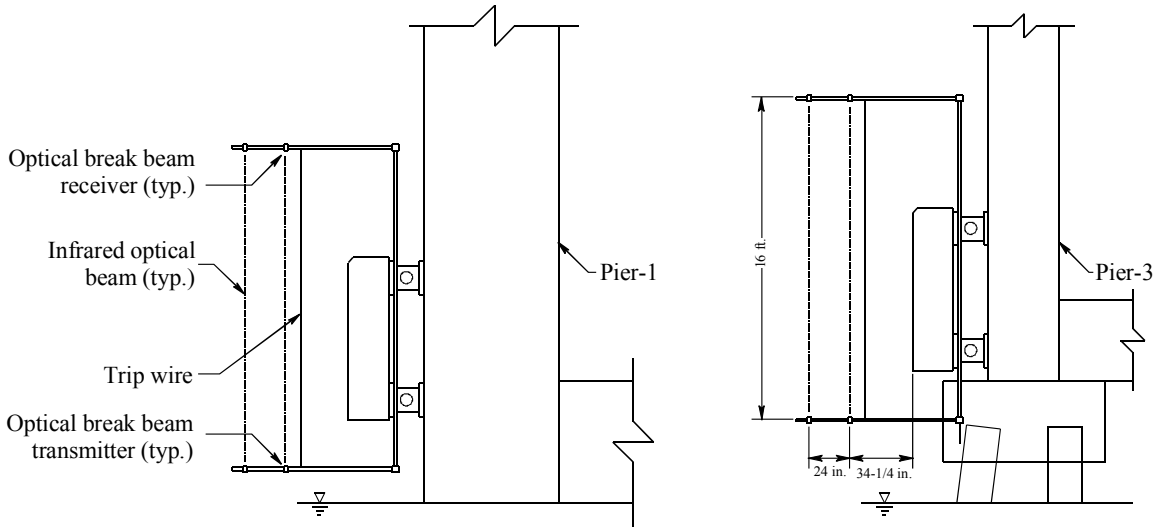

Figure 6.19 Optical break beam brackets for Pier-1 and Pier-3

Prior to each impact test, the DAQ system on the pier was entered into a mode in which it continuously monitored output from the outer most receiver (the receiver farthest from the impact block face). When the moving test barge crossed this outer beam on its way toward the impact block, it blocked reception of the outer infrared beam at the receiver and the receiver output signal dropped from high to low voltage. This “crossing event” triggered the DAQ system on the pier to begin recording data from all sensors in the pier network at a rate of 2000 samples/second/channel. Subsequently, as the barge crossed the inner beam, a second crossing event was recorded prior to impact. By knowing the duration of time that elapsed between the two cross events, and by knowing the exact distance between the two sets of beams (2 ft.), the impact speed could be determined.

Figure 6.20 Break beam sensors installed on aluminum bracket adjacent to impact block

Table 6.3. Specifications for optical break beam sensors

Manufacturer	Balluff
Receiver model	BLE-S51-PA-2-FOO-PK
Transmitter model	BLS-S51-PA-2-GOO-XG
Range (ft)	40
Input (V)	24
Output (V)	0 or 6

6.4.2 Impact blocks and load cells

Measurement of dynamic impact loads generated during the barge collision tests was achieved using instrumented impact blocks, which were attached to the west column of each test pier. Each impact block consisted of a heavily reinforced concrete block with four biaxial clevis-pin load cell assemblies attached (Figure 6.21). The blocks were positioned vertically such that the headlog of the barge bow would make contact with some portion of the block regardless of tidal fluctuations at the test site (Figure 6.22). During each impact test, the load imparted by the test barge was distributed through the block to the four load cells, and then into the pier column. Based on results from dynamic finite element barge impact simulations, loads during the tests were not expected to exceed 1500 kips horizontally nor 600 kips vertically on Pier-1, and 600 kips horizontally nor 200 kips vertically on Pier-3. Despite the

differences in expected loads, the impact blocks for both for Pier-1 and Pier-3 were fabricated identically so that they would be fully interchangeable at the test site.

Each impact block was designed to match—as closely as was feasible—the shape and stiffness of the pier column. This was done so that interaction between the barge and impact block would closely mimic the interaction that would have occurred had the barge struck the pier column directly. Each block was consequently designed as a heavily reinforced deep concrete slab. Sufficient stiffness was provided such that local deflections within the block would be minimal in comparison to barge deformations and pier displacements.

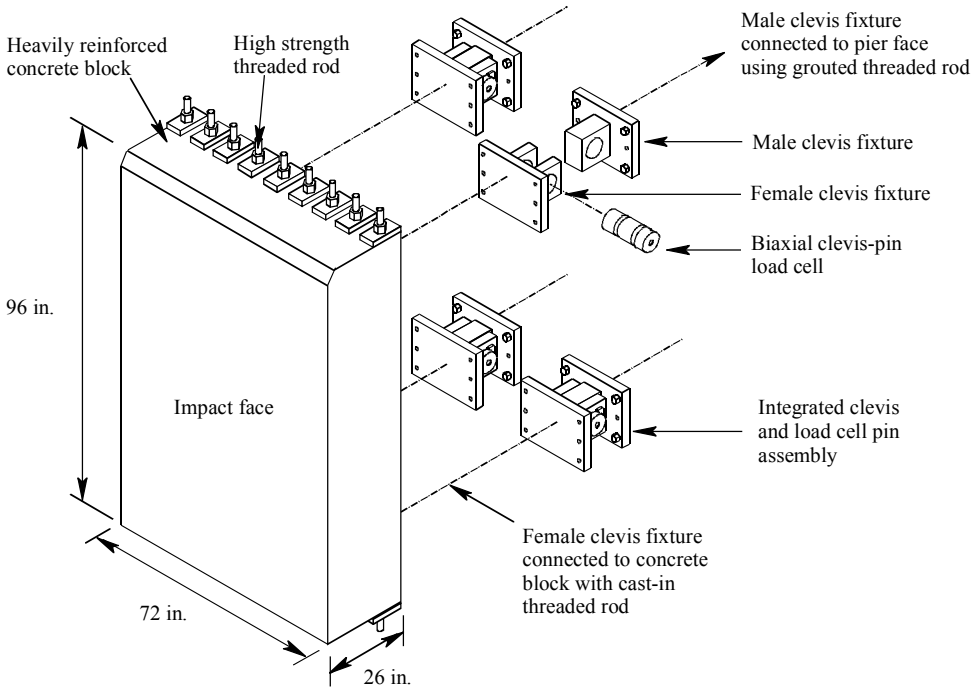

Figure 6.21 Impact block with attached load cell assemblies

Each block was 8 ft. tall, 6 ft. wide, and 26 in. thick and was reinforced vertically (the span direction) using nine 1.375 in. diameter, 150 ksi all-thread bars (obtained from Williams Form Engineering Corp). All-thread rods were extended beyond both ends of the blocks so that 5 in. by 10 in. by 1.5 in. thick steel bearing plates could be externally secured with nuts (Figure 6.21). The nuts were not torqued sufficiently to generate post-tension forces, but rather they were tightened only enough to bring the bearing plates into positive contact with the ends of the impact block. The bearing plates served to help confine the concrete at the ends of the blocks (necessary to avoid pullout of the anchor bolts connecting the blocks to the pier face) and eliminated the need to provide development length for the threaded rods.

Figure 6.22 Test barge nearing contact with impact block

In addition to the main longitudinal reinforcement steel, five 8x8-D11xD11 welded wire sheets—approximately equivalent to #3 reinforcing bars spaced at 8 in. on center in each direction—made of 60 ksi steel were distributed throughout the thickness of the impact blocks (see Figure 6.23) to provide shrinkage reinforcement, temperature reinforcement, and confinement (Ivy Steel and Wire is gratefully acknowledged for donating the welded wire sheets to this project). Shear reinforcement hooks, made of 60 ksi #4 rebar, were also installed at spacings of 8 in. on center in each direction. Fabrication of the impact blocks was carried out by the Florida Department of Transportation (FDOT) Structures Research Laboratory (Tallahassee, Florida).

Figure 6.23 Internal steel reinforcing used in impact blocks

The four load cell assemblies attached to the impact blocks each consisted of a stainless steel biaxial shear pin load cell and two hot rolled 1020 steel clevises (Figure 6.24). Biaxial load cells were used so that loads in both the horizontal and vertical directions could be directly quantified. To prevent the pin from rotating within the clevis or sliding out, a steel keeper plate was used to lock the pin into position on each assembly.

The four clevis fixtures were attached to the back (non-impact) face of each concrete impact block using sixteen 1.375 in. diameter B7 thread bars that had been previously cast into the blocks during fabrication. In Figure 6.25, serial numbers and positive directions are provided for each of the load cells used on Pier-1 and Pier-3.

Specifications for the shear pins used in this study are given in Table 6.4. Each pin contained two full-bridge circuits—one for each direction of load measurement. Uniaxial calibrations along each of the two primary orthogonal pin axes were conducted by the manufacturer at load levels of 160, 320, 480, 640, and 800 kips. During the calibration process, the load cells were given an excitation voltage of 10 V. Consequently, during the barge impact test program, each load cell was provided with a 10 V excitation. Data from each of the eight load cell channels (four load cells per impact block with two orthogonal load channels per load cell) were captured by the pier DAQ system at a rate of 2000 samples/second/channel. The sensor input ranges for all load cell channels connecting to the DAQ was set at -0.1 V to +0.1 V.

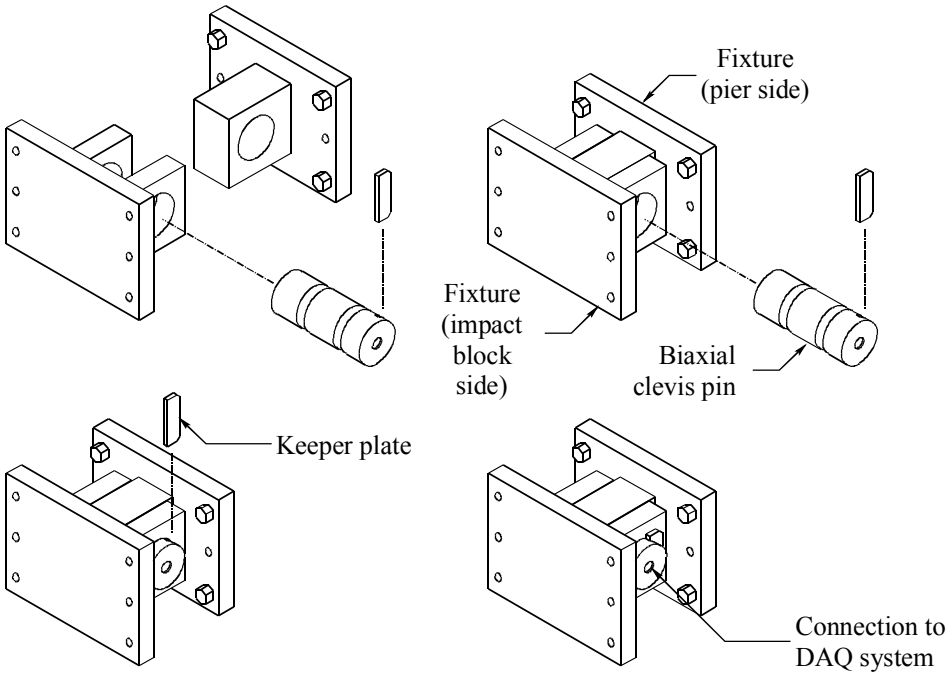

Figure 6.24 Exploded views of a clevis pin load cell assembly

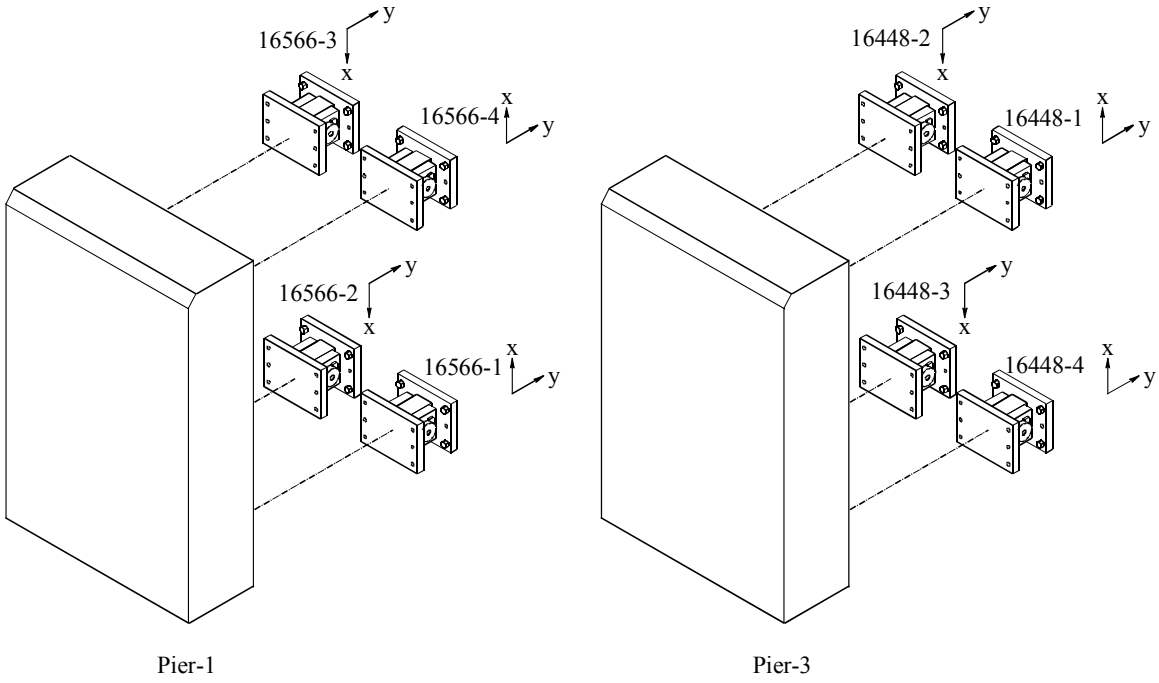

Figure 6.25 Serial numbers and positive directions for load cells

Table 6.4 Specifications for shear-pin load-cells

Manufacturer	StrainSert
Model number	CPA-8
Orthogonal load sensing axes per pin	2
Range (kips)	+/- 800
Pin diameter (in.)	7
Excitation, maximum permissible (V)	12
Excitation, during calibration and impact testing (V)	10
Nominal output at full range load (mV/V)	2
Non-linearity, nominal (%)	+/- 0.5

Pre-field-installation testing of the clevis pin load cell assemblies was conducted by the University of Florida and the FDOT at the FDOT Structures Research Laboratory. After attaching four load cell assemblies to each impact block, the integrated units were placed on the FDOT Structures lab floor and subjected to statically applied loads ranging in magnitude from zero to 600 kips at the center and the top of the block (Figure 6.26). Results from this series of tests revealed that the impact blocks were extremely stiff. However, while such stiffness was desirable from the stand point of preventing introduction of a "soft layer" between the impacting barge and test pier, it also introduced unintended consequences.

During the lab testing, it was found that even subtle slopes in the lab floor—provided for drainage purposes—were sufficient to result in two diagonally opposed load cells carrying *all* of the applied load. Load redistribution that would normally be expected to occur in a more flexible system—eventually producing a more balanced distribution of load in all

four load cells—did not occur due to the very high stiffness of the impact blocks. Additionally, the close lateral proximity of the load cells at the block ends and the stiffness of the 3 in. thick steel clevis bearing plates were suspected to be contributing factors to the skewed load distributions that were observed.

If similar non-uniform distributions of load were to occur during the full-scale barge impact testing—due to the fact that the blocks would be installed against pier column surfaces that clearly would not be precisely planar in nature—then a strong potential for overloading individual load cells existed. To avoid such a condition, it was determined that grout would need to be placed between the clevis fixture base plates and the pier column surfaces during the field installation of the impact blocks. This procedure would ensure that all four load cells on each impact block were in full contact with the pier face prior to any application of external impact load.

Prior to transporting the impact blocks to the test site at St. George Island for use in the full-test barge impact program, additional laboratory tests were conducted to evaluate the effectiveness of the proposed grouting procedure. In this second series of lab tests, the impact blocks were suspended above the lab floor and grout pads—made of MB 928 grout from Master Builders Inc.— were poured beneath each clevis base plate (Figure 6.27). Results from this series of additional tests confirmed that the new installation procedure produced much more uniform loading of all four load cells.

Figure 6.26 Laboratory testing of an impact block and load cells

Figure 6.27 Load cell base plates supported on grout pads during laboratory testing

After transporting the impact blocks to St. George Island, they were taken by barge to the bridge and installed on Pier-1 and Pier-3 by Boh Brothers Construction, Inc. Attaching the clevis base plates to the test piers was accomplished by core drilling holes into the faces of the pier columns and grouting (using a structural adhesive) in 1.375 in. diameter B7 thread bars with a 20 in. embedment length. Using a crane barge, the impact blocks were then lifted into place leaving voids between the clevis base plates and the pier surfaces. After installing wooden dams around each clevis base plate, MB 928 grout pads were poured and allowed to cure. In this manner, each load cell was placed into direct contact with the pier surface.

6.4.3 Accelerometers

Based on results obtained from dynamic finite element barge impact simulations conducted for the purpose of planning the experimental tests, all barge, pier, and superstructure accelerations of interest were expected to be below 10 g. Primary intended uses of the measured acceleration data were calculation of impact forces, calculation of load-sharing through the superstructure, and calculation of displacements of the impacted pier. The last calculation involved double time integration of the measured acceleration data (see Appendix I for additional information). For all three of these intended uses, only relatively low frequencies—below approximately 100 Hz—were important. The accelerometers chosen for this study therefore needed to be capable of accurately recording data at relatively low acceleration levels (<10 g) and relatively low frequency levels.

Based on these requirements, variable capacitance accelerometers were chosen due to their ability to produce data of sufficient accuracy for double time integration. This type of device measures acceleration by sensing changes in capacitance between electrically charged plates contained inside the accelerometer. Specifically, two outer stationary plates straddle an inner plate that has an attached mass. As the device is subjected to acceleration, inertial forces acting on the mass deflect the inner plate, moving it closer to one of the outer plates

and farther from the other. These deflections cause the capacitances between the inner and two outer plates to become unbalanced resulting in unequal current flows through the two capacitive circuits that make up the sensor. The differential current flow is then used to generate a sensor output voltage that is proportional to the applied acceleration level. Capacitive accelerometers are generally very accurate at low levels of acceleration (<100 g) and have a wide enough frequency response range to capture the full frequency content of the accelerations of interest in this project.

Summary specifications for the accelerometers used in this study are given in Table 6.5. All of the accelerometers used were of the uniaxial type, thus measuring acceleration only in a single direction. Circuitry contained within each accelerometer filtered and regulated the incoming supply voltage such that any unregulated direct current (DC) source exceeding 12 V may be used to power the sensor. Accelerometers with peak ranges of 1, 5, and 10 g were installed at various positions on the barge, piers, and superstructure based on acceleration results obtained from numeric impact simulations. Selection of the accelerometer g-level range for each position was based on the need to avoid sensor over-ranging while also ensuring that sufficient resolution was retained in the data collected. The range on the accelerometer channels in the DAQ system was set to –10V to 10V.

Table 6.5 Specifications for accelerometers

Manufacturer	Model number	Range (g)	Max shock (g)	Frequency range (Hz)	Noise (RMS milli-g)	Input (V)	Output (V)
Summit Instruments	13203	1	500	0-223	2.25	8-30	0-5
Summit Instruments	13203	5	500	0-223	2.25	8-30	0-5
Summit Instruments	13200	10	500	0-223	10	8-30	0-5

Pre-deployment testing of the accelerometers was conducted at the UF Structures Research Lab using a small dynamic shake table. Accelerometers were attached to the shake table platform such that the uniaxial sensing direction of each was oriented in the translational direction of the table. Time histories of barge and pier accelerations—obtained from dynamic finite element barge impact simulations—were then loaded into the computer system that controlled the shake table. As the shake platform moved through the specified barge or pier motions, accelerations measured by the attached capacitive accelerometers were captured and recorded. In addition, displacement transducers were also attached to the shake platform during selected tests to directly record displacement time histories. Applying frequency based filtering techniques and double time integration to the acceleration data produced displacements that could be compared to data measured directly with the displacement transducers and to the known motion of the shake table platform. Comparisons of this type confirmed that the accelerometers were capable of yielding data of sufficient accuracy for this study.

At the St. George Island bridge test site, accelerometers were attached to the piers and bridge superstructure using 2 in. x 2 in. x 2 in. x 1/8 in. aluminum mounting angles (Figure 6.28). Each angle was attached to the concrete surface using 1/4 in. inner diameter x 1 in. long expansion anchors (Figure 6.29). Each mount also included two set-screws that permitted adjustment of bracket alignment on sloped surfaces of the concrete piers. Care was taken to ensure that each mount was installed in an orientation direction that produced shear

loading of the mounting angle rather than flexure. This procedure ensured that the accelerations measured were not affected by flexural deformations of the mounting angles.

The method of mounting accelerometers to the steel surfaces on the barge was similar to that used for mounting to the concrete surfaces of the piers. However, instead of using anchor bolts, a rapid setting two-part commercial epoxy (J–B Kwik Weld, tensile strength: 2.1 ksi) was used to bond the bottom flange of each aluminum mount to the barge (Figure 6.30). Prior to attaching each accelerometer mount, a grinder was used to remove all surface paint at the installation point and expose the bare steel of the barge deck plates.

Figure 6.28 Accelerometer mounted to vertical concrete pier surface

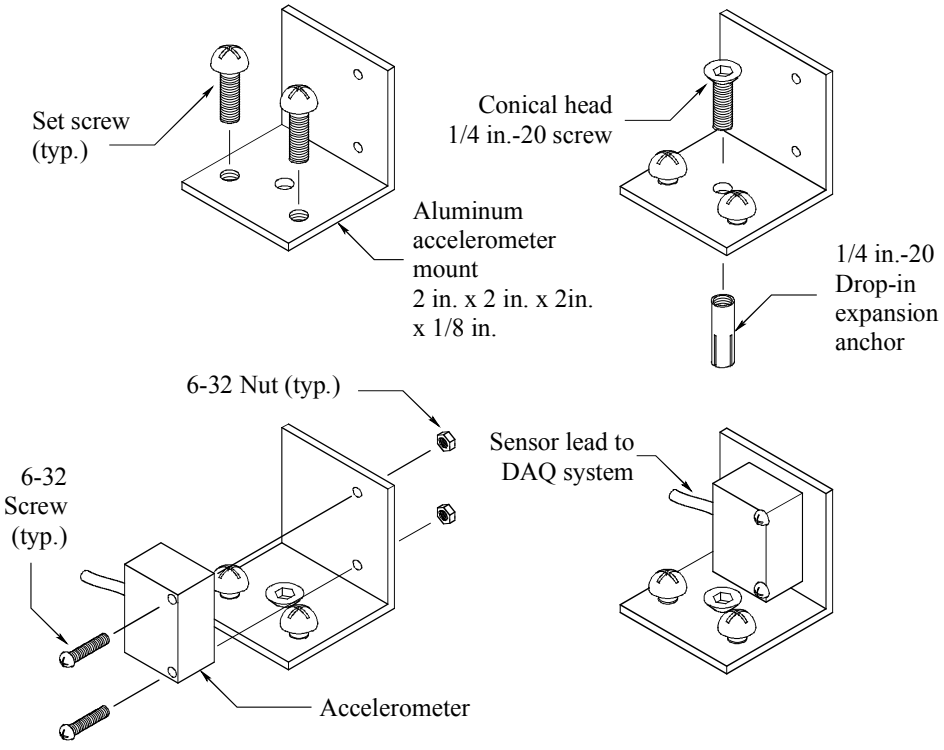

Figure 6.29 Procedure for mounting accelerometers to concrete surfaces

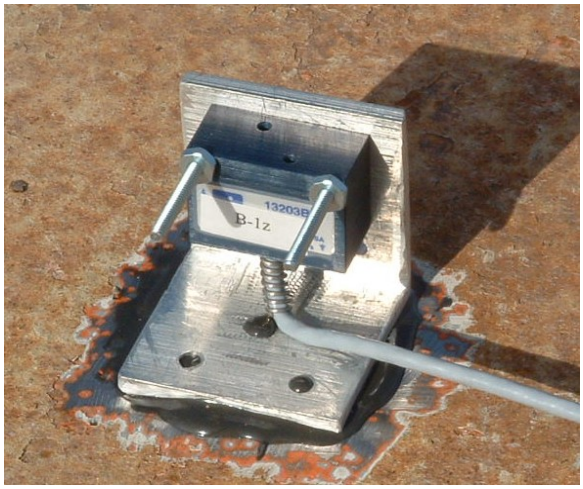

Figure 6.30 Accelerometer mounted to the steel deck plate of the test barge

6.4.4 Displacement transducers

Direct measurement of the translational motions of Pier-1 and Pier-3 in response to barge impact loading was accomplished using displacement transducers. Stationary reference points (datums) for each displacement transducer were established by driving timber piles on the east (non-impact) sides of the test piers and then erecting cross-framing and timber platforms (Figures 6.31 and 6.32). The timber platforms were located approximately 30 ft. east of the piers so that they would be outside the soil zone of influence of the pier, and would therefore remain stationary during each impact test. Unfortunately, post-test examination of data obtained from test series P1 revealed that, due to soil-embedment of the Pier-1 cap and tremie seal, the timber platform east of Pier-1 was still within the soil-zone-of-influence even at 30 ft. away. As a result, the anchor platform displaced during the tests, thereby rendering the collected displacement data unusable (see Appendix D for additional details). For Pier-3, the 30 ft. separation distance between pier and timber platform was proven to be adequate, and reliable displacement transducer data was recovered for test series B3 and P3.

To span the distance from the pier to the platform, light gage pre-stretched cables were pre-tensioned with large-deformation linear springs and connected to the pier and timber platform. Displacement transducers were then attached to the cables, thus measuring the movement of the pier relative to the platform (Figure 6.33). The cables were attached near the northeast and southeast corners of the east column of each pier. Recording displacement histories at these two locations, rather than solely at the centerline of the pier, allowed for an examination of overall pier rotation during impact as well as providing measurement redundancy. Specifications for the displacement transducers are given in Table 6.6. Figure 6.34 shows a typical DT-40 transducer both as an individual unit, and as installed on a stationary timber platform. The range of the DAQ channels used to record data from the displacement transducers was set to –10 to 10V.

Figure 6.31 Stationary timber platform on east side of Pier-1
as viewed from a position adjacent to the pier

Figure 6.32 Stationary timber platform on east side of Pier-3 as viewed from above

Table 6.6 Specifications for displacement transducers

Manufacturer	Scientific Technologies
Model number	DT-40
Range (in.)	40
Tension (oz. of force)	24
Accuracy (in.)	0.04

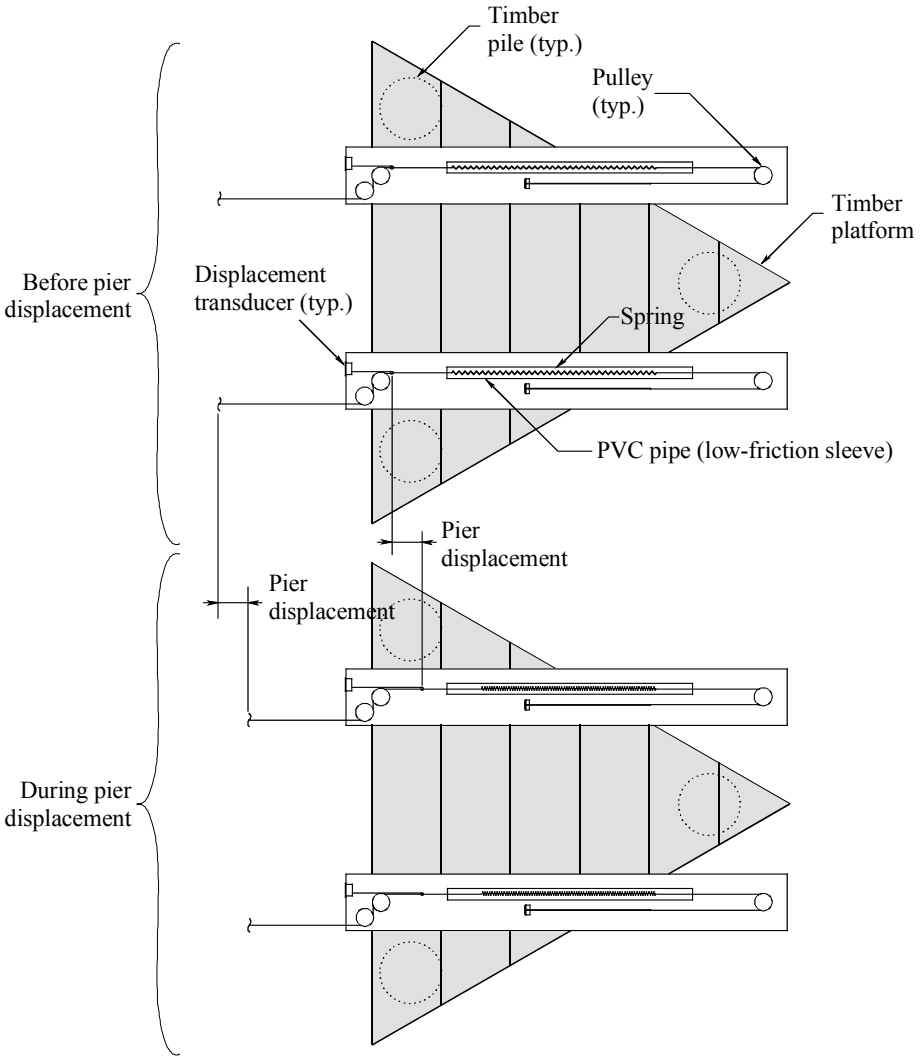

Figure 6.33 Stationary timber platform and displacement transducers

Figure 6.34 Displacement transducer (individually and as installed on timber platform)

6.4.5 Strain gages (strain rings)

During test series B3 and P3, strain gages were used to record strains in the prestressed concrete piles supporting Pier-3. The type of strain gage selected needed to have a long enough gage length (>2 in.) to be able to measure average strains at the concrete pile surfaces. Using too small a gage length would result in erroneous measurements if the gage happened to be positioned near localized surface cracks. Furthermore, the strain gages needed to be capable of being mounted to concrete pile surfaces at locations below water level and in a saltwater environment.

To meet these requirements, devices called "strain rings" (see Figure 6.35) were selected. Strain-rings are essentially long-gage-length strain gages with built-in bridge completion circuitry. Specifications for the specific model of strain ring used in this study are given in Table 6.7. In particular, note that the devices are designed to be water tight to a depth of over 300 ft., thus providing more than sufficient environmental protection for the present application. The sensor input ranges for all strain sensor channels connecting to the DAQ was set at -0.01 V to +0.01 V. As previously noted, strain rings were installed at 32 different locations on the piles of Pier-3 (recall Figure 6.5).

Figure 6.35 Strain ring with integrated stainless steel mounting blocks

Table 6.7. Specifications for strain rings

Manufacturer	Strainstall UK Ltd.
Model number	5745 Strain Ring
Range (microstrain)	+/- 2000
Linearity (%)	+/- 1
Input (V)	1-5
Gage length, nominal (in.)	5.59
Water depth limit (ft)	330
Force on sensor mounts at 2000 microstrain (lbs)	22.5

Prior to installing the strain ring devices at the St. George Island bridge test site, preliminary tests were conducted at the UF Structures Research Laboratory to independently assess sensor linearity and to cross-check (for randomly selected sensors) the calibration data

that was provided by the manufacturer. Strain rings were mounted on both sides of a milled steel coupon and loaded axially in tension using a 400 kip Tinius Olsen Universal Test Machine (Figure 6.36). In addition to strain rings, foil-type strain gages were also attached to the steel coupon. Strains recorded by the strain rings were then averaged and compared to strains measured by the steel foil gages. Acceptable levels of device linearity and agreement with calibration data were obtained from the laboratory tests.

Figure 6.36. Axial loading of a steel coupon instrumented with strain rings and foil strain gages

Attachment of the devices to the concrete piles of Pier-3 was accomplished by fabricating 3 in. x 1 in. x 5/8 in. thick stainless steel mounting blocks and installing them against the pile surfaces using stainless steel hardware and expansion anchors (Figure 6.37). Installation of the expansion anchors required underwater drilling of holes into the concrete piles using a heavy-duty submersible pneumatic impact hammer-drill. Although the drilling operation made use of a drilling template, for some of the strain rings there were nevertheless minor deviations between the intended and actual expansion anchor positions.

As fabricated, the strain ring devices offer very limited capabilities with regard to accommodating deviations in mounting-point locations. To increase the device tolerance for mounting-point position deviations, extension plates were fabricated. The extension plates were then installed between the integrated strain ring mounts and the pile-surface mounting blocks (Figure 6.37). Machining oversized holes into one end of the extension plates allowed variations in mounting-point location to be accommodated without introducing preload into the strain rings during installation (or introducing significant changes in gage length).

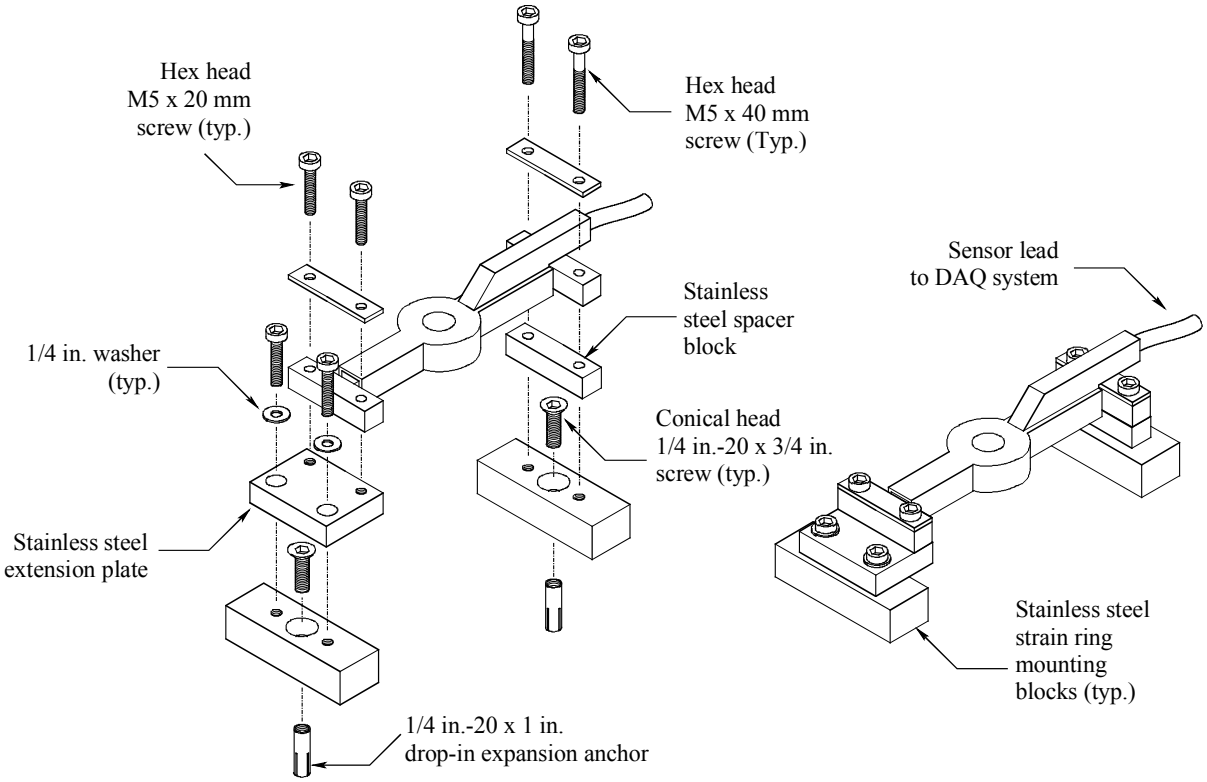

Figure 6.37 Strain ring mounting procedure

6.4.6 Pressure transducer

During test series P1, a pressure transducer was placed below water level on the east (non-impact) side of Pier-1 to record water pressure variations during the impact tests. A significant increase in water pressure along the submerged vertical east face of Pier-1 during impact would indicate that water surrounding the pier footing momentarily contributed dynamic resistance to the applied loading. A pressure transducer was therefore installed to quantify the extent to which water pressure changes occurred.

Figure 6.38 Water pressure transducer

The pressure transducer was installed by suspending it at an elevation approximately 8 ft. below mean sea level at a location adjacent to the east vertical face of the pier. Specifications for the pressure transducer used in this study are given in Table 6.8. The sensor input range for the pressure transducer channel that was connected to the DAQ system

was set to -10 V to +10 V. Water pressure data were recorded during test series P1 but not during test series B3 or P3 due to the much smaller submerged surface area of Pier-3 (in comparison to that of Pier-1).

Table 6.8 Specifications for waste pressure transducer

Manufacturer	Trans-Metrics (a division of United Electric Controls)
Model number	P21-LA
Range (psi, absolute)	0-50
Input (V)	12
Output (V)	0-5

CHAPTER 7
EXPERIMENTAL TEST RESULTS

7.1 Introduction

On February 27, 2004, the newly constructed St. George Island Causeway Bridge was completed and officially opened to the public. With traffic removed from the old bridge, instrumentation networks described in the previous chapter were installed on the piers and bridge superstructure. During the same time period, Boh Bros. Construction removed the three-span steel girder roadway section that crossed over the intracoastal waterway and removed the western portion of the fender at Pier-1.

Barge impact testing began at the end of March 2004 and continued through the end of April 2004. Specific test dates are listed in Table 7.1. Following completion of all tests, the piers were demolished. In total, fifteen barge impact tests were successfully conducted: eight in series P1, four in series B3, and three in series P3. Weather conditions on the test dates varied from clear and calm to windy and choppy (Table 7.2). Maximum safely achievable impact speeds were generally dictated by equipment limitations and weather conditions (e.g., the ability to control the trajectory of the test barge in windy/choppy weather). Similarly, the elevations at which the barge came into contact with impact blocks on the test piers were generally as much a function of weather conditions as of tidal conditions. Due to the significant wind fetch-length of Apalachicola Bay and the water-flow restriction created by the causeway island (see Chapter 3), wind speeds on the test dates had as much influence on water levels at the test piers as did normal tidal fluctuations. As water levels rose and fell, so did the elevations at which the test barge struck Pier-1 and Pier-3 (Figure 7.1). Impact elevations for all tests are summarized in Table 7.3.

Optical break beam data collected during each test were later used to compute barge speeds—just prior to impact—for all tests. Overall, the speeds ranged from a low of 0.75 knots for the initial diagnostic test (P1T1) to a maximum of 3.45 knots. Combining these speeds with the measured barge masses (loaded and empty, discussed in Chapter 4), the initial kinetic impact energies for the tests were computed as $KE = C_H \left(1/2\right) MV^2$. The hydrodynamic mass coefficient, C_H, was determined to be 1.05 for all tests based on barge draft depths (both loaded and empty), Apalachicola Bay water depths at the test locations, and the AASHTO criteria cited in Chapter 2. Impact conditions and initial kinetic energies for all tests are reported in Table 7.4.

In addition to initial kinetic energies, imparted kinetic energies are also reported in Table 7.4. During test series P1, the 55 ft. bridge spans that served as barge payload did not remain stationary with respect to their initial positions on the barge deck. Rather, measurable levels of payload sliding were detected during the tests. In the highest energy impacts, the average slide-distance of the two payload spans was limited to approximately 1.25 ft. As a result of friction between the top of the barge deck and the timber mats, that supported the payload spans, the measured sliding motions constituted a form of impact energy dissipation. Hence, the amount of *imparted* kinetic energy available to generate pier motion, soil deformation, and barge deformation during each test was given by the expression $KE_{imparted} = KE_{initial} - E_{friction}$ where $KE_{initial} = C_H \left(1/2\right) MV^2$ and $E_{friction}$ = energy

dissipated due to frictional sliding of the payload. The latter parameter was computed as $E_{friction} = W_{payload}\ D_{slide}\ \mu_{dynamic}$ where $W_{payload}$ was the total weight of both payload spans (see Chapter 4), D_{slide} was the payload slide distance, and $\mu_{dynamic}$ was the dynamic (i.e. "sliding") coefficient of friction between the timber mats and the barge deck. $W_{payload}$ and D_{slide} were experimentally measured quantities while $\mu_{dynamic}$ was estimated to be 0.225 based on published frictional data and the observed surface condition of the barge (painted texture, cleanliness, and presence of moisture).

Table 7.1 Test dates and times

Test series	Test identifier	Test date	Test time (Eastern Standard Time)
P1	P1T1	2004-03-29	15:51
	P1T2	2004-04-05	17:18
	P1T3	2004-04-05	18:31
	P1T4	2004-04-06	15:09
	P1T5	2004-04-06	15:56
	P1T6	2004-04-06	18:40
	P1T7	2004-04-08	12:25
	P1T8	2004-04-08	14:23
B3	B3T1	2004-04-20	12:21
	B3T2	2004-04-20	16:25
	B3T3	2004-04-20	17:12
	B3T4	2004-04-20	17:45
P3	P3T1	2004-04-27	11:22
	P3T2	2004-04-27	15:17
	P3T3	2004-04-27	15:36

Table 7.2 Weather conditions

Test date	Sky	Sea	Minimum air temperature °F	Maximum air temperature °F	Mean wind speed knots	Max. sustained wind speed knots	Mean pressure mb
2004-03-29	Clear	Calm	55.0	80.1	4.7	11.1	1020.7
2004-04-05	Clear	Calm	42.1	77.0	6.4	11.1	1016.8
2004-04-06	Clear	Calm	42.1	73.0	4.5	9.9	1017.9
2004-04-08	Cloudy	Choppy	66.2	79.0	11.4	20.0	1009.0
2004-04-20	Cloudy	Calm	51.1	75.9	4.4	8.9	1022.4
2004-04-27	Clear	Calm	62.6	80.6	8.4	14.0	1016.7

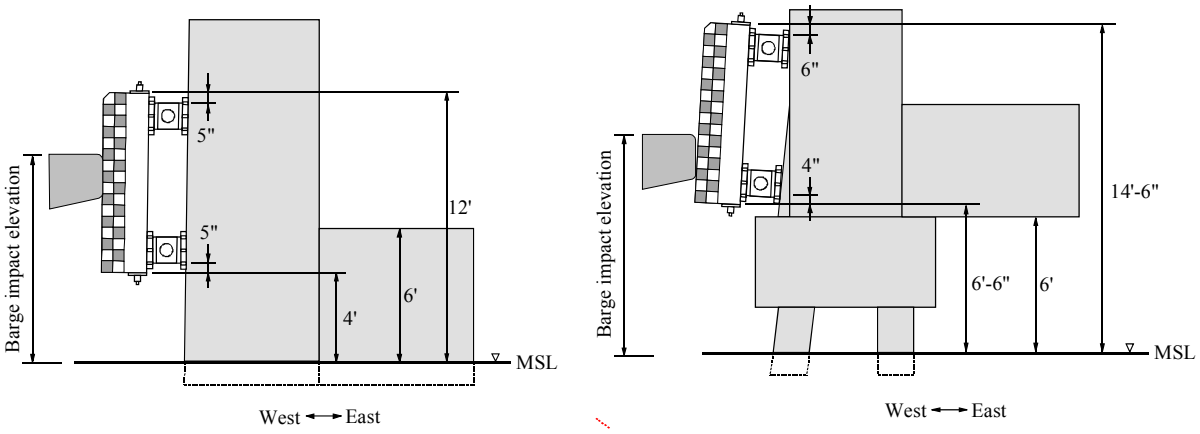

a) Pier-1 b) Pier-3

Figure 7.1 Barge impact elevations

Table 7.3 Impact elevations

Test series	Test identifier	Elevation[+] of top of impact block ft.	Elevation[+] of top of barge headlog ft.	Distance between top of impact block and top of barge ft.
P1	P1T1	12.0	9.0	3.0
	P1T2	12.0	9.5	2.5
	P1T3	12.0	9.0	3.0
	P1T4	12.0	9.0	3.0
	P1T5	12.0	9.5	2.5
	P1T6	12.0	9.25	2.75
	P1T7	12.0	9.0	3.0
	P1T8	12.0	10.0	2.0
B3	B3T1	14.5	10.5	4.0
	B3T2	14.5	10.0	4.5
	B3T3	14.5	9.5	5.0
	B3T4	14.5	9.5	5.0
P3	P3T1	14.5	9.5	5.0
	P3T2	14.5	9.5	5.0
	P3T3	14.5	9.5	5.0

[+]Above mean sea level (MSL)

In Table 7.4, imparted kinetic impact energies are reported for all test series conducted (P1, B3, and P3). For the series P1 tests, the imparted energies include the influence of frictional energy dissipation. For test series B3 and P3 (conducted on Pier-3), 55 ft. payload spans were not present on the test barge, hence frictional energy dissipation did not occur and the imparted kinetic energies were equal to the initial kinetic energies. In Figure 7.2, the imparted kinetic energies generated during test series P1, B3, and P3 are illustrated and compared. Since imparted kinetic energies are the primary quantities of interest in this study, from this point forward these energies will be referred to simply as kinetic energies of impact. No further mention of initial kinetic energies will be made.

During each test, measurements of impact forces (loads), accelerations, displacements, deformations, and pressures were collected using high-speed sensor networks and data acquisition systems. Detailed time-histories of the experimentally collected test data are presented in Appendices A – I of this report. Quantities that were directly obtained from measured sensor data are presented in Appendices A – G, whereas quantities that were indirectly obtained, via back-calculation techniques, are presented in Appendices H and I.

In the following sections of this chapter, discussions of key experimentally collected data are presented. Primary focus is placed on results that can be interpreted directly, without the need for supplementary interpretation aids such as computer models. Later in this report (Chapter 10), additional discussion of test results will be presented in which experimentally collected data and computer models are merged together for the purpose of quantifying parameters that could not be directly measured during the experimental test program.

Table 7.4 Impact conditions

Test series	Test identifier	Impact speed knots	Impact speed ft./sec.	Pushboat connection to barge	Impact weight tons	Initial Kinetic energy kip-ft.	Imparted kinetic energy kip-ft.
P1	P1T1	0.75	1.27	Hard rigging	626	33	25
	P1T2	1.75	2.95	Soft line	604	172	130
	P1T3	1.98	3.34	Soft line	604	220	167
	P1T4	2.59	4.37	Soft line	604	376	285
	P1T5	2.42	4.08	Soft line	604	329	249
	P1T6	3.45	5.82	Soft line	604	668	506
	P1T7	3.41	5.76	Soft line	604	653	494
	P1T8	3.04	5.13	Soft line	604	519	393
B3	B3T1	0.96	1.62	Hard rigging	344	29	29
	B3T2	0.89	1.50	Hard rigging	344	25	25
	B3T3	0.86	1.45	Hard rigging	344	24	24
	B3T4	1.53	2.58	Hard rigging	344	75	75
P3	P3T1	0.77	1.30	Hard rigging	344	19	19
	P3T2	1.33	2.24	Hard rigging	344	57	57
	P3T3	1.84	3.11	Hard rigging	344	108	108

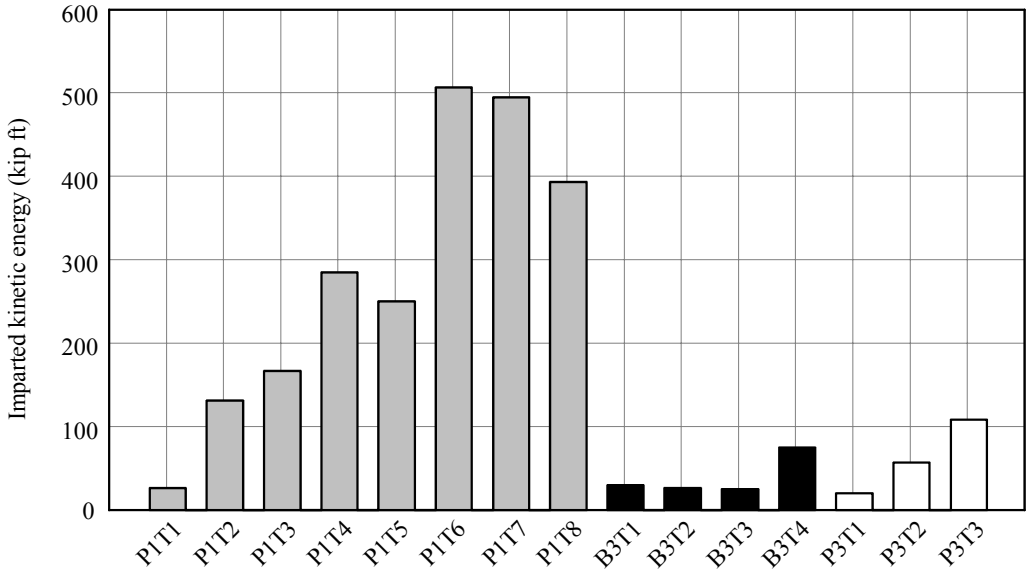

Figure 7.2 Kinetic impact energies generated during tests

7.2 Impact Loads

Time histories of impact loads (forces), directly quantified using the impact block and load cell assemblies described in the previous chapter, are presented in Figure 7.3 through Figure 7.6. Peak magnitudes and total time durations of measured loads are summarized in Table 7.5. Load histories for test series P1 are separated into two sub-categories: tests in which the impacts occurred at undamaged sections of barge bow (Figure 7.3) and tests in which previously damaged (deformed) sections of bow were re-impacted (Figure 7.4). Test P1T1 was a low-speed diagnostic impact used to test the sensor arrays and data acquisition systems. As a result, loads generated during this test were small. In contrast, the largest impact load that was recorded for the entire test program occurred during test P1T4 in which a peak force of 1056 kips was generated.

Comparing the kinetic energies of tests P1T4 and P1T5 (Figure 7.2), one would expect to see time histories of impact load in Figure 7.3 that match somewhat more closely than is shown. Review of impact test video for these tests (Figure 7.7), however, reveals that test P1T4 was a nearly-perfect head-on impact, while in test P1T5 the test barge struck the pier at a mildly oblique impact angle. The data in Figure 7.3 thus indicate that worst case, maximum magnitude impact loads for flat-faced pier columns (e.g., square and rectangular in cross-section) are those generated by perfectly head-on collision conditions. In such cases, the entire width of the pier-column face comes into contact with the barge bow at the same instant in time. As a result, multiple stiffening frames inside the barge bow (see Chapter 4) are immediately subjected to deformation and the barge bow behaves in a manner that is very stiff, in turn generating maximum possible impact forces.

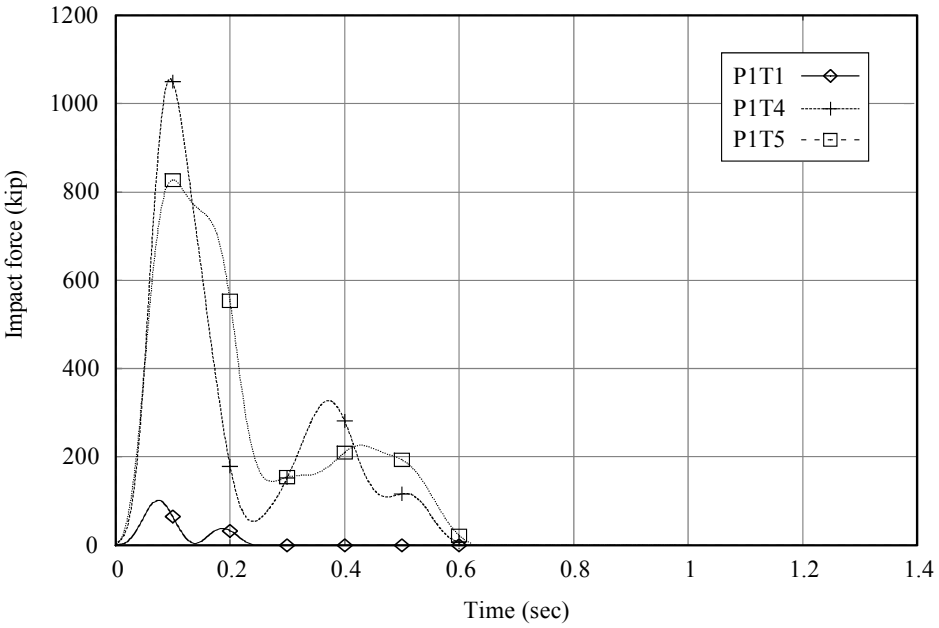

Figure 7.3 Dynamic impact loads measured during Pier-1 tests on undamaged portions of barge bow

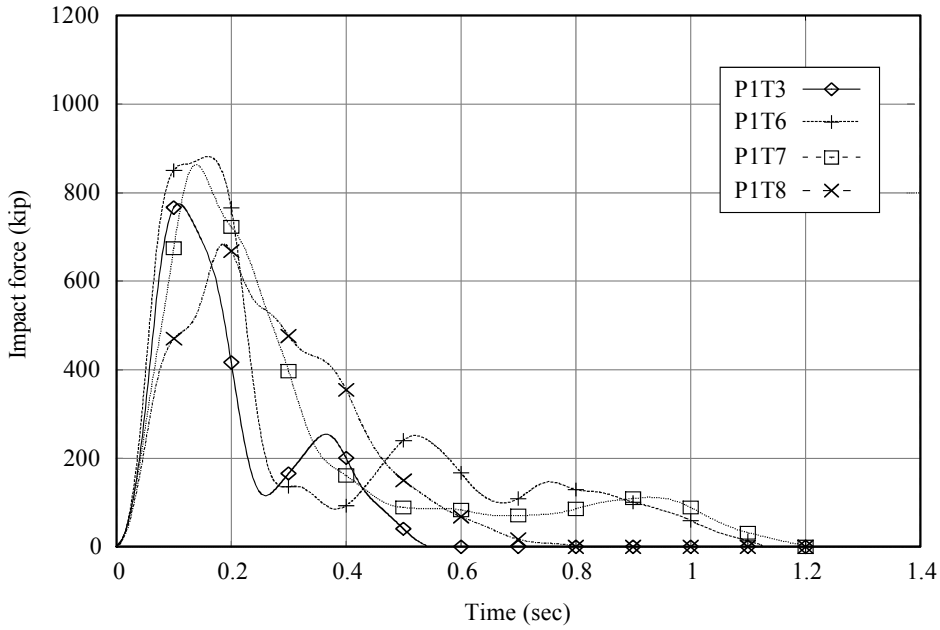

Figure 7.4 Dynamic impact loads measured during Pier-1 tests on damaged portions of barge bow

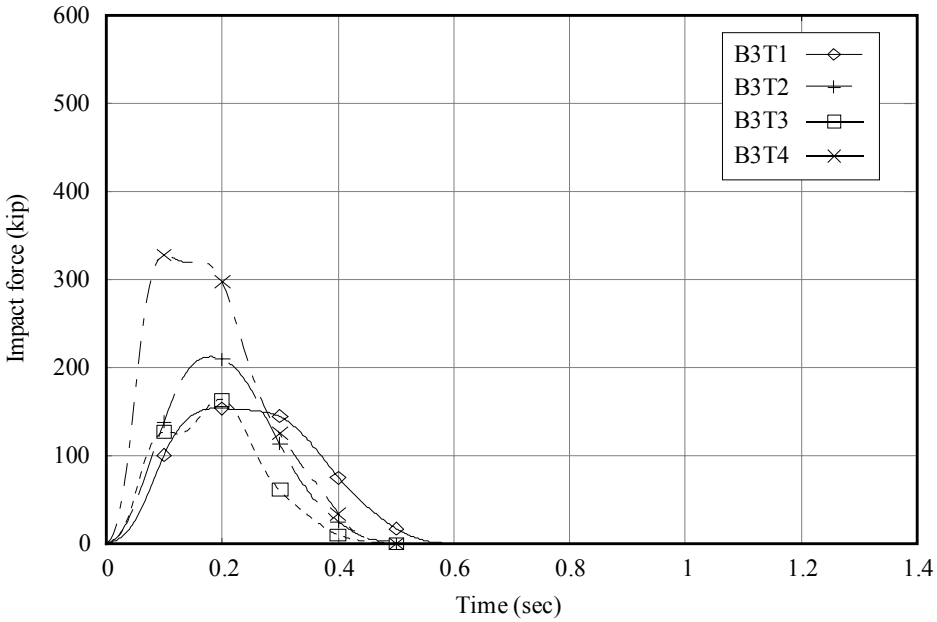

Figure 7.5 Dynamic impact loads measured during test series B3

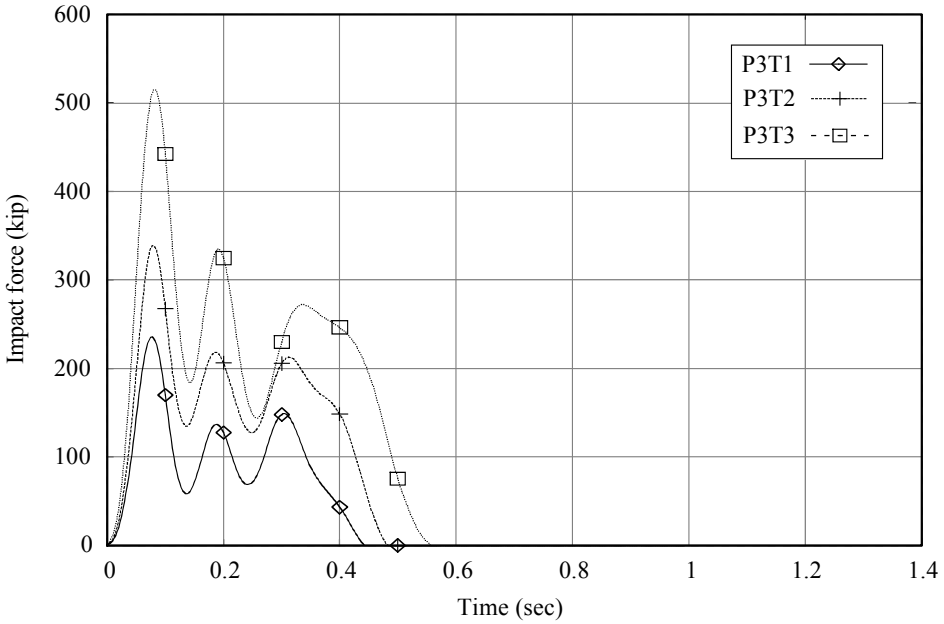

Figure 7.6 Dynamic impact loads measured during test series P3

Table 7.5 Experimentally measured impact loads

Test series	Test identifier	Peak impact load kips	Impact load duration sec	Condition of barge impact zone prior to test
P1	P1T1	102	0.25	undamaged
	P1T2	N/A[+]	N/A[+]	undamaged
	P1T3	775	0.54	damaged
	P1T4	1056	0.6	undamaged
	P1T5	827	0.62	undamaged
	P1T6	882	1.12	damaged
	P1T7	864	1.19	damaged
	P1T8	684	0.79	damaged
B3	B3T1	154	0.58	undamaged
	B3T2	212	0.48	undamaged
	B3T3	164	0.48	undamaged
	B3T4	328	0.50	undamaged
P3	P3T1	235	0.44	undamaged
	P3T2	339	0.48	undamaged
	P3T3	516	0.56	undamaged

[+] Data acquisition system on pier failed to trigger during test P1T2

In contrast, oblique impact conditions produce a point-contact between the barge bow and a corner of the pier cross-section. Due to the more limited contact area, fewer internal stiffening frames are initially mobilized, and the barge deforms in a manner that is softer than that of a perfectly head-on condition. Eventually, the contact area grows—as the crush depth grows—until sufficient force has been generated to halt forward motion of the barge. Generally, an oblique impact at a particular energy level will produce smaller impact loads than a corresponding head-on impact at the same energy level. However, for very high-energy impact conditions (beyond the range conducted in this study), initial interaction (contact) between the barge bow and the pier columns may be of less importance than the overall resulting pier penetration-depth into the barge. In such instances, differences between head-on and oblique impact loading conditions may be less pronounced.

It is worth noting that these phenomena may also be effectively studied using finite element impact simulation techniques, particularly now that calibration and validation data have been experimentally collected using full-scale testing. For example, previous numerical studies (Consolazio and Cowan 2003, 2005) have been conducted to study differences in loads generated by barge collisions with circular cross-section pier columns versus head-on and oblique collisions with flat-faced rectangular pier columns. These studies have illustrated that the point-contact phenomenon occurs in *all* barge impacts on pier columns having circular cross-sectional shapes and that in many cases, the use of circular column cross-sections can result in smaller magnitude impact loads.

a) Barge bow parallel to impact block (head-on impact) during test P1T4

b) Barge bow not parallel to impact block (mildly oblique impact) during test P1T5

Figure 7.7 Comparison of impact angles for tests P1T4 and P1T5

Comparing load histories obtained from series B3 (Figure 7.5) and series P3 (Figures 7.6), it is evident that the bridge superstructure influenced the characteristics of impact loads that were generated. During series B3, stiffness and inertia from the superstructure added to the resistance of Pier-3, leading to time histories of impact force that appear similar in form—although lesser in magnitude—to those obtained from tests on the far stiffer Pier-1. However, once the bridge superstructure was removed, Pier-3 became much more flexible. Load histories obtained from test series P3 exhibit much greater levels of fluctuation than did series B3. In each P3 test, distinct cycles of loading/unloading are clearly evident in the time histories (Figure 7.6). Each of these cycles involves contact of the barge with the pier, generation of impact load, momentary acceleration of the pier away from the barge (which produces a decrease in the impact load), and subsequent rebound of the pier

back into contact with the still-forward-moving barge. In each P3 test, this process repeated approximately three times before the barge was brought to a complete stop. Vessel-pier-soil interaction of this type is unquestionably dynamic in nature and will vary with respect to the stiffness and mass characteristics of the barge, pier, foundation, and soil.

A characteristic common to the P1, B3, and P3 load time histories presented here is that, in all cases, very short rise-times were required to transition from zero load to peak (maximum) load magnitude. In all cases, less than 0.2 sec.—and in most cases, less than 0.1 sec.—was all the time that was required to reach peak impact load. Given such short rise times, it is clear that responses of both the structure and soil involved dynamic components of resistance. This issue will be addressed in greater detail later in this chapter.

Comparisons of peak experimentally measured dynamic impact loads and equivalent static loads predicted by the AASHTO barge impact provisions are presented in Figure 7.8. Two separate AASHTO curves are presented: one for a barge width of 49 ft. 6 in. (the width of the test barge), and a second for a barge width of 35 ft. (the width of a jumbo hopper barge). Below an impact energy level of approximately 400 kip-ft., the two AASHTO curves are identical to one another. Examination of the experimental data suggests a functional relationship between kinetic energy and impact force that is similar in form to the AASHTO relationships but different in magnitude. Similar to the AASHTO curves, the experimental data follow a linear trend line up to a transition point after which the impact loads plateau with respect to further increases in kinetic impact energy. However, the experimental and AASHTO plateau levels (force magnitudes) differ considerably.

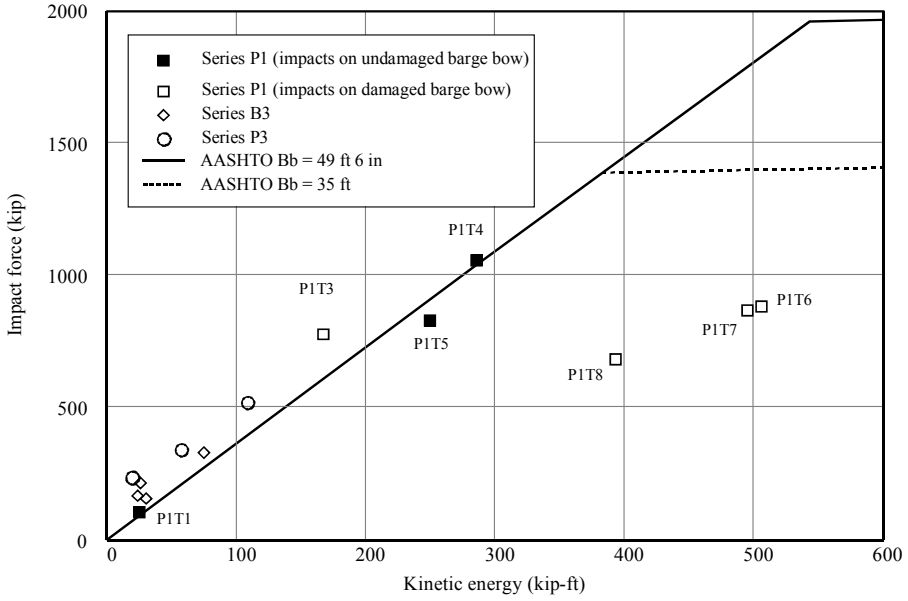

Figure 7.8 Comparison of measured dynamic loads and AASHTO static loads

For the two highest energy impact tests conducted in this study—P1T6 and P1T7—the peak impact loads measured were 882 kips and 864 kips, respectively. At an impact energy level equal to those generated by these tests (500 kip-ft.), the AASHTO curve for the test barge (i.e., for a width B_B = 49 ft. 6 in.) yields a static equivalent impact load of

1810 kips—approximately 100% greater than the experimentally measured loads. Examination of data for tests P1T3 through P1T8 suggests an apparent plateau in load level at approximately 1100 kips. Presence of the plateau logically indicates that maximum possible impact load magnitudes are primarily a function of the load carrying (crushing) capacity of the barge bow. Once significant yielding and fracturing of steel plates in the barge bow begin, major increases in load magnitude are not likely to occur solely as a result of additional crushing deformation.

With regard to the load plateau observed at 1100 kips, it must also be noted that the three highest-energy impact tests—P1T6, P1T7, and P1T8—were all conducted on portions of the barge bow that had been damaged by previous tests. It is not possible to determine, based exclusively on the measured test data, whether impact loads at these energy levels would have been higher had the impacts occurred on undamaged portions of the barge bow. Such determination, however, will be possible in the future once experimental data collected during this study have been integrated together with high-resolution finite element barge impact simulation techniques.

Results obtained from the B3 and P3 series of impact tests, which were conducted at much lower kinetic energies than the P1 tests (excluding diagnostic test P1T1), revealed that the measured dynamic loads exceeded the corresponding static AASHTO loads. In Figure 7.9, experimental load data for all tests conducted at impact energies below 300 kip-ft. are compared to the AASHTO provisions. Below impact energies of 200 kip-ft., experimentally measured dynamic loads consistently exceeded the static loads specified by AASHTO. Moreover, at energies below 50 kip-ft., experimentally measured dynamic loads exceeded the AASHTO loads in many cases by more than 100%.

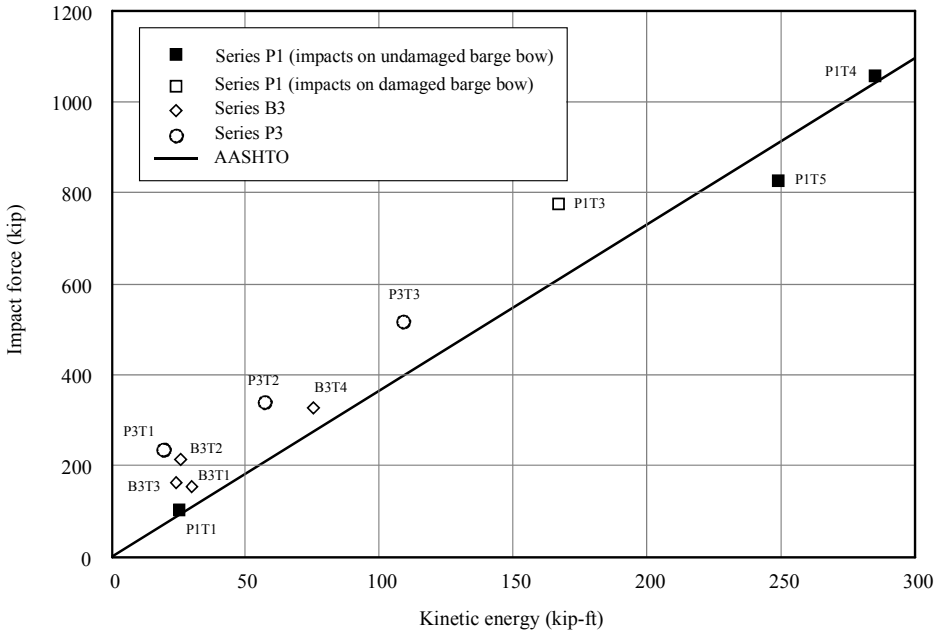

Figure 7.9 Comparison of measured dynamic loads and AASHTO static loads for low energy impact conditions

For bridges crossing navigable waterways, the AASHTO provision require that all bridge elements (e.g., piers) located in water depths of 2 ft. and greater be designed for barge impact loads. For piers distant from the vessel transit path, AASHTO specifies that minimum design impact loads "… be computed using an empty hopper barge drifting at a speed equal to the yearly mean current for the waterway location" (AASHTO 1991). Considering typical barge types (e.g., jumbo hopper barges) and typical waterway currents, impact energies for this "drifting barge condition" generally fall approximately within the range of 25 kip-ft. to 50 kip-ft.

Hence, the fact that, at energy levels below 50 kip-ft., measured dynamic loads significantly exceeded the corresponding AASHTO static loads is important in its implications for the design of piers distant from vessel transit paths. However, only so much can be concluded from a comparison of peak *dynamic* (time-varying) loads and *static* (time-invariant) loads. Because dynamic loads vary in magnitude through time, the severity of structural demand (response) that is generated will depend on the relationship between characteristics of the load (magnitude, duration) as well as characteristics of the pier (stiffness, natural period). If the time-duration of load is very short relative to the natural period of the structure (i.e., the load is essentially "impulsive" in nature), then structural response to the load will generally be less severe than response to an equal-magnitude load applied in a static (infinite duration) sense. Conversely, if the time-duration of the loading is on the same order of magnitude as the natural period of the structure, then significant potential exists for dynamic interaction between the load and the structure. In such cases, dynamic *amplification* of structural response can occur and can ultimately result in structural response that is greater than that which would be produced by an equal-magnitude static load.

In attempting to quantify the relative severity of two different loading conditions, a comparison of structural design forces (shears, moments) generated for each loading condition is more meaningful than a comparison of raw load magnitudes. In this study, such comparisons are carried out (in Chapter 10) using numerical pier and soil models that have been calibrated and validated against the experimentally collected test data. By then applying experimentally measured time-varying dynamic loads and static AASHTO loads to the numerical models, design forces for various structural elements (piles and pier columns) can be computed and compared using dynamic and static analysis procedures.

7.3 Barge Deformations

As noted earlier, tests P1T2 through P1T8 generated permanent inelastic deformations at the bow of the test barge (Figure 7.10). Using procedures previously presented in Chapter 4, measurements of barge bow damage were made and damage profiles were recorded. (Detailed damage profiles for tests P1T2 through P1T8 are provided in Appendix G of this report.) Using the damage profile data collected after each impact test, incremental barge deformation (crush) areas, A_B, were computed as indicated in Figure 7.11. Generally, the geometries of the incremental barge crush areas generated by the impact tests were not of the ideal rectangular form assumed by AASHTO. Hence, to permit comparisons

Figure 7.10 Permanent deformation of barge bow resulting from series P1 tests

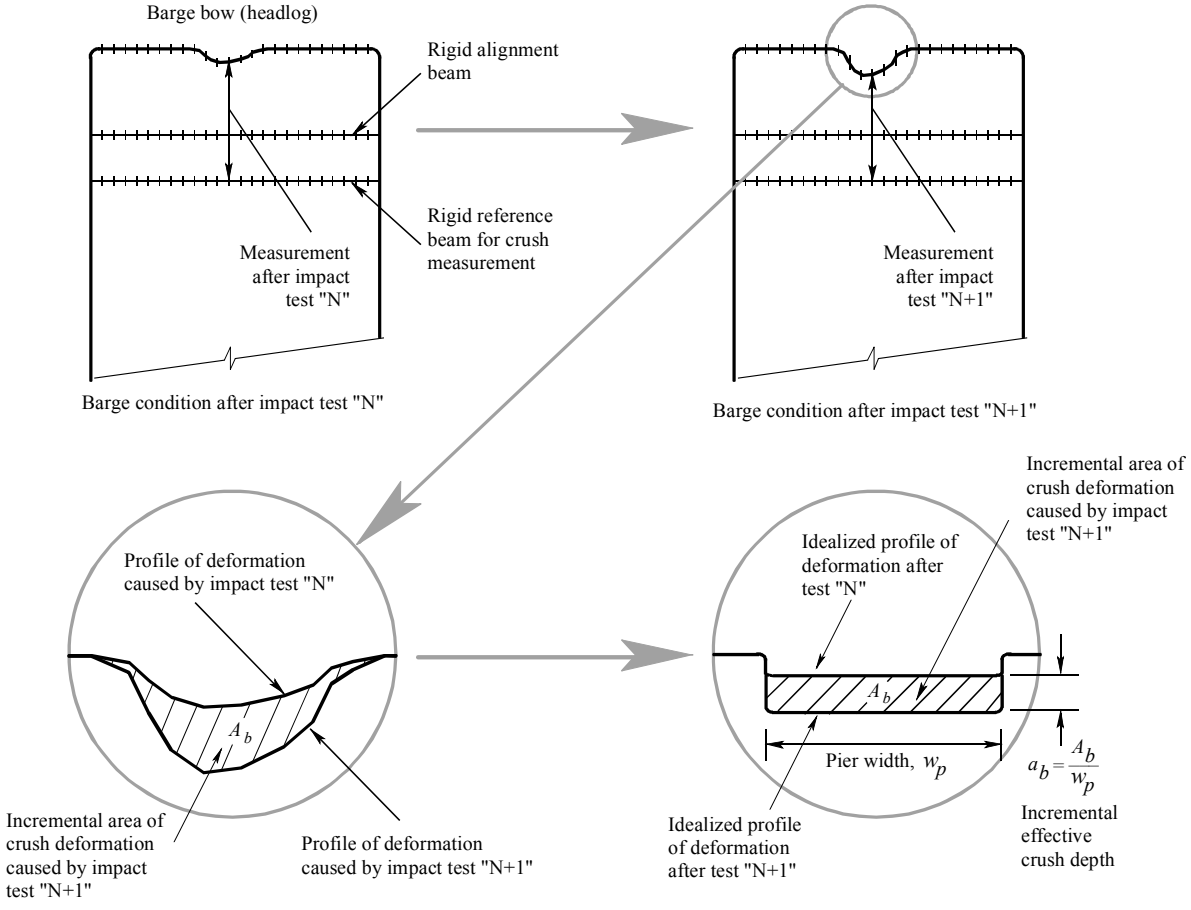

Figure 7.11 Determination of incremental effective crush depth

Table 7.6 Experimentally measured barge deformations

Test series	Test identifier	Condition of barge impact zone prior to test	Barge impact zone response	Incremental crush area in.^{2}	Inc. effective crush depth in.
P1	P1T1	undamaged	elastic	negligible	negligible
	P1T2	undamaged	inelastic	39	0.55
	P1T3	damaged	additive	112	1.55
	P1T4	undamaged	inelastic	89	1.24
	P1T5	undamaged	inelastic	105	1.45
	P1T6	damaged	additive	393	5.46
	P1T7	damaged	additive	339	4.71
	P1T8	damaged	additive	344	4.78
B3	B3T1	undamaged	elastic	negligible	negligible
	B3T2	undamaged	elastic	negligible	negligible
	B3T3	undamaged	elastic	negligible	negligible
	B3T4	undamaged	elastic	negligible	negligible
P3	P3T1	undamaged	elastic	negligible	negligible
	P3T2	undamaged	elastic	negligible	negligible
	P3T3	undamaged	elastic	negligible	negligible

between experimentally measured crush data and corresponding AASHTO predicted data, the measured incremental crush areas, A_B, were converted into equivalent rectangular areas having width w_P equal to the width of the impact block. Subsequently, incremental effective crush depths, a_B, were computed as $a_B = A_B / w_P$ (Figure 7.11).

Quantitative, as well as qualitative, data relating to sustained barge bow deformations are reported in Table 7.6. Comparison of this data to the AASHTO provisions requires that consideration be given to the accumulation of deformations that occurred due to repeated impacts at the same locations on the barge bow. By inspecting the crush profiles for each test (Appendix G), it was determined that generally three zones on the barge bow were subjected to impact loads. One zone was subjected only to load from test P1T4. A second zone was subjected to accumulated damage caused by tests P1T2 and P1T3. A third zone was subjected to accumulated damage from tests P1T5, P1T6, P1T7, and P1T8. Thus, the relationship between accumulated kinetic energy and accumulated crush depth can be plotted by summing the appropriate incremental kinetic energies and incremental crush depths given in Table 7.6. In Figure 7.12, curves of this form—computed using the experimentally measured crush data—are compared to the AASHTO relationship between kinetic energy and crush depth.

AASHTO curves are shown for two separate cases: one for a barge width of 49 ft. 6 in. (the width of the test barge), and a second for a barge width of 35 ft. (the width of a jumbo hopper barge). At low impact energy levels (<300 kip-ft.), all three experimental test sequences produced crush-energy curves that were shallower in slope than either of the two AASHTO curves. In this energy range, the AASHTO curve corresponding to the actual barge

width (49 ft. 6 in.) was a better match to the experimental data. However, for the higher-energy impact sequence P1T5-P1T6-P1T7-P1T8, the experimental crush versus energy curve was more closely matched by the steeper AASHTO curve corresponding to a barge width of 35 ft. Based on the experimental results presented here, as well as supplementary analytical studies (Consolazio and Cowan 2003, 2005), it is evident that the relationship between barge kinetic energy and barge bow crush depth is more strongly a function of the ratio s_S/w_P, (where s_S is the lateral spacing between internal stiffening frames in the barge bow and w_P is the width of the impacted pier column) than of the overall barge width B_B, as is assumed by the AASHTO provisions. Based upon this observation, future modifications to the AASHTO provisions may be warranted.

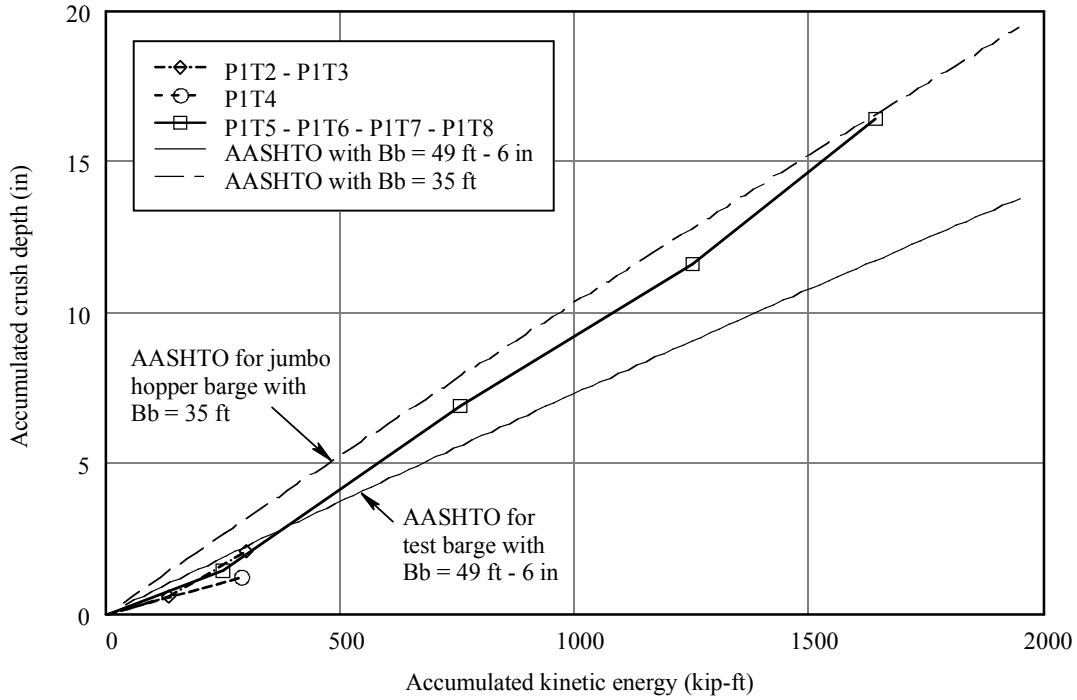

Figure 7.12 Comparison of experimental and AASHTO relationships between kinetic energy (KE) and barge crush depth (a_B)

7.4 Discussion of structural and geotechnical response data for test P1T7

During selected series P1 impact tests, geotechnical sensors at Pier-1 were monitored for the purpose of supplementing the data collected by the barge and pier sensor networks described earlier. Installation and monitoring of the geotechnical sensors were carried out as part of a separate investigation that was conducted in parallel to the study described in this report. For a complete description of the geotechnical study, the reader is referred to McVay et al. (2005). Measurements recorded by the geotechnical sensor network included soil pressures in areas adjacent to the foundation of Pier-1, pile strains, and pile accelerations.

Pile strain and acceleration measurements were accomplished via pre-test installation of an instrumented pipe pile at the east face of the Pier-1 foundation (Figure 7.13). Strain gages and accelerometers were attached to a reinforcing cage placed inside this pile, and then cast in concrete to form a composite hollow circular cross-section (Figure 7.14). Dimensions of the instrumented pile were chosen to produce a flexural stiffness that was of the same order of magnitude as that of the steel HP 14x73 piles that supported Pier-1. Fixity at the pile head was provided by boring through the tremie seal (Figure 7.13), and additionally clamping the pile to the top of the pile cap with a heavy steel bracket.

During tests P1T1, P1T6, and P1T7, all three instrumentation networks—barge, structural, and geotechnical—were used to simultaneously monitor and record high-speed dynamic load and response data. Measured time histories of impact loads generated during these three tests are compared in Figure 7.15. Being a diagnostic test, P1T1 generated only very small loads and therefore minimal foundation/soil response.

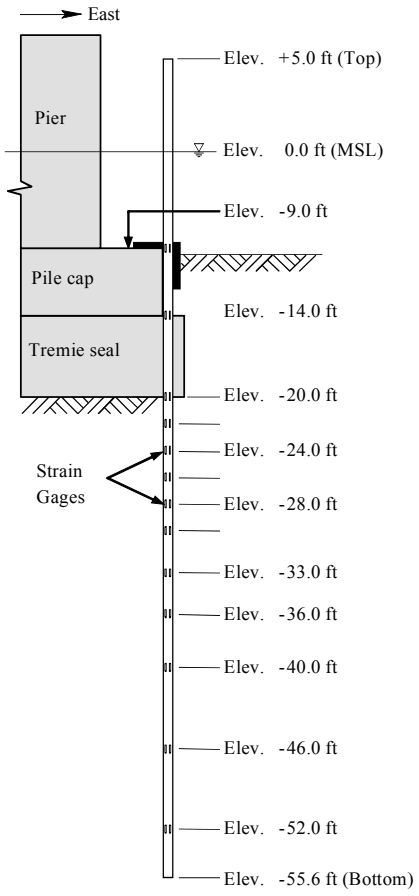

Figure 7.13 Elevation view of instrumented pile attached to Pier-1 (from McVay et al. 2005)

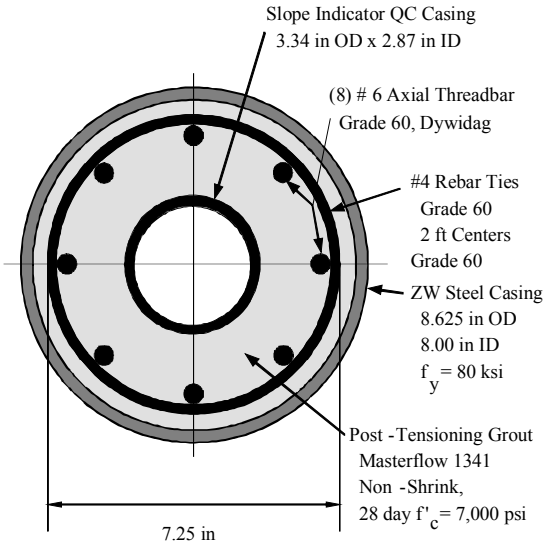

Figure 7.14 Cross-section of instrumented pile (from McVay et al. 2005)

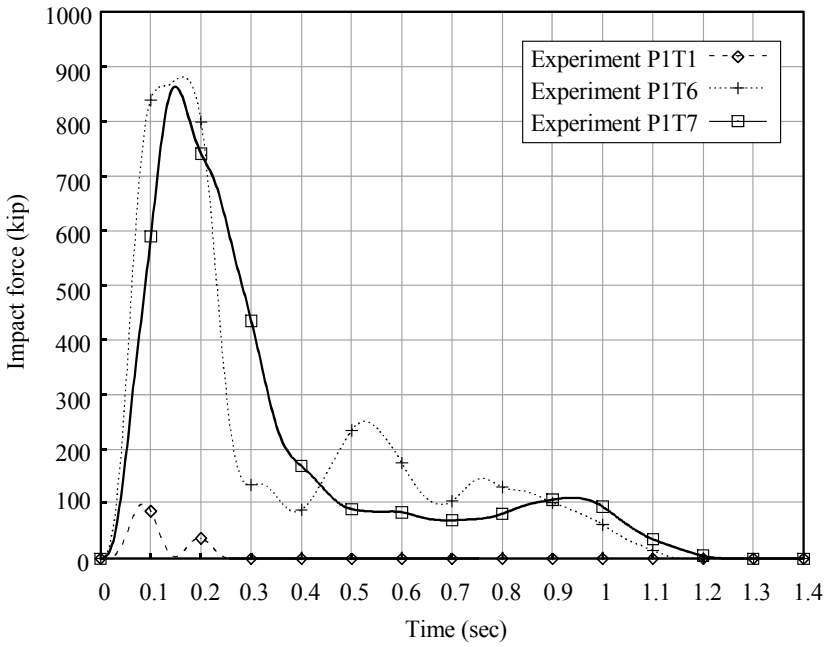

Figure 7.15 Load history plots of experiments P1T1, P1T6, and P1T7

In contrast, tests P1T6 and P1T7 were the two highest impact energy tests conducted (Figure 7.2) and thus generated significant impact loads. Detailed pier displacement data included in Appendix I of this report illustrate that among all of the series P1 tests, the largest magnitude pier motions (displacements) were generated during test P1T7. Accordingly, significant levels of soil response were also generated during this test. In the remainder of

this section, focus is given to describing relationships between impact loads, structural displacements, and soil responses measured during test P1T7.

Dynamic impact loads generated on Pier-1 during test P1T7 reached a maximum value of 864 kips and produced a maximum lateral pier displacement of 0.61 in. However, due to the dynamic nature of the collision, and hence the presence of dynamic forces, the load and displacement did not maximize at the same point in time. In Figure 7.16, applied impact loads, pier displacements, and structural inertia forces generated during test P1T7 are presented in normalized format to permit temporal (time-oriented) comparisons. Inertia forces shown in the figure were computed as the products of experimentally measured lateral pier accelerations and the total mass of all reinforced concrete pier elements (pier cap, pier columns, pile cap, and tremie seal).

Inertia forces that are shown as positive values in Figure 7.16 are forces that contributed to resisting the applied barge impact load. Hence, during the early portion of the impact, these forces aided the soil in resisting the applied impact load. The inertia forces were also mobilized rapidly, maximizing at approximately 0.08 sec.—well before either the impact load or pier displacement maximized. At approximately 0.15 sec., the inertia forces changed from positive to negative and became a form of loading rather than of resistance. The combined effect of the barge impact load and the inertia load produced a pier displacement that maximized at approximately 0.25 sec.

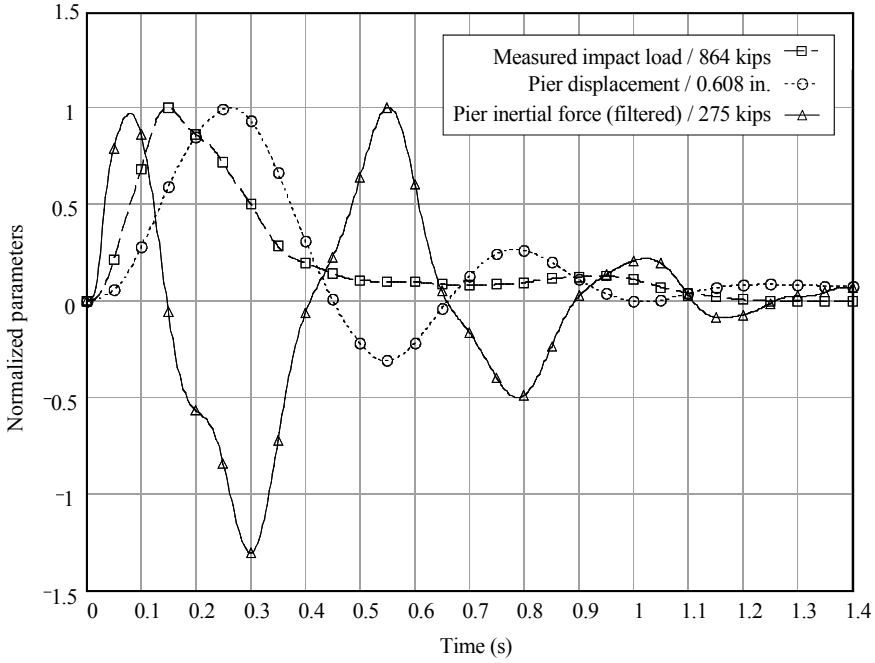

Figure 7.16 Normalized data for test P1T7

Had the measured impact loads and pier displacements maximized at approximately the same point in time, it would have been concluded that the collision event was primarily dominated by static behavior. This, however, was clearly not the case. Instead, observed differences in the timing of maximum load and pier response indicated the presence of dynamic phenomena in the structural response of the pier. Similarly, soil response may also

contain both static and dynamic (rate-dependent) components when loads are applied rapidly (as in a collision). The data presented in Figure 7.16, therefore constitute only a partial picture of the overall impact event. Soil resistance forces, both static and dynamic in nature, also significantly influenced pier response during test P1T7.

In order to fully characterize and compare all of the sources of impact resistance that were mobilized, soil forces were also quantified. These forces may be broadly classified into two categories: those determined directly from experimental measurements and those determined indirectly through the use of calibrated numerical models. In the following sections, soil forces determined directly from experimental measurements are discussed. Later in this report (Chapter 10), numerical models are used to indirectly quantify soil forces that could not be measured experimentally.

7.4.1 Soil resistance

Shear forces that were measured during test P1T7 using the instrumented pile (Figure 7.13) are shown in Figure 7.17 (McVay et al. 2005). In order to determine whether the soil response was predominantly static or a mixture of static and dynamic components of resistance, the pier displacements, pile shear forces, and soil reactions measured during the test are presented in normalized format in Figure 7.18. The figure reveals that the pile shear forces and the soil reactions at the head of the pile both maximized at approximately the same point in time (0.15 seconds).

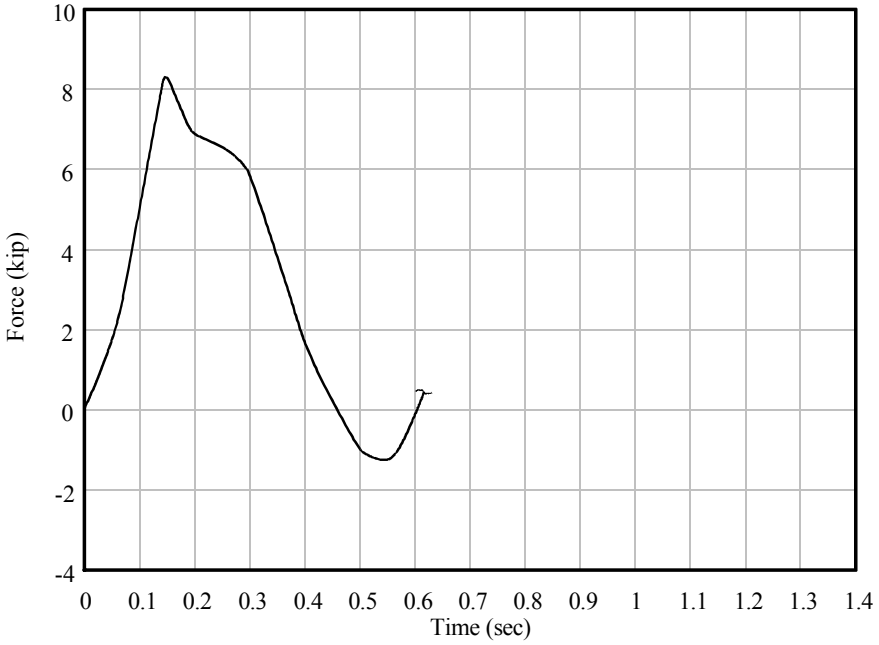

Figure 7.17 Shear forces at head of instrumented pile during test P1T7

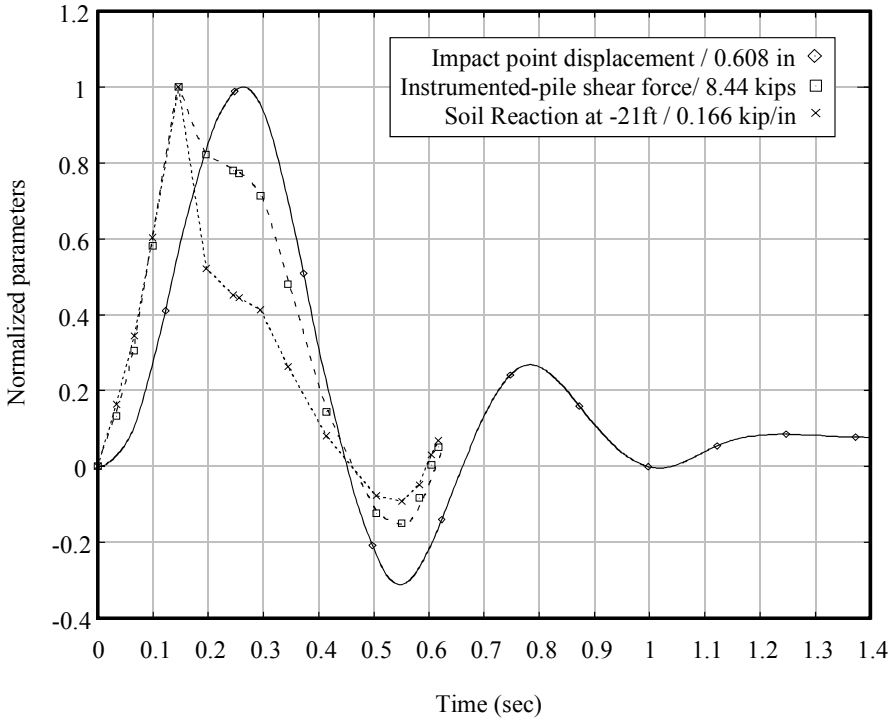

Figure 7.18 Normalized data for test P1T7

Maximum pile velocity occurred at approximately this same point in time, as is indicated by the slope of the displacement curve; thus, dynamic rate-dependent (e.g., velocity-dependent) components of soil resistance maximized at this same point in time. As the velocity decreased between 0.15 sec. and 0.25 sec., the dynamic component of the soil resistance also decreased. Thus, although lateral displacements continued to increase in magnitude between 0.15 sec. and 0.25 sec., the pile shear actually decreased slightly during this time frame. The fact that the maximum pile shear force did not occur at the point of maximum pile head displacement is a clear indication of dynamic soil response.

7.4.2 Dynamic resistance of soil adjacent to piles

From flexural strains measured by strain gauges attached to the instrumented pile, the time-varying curvatures and moments of the pile were determined. Lateral pile displacements (*y*-values) were then calculated through double integration of the curvature equations, and soil reactions (*p*-values) were derived through double differentiation of the moment equations along the pile (see McVay et al. 2005 for additional details). Using these procedures, time histories of pile displacements and soil reactions between elevations -21 ft. and -50 ft. were computed from measured geotechnical data.

At elevation -21 ft., measured soil resistance was observed to be well in excess of the static capacity of the soil (as quantified via pre-impact-test insitu soil testing). The difference between the measured (total) soil resistance and the smaller static capacity was attributed to dynamic load-rate effects in the soil. Under rapid loading, total soil resistance is composed of both dynamic (rate-dependent) and static (rate-independent) components. Results obtained

from test P1T7 demonstrated that the dynamic soil resistance components can be quite substantial under impact loading conditions.

Between elevation -21 ft. and elevation -26 ft, the dynamic component of soil reaction was found to decrease rapidly (due to decreasing soil particle velocities). At elevation -26 ft. and below, dynamic resistance was not evident, leaving only the static component of soil resistance. Therefore, the range of depths of primary interest here extend from approximately -21 ft. to approximately -26 ft. In Figure 7.19 and 7.20, time histories of experimentally determined pile displacements and corresponding soil reactions are presented for elevations -21 ft. and -26 ft.

It is noteworthy that maximum displacements near the pile head (at elevation -20 ft.) occurred at 0.25 sec. but that maximum soil reactions occurred earlier in time—soil reactions acting on the instrumented pile at elevations -21 ft. and -26 ft. reach maximum values at 0.15 sec. and 0.2 sec. respectively. For static loading conditions, maximum soil reactions occur at the points of maximum pile displacement. However, this need not be the case in dynamic loading situations where total soil reactions consist of both dynamic (rate-dependent) and static components. Dynamic (damping) forces generated on a pile are a function of several parameters including rate of loading, particle velocity, and soil properties.

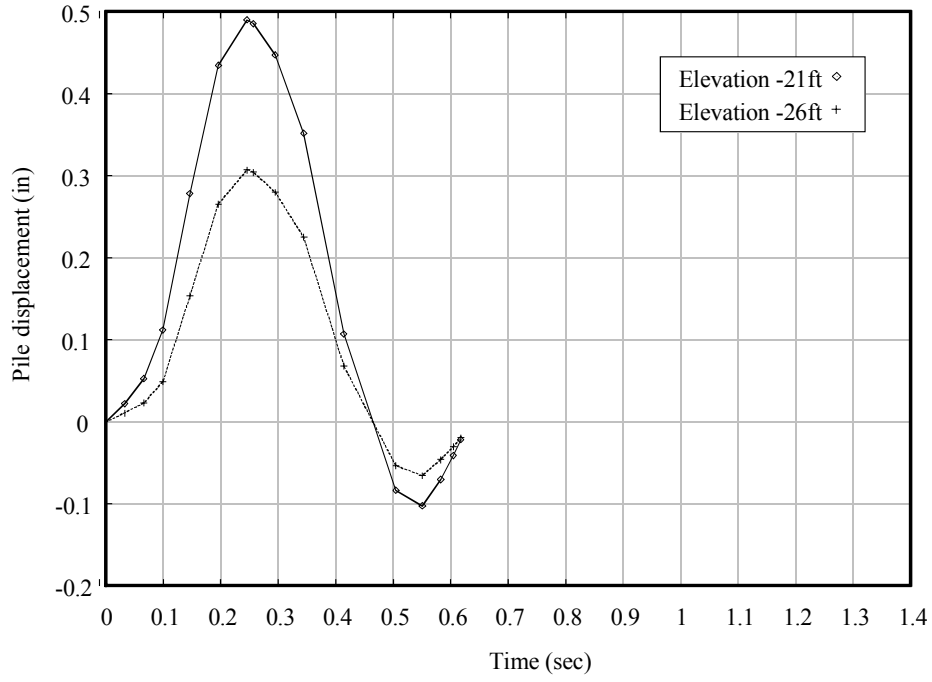

Figure 7.19 Lateral pile displacements (*y*-values) at elevations -21 ft. and -26 ft.

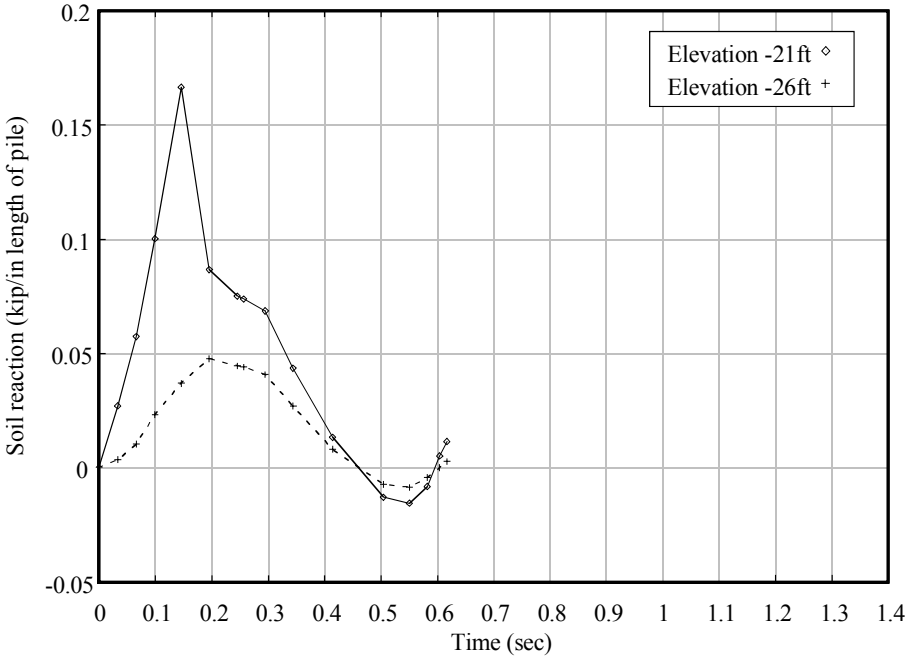

Figure 7.20 Lateral soil reactions (*p*-values) at elevations -21 ft. and -26 ft.

In Figure 7.19, points of maximum velocity are seen to occur at approximately 0.14 sec. where the slopes of the displacement-time curves, i.e. the velocities, reach their greatest positive values. Consequently, at this point in time, pile velocities have also reached their maximums and hence maximum dynamic damping forces are mobilized. As shown in Figure 7.20, soil reactions at elevations -21 ft. and -26 ft. maximize at approximately 0.14 sec. and 0.19 sec., respectively. When the pile reaches the point of maximum displacement and starts to rebound, velocities are reduced to zero and the dynamic (damping) force disappears. At this point in time, the soil reaction is attributable only to static resistance.

By plotting soil reaction forces as functions of pile displacements, experimentally determined dynamic *p-y* curves for elevations -21 ft. and -26 ft. were generated (Figure 7.21). To quantify the contribution of the dynamic damping force to the total soil reaction, estimated static *p-y* curves for elevations -21 ft. and -26 ft. are compared to the experimentally determined dynamic curves in Figure 7.22 and Figure 7.23. The dynamic and static *p-y* curves have the same initial slope and intersect one another at the point of maximum displacement. Figure 7.22 reveals that, near the top of the pile where velocities are greatest, the damping resistance component (the distance between the dynamic and static curves) may be larger than the static resistance component. At elevation -26 ft., velocities are smaller, and therefore, differences between the dynamic and static *p-y* curves are less pronounced.

The dynamic p-y curves shown in Figure 7.22 and Figure 7.23 also indicate that the slopes of the unloading curves were smaller than the initial slopes of the loading curves and that the unloading curves pass through the point of zero displacement at zero force. This indicates that upon unloading, the piles and the soil are still in contact to some degree. In clayey soils, separation at the soil-pile interface (gapping) under cyclic loading may occur

due to inelastic deformation. In sandy soils, however, gapping at the pile-soil interface may not occur.

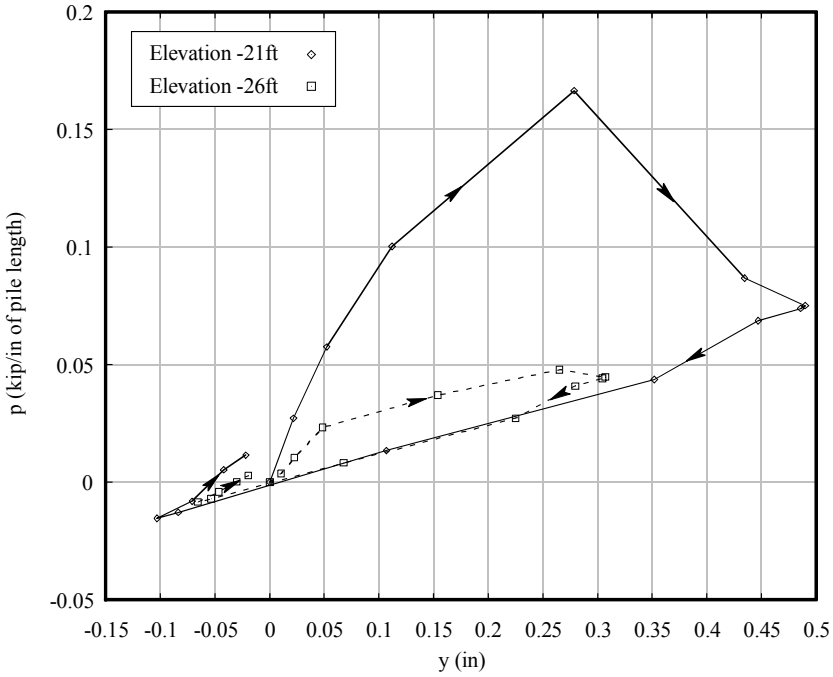

Figure 7.21 Experimentally determined dynamic *p-y* curves for elevations -21 ft. and -26 ft.

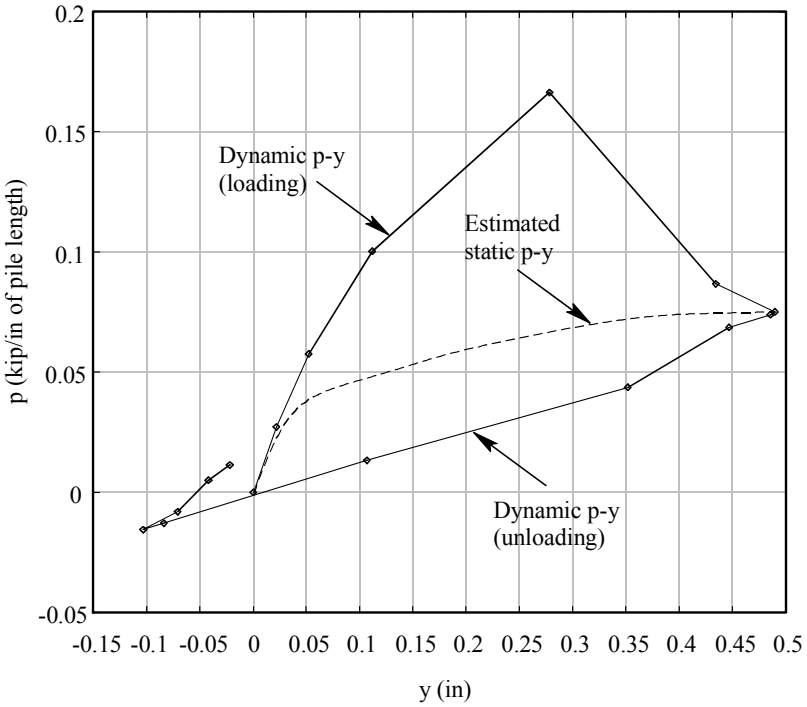

Figure 7.22 Comparison of dynamic and static *p-y* curves for elevation -21 ft.

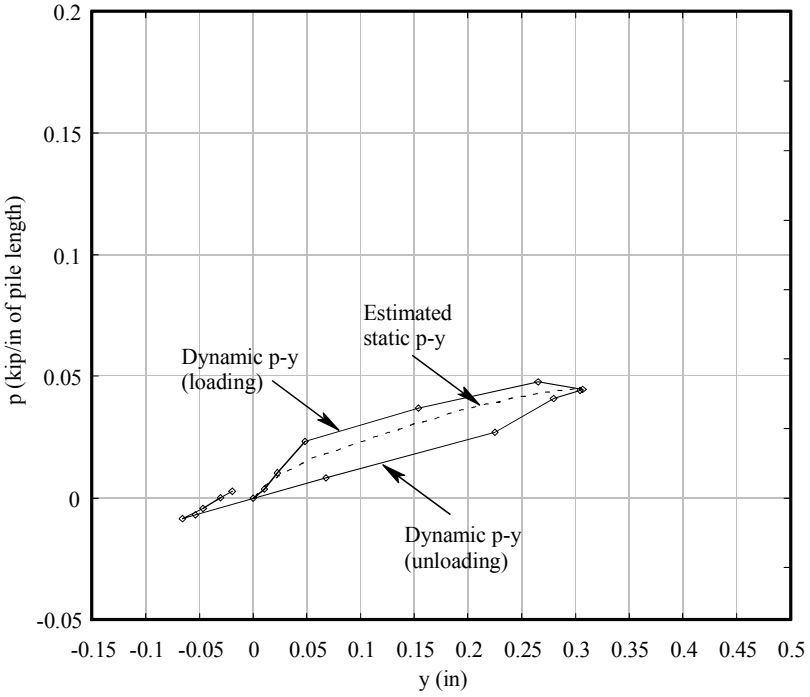

Figure 7.23 Comparison of dynamic and static *p-y* curves for elevation -26 ft.

Sands may cave-in and backfill around a pile during cyclic loading. The soil layering profile for Pier-1 (presented earlier in Chapter 3), indicates that the soil located between elevations -21 ft. and -26 ft. was sandy in nature. Thus, the fact that no significant soil gapping is apparent in Figure 7.22 or Figure 7.23 is consistent with the characteristics of the type of soil present.

7.4.3 Dynamic resistance of soil adjacent to pile-cap and tremie seal

Procedures for calculating the lateral resistance of a pier often ignore the contribution of soil surrounding the pile cap. This is partially due to the fact that embedment conditions may change due to scour and partially due to the fact that methods for quantifying such resistance have not been well established. Researchers have, however, found that lateral resistance provided by embedded caps can be very significant. Neglecting soil-cap resistance may lead to inaccuracies of 100% or more (Mokwa 1999). From the design perspective, neglecting cap-soil resistance means underestimating foundation stiffness which can lead to incorrect estimates—either conservative or unconservative—of shear, bending moment, and deflection of the piles.

At Pier-1, the pile cap measured 21 ft. x 39 ft. 2 in. x 5 ft. thick, and the tremie seal below the cap measured 24 ft. x 42 ft. 2 in. x 6 ft. thick (see Chapter 3 for additional details). At the time of the series P1 impact tests, the elevation of the bay bottom (mudline) was determined to be approximately at the elevation of the top of the pile cap. Thus both the pile cap and the seal were fully embedded in soil. At the east end of the pier, the interface area between the combined cap+seal, and the soil was then (21 ft. x 5 ft.) + (24 ft. x 6 ft.) = 249 ft ^{2}.

The current state of knowledge and practice regarding lateral cap resistance, especially dynamic soil-cap interaction and the mechanics of load transfer, is limited. To develop an improved understanding of soil-cap interaction and to quantify the lateral cap+seal resistance, push-in total stress cells were installed (McVay et al. 2005) in the soil at both the lead and trail sides of the cap and tremie seal of Pier-1. Soil forces acting on the cap and seal during impact were then determined from net changes of stress at both sides of the pier.

Figure 7.24 presents measured passive soil forces on the cap and seal for impact test P1T7. In reality, the forces shown are actually net *changes* of force relative to the initial, insitu soil pressure conditions. Maximum passive forces on the cap and seal in Figure 7.24 are 60 kips and 140 kips, respectively. For comparison, recall that the peak measured impact load for test P1T7 was 864 kips. Therefore, the total passive cap+seal force of 60 + 140 = 200 kips indicates a considerable contribution to overall lateral resistance of the pier. To further study the dynamic cap+seal-soil interaction during test P1T7, key experimental parameters have been normalized and plotted together in Figure 7.25.

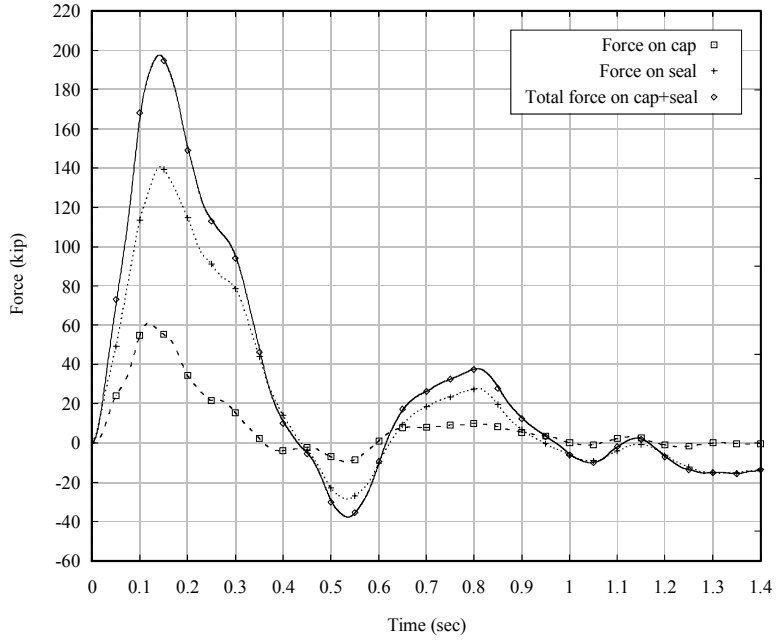

Figure 7.24 Experimentally determined passive soil forces on cap and seal during test P1T7

Displacements at the bottom of the seal (elevation -20 ft.) and at the top of pier shear wall (elevation +6 ft.) are in close agreement. Therefore, displacements and velocities of the cap, seal, and shear wall are all approximately equal. Forces acting on the cap and seal in Figure 7.25 show important similarities to results presented earlier in Figure 7.18 for the instrumented pile. In Figure 7.25, maximums of cap and seal force occur at points in time that are approximately the same as the point in time at which the slopes of the displacement curves are greatest—i.e., at the point of maximum lateral pier velocity. The fact that the maximum forces occur when velocity is greatest, rather than when displacement is greatest, clearly indicates the presence of a dynamic (damping) component of soil resistance against the pile cap and tremie seal.

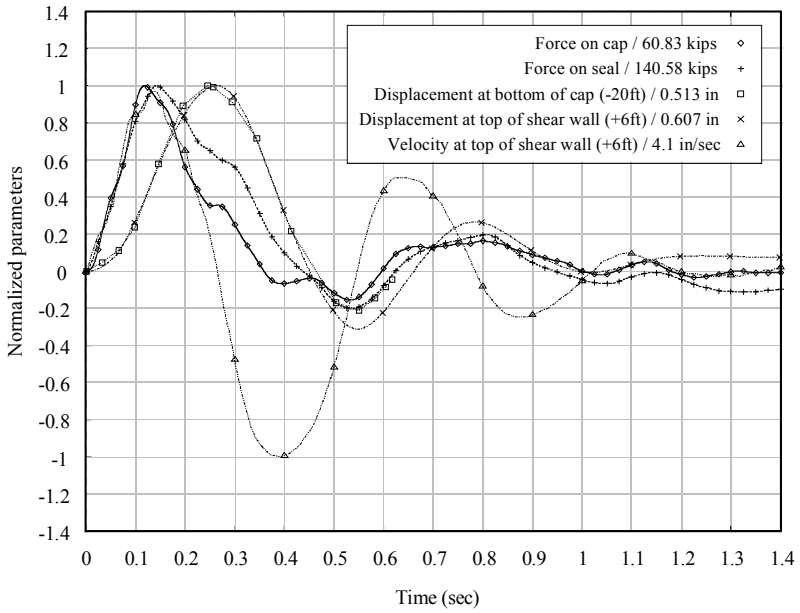

Figure 7.25 Normalized data for test P1T7

By plotting cap+seal soil forces as functions of lateral displacements, an experimentally determined dynamic *p-y* curve for the combined cap+seal system was generated. In Figure 7.26, the resulting dynamic curve is plotted together with an estimated static *p-y* curve. Clearly indicated in the figure is an approximately 120 kip maximum contribution to overall resistance that is attributable to dynamic damping forces (rate-dependent forces). In contrast, when the cap+seal reaches the point of maximum displacement, pier velocity drops to zero, dynamic damping forces vanish, and the passive force acting on the cap+seal—approximately 105 kips—is purely static in nature. In Figure 7.26, the area between the dynamic loading curve and the estimated static curve represents energy dissipated by radiation damping in the soil, whereas the area between the estimated static loading curve and the unloading curve represents energy dissipated by hysteretic damping of the soil.

Forces acting on the lead and trail sides of the cap+seal are separated and plotted individually in Figure 7.27. At 0.44 sec. after impact, the pier had completed an initial positive cycle of motion, and had rebounded back to its original position (zero displacement). However, it is noted that the soil force at the trail (west) side of the pier was positive, not zero. This fact indicates that soil at the west pier face caved-in during the initial forward (west-to-east) motion of the pier. Later, after moving through a negative cycle of motion, the displacement of the pier once again passed through zero at 0.68 sec. Here, the soil force on the lead (east) side of the pier was positive due to soil backfilling at the lead side. Based on the results obtained, it is evident that gapping did not occur at either the lead or trail-side interfaces between the cap+seal and the soil. This observation is consistent with the sandy nature of the soil surrounding Pier-1.

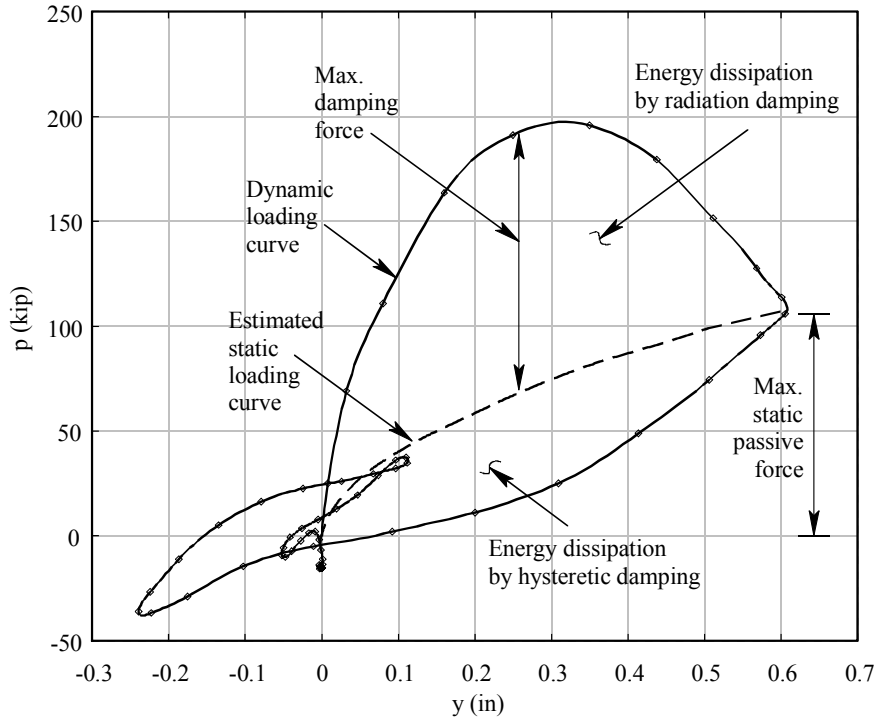

Figure 7.26 Experimentally determined dynamic *p-y* curve for the cap+seal

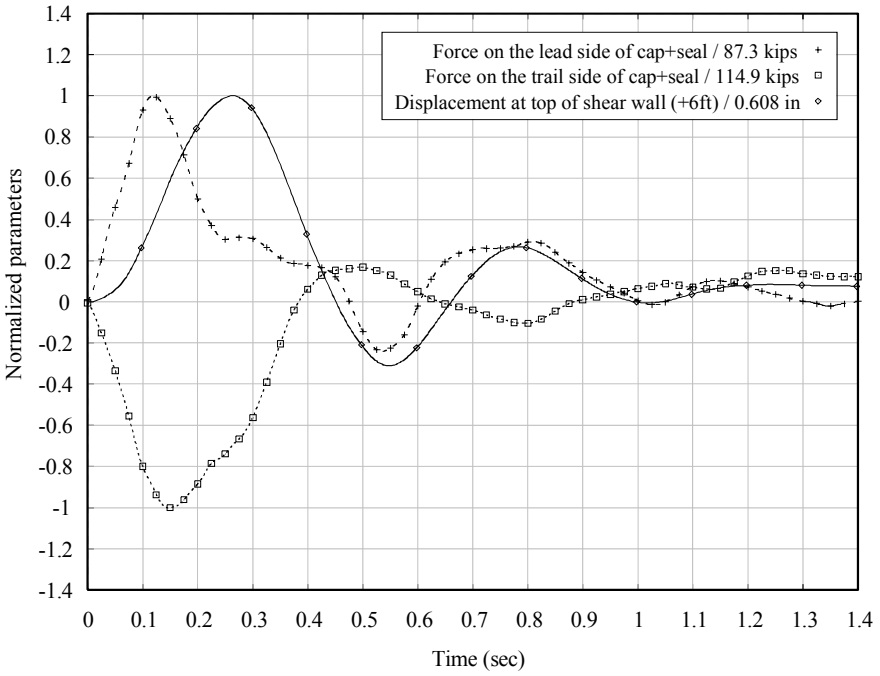

Figure 7.27 Experimentally determined lead and trail side forces on the pier cap and seal

7.5 Fluid forces on Pier-1

During the series P1 tests, a pressure transducer was installed below water level on the east side of Pier-1 to record water pressure changes during each test. A significant increase in water pressure along the east face of Pier-1 during impact would indicate that water surrounding the footing of the pier momentarily contributed dynamic resistance against the applied loading. Detailed time histories of the experimentally measured pressure water pressure data are presented in Appendix E of this report.

In order to quantify the dynamic resistances contributed by water pressure, the peak pressure changes for each series P1 test were multiplied by the submerged area of the east face of Pier-1. In Table 7.7, forces and resistance-contributions associated with water pressure changes are summarized. In all cases, except diagnostic test P1T1, the forces associated with water pressure were less than 1% of the applied loads.

Table 7.7 Experimentally determined dynamic water pressure data

Test series	Test identifier	Peak water pressure psi	Equivalent change in head in.	Water "pressure" force kips	Peak applied dynamic impact load kips	Ratio of water pressure to applied load %
P1	P1T1	0.36	9.66	4.06	102	4.0
	P1T2	N/A[+]	N/A[+]	N/A[+]	N/A[+]	N/A[+]
	P1T3	0.28	7.62	3.20	775	0.4
	P1T4	0.55	14.72	6.18	1056	0.6
	P1T5	0.33	8.89	3.74	827	0.5
	P1T6	0.30	8.22	3.45	882	0.4
	P1T7	0.39	10.45	4.39	864	0.5
	P1T8	0.16	4.21	1.77	684	0.3

[+] Data acquisition system on pier failed to trigger during test P1T2

CHAPTER 8
FINITE ELEMENT MODELING OF PIER STRUCTURES

8.1 Introduction

Nonlinear dynamic finite element analysis served two principal roles in this study: to provide data for use in planning the physical tests, and to aid in interpreting the experimental test results. Prior to conducting the physical impact tests, detailed finite element models of Pier-1, Pier-3, estimated soil conditions, and a barge were developed and dynamically analyzed to help establish close-to-optimal ranges for key test parameters. Using numerical impact simulation, various combinations of barge impact speed and mass were evaluated, and used to estimate anticipated impact forces as well as pier, soil, and barge responses. Dynamic load, acceleration, and displacement time-histories obtained from these preliminary analyses were then used to design instrumentation devices (e.g., impact blocks) and to "range" the specific sensors that would be needed for the tests.

Following completion of the experimental phase of the study, primary use of the models transitioned from test-planning to facilitating in-depth interpretation of the measured data. In the previous chapter, focus was given to the interpretation of test results determined via direct reduction of sensor data. Later in this report, additional discussion of test results will be presented in which experimental data are combined with numerical pier and soil models to quantify sources of impact resistance that could not be directly measured during the field tests. The remainder of the present chapter is devoted to providing brief descriptions of finite element models of the two test piers and the two finite element codes used to analyze them. Descriptions of the soil models used for each pier will be presented in the following chapter.

8.2 Finite element analysis codes

Two classifications of finite element models were created in this study. The first involved discretely meshed finite element models developed for analysis by a general purpose finite element code. The second classification involved more coarsely meshed models developed for analysis using software specifically designed for analyzing bridge piers. The nonlinear explicit dynamic finite element code LS-DYNA (LS-DYNA 2003) was chosen to analyze the discretely meshed finite element models. LS-DYNA was selected mainly for its dynamic capabilities, as well as its ability to model nonlinearity and contact. For the coarser finite element models, the FB-MultiPier analysis package (FB-MultiPier 2005) was used.

LS-DYNA models were used to help calibrate the FB-MultiPier models, as well as provide confidence in the FB-MultiPier results, and vice versa. A brief overview of the key techniques used in modeling the pier structures in each analysis code will be discussed in the following sections.

8.3 LS-DYNA Pier-1 model

For dynamic LS-DYNA analysis, Pier-1 was modeled (Figure 8.1) using a combination of eight-node solid brick elements for the pier structure, pile cap, and tremie seal; resultant beam elements for the piles; and inelastic non-linear discrete spring elements to model soil (not shown in Figure 8.1 for clarity). As indicated in the figure, nearly all of the pier components—the pier cap, pier columns, shear wall, and pile cap—were made continuous by ensuring that the meshes for each sub-component shared common nodal locations at common interfaces. The exception to this was the tremie seal, for which the mesh did not match that of the pile cap at the interface between the two. In this instance, a tied-surface algorithm was used to join together the common surfaces of the pile cap and seal.

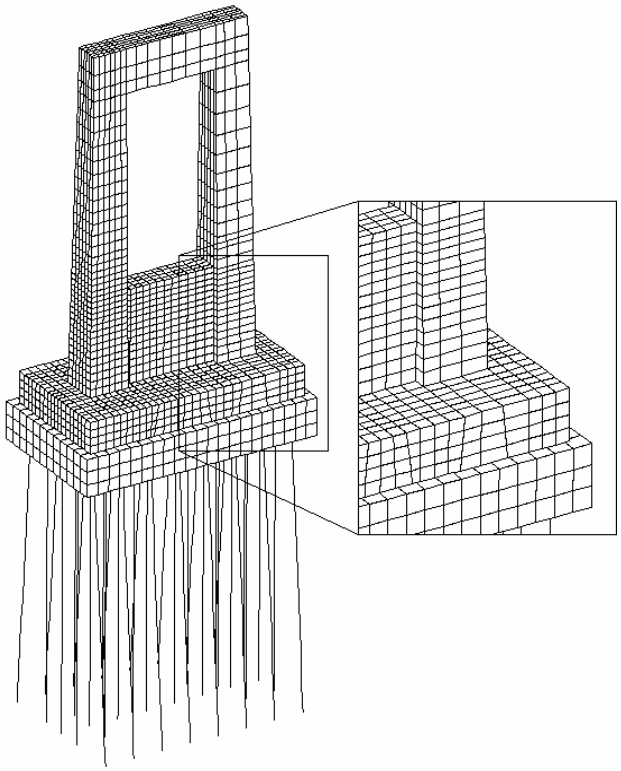

Figure 8.1 Pier-1 high-resolution LS-DYNA model

The forty steel HP 14x73 piles supporting Pier-1 were modeled using resultant beam elements that extended through the full thickness of the tremie seal, and through half the thickness of the pile cap. All pile nodes located inside either the pile cap or tremie seal were linked to the pile cap or tremie seal solid element meshes to provide continuity, thus simulating embedment and fixity of the piles within the cap and seal.

Because the pier impact tests conducted in this study were non-destructive in nature, the use of relatively simple material models was deemed suitable. Hence, an isotropic linear

elastic material model was used to model all concrete structural elements in the pier. Concrete material parameters were determined from cores taken at the bridge site. Those properties were presented in Chapter 3, together with physical descriptions of the pier.

8.4 FB-MultiPier Pier-1 model

A supplementary finite element pier model for Pier-1 (Figure 8.2) was also developed using the FB-MultiPier structural analysis package. The key difference between the FB-MultiPier model and the LS-DYNA model was that instead of using solid brick elements to model components of the pier structure, as was the case in the LS-DYNA model, each of these components was represented using fiber-based frame elements (FB-MultiPier 2005). Similar to the LS-DYNA model, all structural elements in the FB-MultiPier model were assumed to be linear elastic.

In FB-MultiPier models, flat shell elements are used to model the stiffness and mass of the pile cap. Pile elements therefore connect to nodes located at the mid-plane (mid-thickness) of the cap. In Pier-1, the pile cap was 5 ft. thick and the tremie seal was 6 ft. thick. Therefore, the top portion of each pile was embedded (5 ft./2) + (6 ft) = 8.5 ft. inside the concrete cap and seal. Within this distance, the piles were restrained against flexure so that the flexible portions of the piles extended downward from the bottom surface of the tremie seal. To account for fixity of the piles within the cap and seal, as well as the added flexural stiffness contributed by the tremie seal, a network of cross-bracing frame elements was added to the model to stiffen the top 8.5 ft. of the piles (Figure 8.2). Mass densities of the cross-bracing frame elements were selected to produce a total additional mass equal to the total mass of the tremie seal.

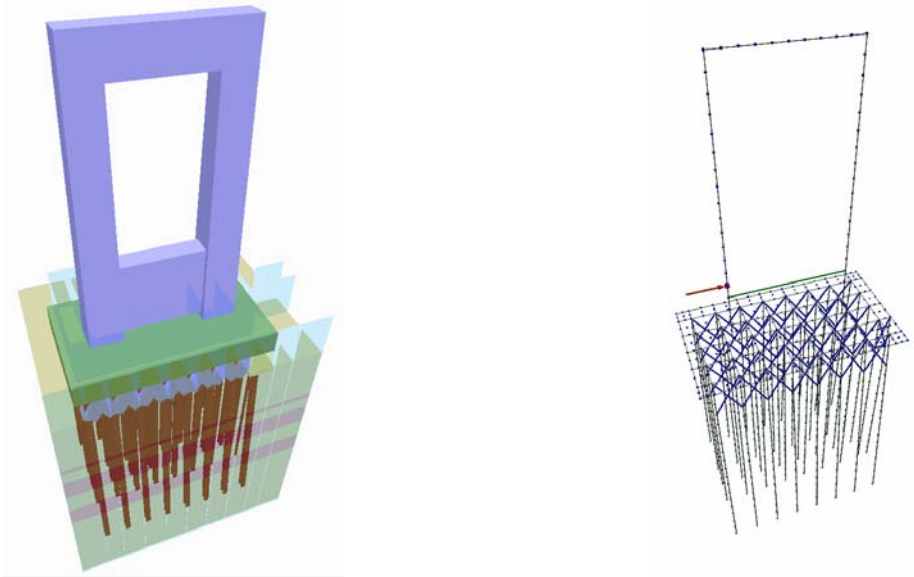

a) Physical dimensions of model b) Underlying numerical model

Figure 8.2 Pier-1 FB-MultiPier model

8.5 FB-MultiPier Pier-3 model

All components of Pier-3—except the pile caps—were modeled in FB-MultiPier using fiber-based frame elements (Figure 8.3). Due to the flexibility of Pier-3, modeling interaction between the lateral strut element and the pile caps was found to be important. Although not monolithically cast together, the bottom surface of the strut and the top surfaces of the pile caps were in contact with each other in the physical pier. When lateral deformation caused the surfaces to make contact in compression, an increase in lateral pier stiffness resulted. In order to approximate this effect in the FB-MultiPier model, cross bracing elements were added at locations where the strut met the pile caps.

Material properties for the pier elements (elastic modulus, weight density, etc.) were chosen to match those of concrete. Damping coefficients for structural (non-soil) pier elements were selected to produce a structural damping ratio of approximately 5%.

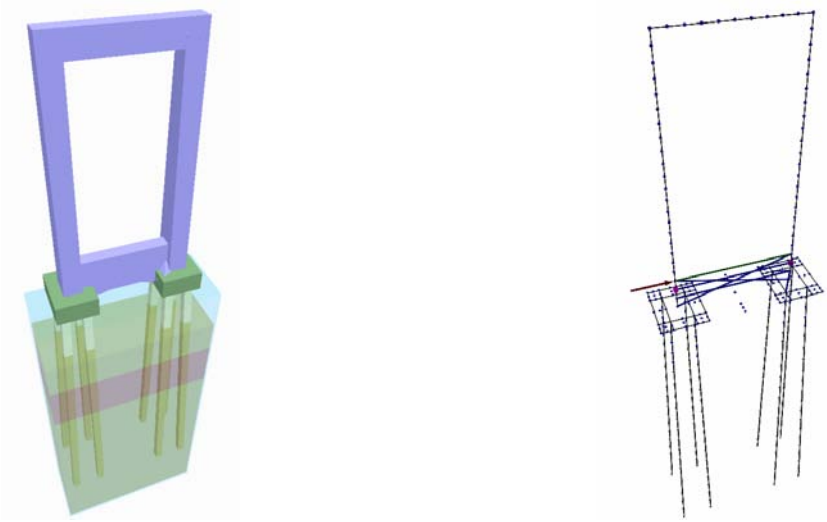

a) Physical dimensions of model b) Underlying numerical model

Figure 8.3 Pier-3 FB-MultiPier model

8.6 FB-MultiPier bridge model

During test series B3, Pier-3—the pier struck by the test barge—was linked to Pier-2, Pier-4, Pier-5, Pier-6, etc. through bridge superstructure spans. Each of these superstructure spans was a simple-span unit consisting of prestressed concrete girders compositely connected to a concrete bridge deck. In the FB-MultiPier model (Figure 8.4) developed to represent this "partial bridge" structural configuration, each simple-span superstructure segment was modeled using a mesh of beam elements. Cross-sectional properties for the elements were computed from the cross-sectional geometry of the superstructure units (slab plus girders). Material properties for the superstructure elements (elastic modulus, weight density, etc.) were chosen to match those of concrete. Damping coefficients for both superstructure elements and structural (non-soil) pier elements were selected to produce a structural damping ratio of approximately 5%.

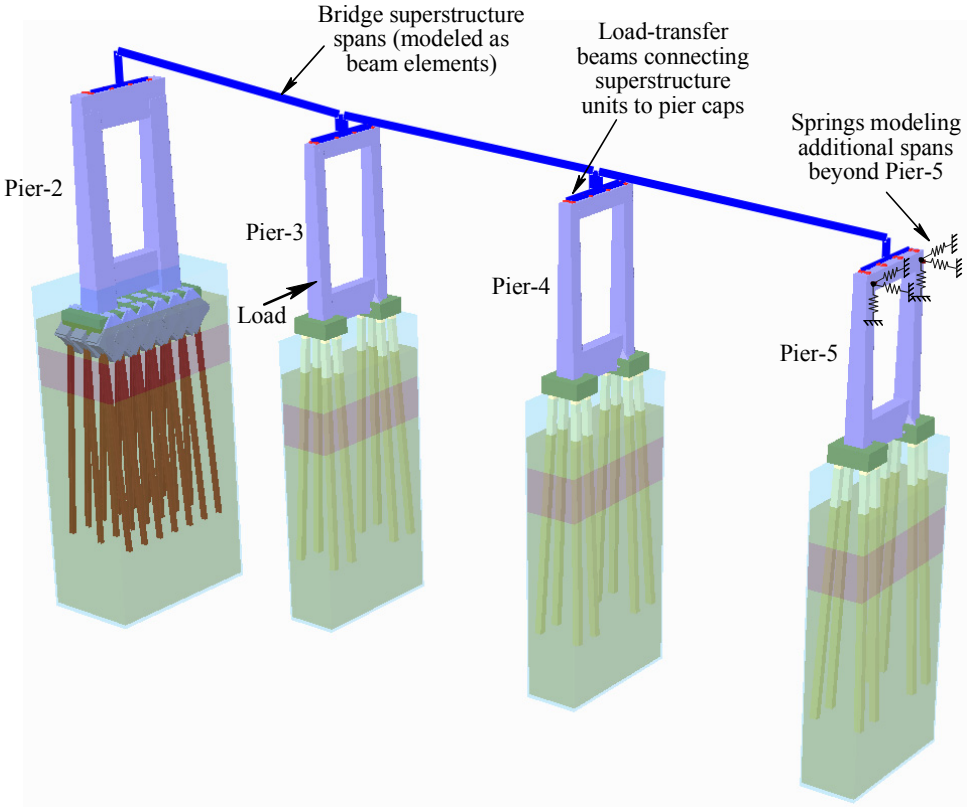

a) Physical dimensions of model

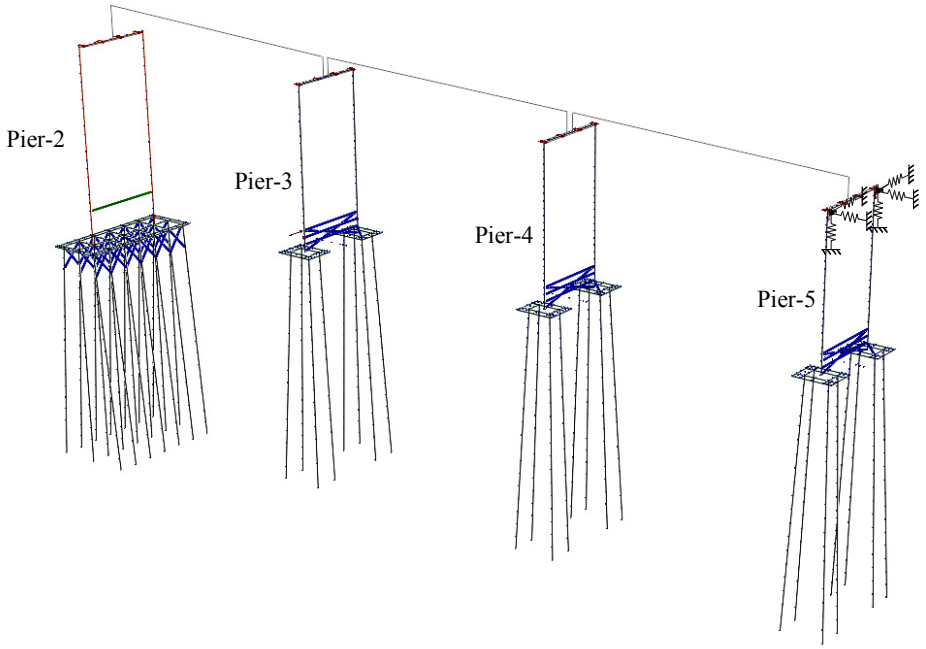

b) Underlying numerical model

Figure 8.4 Bridge FB-MultiPier model

In multiple-pier, multiple-span FB-MultiPier models, connecting the superstructure elements to the supporting piers is accomplished using load transfer beams and specification of bearing behavior (stiffnesses or constraints). Each transfer beam connects the end of a superstructure span to multiple individual bearing locations across the width of the pier cap. In the bridge segment under consideration here, two parallel rows of bearings were located at the top of each pier—one for each of the two simple-span superstructure units meeting at the pier. Based on a review of construction drawings for the bearings, direct visual inspection of the bearings, and observations made during the series B3 barge impact tests, it was determined that the bearing behavior could be suitably approximated using translational constraints between the transfer beams and the bearing locations on the pier caps.

During the series B3 tests, bridge superstructure spans beyond Pier-5 were also left intact. Motions of these spans—and their supporting piers—were expected to be significantly less than those of Pier-2, Pier-3, or Pier-4. In the numerical model, the influence of these additional spans was represented by adding two triads of orthogonal springs at each end of the Pier-5 pier cap (Figure 8.4).

CHAPTER 9
FINITE ELEMENT MODELING OF SOIL-STRUCTURE INTERACTION

9.1 Introduction

Dynamic responses of bridge piers to barge impact loading may be strongly influenced by soil-pile interactions (and soil-cap interactions in cases of buried footings). In order to numerically simulate such collisions, it was necessary to model the resistance of soil surrounding the bridge piles and the pile cap+seal. Traditional methods of modeling interactions between piles and soil utilize nonlinear *p-y*, *t-z*, and *q-z* curves to represent lateral resistance, skin friction, and end-bearing resistance, respectively. Such methods yield adequate results for static and slow cyclic loading conditions. However, accurate prediction of pier response to rapid vessel collision loading conditions requires that both static and dynamic soil-structure interactions (e.g., radiation damping, rate-dependency of soil stiffness, degradation of soil stiffness under cyclic loading, nonlinear behavior of soil, and lateral cap resistance) be included.

In the previous chapter, structural modeling techniques were documented that will be employed later to numerically simulate—using LS-DYNA and FB-MultiPier—selected experiments from the physical test program. In the present chapter, soil-structure interaction modeling techniques, applicable to LS-DYNA and FB-MultiPier analyses, are discussed. Additional information relating to experimental determination of soil properties at the test site, as well as numerical modeling of soil resistance, can be found in McVay et al. (2005).

9.2 LS-DYNA modeling of interaction between soil and piles for Pier-1

Soil-pile interaction modeling for LS-DYNA analysis was accomplished in this study through the use of nonlinear springs positioned at nodes along the lengths of the piles (Figure 9.1). At each of the pile nodes—which were spaced at 4 ft. vertical intervals—lateral resistance was modeled using two perpendicular sets of soil springs; pile skin resistance was modeled using a single vertical axial spring. A single axial spring was also used at the tip of each pile to model end bearing resistance.

9.2.1 Lateral soil resistance

Lateral soil resistance springs were modeled using an LS-DYNA non-linear spring material model that permits specification of separate loading and unloading curves, each describing a force versus displacement relationship. Each of these curves—loading or unloading—may be specified as being either linear or nonlinear in form. Non-linear curves were used to represent the lateral behavior of soil-pile interaction in static and, in special cases, dynamic loading conditions. Linear curves were used to approximate soil unloading behavior. By connecting two compression-only (zero-tension) springs to the pile nodes (Figure 9.1) in each lateral direction (*x* and *y*), energy dissipation associated with hysteretic damping and gap formation within the soil was taken into account.

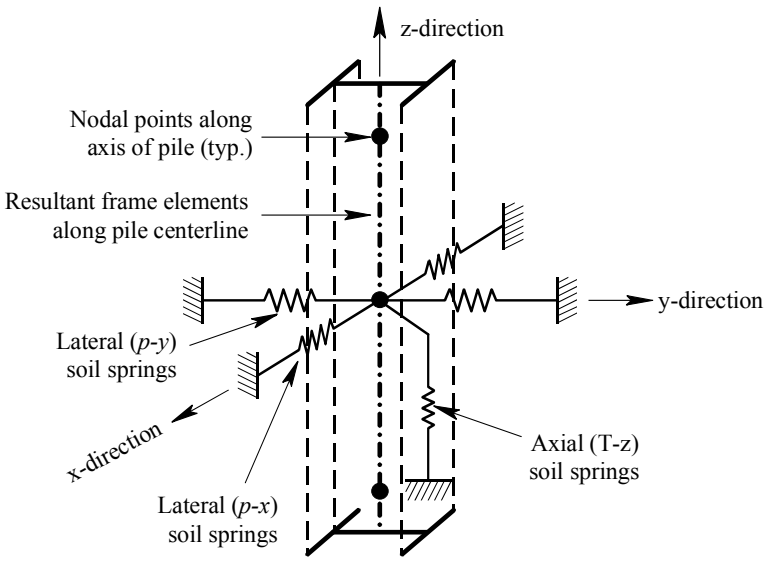

Figure 9.1 Soil spring group at a typical pile node in the Pier-1 model

A schematic diagram illustrating the gap formation process, i.e. soil response with plastic deformations included, is given in Figure 9.2. From state 1 to 2, the pile moves in the +y direction and deforms the undisturbed soil. The +y spring is compressed with increasing force following the *p-y* loading curve. The –y spring, being a compression-only (zero-tension) element, provides no resistance. After reaching a point of maximum displacement, the pile starts to rebound. The compressed soil unloads following the unloading curve (state 2 to 3), which is typically an elastic curve; elastic deformation is fully recovered at state 3. Due to inelastic behavior, at state 3, the soil has undergone permanent deformation and a gap is formed. Hence, from state 3 to 4, the soil is not in contact with the pile and the pile is free to move without resistance from the soil (the force in both springs is zero) until it reaches the soil in the -y direction.

From state 4 to 5, the pile deforms the soil in the -y direction. Soil resistance follows the *p-y* loading curve with the assumption that the soil on the -y side of the pile has not been affected by the previous loading in the +y direction. When moving in the reverse direction, the soil unloads and follows the pile from state 5 to 6. At state 6, soil reactions at both sides of the pile are zero and an additional gap in the -y direction has been formed.

Depending on the nature of the loading conditions and stored strain energy in the structural system, the pile may continue to move through the entire gap (state 6 to 7) and once again reach the soil in the +y direction (state 7). At this point, the soil reloads along the same curve (state 7 to 8) that it previously unloaded along (state 2 to 3). When the load reaches the level equal to that of state 2, the soil will follow the original *p-y* loading curve (state 8 to 9). The next time the load reverses, the soil will unload following a linear unloading curve (state 9 to 10). At state 10, the gap in the +y direction has been increased. Loading in the -y direction will cause the pile to traverse the entire gap without resistance (state 10 to 11). At state 11, the soil will load along the previously unloaded curve in the -y direction (state 11 to 12). Once the pile reaches the force level previously reached before earlier unloading in the -y direction, the soil will continue to load following the original *p-y* loading curve. This process continues until the kinetic energy of the system has been fully dissipated.

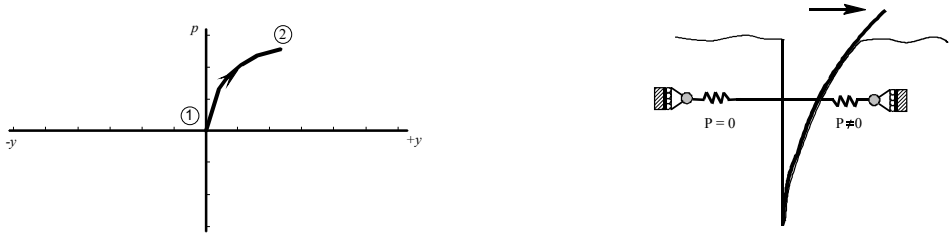

a) Initial deformation in positive direction

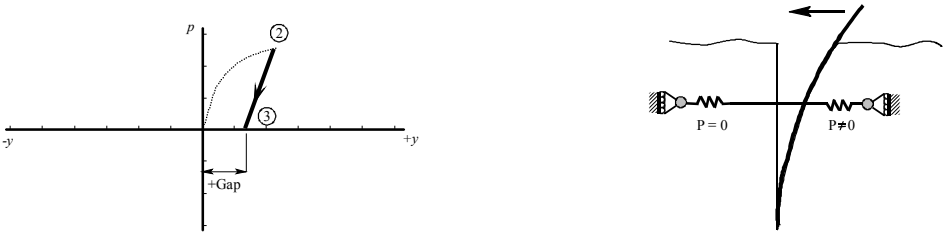

b) Unloading from positive deformation

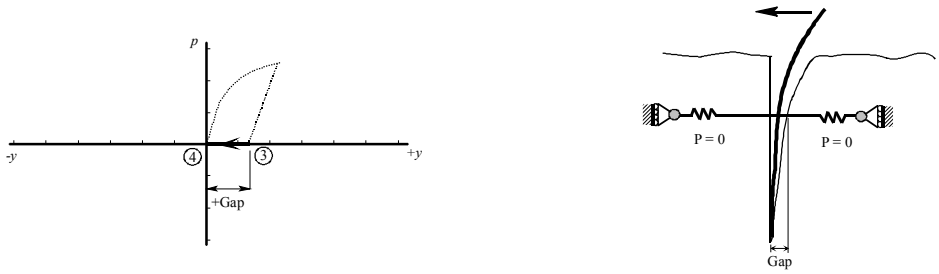

c) Moving within the gap

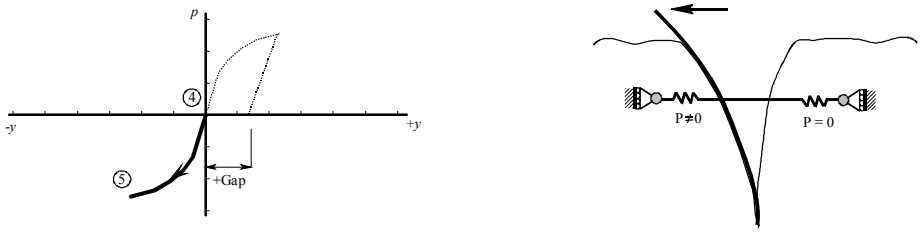

d) Initial deformation in negative direction

Figure 9.2 Force versus deflection (*p*-*y*) curves for soil gap model

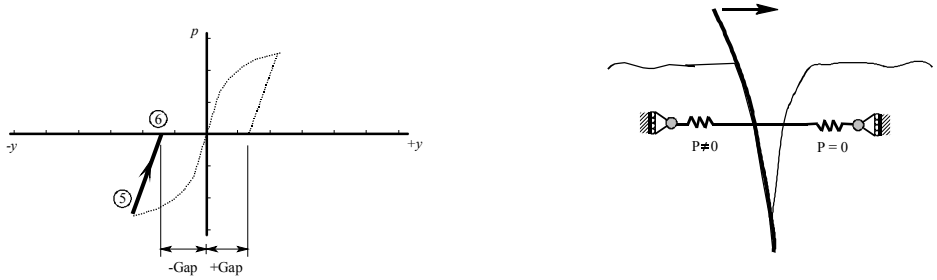

e) Unloading from negative deformation

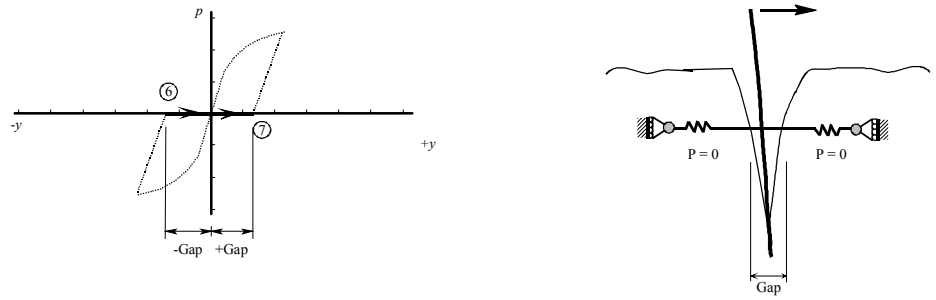

f) Moving within the gap

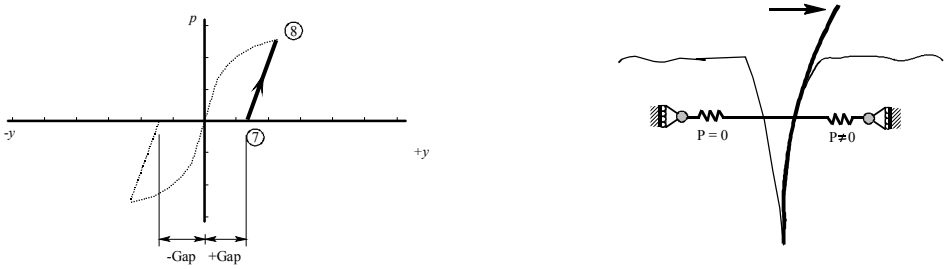

g) Reloading in positive direction

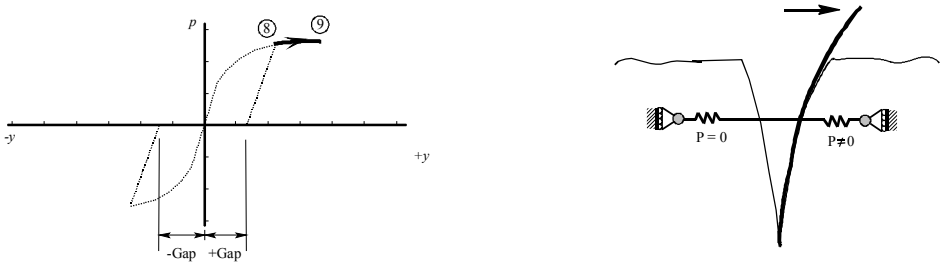

h) Additional deformation in positive direction

Figure 9.2 (cont.) Force versus deflection (*p*-*y*) curves for soil gap model

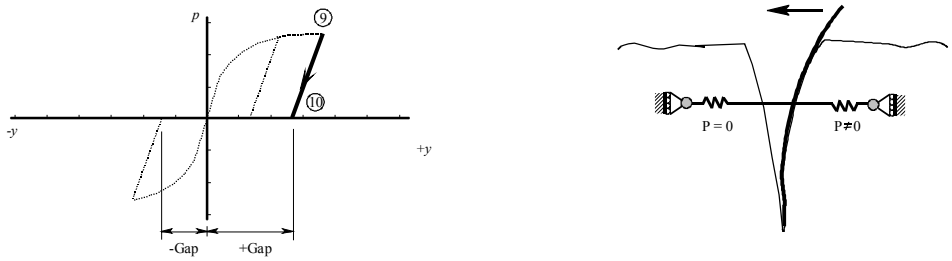

i) Unloading from positive deformation

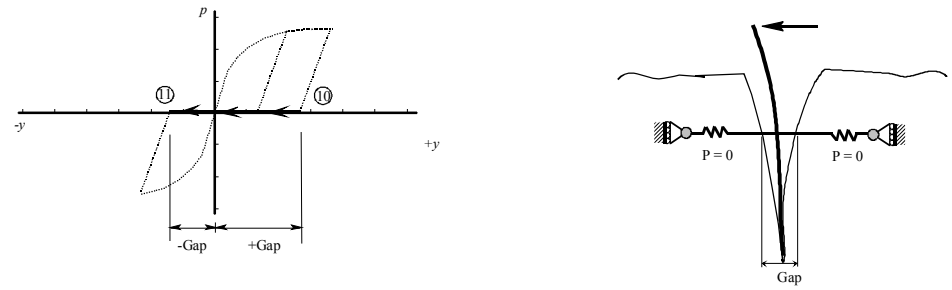

j) Moving within the gap

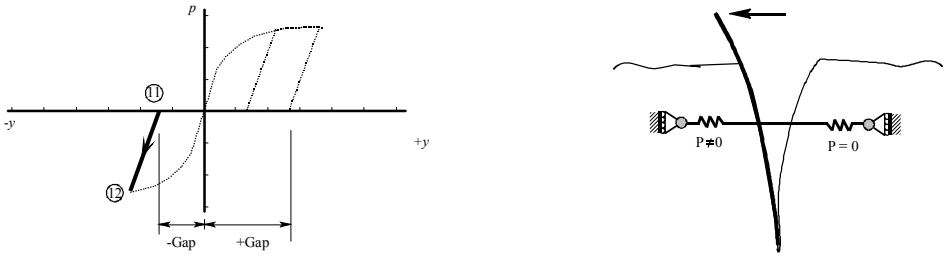

k) Reloading in negative direction

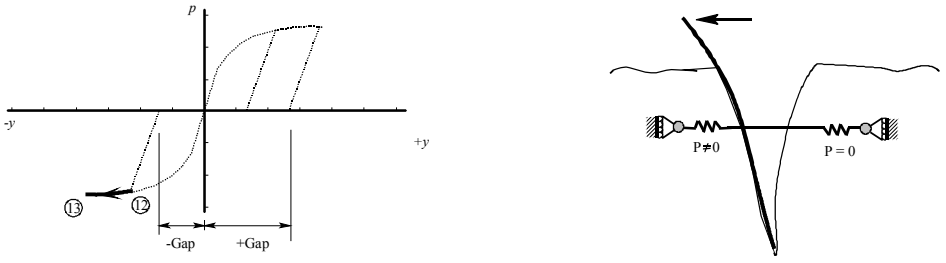

l) Additional deformation in negative direction

Figure 9.2 (cont.) Force versus deflection (*p*-*y*) curves for soil gap model

Numerical methods for determining static and low frequency cyclic soil-pile interaction (*p-y*) curves of this type have been derived empirically in the literature based on experimental testing and analytical modeling. In the present study, in-situ soil data (McVay et al. 2005) were used to generate static *p-y* curves for lateral soil springs from elevation -32 ft. down to the pile tips. At these elevations, lateral pile displacements and velocities were an order of magnitude smaller than those near the pile-heads. Damping forces and loading rate effects at these elevations were hence considered negligible.

Static p-y curves were constructed using the Reese, Cox and Koop method for sandy soil layers, and the Matlock method for soft-clay-in-the-presence-of-water for clayey soil layers. The Reese, Cox, and Koop method requires pile diameter, soil depth at the analysis point, and in-situ data such as internal friction angle (ϕ), soil unit weight (γ), and subgrade modulus (k). Because all soil was below the water table, the submerged unit weight was used. For the Matlock method, in addition to pile diameter and soil depth at the analysis point, it was necessary to estimate the undrained shear strength (c), submerged soil unit weight, and ε_{50} (the strain corresponding to one-half (50%) of the maximum principal stress difference). Both methods assume the presence of only a single layer of soil. Before using these methods to construct the static *p-y* curves, the soil layers were transformed using the method of Georgiadis (FB-MultiPier 2005), to obtain an equivalent soil profile. Unloading curves for the lateral springs were defined as elastic curves that had the same slopes as the initial slopes of the corresponding *p-y* loading curves.

Above elevation -32 ft., dynamic *p-y* curves, based on experimentally measured soil response data (see Chapter 7) were used to model soil resistance on the piles. Each of the experimentally determined curves (Figure 9.3) were extended before introduction into the LS-DYNA model. Maximum pile displacements predicted by LS-DYNA simulation can exceed the maximum pile displacements experimentally measured. If the dynamic *p-y* curves are not extended, LS-DYNA will assume that the forces in the non-linear spring elements are zero whenever the pile displacements exceed the maximum displacements described in the loading curves. To prevent this condition, the experimentally measured *p-y* curves were extended to accommodate a displacement of up to 1 in. The force in the lateral soil springs is then constant whenever the pile displacement exceeds the maximum pile displacement from the measured dynamic *p-y* data.

9.2.2 Pile group effects

Due to pile "group effects", the load carried by a pile located within a group will be less than that of a single isolated pile at the same level of lateral deflection. Piles in trailing rows carry less load than piles in leading rows. One method of accounting for group reduction effects is to scale down the soil resistances (*p* values) from *p-y* curves generated for single isolated piles. Reduction factors called row-multipliers (or *p*-multipliers) are used to accomplish this scaling. Multiplier magnitudes are dependent on both the location of the pile within the pile group, and the pile spacing. Additionally, during barge impact loading, a pile group may undergo cyclic motion back and forth, turning leading-row piles into the trailing-row piles and vice versa during cyclic reversal. Hence, the positional classification of piles within the group ("leading" or "trailing") changes with the direction of movement of the piles. To represent soil resistance for dynamic impact simulation, *p*-multipliers should be specified such that they may change depending on the direction of motion of the pile group.

The *p*-multiplier values applied to the lateral soil springs in the LS-DYNA model of Pier-1 are presented in Figure 9.4.

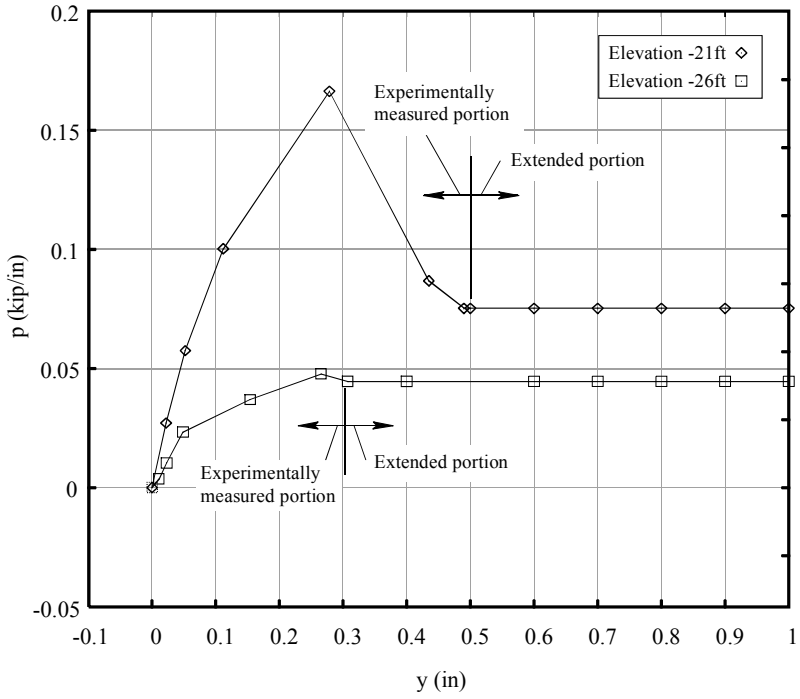

Figure 9.3 Extension of dynamic *p-y* soil curves in LS-DYNA model

9.2.3 Axial skin friction along piles

Barge impact load is transferred from the pier structure to the soil not only through lateral resistance of the soil but also through vertical skin friction of the soil along the pile length. Therefore, in addition to the springs representing lateral soil resistance on the piles, axial springs were also introduced into the model to represent axial skin friction. At each pile node, an axial spring was added using a nonlinear, but elastic, material model. Load-deformation curves of this type are known as *t-z* curves. The *t-z* curves used in this study were constructed based on a method developed by McVay et al. (1989) using in-situ soil data.

9.3 LS-DYNA modeling of interaction between soil and cap+seal for Pier-1

Recognizing the importance of buried cap+seal lateral soil resistance (discussed in detail in Chapter 7), a soil-cap+seal interaction model was incorporated into the Pier-1 model. Soil resistance on the cap+seal consisted of two sources: passive+active soil resistance on the leading and trailing surfaces of the cap+seal (modeled with *p-y* spring and dampers) and skin friction resistance acting on the bottom and side surfaces of the cap+seal (modeled with *t-z* springs and dampers).

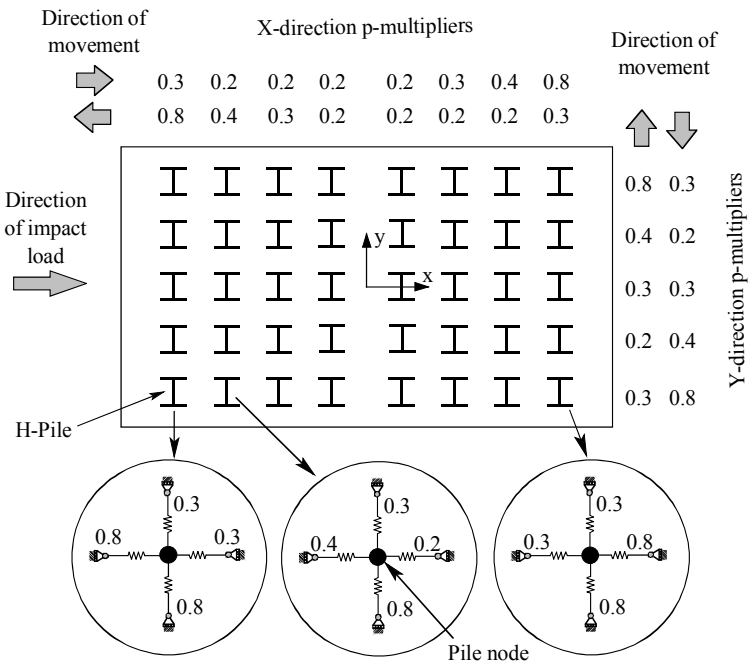

Figure 9.4 Group-effect row-multipliers used in LS-DYNA model of Pier-1

9.3.1 Passive+active resistance of cap+seal

Construction of the cap+seal *p-y* curves utilized the same techniques that were used to construct the *p-y* curves for the piles. Soil at the leading side of the cap was modeled using a collection of nonlinear *p-y* springs arranged in a grid of 5 columns by 4 rows (Figure 9.5), with row elevations of -10.25 ft, -11.5 ft, -12.75 ft, and -14 ft. Soil at the leading side of the seal was similarly modeled using nonlinear *p-y* springs arranged in a grid of 5 columns by 3 rows, with row elevations of -16 ft, -18 ft, and -20 ft. For the purpose of generating *p-y* curves, the cap and the seal were treated as if they were composed of 5 square pseudo-piles standing side by side. The width of each of these pseudo-piles was equal to $1/5^{th}$ of the pile cap width or seal width, as appropriate. Pile cap width and seal width are the plan-view dimensions perpendicular to the direction of the barge impact.

Stiffnesses of the cap and seal *p-y* springs were calibrated such that their total maximum force was approximately equal to the maximum static lateral resistance of the cap and seal as determined from in-situ soil tests (McVay et al. 2005). Lateral resistance soil springs for the cap and seal were modeled in LS-DYNA using a nonlinear elastic material model. An elastic material model was chosen because, during the physical test program, gap formation at the interface between the soil and the cap+seal was not apparent from the measured test data. At the trailing side of Pier-1, a similar arrangement of nonlinear elastic cap+seal soil springs was incorporated into the model to represent soil resistance at the trailing side of the structure.

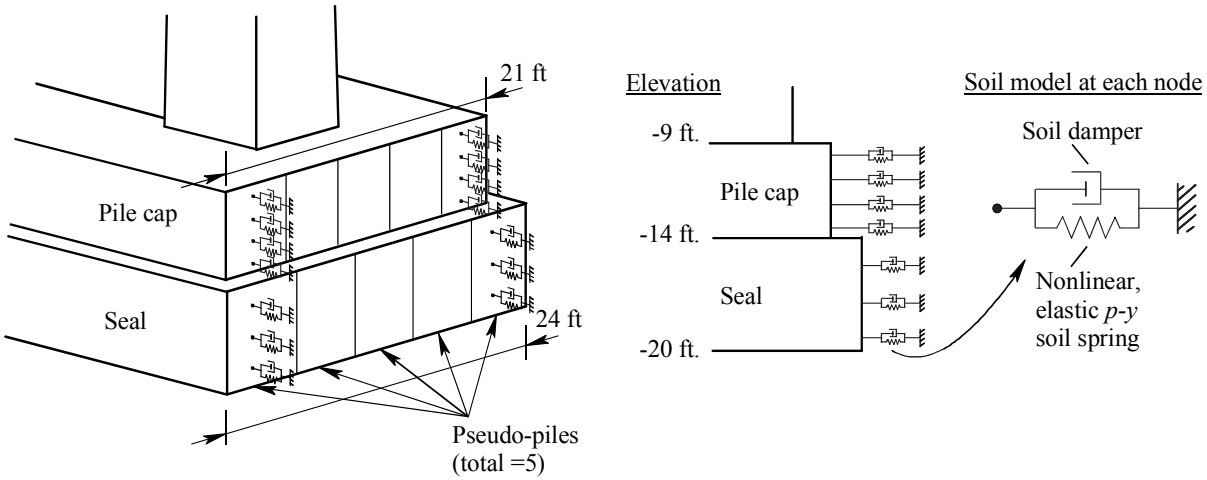

Figure 9.5 Lateral soil-cap and soil-seal interaction model

To account for the rate-dependent increase of soil resistance under dynamic loading, as well as energy dissipation associated with radiation damping, linear dashpot elements were added—in parallel to the *p-y* springs—to the soil-cap+seal interaction model (Figure 9.5). Soil damping values (linear viscous damping coefficients) were determined from measured geotechnical test data and comparisons to numerical analysis results (see McVay et al. (2005) for additional details).

Modeling soil-cap+seal interaction also required additional considerations be given with regard to loss of soil stiffness that occurs during cyclic (repeated) dynamic loading. Cyclic stiffness degradation (Figure 9.6) is generally attributed to the effect of repetitive remolding of the soil. Currently, LS-DYNA does not feature a spring material model capable of directly representing cyclically degrading stiffness. To approximate this behavior, each undisturbed *p-y* spring was split into two separate springs having complimentary characteristics.

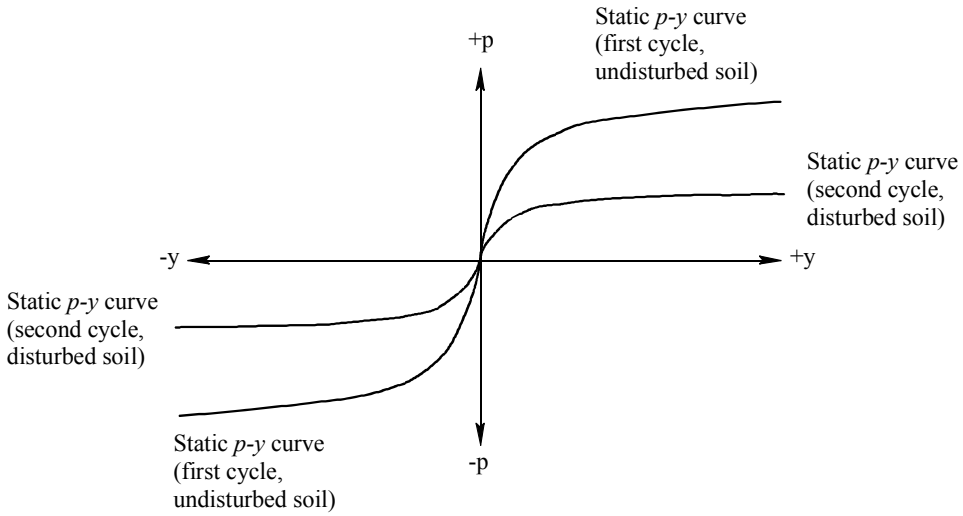

Figure 9.6 Cyclic degradation of soil stiffness

During the initial cycle of loading, both of the springs are active and the total stiffness of each spring pair is the sum of the two individual stiffnesses. At a later point in time—selected to correspond to the end of the first cycle of loading—one of the two springs is terminated leaving only the stiffness of the "degraded" spring (Figure 9.7). Ideally, it would be desirable to split the undisturbed *p-y* stiffness of the soil (Figure 9.7a) into two sub-components that each have a shape similar to that of the overall curve but which are reduced in magnitude. Presently, however, LS-DYNA does not feature a *nonlinear* spring material model that permits the contribution of an element to be "terminated" after a given number of cycles or given amount of elapsed time.

As an approximate solution to this problem, one of the linear spring material models, which does permit element termination at a user-specified time, was used instead (Figure 9.7c). During the first cycle of loading, the stiffness of this linear spring is added to the stiffness of the nonlinear "degraded" spring (Figure 9.7b) thus producing a cumulative stiffness approximately equal to the initial undisturbed (non-degraded) soil stiffness. Subsequently, at a time corresponding to the end of the first cycle of loading—determined from examination of the experimental test data—the linear spring was terminated leaving only the degraded nonlinear spring. Such an approach is an adequate approximation for modeling events of known duration, such as the barge impact tests. However, in the future, an improved approach to modeling cyclic degradation will need to be developed.

The extent to which *p-y* curves for a particular soil degrade depends on many factors including the type of soil, variation and rate of loading, and the width and height of the cap+seal. Precise quantification of soil degradation under barge impact loading will require further research. For this study, the magnitude of each degraded *p-y* curve was estimated as being 30% of the original (undisturbed) *p-y* curve.

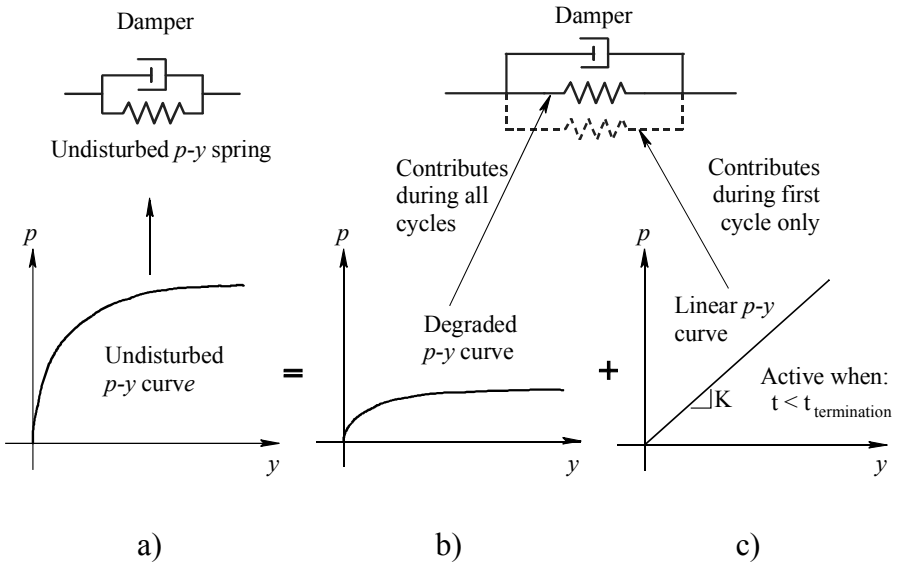

Figure 9.7 Approximating cyclic soil stiffness (*p-y*) degradation in LS-DYNA

9.3.2 Skin resistance of cap+seal

Adding to the soil resistance associated with the leading and trailing sides of the cap+seal, frictional soil forces ("skin" forces) were also mobilized during tests on Pier-1. Frictional forces acting along the bottom of the seal and along the two sides of the cap and seal were modeled using nonlinear skin-friction springs. Load-deformation curves for these springs were similar in form to the *t-z* curves used for the pile axial soil springs. However, the skin-spring *t-z* curves were modeled using a nonlinear—specifically, a bilinear—elastic model with a quake at 0.1 in. (a representative value for most soil types). Beyond a soil deformation of 0.1 in., a plateau in the *t-z* curve for the skin springs produced a fixed (constant) level of lateral resistance.

Just as rapid load application leads to a dynamic increase of soil *p-y* stiffness, it is assumed here that rapid loading also leads to an increase in frictional *t-z* soil stiffness on the cap+seal. Linear dampers were thus incorporated into the soil friction model to account for this effect and to represent energy dissipation due to damping. Methods for quantifying the increase that occurs in skin friction resistance due to loading rate are not well established in the literature. In this study, values used for skin friction dampers were determined through a calibration process in which key simulation results (peak displacements, time-to peak, period of vibration, pile forces, etc.) were brought into an acceptable level of agreement with experimental test data.

Cyclic degradation of skin-friction stiffness was also taken into account using a technique similar to that described earlier for the cap+seal *p-y* soil springs. The load-deformation *t-z* curve for each skin-friction spring was divided into two components—an initial component and a degraded component (Figure 9.9). The magnitude of the degraded *t-z* curve was taken as 30% of the original (undisturbed) *t-z* curve.

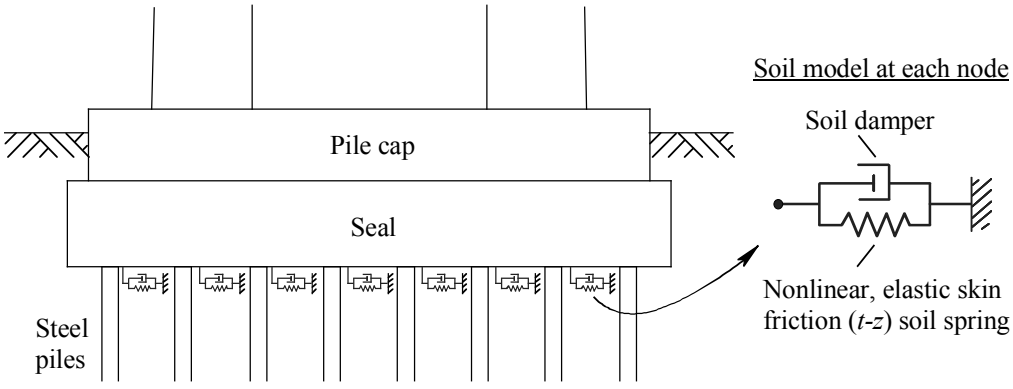

Figure 9.8 Model of skin-friction between cap+seal and soil

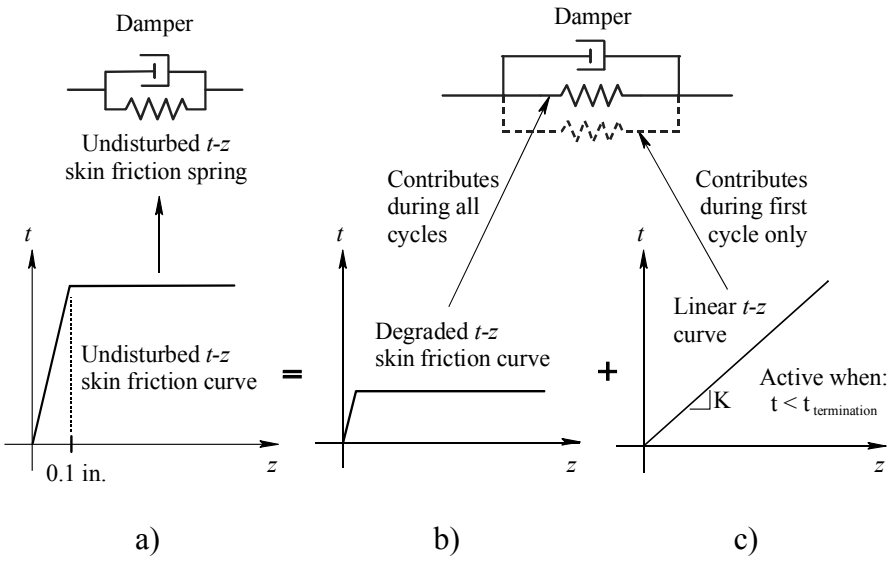

Figure 9.9 Approximating cyclic soil skin friction stiffness (*t-z*) degradation using LS-DYNA

9.4 FB-MultiPier modeling of interaction between soil and piles for Pier-1

Soil-pile interaction in FB-MultiPier was modeled using nonlinear springs attached at the pile nodes. However, the FB-MultiPier program does not require the user to explicitly define spring elements individually as in an LS-DYNA model. Instead, soil springs are implicitly incorporated into the analysis model to represent soil reactions on the piles. Based on user specified soil properties, the program can construct nonlinear load-deformation curves automatically. However, FB-MultiPier also permits the user to specify custom—or "user-defined"—load-deformation curves. As discussed in detail in Chapter 7, experimentally measured soil data for Pier-1 indicated dynamic (rate-dependent) soil behavior at elevation -21 ft., diminishing to essentially static behavior by elevation -26 ft. The same data also indicated that soil deformations were essentially negligible below elevation of -32 ft., making this elevation an approximate point of fixity.

In the FB-MultiPier model of Pier-1, user defined *p-y* curves were specified for all soil layers between the pile head elevation and -32 ft., i.e. all elevations for which experimentally measured dynamic soil response data were available. Below -32 ft., soil properties were obtained from in-situ static soil tests (McVay et al. 2005). Using these properties, FB-MultiPier was permitted to internally calculate *p-y* curves for soil layers below elevation -32 ft. To maintain consistency between the methods used in constructing soil curves for the FB-MultiPier model and the LS-DYNA model, the Reese, Cox, and Koop method was used for sandy soil layers. For clayey soil layers, the Matlock method for soft-clay-in-the-presence-of-water was employed.

Pile group effects were also included in the FB-MultiPier model using the same row-multipliers that were used in the LS-DYNA model (recall Figure 9.4). For axial soil springs attached to the piles, FB-MultiPier was permitted to automatically compute *t-z* curves using the method developed by McVay et al. (1989) for driven piles.

9.5 FB-MultiPier modeling of interaction between soil and cap+seal for Pier-1

Currently, FB-MultiPier represents load transfer from a pier structure to surrounding soil only through soil-pile interaction. Therefore, it is well suited to applications involving pier structures in which the pile cap is above ground level (not buried). For structures with buried pile caps, pier responses computed by FB-MultiPier may be in error unless additional measures are taken to model lateral soil resistance against the cap+seal. In FB-MultiPier models, soil reactions act only at pile nodes, not at nodes located in the pile cap. To represent soil reactions acting directly on the cap+seal, the properties of selected pile elements in the leading row of the pile group were modified.

Cross-sectional properties for H-piles in the leading row were defined in two distinct zones for each pile (Figure 9.10). The first zone consisted of a square pseudo-pile 8.5 ft in length, starting at the mid-plane of the pile cap—which is modeled in FB-MultiPier using flat shell elements—and extending to the bottom surface of the seal. The cross-sectional width of each pile in this zone was 54 in.—the average width of the cap+seal divided by the number of piles in the leading row. Cap+seal resistance was therefore equal to the total resistance of five leading row piles acting side by side. The second zone for H-piles in the leading row extended from the bottom of the seal to the bottom tip of the piles and utilized the normal cross-sectional properties of the HP 14x73 steel piles.

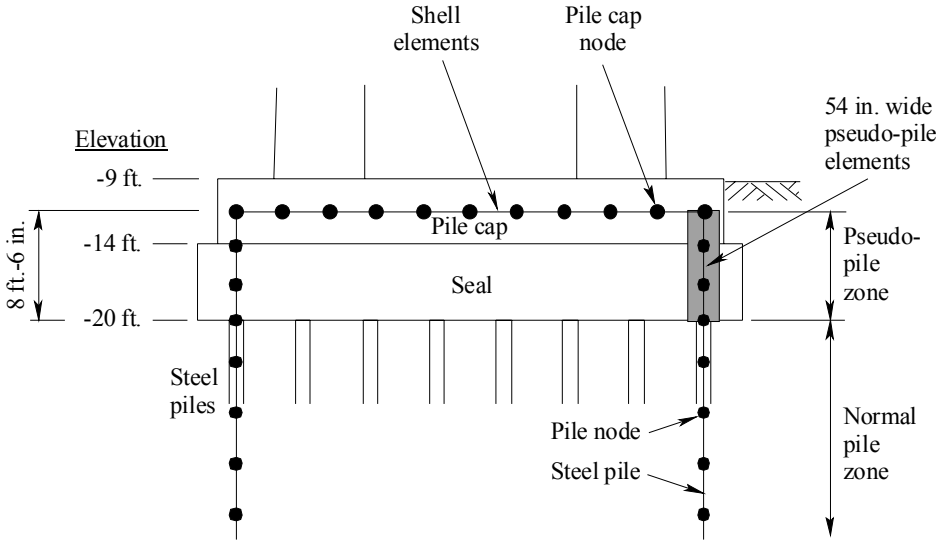

Figure 9.10 Use of modified pile element properties in FB-MultiPier to model soil forces acting on cap+seal

For piles in rows other than the leading row, all pile elements—extending from pile cap mid-plane to pile tip—were assigned the normal properties of an HP 14x73 section. However, modeling soil reactions along these piles required special care. Within the volume defined by the boundaries of concrete cap+seal, soil is not present. However, in FB-MultiPier models, soil reactions are still assumed to exist at pile nodes located within the cap+seal thickness. Additionally, FB-MultiPier has no direct means of modeling soil skin friction forces that act along the side or bottom surfaces of the cap+seal. In order to address both of these issues simultaneously, user defined *p-y* curves were assigned to all pile nodes located

within the thickness of the cap+seal (excluding the leading row). Each of these curves was nonlinear and elastic (non-gapping) in nature, matching the skin friction behavior model used in the LS-DYNA model (discussed earlier).

A cyclic stiffness degradation factor of 0.3 was assigned to all *p-y* springs that represented soil forces acting on the cap+seal. Energy dissipation through radiation damping and rate-dependent increases of soil resistance under rapid dynamic loading were represented in the FB-MultiPier model by connecting dampers to nodes along the leading edge of the pile cap (Figure 9.11). Total damping provided by these dampers matched the total damping that was included in the LS-DYNA model, which was in turn based on measured experimental test data (McVay et al. 2005).

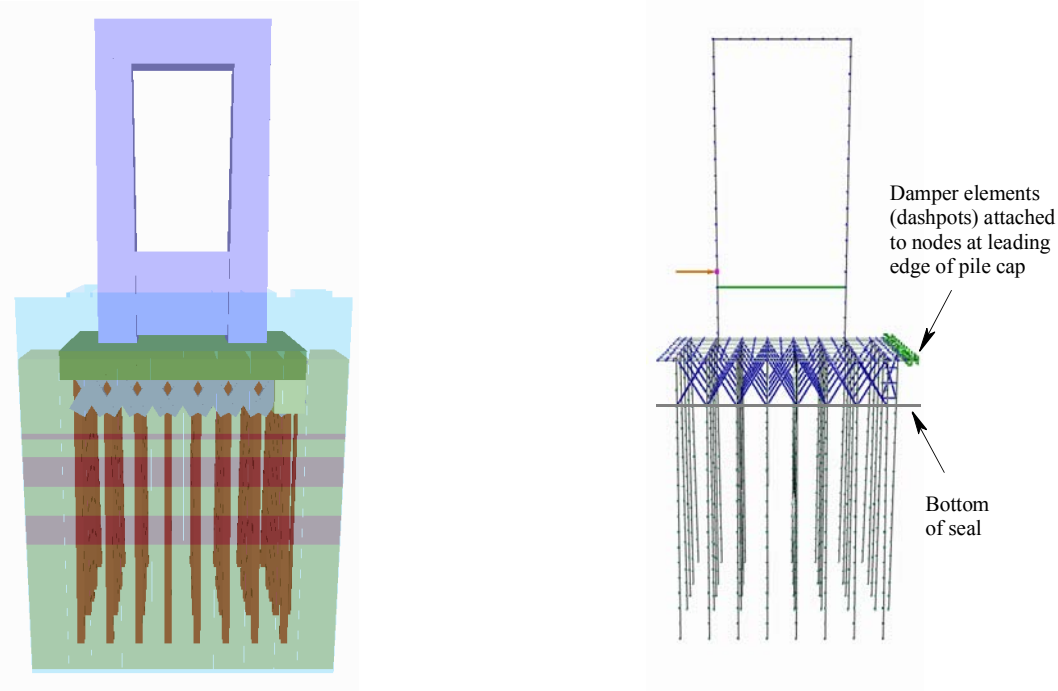

a) Soil layering b) Locations of dampers (dashpots)

Figure 9.11 FB-MultiPier soil model for Pier-1

9.6 FB-MultiPier modeling of interaction between soil and piles for Pier-3

Modeling the soil load-deformation relationships in the lateral and vertical directions for Pier-3 was achieved in FB-MultiPier using built-in (internally generated) static *p-y* and *t-z* curves. For the four cohesionless layers, the Reese, Cox, and Koop method for sands was used for the lateral soil resistance. For the single cohesive layer, the Matlock method for soft-clay-in-the-presence-of-water was used for lateral resistance. All layers used the driven pile model developed by McVay et al. (1989) to represent vertical skin friction and tip resistance.

Rate dependent soil resistance and energy dissipation due to radiation damping in the soil were both modeled by attaching damping elements to each pile node located below the mudline but above the approximate point of pile fixity. Determination of damping values was based on measured in-situ soil parameters (McVay et al. 2005).

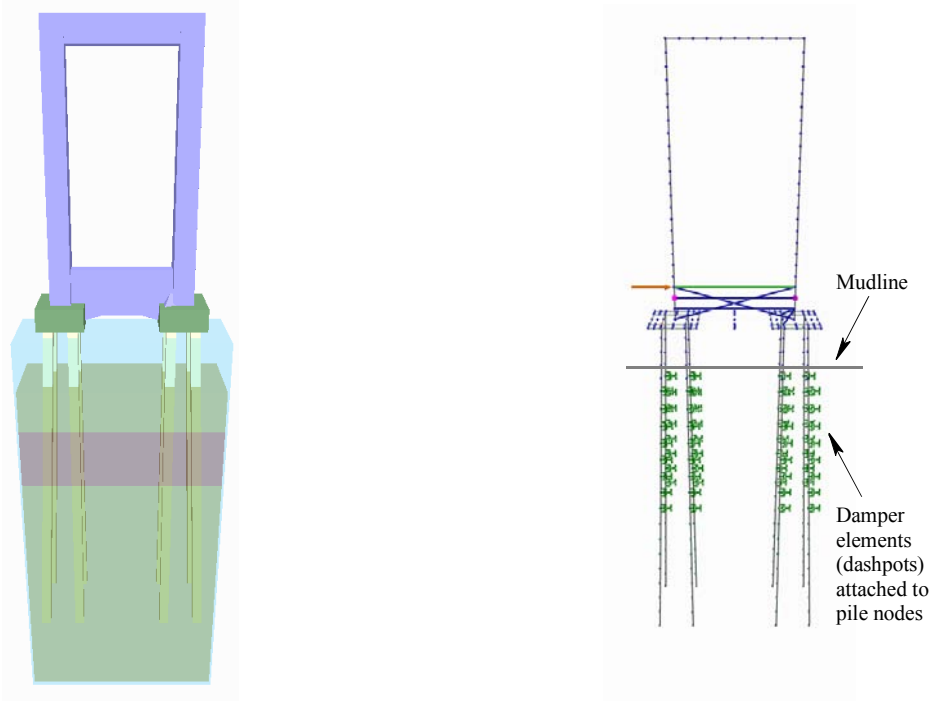

a) Soil layering b) Locations of dampers (dashpots)

Figure 9.12 FB-MultiPier soil model for Pier-3

9.7 FB-MultiPier modeling of interaction between soil and piles for Pier-2 through Pier-5 in the partial-bridge configuration

Because geotechnical measurements were made only at Pier-1 and Pier-3, modeling soil behavior at Pier-2, Pier-4, and Pier-5—all of which were included in the partial bridge model corresponding to test series B3 (Figure 9.13)—required simplifying assumptions. Observations made at the test site indicated that bay bottom depths (mudline depths) at Pier-2, Pier-4 and Pier-5 did not vary greatly from that at Pier-3. A review of construction plans and soil boring logs from the 1960s—when the bridge was originally constructed—indicated a similar condition. For Pier-4 and Pier-5, the best available data—based on spatial proximity and recentness—were the in-situ data collected at Pier-3 by McVay et al. (2005). Regarding Pier-2, in-situ data from Pier-1 or Pier-3 were both considered, however, data measured at Pier-3 were selected for use. With regard to spatial proximity, Pier-2 was closer to Pier-3 than to Pier-1. A review of the 1960s bridge construction plans also indicated significant amounts of material movement near the navigation channel, and therefore near Pier-1 (located adjacent to the channel). It was concluded that in-situ soil data recently measured by McVay et al. at Pier-1 might not match the soil layering at Pier-2 due to material movement (e.g. dredging) near the channel. As a result, soil layering, soil stiffness, and soil damping models for Pier-2, Pier-4, and Pier-5 were all assumed to be identical to those at Pier-3.

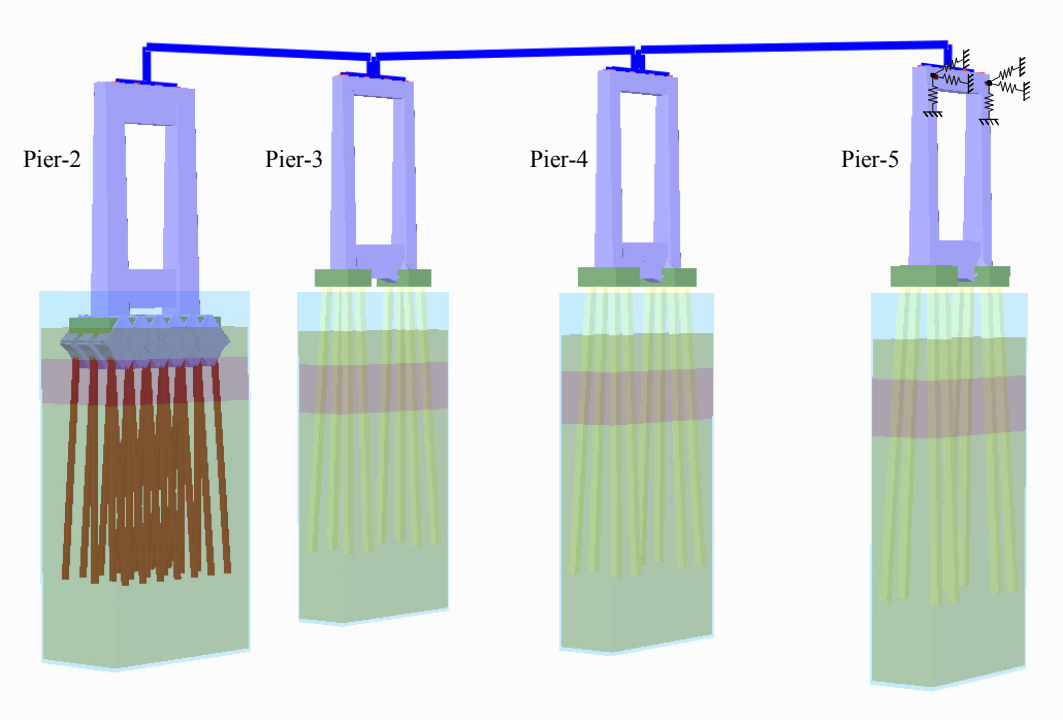

a) Soil layering

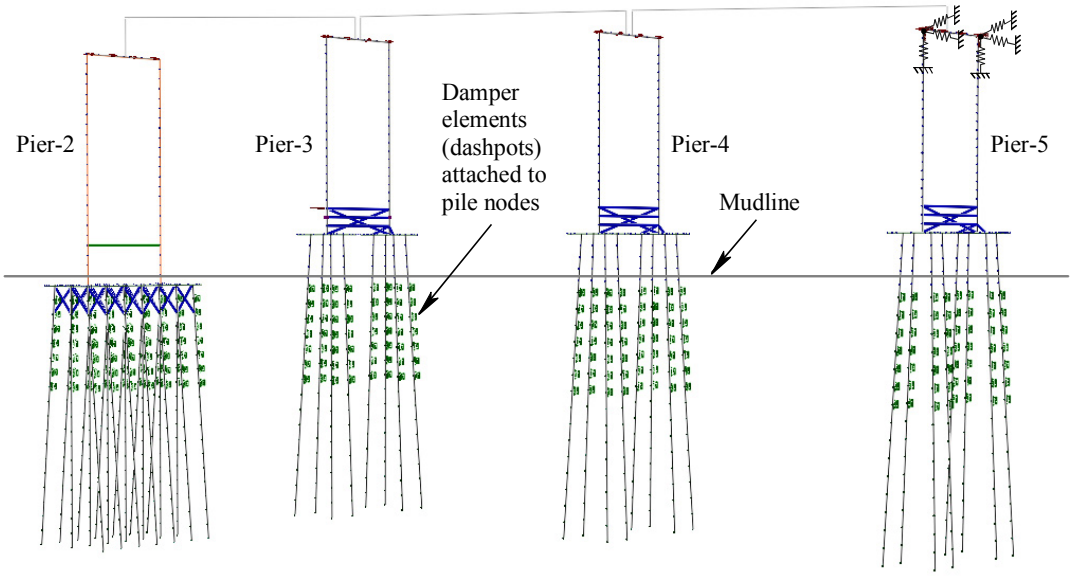

b) Locations of dampers (dashpots)

Figure 9.13 FB-MultiPier soil model for Pier-2 through Pier-5 in the partial bridge configuration

CHAPTER 10
CHARACTERIZING PIER RESISTANCE AND RESPONSE TO IMPACT LOADS

10.1 Introduction

To fully understand the sources of pier resistance—both structural and geotechnical—that were mobilized during the barge impact tests, it is necessary to quantify all of the forces that arose, not just those that could be directly measured experimentally. In Chapter 7, forces—both static and dynamic in nature—that were directly quantifiable through experimental measurement were discussed. In this chapter, experimentally measured data are combined with structural and geotechnical modeling and analysis techniques, described in Chapters 8 and 9, for the purpose of quantifying forces (sources of impact resistance) that could not be directly quantified through experimental measurement.

The basic strategy employed here consists of applying experimentally measured impact loads to dynamic computer models of the tests piers, and then calibrating the properties of the models such that the numerically predicted pier responses match all available experimental data—measured displacements, velocities, accelerations, pile shears, pile deflections, passive and active soil forces, etc.—as closely as possible. Once the numerical models have been calibrated in this manner, sources of resistance that could not be directly measured during the experimental test program may instead be estimated by extracting the appropriate force data from the numerical analysis results. This process is carried out in this chapter for three of the most severe impacts conducted: P1T7 for Pier-1, P3T3 for Pier-3, and B3T4 for Pier-3 with the bridge superstructure intact.

In addition to dynamically analyzing the pier models, static analyses are also conducted using AASHTO specified static loads that correspond to the impact energies imparted during tests P1T7, P3T3, and B3T4. By comparing static and dynamic predictions of structural demand in the piles and pier columns of Pier-1 and Pier-3, conclusions may be drawn regarding the level of accuracy that is incorporated in the current AASHTO barge impact provisions.

10.2 Impact test P1T7

Due to the embedded nature of the pile cap and tremie seal at Pier-1, dynamic interaction between the pier and the surrounding soil during test P1T7 involved a relatively complex collection of loads and resistances. In Figure 10.1, a schematic diagram illustrating the basic force groups is provided. Note that the cap+seal soil forces indicated in the figure—both passive+active and frictional—may be further broken down into separate static and dynamic components, as will be discussed later. Among the forces shown in the figure, experimental measurements were available for the impact force, inertia force, instrumented pile shear, and cap+seal passive+active soil force.

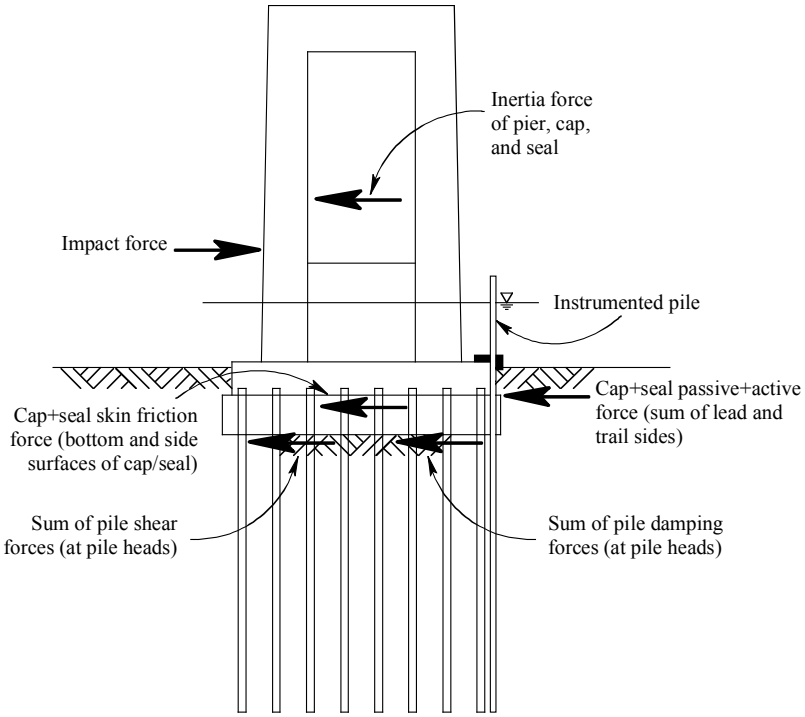

Figure 10.1 Forces acting on Pier-1 during test P1T7

The forces for which direct experimental measurements were unavailable included the cap+seal friction force and the sum of pile damping forces (at the pile heads). Of these, the latter was estimated—based on measured pile deflection and velocity data, as well as representative values of natural damping in steel piles—to be considerably smaller than all other resistance terms. Hence, by calibrating the numerical models against measured force data, it was possible to use results from the models to estimate the major remaining source of impact resistance—the cap+seal friction force. Calibration of the models was carried out by formulating and evaluating several different models of dynamic soil stiffness to determine which model best represented the observed pier and soil response. Dynamic soil behavior models that were tested included combinations of the following:

1. Linear damping (dashpots) to represent rate-dependent (velocity-dependent) soil forces
2. Cyclic degradation of soil stiffness
3. Cyclic degradation of linear damping
4. Soil-gapping during cyclic loading
5. Independent soil mass degrees of freedom to represent soil inertia forces

In order to evaluate the merits of each method above, computer models of the piers and soil were constructed for, and analyzed using, both the LS-DYNA (LS-DYNA 2003) and FB-MultiPier (FB-MultiPier 2005) nonlinear dynamic finite element analysis (FEA) codes. Using two FEA codes—each with unique modeling capabilities—rather than one, permitted a wider variety of soil models to be implemented and tested. Additionally, the use of two codes

permitted cross-checking of results to ensure that accurate and repeatable (non-program-specific) predictions of response were being obtained. Ultimately, it was determined through an iterative calibration process that the first two items noted above—inclusion of linear dampers and inclusion of cyclic soil-stiffness degradation—were sufficient to produce satisfactory agreement between FEA results and the measured test data.

The impact force (i.e., load) that was experimentally measured during test P1T7 is illustrated in Figure 10.2. In each dynamic pier analysis conducted—either using LS-DYNA or FB-MultiPier—the experimentally measured impact force was applied to the numerical pier model as a prescribed time-varying dynamic load (Figure 10.3). The point of load application in each model was chosen to match the observed elevation at which the barge struck Pier-1 during test P1T7.

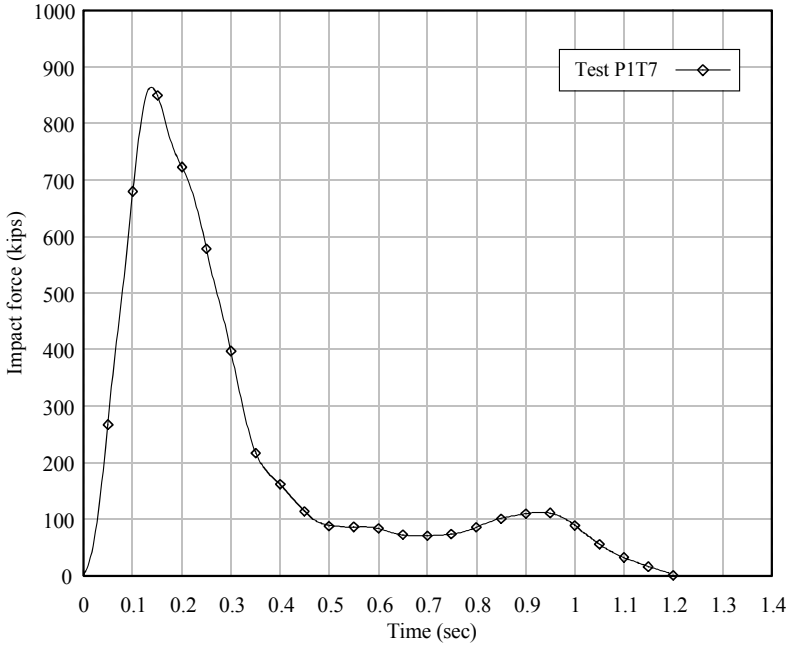

Figure 10.2 Impact force applied to Pier-1 during test P1T7

Comparisons of pier displacements obtained from calibrated LS-DYNA and FB-MultiPier models and the experimental test are presented in Figure 10.4. The pier displacement time-histories compare well, achieving nearly the same peak value and time-to-peak. Pier motions during the most dominant forced-vibration portion of the loading history, from zero to approximately 0.5 sec, are in good agreement. This indicates that the pier velocities are also in agreement and that the level of structural demand imposed on pier and foundation elements is well represented during the most important portion of the collision.

Of equal importance in validating the pier+soil modeling procedures is the ability to predict pile shears, pile deflected shapes, and forces acting on the cap+seal that agree with experimental results. In Figure 10.5 the time-history of shear force measured by the instrumented-pile in the experimental test is compared to data computed using LS-DYNA and FB-MultiPier analyses. Agreement is generally observed with regard to shear force magnitude and duration.

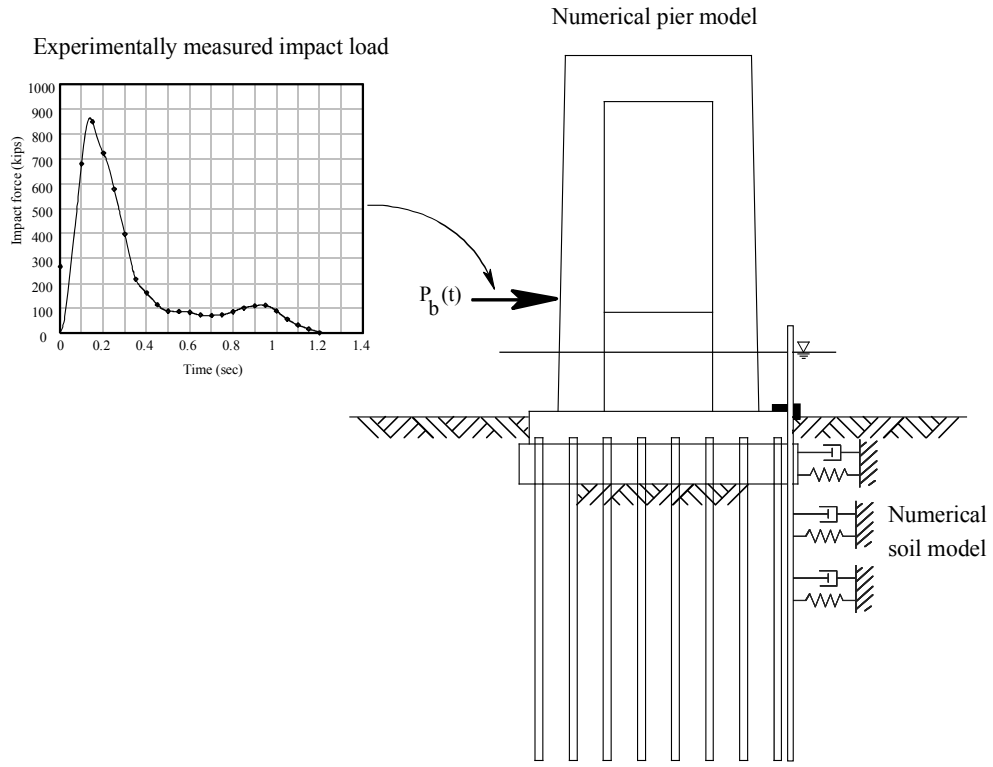

Figure 10.3 Application of measured P1T7 impact force to numerical model of Pier-1

In order to quantify the relative magnitudes of impact resistance forces mobilized during the test, the *sum* of all pile shear forces (at the pile heads) must also be quantified. It was not possible to experimentally measure the shear forces in each of the forty HP 14x73 steel piles that supported Pier-1. However, given the agreement between experiment and FEA models in terms of displacement and instrumented-pile shears, the sum of all pile shear forces may be estimated by extracting the appropriate data from the FEA models. Total (summed) pile shear forces predicted by LS-DYNA and FB-MultiPier (Figure 10.6) are in good agreement, and maximize at an approximate average of 275 kips. In comparison to the peak magnitude of the applied impact load (864 kip), the total pile shear force constitutes an important component of pier resistance. It should be noted that since pile group effects were incorporated into each of the FEA models (LS-DYNA and FB-MultiPier), each row of piles contributed differently to the shear total.

To compare pile deflections predicted analytically to those measured experimentally, deflected shapes for the instrumented-pile at the time of maximum pier displacement are presented in Figure 10.7. General agreement between simulation and experiment is indicated, implying a suitable numerical representation of soil resistance forces acting on the piles.

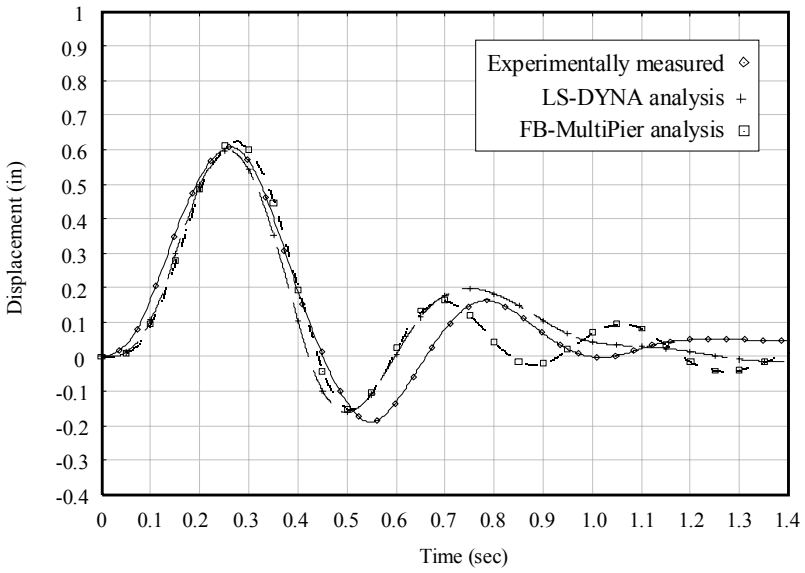

Figure 10.4 Comparison of measured and predicted pier displacement for test P1T7

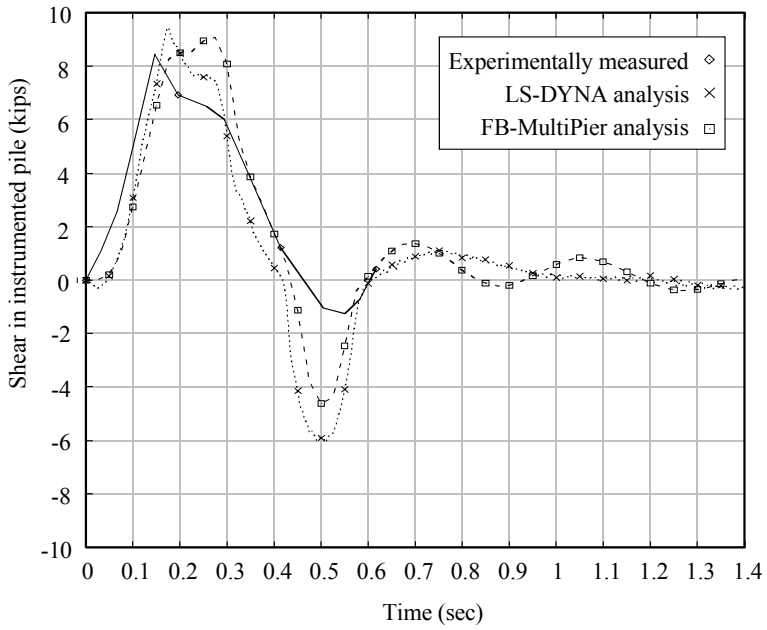

Figure 10.5 Shear force at head of instrumented pile for test P1T7

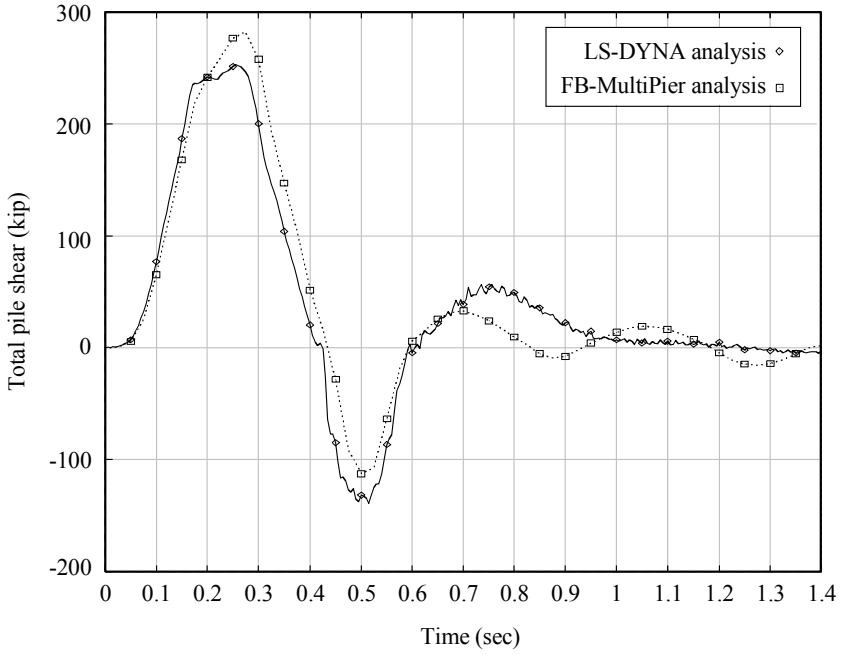

Figure 10.6 Sum of pile shear forces for all piles

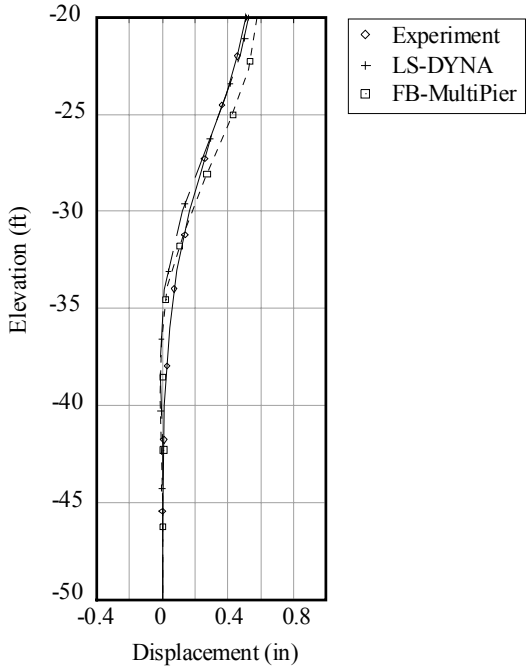

Figure 10.7 Pile deflections at maximum displacement for test P1T7

Further model calibration and validation requires that comparisons be made of measured versus FEA-predicted passive+active soil forces acting on the cap+seal. Shown in Figure 10.8 are resultant (passive+active) forces acting on the "front" (non-impact) and "back" (impact) sides of the cap+seal. Forces plotted in the figure are the total of both static (displacement- dependent) and dynamic (velocity-dependent) soil resistance. While agreement between experimental and numerical results here is not as apparent as in previous comparisons, general agreement is still observed in terms of maximum force level achieved, approximate time-to-peak, and duration of the initial (and dominant) force pulse. It is noted that a greater level of variability is contained within the experimental data shown in Figure 10.8 than in previous experimental data plots because the experimental passive and active soil forces were determined by measuring soil pressure changes only at a discrete set of sampling locations (McVay et al. 2005). Thus, spatial variations of soil pressure not completely captured by the geotechnical instrumentation network may account for the differences in measured versus predicted total resistance force.

Conversely, the computational soil modeling features included in the final FEA models—linear damping and cyclic stiffness degradation—may have been incapable of capturing secondary soil phenomena that account for the observed differences. Modifications to the models to improve agreement between measured and predicted passive+active soil pressure forces could have been achieved; however, doing so would also have caused other comparisons—e.g., of displacements, pile shears, and pile deflections—to possibly diverge. Given the moderate uncertainties in the measured data and the limitations of the numerical modeling features, the agreement shown in Figure 10.8 is regarded as acceptable.

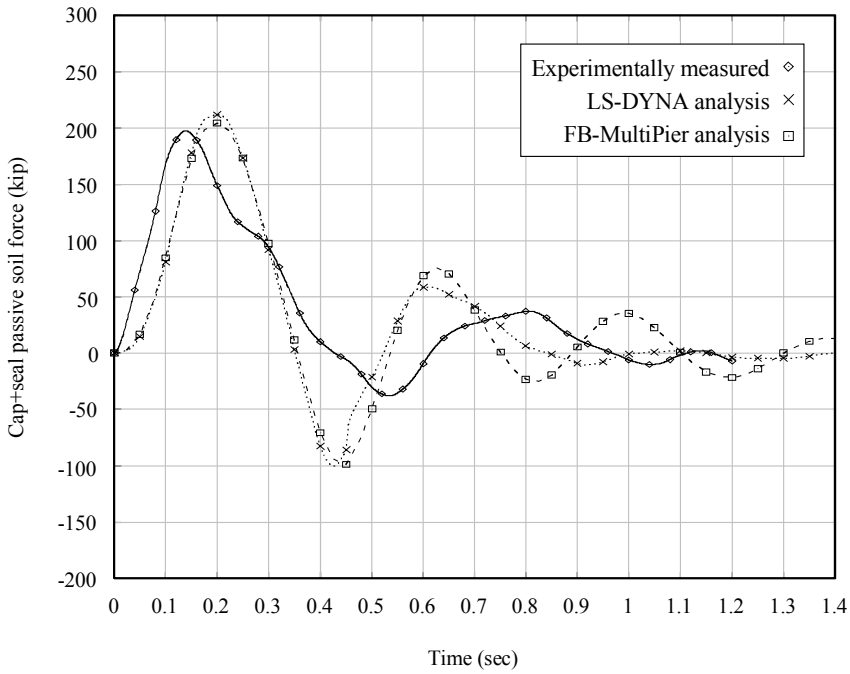

Figure 10.8 Passive+active soil force (sum of lead and trail sides) acting on the pile cap+seal for numerically simulated test P1T7

Having achieved an acceptable level of agreement between measured experimental data and numerical predictions, focus is now given to quantifying and comparing all of the major forces—loads and resistances—that were generated during test P1T7. Because the FB-MultiPier and LS-DYNA numerical results presented above generally agree closely, only results obtained from an FB-MultiPier dynamic analysis of test P1T7 will be presented from this point forward. Resistance forces presented below can generally be classified into one of three categories:

1. Displacement-dependent forces; referred to as "spring" forces
2. Velocity-dependent forces; referred to as "damping" forces
3. Acceleration-dependent forces; referred to as "inertia" forces

In Figure 10.9-a and Figure 10.9-b, a summary of the forces acting on Pier-1 during test P1T7, as predicted by dynamic FB-MultiPier analysis, is presented. Corresponding pier displacements are presented in Figure 10.9-c. Forces shown as positive in the figure are in the directions previously indicated in Figure 10.1. In each force plot, both applied load and effective load are repeated so that resistance force levels can be directly compared to loads. The effective load is defined here as the externally applied load (i.e., the experimentally measured impact load) plus the absolute value of the negative phases of the inertia force. In Figure 10.1, the inertia force is shown as acting in the direction opposite to that of the applied load, suggesting that inertia is a form of resistance to applied load. However, in reality, the inertia force always acts in a direction that is opposite to the direction of the acceleration of the pier. Hence, as the pier oscillates back and forth (as indicated by the displacements shown in Figure 10.9-c) the direction (and sign) of the inertia force will periodically reverse.

Inertia forces shown in Figure 10.9-a as positive constitute a form of resistance to the applied load. However, when the inertia forces reverse direction and become negative, they become a source of additional loading on the pier and add to the effect of the externally applied load. It is therefore useful to define effective load as the sum of the directly applied external load plus the absolute value of the inertia force when the latter is determined to be negative. Effective load may then be thought of as a simplified means of characterizing the force that drives the motion of the pier.

Examining the data in Figure 10.9-a, it is evident that inertia forces are mobilized more rapidly than any other form of resistance. At 0.1 sec., the inertia resistance force maximizes at approximately 250 kips. A short time later, at approximately 0.16 sec., the velocity of the pier reaches a maximum (as indicated by the maximum slope of the displacement curve in Figure 10.9-c). Hence, at this point in time, the acceleration, and therefore, the inertia force vanishes (becomes zero). As the pier undergoes a reduction of velocity (a deceleration) after 0.16 sec., the inertia force adds to the impact load in driving the pier forward (in a positive displacement direction). From 0.16 sec. to 0.4 sec., the inertia force is negative indicating that it acts as a component of loading. During this time frame, the absolute value of the (negative) inertia force is added to the applied load to form the effective load acting on the pier.

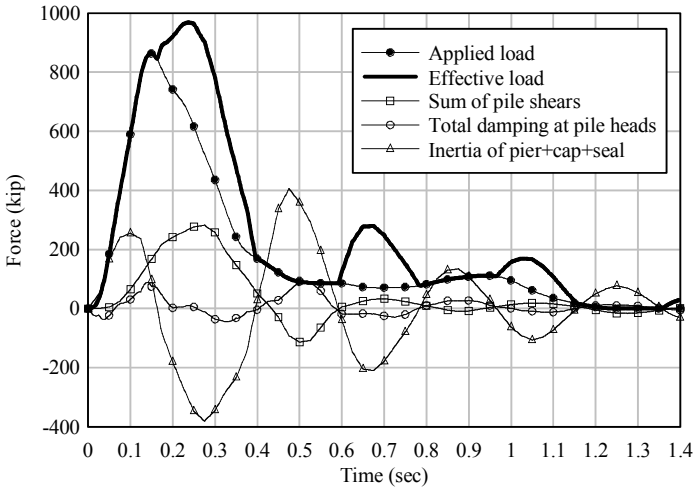

a) Forces acting on pier

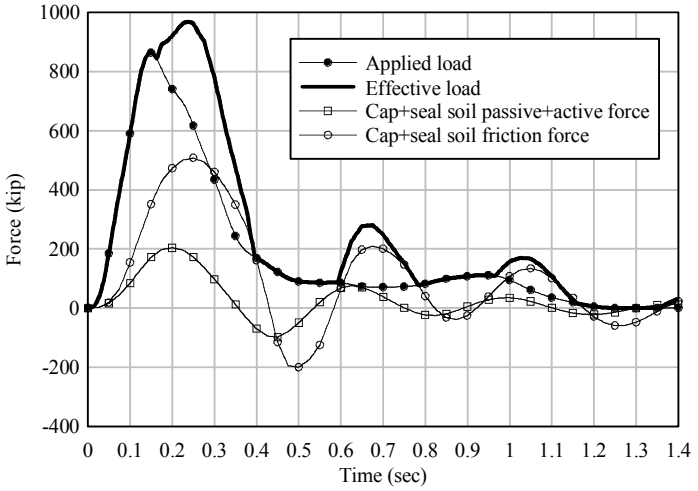

b) Comparison of passive+active and friction soil forces acting on the cap+seal

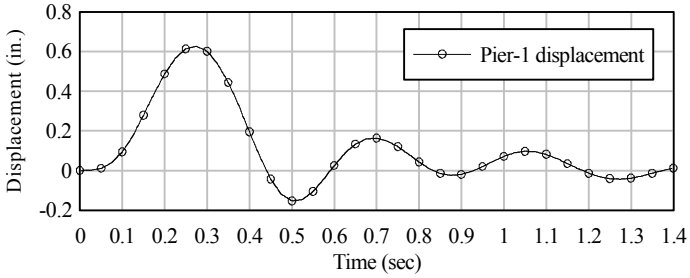

c) Pier displacement at impact elevation

Figure 10.9 Impact resistance forces and displacements for numerically simulated test P1T7

Comparing the resistance force data presented in Figure 10.9-a and Figure 10.9-b, four primary sources of impact resistance are apparent:

1. Inertia forces on pier:
   Approximate max. 250 kips at 0.10 sec.
2. Sum of pile shears:
   Approximate max. 275 kips at 0.27 sec.
3. Passive+active (pressure) soil forces on the lead and trail ends of the cap+seal:
   Approximate max. 200 kips at 0.20 sec.
4. Frictional (sliding) soil forces on the bottom and side surfaces of the cap+seal:
   Approximate max. 500 kips at 0.25 sec.

Soil forces acting on the steel piles, rather than directly on the surfaces of the cap+seal, are accounted for within the computed pile-head shear forces. Note that in comparison to the maximum 970 kip effective load, the impact resistance contributed by pile shears accounts for only about one-quarter of the total resistance mobilized. Instead, the dominant sources of resistance are associated with soil forces acting directly on the buried pier cap+seal.

In Figure 10.9-b, the relative contributions of friction versus passive+active soil pressures are compared. In addition to the obvious difference in force magnitude, timing differences are also apparent. The friction force on the cap+seal maximizes at nearly the same point in time that the pier displacements maximize (Figure 10.9-c). In contrast, the passive+active soil force on the cap+seal maximizes earlier in time, indicating the influence of dynamic damping (velocity-dependent) forces.

To examine this difference in greater detail, Figure 10.10 presents total soil forces, static (spring, displacement-dependent) component forces, and dynamic (damping, velocity-dependent) component forces for both the passive+active and friction cases. In the passive+active case, Figure 10.10-a, the dynamic and static components are closer in magnitude (i.e., more balanced) than in the friction case, Figure 10.10-b, where the static (displacement-dependent) component clearly dominates. In the passive+active case, the influence of the dynamic damping component causes the total force to peak before maximum displacement has occurred. Conversely, the friction case is dominated by static behavior and thus maximizes later in time, when the maximum pier displacement is reached. Despite these differences, the influence of soil forces acting directly on the cap+seal of Pier-1 clearly dominates the overall response of the pier.

10.3 Impact test P3T3

Among the series P3 tests conducted on Pier-3, test P3T3 involved the highest impact energy level and generated the largest recorded dynamic impact load. For this reason, test P3T3 is chosen for the purpose of comparing experimental data to dynamic FEA predictions. Unlike the Pier-1 tests, geotechnical instrumentation was not available to record transient (time-varying) soil response data (e.g., soil pressure changes) during the Pier-3 tests. However, interaction between the foundation of Pier-3 and the surrounding soil was less complex than that of Pier-1. In the case of Pier-3, only the piles interacted with the soil; the

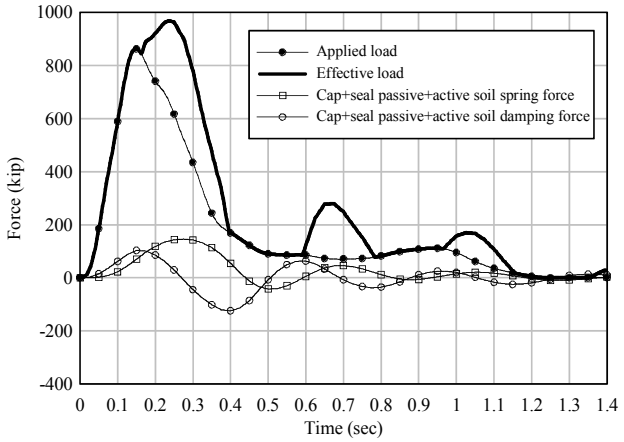

a) Passive+active soil forces on cap+seal broken down into static (spring) and dynamic (damping) components

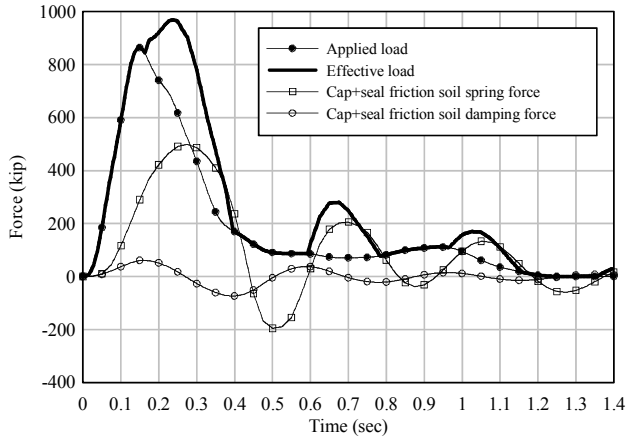

b) Friction soil forces on cap+seal broken down into static (spring) and dynamic (damping) components

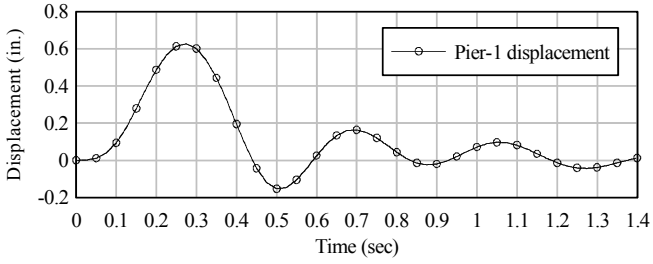

c) Pier displacement at impact elevation

Figure 10.10 Static and dynamic soil resistance forces for numerically simulated test P1T7

pile caps were not in direct contact with the soil. Consequently, the number of separate sources of impact resistance in test P3T3 was less than in test P1T7. In Figure 10.11, a schematic diagram of the force groups active during test P3T3 is provided.

Given the general agreement between the FB-MultiPier and LS-DYNA results obtained in the previous section (dealing with test P1T7), only FB-MultiPier is used to analyze test P3T3. Dynamic analysis of test P3T3 was accomplished by applying the experimentally measured impact load (Figure 10.12) to the numerical pier model as a prescribed time-varying dynamic load (Figure 10.13). The point of load application was chosen to match the observed elevation at which the barge struck Pier-3 during test P3T3.

A comparison of experimentally measured pier displacement data and results obtained from dynamic FB-MultiPier analysis of test P3T3 is provided in Figure 10.14. Good agreement is observed between the maximum measured and maximum predicted displacements. Moreover, once the impact load has terminated (at 0.55 sec., Figure 10.12), and the pier goes into free vibration, the measured and predicted natural periods (or frequencies) of vibration are in close agreement. Hence, the stiffness-to-mass ratios of physical pier and the numerical model are quite similar. Noting that the displacement decay rates for the physical and numerical systems are similar, it is evident that the mechanisms of energy dissipation in the FEA model adequately represent the damping that occurred in the physical impact test.

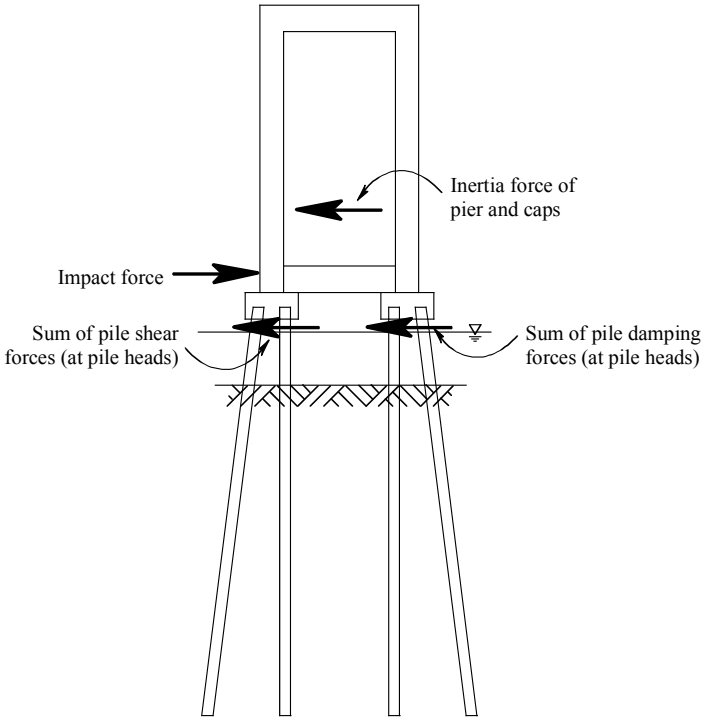

Figure 10.11 Forces acting on Pier-3 during test P3T3

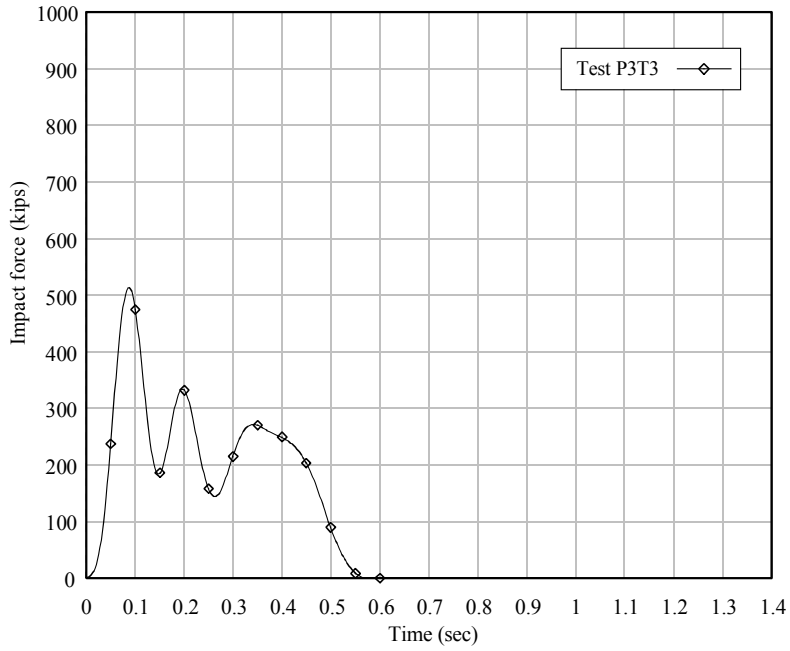

Figure 10.12 Impact force applied to Pier-3 during test P3T3

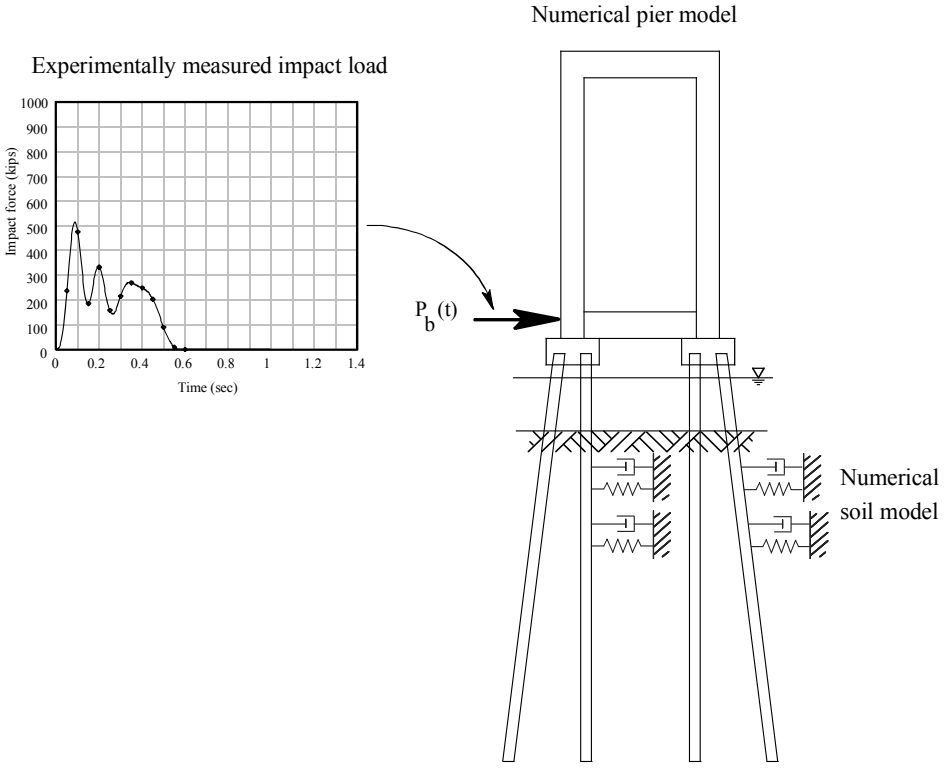

Figure 10.13 Application of measured P3T3 impact force to numerical model of Pier-3

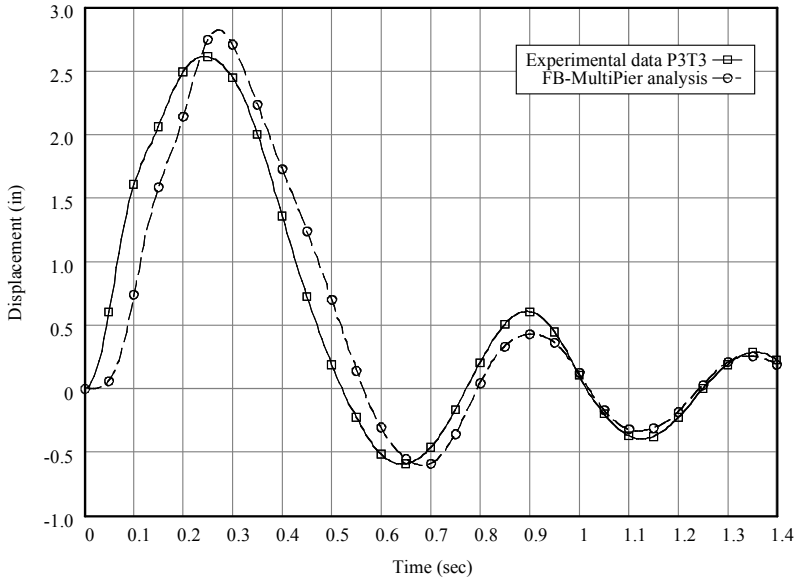

Figure 10.14 Comparison of measured and predicted pier displacements for test P3T3

In Figure 10.15-a, a summary of forces acting on Pier-3 during test P3T3, as predicted by dynamic FB-MultiPier analysis, is presented. Corresponding pier displacements are presented in Figure 10.15-b. Forces shown as positive in the figure are in the directions previously indicated in Figure 10.11. As was the case in test P1T7, inertia forces are mobilized in test P3T3 more rapidly than any other form of impact resistance. After reaching a maximum resistance level of 370 kips, the inertia force rapidly drops back to zero. From 0.12 sec. and 0.4 sec., the inertia force becomes negative, indicating that it constitutes a form of loading on the pier, rather than of resistance. At 0.25 sec., the 300 kip inertia force adds to the 150 kip applied load to produce a substantially increased (effective) load of 450 kips. Although inertia initially aids in resisting the applied impact load, after the velocity of the pier maximizes and deceleration begins, inertia becomes an additional form of load that must be resisted by the pier and, ultimately, the soil.

From an examination the inertia and pile shear force curves in Figure 10.15-a, it is evident that at approximately 0.1 sec., the dominant form of impact resistance transitions from one that is inertia based to one that is deformation based. After 0.1 sec., inertia resistance drops off rapidly, and the majority of impact resistance comes instead from deformation of the concrete piles and the resulting shear forces that are developed. Total pile shear ultimately reaches 400 kips at 0.23 sec., slightly earlier in time than the point at which maximum pier displacement occurs (0.27 sec., Figure 10.15-b).

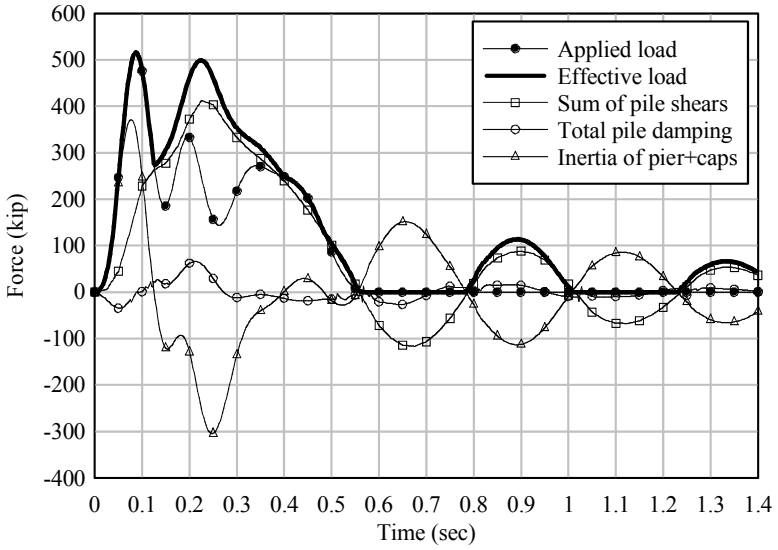

a) Forces acting on pier

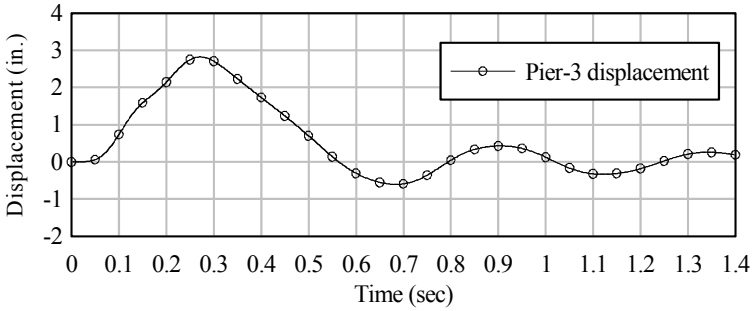

b) Pier displacement at impact elevation

Figure 10.15 Impact resistance forces and displacements for numerically simulated test P3T3

Primary contributions to the total pile shear force derive from static (spring, displacement-dependent) and dynamic (damping, velocity-dependent) soil forces that act on the embedded portions of the piles. Inertia force relating to acceleration of mass within the length of concrete piles also contributes to the total pile head shear force extending from the pile-cap down, but to a much lesser extent than do the soil forces. In Figure 10.16-a, static and dynamic components of soil force acting on the piles are compared. In general, the static component of soil resistance dominates the overall (total) soil force that is developed. The damping soil force is considerably less in magnitude, indicating that the zone of soil within which significant particle velocities were developed was relatively limited in size.

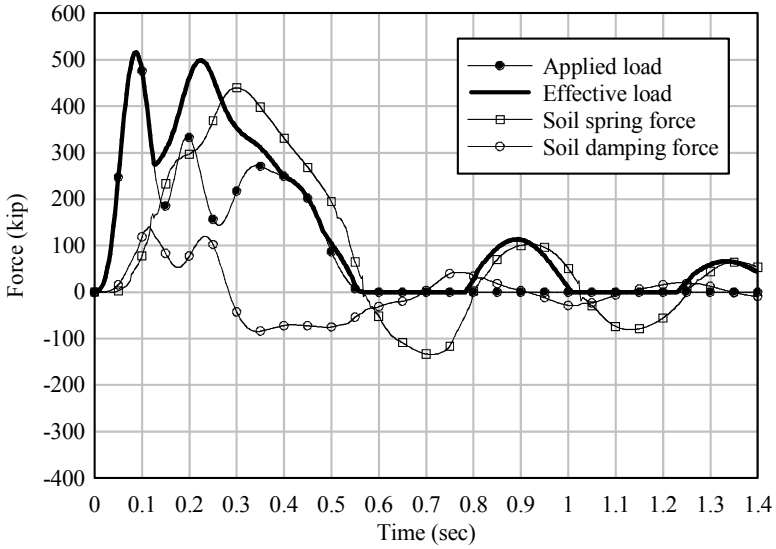

a) Forces acting on pier

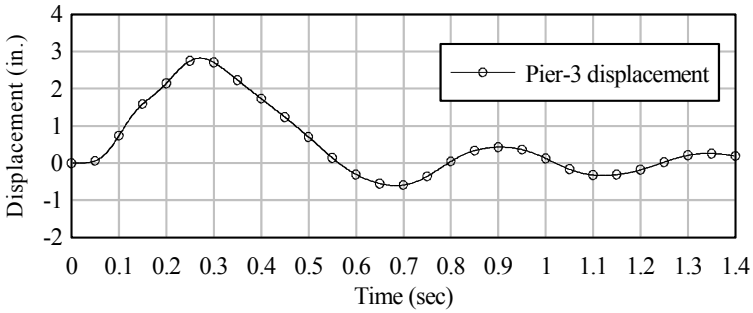

b) Pier displacement at impact elevation

Figure 10.16 Static and dynamic soil resistance forces for numerically simulated test P3T3

10.4 Impact test B3T4

In contrast to tests P1T7 and P3T3, both of which involved impacts on isolated piers, tests in series B3 involved impacts on a partial bridge structure consisting of multiple piers connected together via superstructure spans. By analyzing data from such tests, the force that was transferred from the impacted pier (Pier-3) to the adjacent piers through the superstructure can be quantified. Among the series B3 tests, test B3T4 involved the highest impact energy level and generated the largest recorded dynamic impact load. For this reason, B3T4 is chosen for consideration here. The number of separate sources of impact resistance active during test B3T4 was similar to that of test P3T3 except that an additional bearing shear force was also present at the top of the pier cap (Figure 10.17).

Using the multiple-span structural and soil models described in Chapters 8 and 9, FB-MultiPier was used to dynamically analyze test B3T4. The impact load experimentally measured during the test (Figure 10.18) was applied to the numerical model as a prescribed time-varying dynamic load (Figure 10.19). The point of load application was chosen to match the observed elevation at which the barge struck Pier-3 during the test.

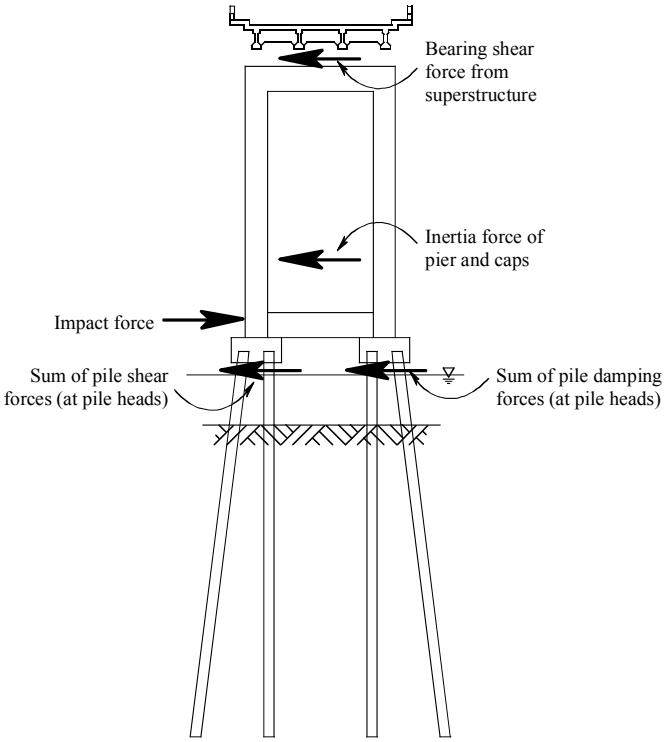

Figure 10.17 Forces acting on Pier-3 during test B3T4

A comparison of experimentally measured and numerically predicted pier displacements at the barge impact elevation on Pier-3 is provided in Figure 10.20. General agreement is observed between the maximum measured and maximum predicted displacements. To determine whether impact loads transmitted through the superstructure from Pier-3 to the rest of the bridge were adequately captured in the numerical model, accelerations at the tops of Pier-2, Pier-3, and Pier-4, for which both experimental and numerical data were available, are compared in Figure 10.21. At the top of Pier-3, the measured and predicted accelerations are in very good agreement. General agreement in terms of peak acceleration levels at the more distant Pier-2 and Pier-4 is also observed, although the times at which the peak accelerations occur differ somewhat between experimental measurement and the numerical model. However, given that site-specific soil data were unavailable for Pier-2 and Pier-4, the level of agreement indicated in Figure 10.21 for these piers is considered to be acceptable based on the soil modeling approximations that were necessary.

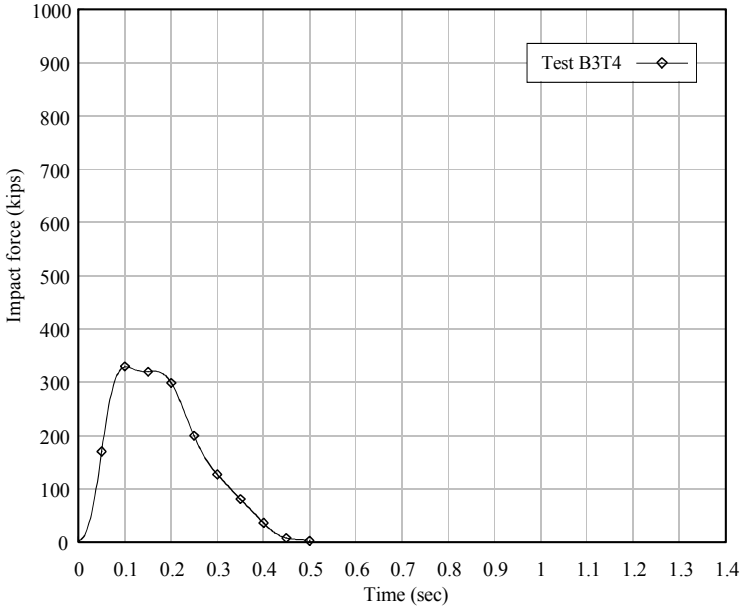

Figure 10.18 Impact force applied to Pier-3 during test B3T4

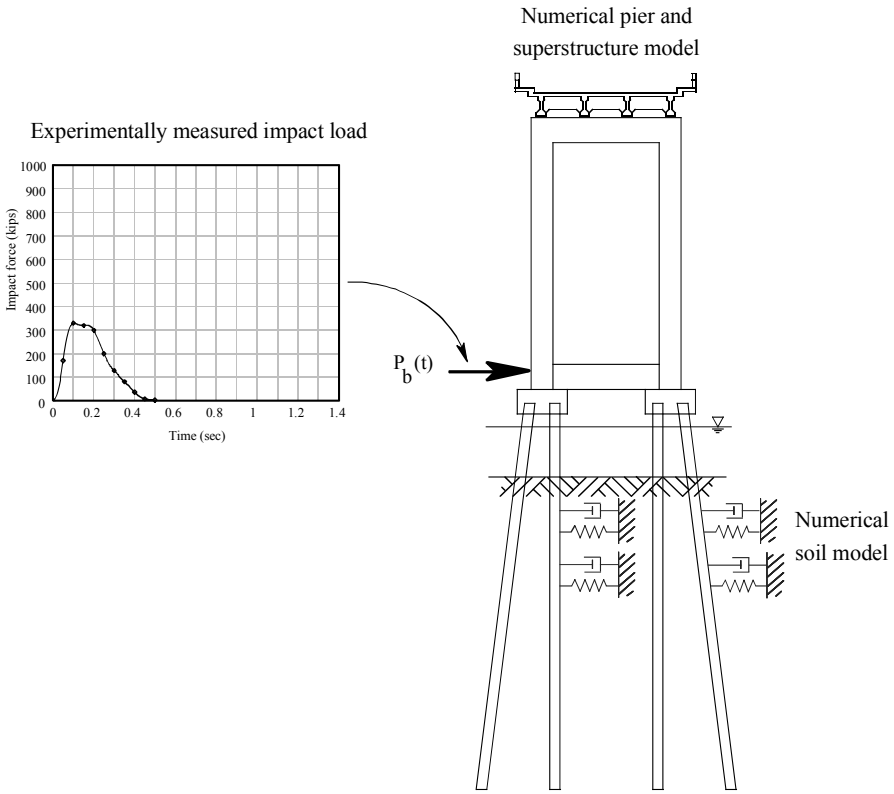

Figure 10.19 Application of measured B3T4 impact force to numerical model of Pier-3

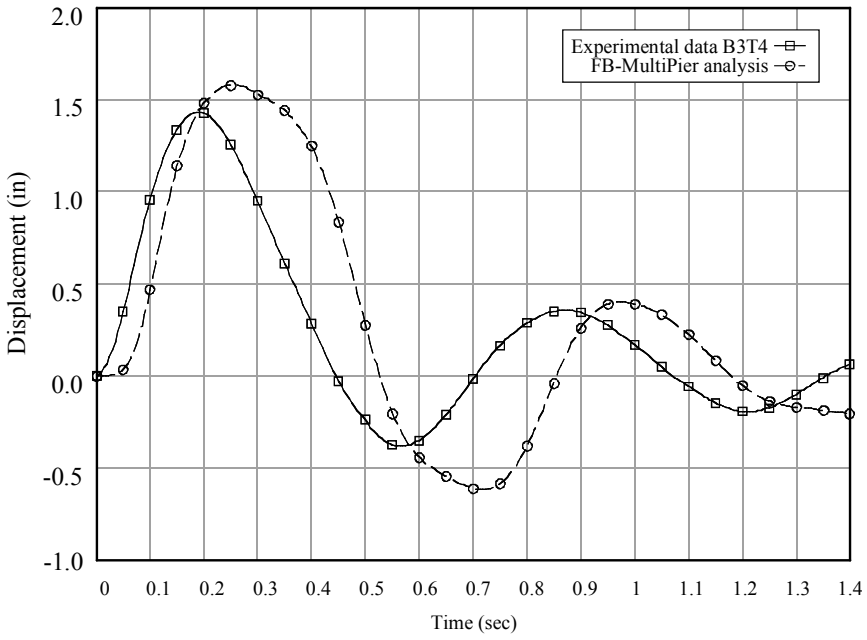

Figure 10.20 Comparison of measured and predicted pier displacements for test B3T4 (Displacements shown are for Pier-3 at the elevation of the barge impact point)

In Figure 10.22-a, a summary of forces acting on Pier-3 during test B3T4, as predicted by dynamic FB-MultiPier analysis, is presented. Corresponding pier displacements are presented in Figure 10.22-b. Forces shown as positive in the figure are in the directions previously indicated in Figure 10.17. Similar to analyses of tests P1T7 and P3T3, pier inertia forces are mobilized in test B3T4 more rapidly than any other form of impact resistance. At approximately 0.08 sec., the pier inertia force maximizes at 190 kips. Simultaneously, but at a slower rate of increase, pile shear forces rise in response to displacements of the pier at the elevation of the pile caps. At 0.2 sec., the total pile shear force maximizes at approximately 260 kips. Trailing both the inertia and pile shear forces, resistance forces from the bridge superstructure develop in the form of bearing shear forces at the top of the pier. At 0.16 sec., resistance from the superstructure maximizes at 130 kips.

Both the pier inertia and superstructure (bearing shear) forces decline rapidly after maximizing. When these quantities become negative, they constitute a form of loading on the pier, rather than of resistance. To graphically illustrate the transition from resistance to load, the effective-load curve in Figure 10.22 includes contributions from both pier inertia (when negative) and bearing shear (when negative). At 0.375 sec., the combined pier inertia plus superstructure load maximizes at a combined sum of 160 kips adding to the applied impact load of 65 kips to produce a total effective load on the pier of 225 kips. As Figure 10.22 indicates, the effective load is both greater in magnitude and longer in duration than the directly applied barge impact load. Further, note that from 0.25 sec. to 0.5 sec., the sum of the pile shear forces is nearly equal to the effective load—the difference being attributable primarily to internal structural damping forces—indicating that effective load, rather than applied load, drives the structural demand placed on the foundation.

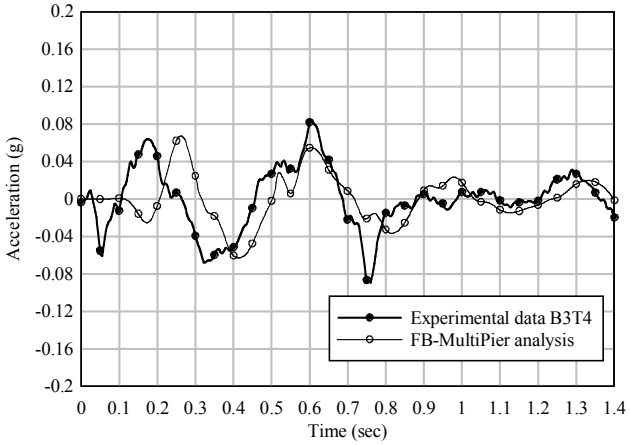

a) Accelerations at top of Pier-2

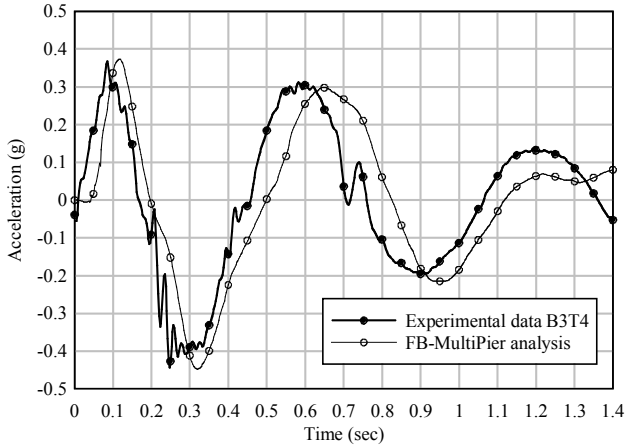

b) Accelerations at top of Pier-3

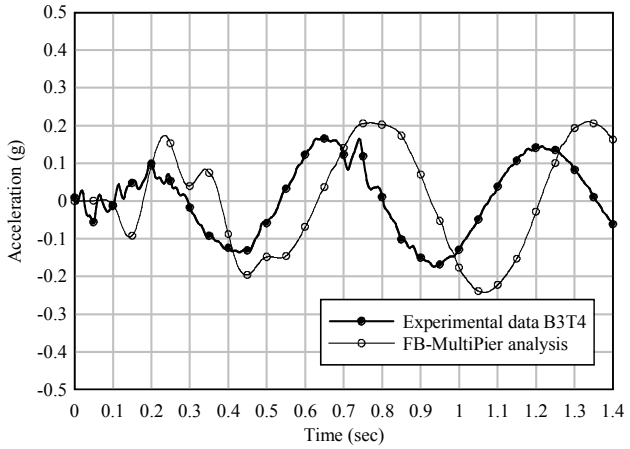

c) Accelerations at top of Pier-4

Figure 10.21 Comparison of measured and predicted pier accelerations for test B3T4 (Accelerations shown are for locations at the tops of the piers)

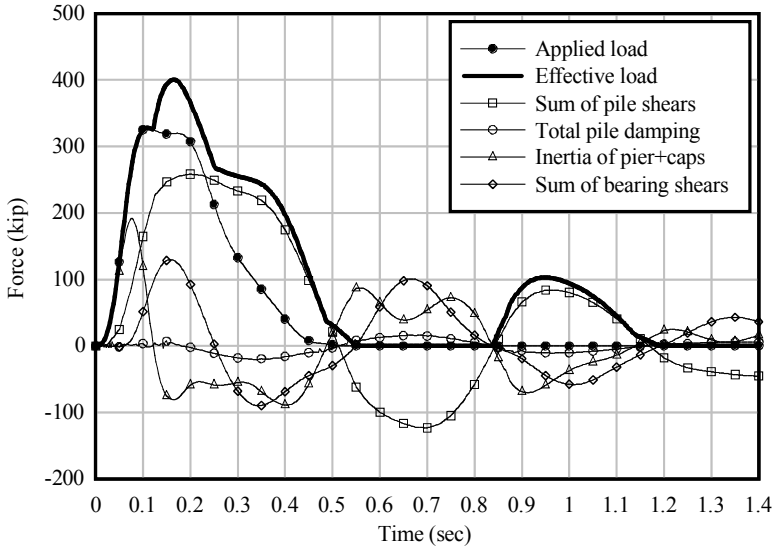

a) Forces acting on pier

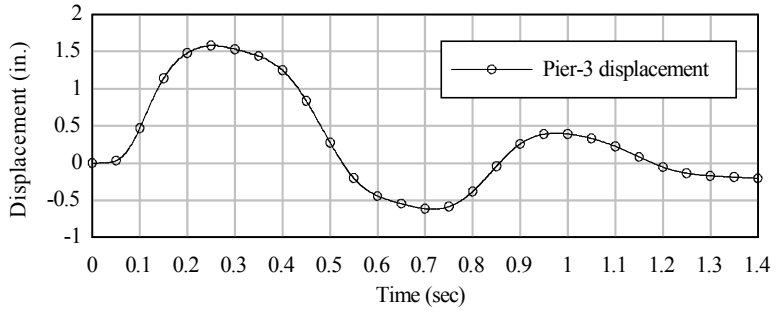

b) Pier displacement at impact elevation

Figure 10.22 Impact resistance forces and displacements for numerically simulated test B3T4

As noted earlier (in the discussion of test P3T3), primary contributions to the total pile shear force derive from static (spring, displacement-dependent) and dynamic (damping, velocity-dependent) soil forces that act on the embedded portions of the piles. In Figure 10.23-a, static and dynamic components of soil force acting on the piles are compared. In test B3T4, as in test P3T3, the static component of soil resistance dominates the overall (total) soil force that is developed. The damping soil force is considerably less in magnitude, indicating that the zone of soil within which significant particle velocities, and therefore damping forces, were developed was relatively limited in size.

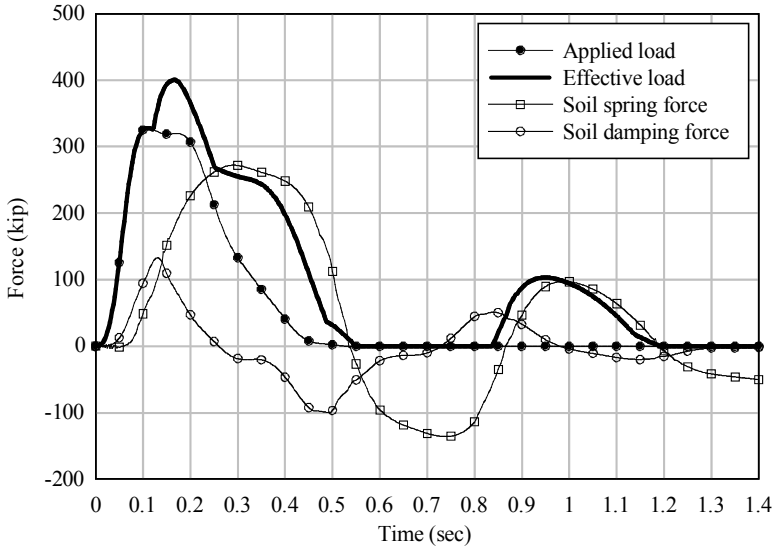

a) Forces acting on pier

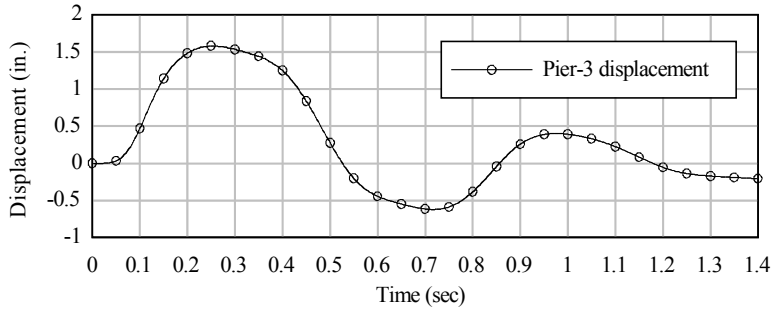

b) Pier displacement at impact elevation

Figure 10.23 Static and dynamic soil resistance forces for numerically simulated test B3T4

10.5 Comparison of dynamic and static pier response

Current bridge design practices for sizing structural pier elements to resist barge impact loading generally involve the use of static load calculation procedures (e.g., the AASHTO barge impact provisions) and static (linear or nonlinear) structural analysis techniques. In the analysis results presented above, the influences of dynamic forces—e.g., inertia and damping—on pier response were evident. Earlier, in Chapter 7, maximum measured dynamic load magnitudes were compared to static equivalent loads specified by AASHTO. However, evaluating the relative severity of dynamic versus static loading conditions can only be partially addressed by such comparisons. Of equal importance is the comparison of structural responses that result from the application of such loads. In the present section, comparisons are made between structural responses (displacements, moments, and shears) computed via dynamic analysis procedures and analogous responses computed using static procedures. By comparing dynamic and static analysis results, assessments of the level of accuracy present in current design specifications may be made.

Barge impact conditions corresponding to the impact energies generated during tests P1T7, P3T3, and B3T4 are considered here. A total of nine dynamic and static analyses, summarized in Table 10.1, are conducted using FB-MultiPier. In all cases, the possibility of nonlinear soil response is included. However, because no damage was evident in either the pier columns or piles during the physical tests, structural properties of the piers and piles are assumed to remain linearly elastic in the FB-MultiPier analyses.

In the three dynamic cases, A, D, and G, the time-varying prescribed loading conditions and calibrated/validated dynamic pier+soil models discussed in the previous sections are utilized. In static cases B, E, and H, the instantaneous peak (maximum) values of impact loads measured during tests P1T7, P3T3, and B3T4 (864 kips, 516 kips, 328 kips respectively) are applied as static loads to static models of Pier-1, Pier-3, and the multiple-pier bridge model, respectively. For case B, a static Pier-1 model was constructed by removing all soil damping elements (dashpots) from the dynamic model and replacing the field-measured dynamic soil-resistance (*p-y*) curves with corresponding static *p-y* curves in which velocity-dependent dynamic stiffness increases were removed. For cases E and H, static models were similarly constructed by removing soil damping (dashpot) elements from dynamic models and utilizing static *p-y* soil resistance curves.

In static cases C, F, and I, the P1T7, P3T3, and B3T4 experimental impact energies (494 kip-ft., 108 kip-ft., and 75 kip-ft. respectively; see Chapter 7), were used in conjunction with the AASHTO barge impact provisions and a hydrodynamic mass coefficient of $C_H = 1.05$ to compute AASHTO equivalent static loads. Applied loads and corresponding dynamic and static structural responses computed for cases A through I are graphically presented in Figure 10.24.

Table 10.1 Dynamic and static analysis cases

Case	Impact condition	Analysis type	Load description	Max. load (kip)	Pier/pile behavior	Soil behavior
A	P1T7	Dynamic	Time-varying P1T7	864	Linear	Nonlinear
B	P1T7	Static	Peak P1T7 load	864	Linear	Nonlinear
C	P1T7	Static	AASHTO	1788	Linear	Nonlinear
D	P3T3	Dynamic	Time-varying P3T3	516	Linear	Nonlinear
E	P3T3	Static	Peak P3T3 load	516	Linear	Nonlinear
F	P3T3	Static	AASHTO	398	Linear	Nonlinear
G	B3T4	Dynamic	Time-varying B3T4	328	Linear	Nonlinear
H	B3T4	Static	Peak B3T4 load	328	Linear	Nonlinear
I	B3T4	Static	AASHTO	276	Linear	Nonlinear

Assessing dynamic effects on structural response can be accomplished by comparing case A to B (P1T7), case D to E (P3T3), and case G to H (B3T4). For Pier-1, dynamic response to time-varying load (case A) results in a maximum pier displacement that is 32% larger than that resulting from application of an equal magnitude static load (case B). Inertia effects are therefore found to amplify the dynamic displacement of Pier-1 in comparison to the static displacement. Because pile forces are strongly influenced by pier displacement, it is consistent that maximum pile shears and moments for case A also exceed those for case B.

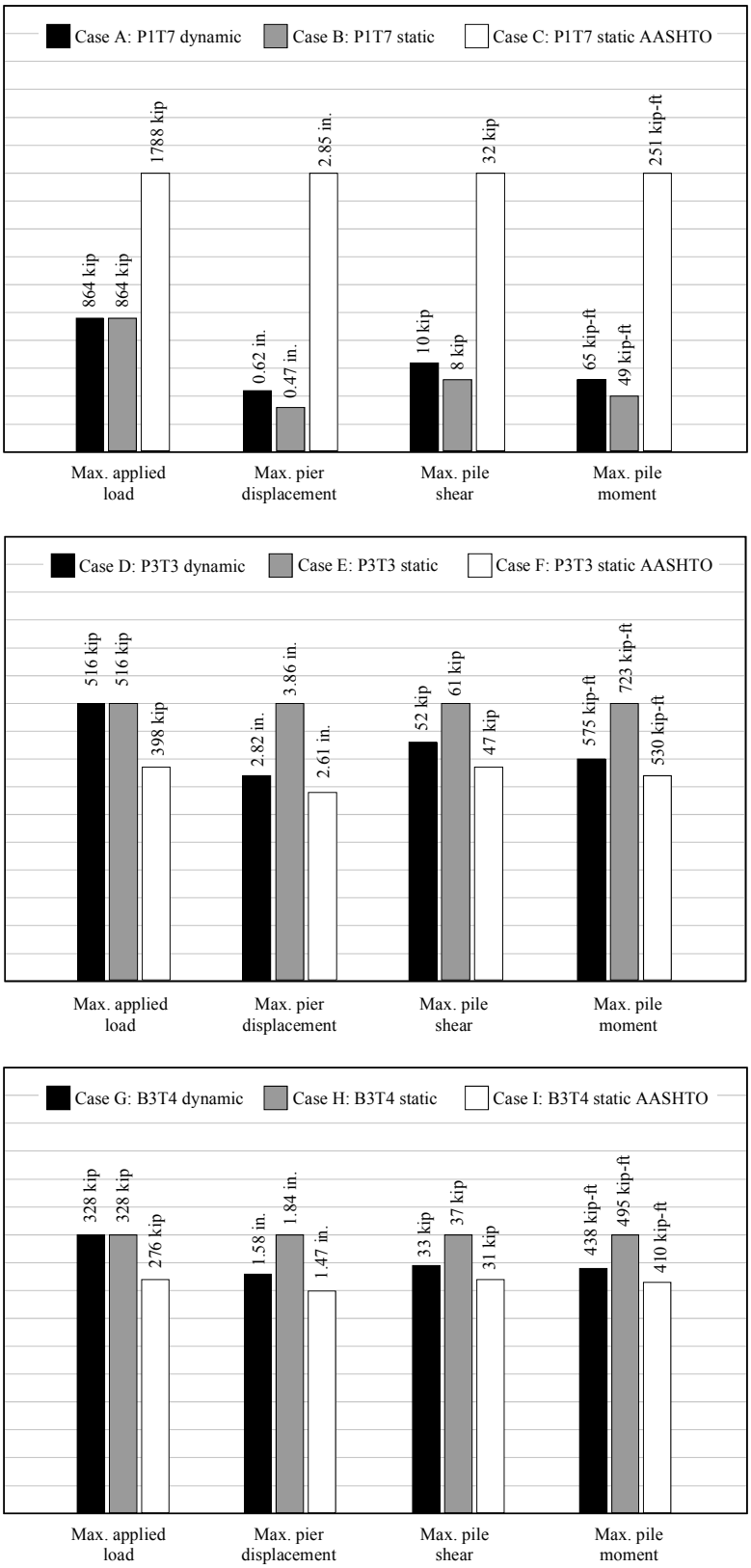

Figure 10.24 Comparison of dynamic and static analysis results for foundation of pier (Max. pier displacements determined at point of load application)

For Pier-3 in isolation (i.e., without superstructure), the situation is reversed, in that the dynamic analysis (case D) yields a maximum pier displacement that is 27% smaller than that generated by application of an equal magnitude static load (case E). Comparisons of pile shears and moments for cases D and E exhibit similarly consistent characteristics in that dynamic pile forces are smaller than corresponding static forces. When Pier-3 is connected to adjacent piers through the bridge superstructure, a similar comparison between dynamic and static response results. Dynamic pier displacement (case G) is 14% smaller than that generated by application of an equal magnitude static load (case H). Consequently, pile shears and moments for case G are also smaller than those for case H.

AASHTO-static analysis results (cases C, F, and I) are also compared to dynamic analysis results (cases A, D, and G) in Figure 10.24. For the impact energy associated with test P1T7, the AASHTO provisions (with $C_H = 1.05$) yield a static impact load (1788 kips) that is 107% larger than the measured peak dynamic load (864 kips). As a result, by all measures of structural response (displacement, shear, moment) considered in Figure 10.24, the AASHTO-static values (case C) are conservative, i.e., larger than corresponding dynamically predicted values (case A). Due to softening that occurs in the nonlinear model of soil stiffness, the AASHTO pier displacement is 360% larger than the dynamic pier displacement. As a consequence, maximum pile shear and maximum pile moment in the AASHTO case are accordingly much larger than values determined via dynamic analysis.

For Pier-3, the relationships between AASHTO-static and dynamic results are reversed. For the impact energy associated with test P3T3, the AASHTO provisions (with $C_H = 1.05$) yield a static load (398 kips) that is 23% smaller than the measured peak dynamic load (516 kips). For the structural responses considered in Figure 10.24, AASHTO-static analysis (case F) produces results that are slightly smaller than corresponding dynamic analysis results (case D). When Pier-3 is connected to adjacent piers through the bridge superstructure, comparisons between dynamic and static response exhibit similar trends. For the impact energy associated with test B3T4, the AASHTO provisions (with $C_H = 1.05$) yield a static load (276 kips) that is 16% less than the measured peak dynamic load (328 kips). For the structural responses considered in Figure 10.24, the AASHTO-static analysis (case I) produces results that are slightly smaller than the corresponding dynamic analysis results (case G).

Overall, the set of results presented in Figure 10.24, in combination with dynamic and static impact force data presented earlier in Chapter 7, suggest that for high-speed, high-energy barge impacts on relatively stiff piers, the current AASHTO barge impact provisions are significantly conservative in regard to both static design load levels and resulting foundation design forces (e.g. pile shears and moments). Conversely, for low-speed, low-energy impacts on flexible piers (e.g. piers with waterline footings), the static design loads specified by AASHTO are smaller than those determined directly from barge impact experiments. However, static analyses performed using the AASHTO loads appear to yield foundation design forces that are consistent with results obtained by more refined analysis techniques (e.g., dynamic analysis combined with experimentally measured dynamic loads). Before these observations can be assumed to be reasonably universal in scope, additional parametric analyses covering a wider range of impact conditions need to be performed.

The structural responses presented in Figure 10.24 focus primarily on foundation-related forces—pile shears and pile moments. Also of interest, however, are comparisons between pier-related forces computed via dynamic and static analysis. In both Pier-1 and

Pier-3, horizontal structural pier elements exist at the elevations of the load application points. In Pier-1, the load application point is located approximately at the elevation of the top of a shear wall, and in Pier-3, the load is applied in line with a horizontal strut. As a result, static analyses of Pier-1 and Pier-3 in isolation (i.e., without superstructure) produce pier column shears and moments that are negligible in magnitude. The connection of a superstructure to the top of a pier, however, fundamentally alters the flow of impact load through the structure, and can therefore generate significant pier column forces.

In Figure 10.25, maximum pier column forces and total bearing shear forces, as computed by dynamic and static analyses, are compared for condition B3T4. Forces predicted by dynamic analysis are found to be substantially larger than corresponding values computed using static analysis. Comparing case H to G, maximum values of pier column shear, pier column moment, and bearing shear force predicted by static analysis (case H) are only 26%, 27%, and 28% (respectively) of the corresponding values predicted by dynamic analysis (case G). When static analysis employing the AASHTO specified load is used (case I), maximum values of pier column shear, moment, and bearing shear force drop to 20%, 21%, and 22% (respectively) of the corresponding dynamic values (case G). In all three of these analysis cases (G, H, and I), lateral resistance at the top of the pier, due to the connected superstructure, is included in the numerical model. However, lateral superstructure resistance generated in response to load application differs significantly—both in type and magnitude—between the dynamic and the static cases.

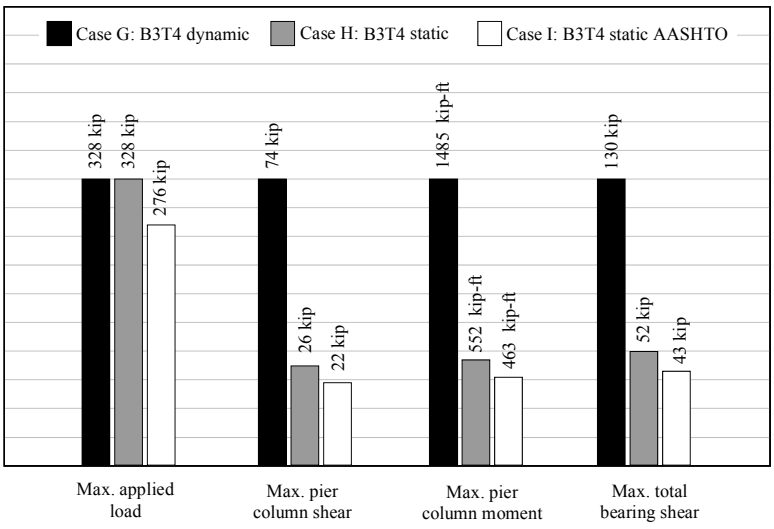

Figure 10.25 Comparison dynamic and static analysis results for pier structure (Max. pier displacements determined at point of load application)

In cases H and I, the static lateral resistance forces generated at the top of Pier-3 are a function of the stiffness of the superstructure and of the adjacent piers (as well as their respective foundations and soil conditions). Relative proportions of impact load that flow into the Pier-3 foundation versus into the superstructure are then determined by satisfying

static equilibrium between the statically applied load and displacement-dependent resistance forces from Pier-3 and from the superstructure.

However, significant mass-dependent inertia resistance forces are also mobilized during dynamic impact events. At the top of Pier-3, mass-proportional inertia forces add to the displacement-dependent stiffness forces to produce the total resistance of the superstructure. Lateral impact resistance contributed by the inertia of the superstructure is evident in Figure 10.25 in that the total bearing shear force in the dynamic case (130 kips) significantly exceeds the corresponding bearing shear force from both static cases. Recalling Figure 10.21c, accelerations at the top of Pier-3 reach approximately 0.35 g for loading condition B3T4. Considering that the concrete superstructure spans connected to Pier-3 have a weight of several hundred kips, it is evident—based on the peak acceleration level noted above—that a significant portion of the 130 kip bearing shear force (Figure 10.25) recorded for dynamic case G is attributable to mass-proportional inertia.

The combined effects of superstructure inertia and superstructure stiffness produce greater momentary (transient) restraint at the top of the pier. This increase in restraint then leads to elevated deformation levels within the pier columns and elevated maximum pier column forces (shear and moment). In Figure 10.26, deflected shapes for Pier-3 are presented based on results obtained from dynamic analysis (case G) and static analysis (case H). Although greater pier displacement at the impact point occurs in the static case, greater relative column deflection occurs in the dynamic case. This dynamic amplification of column deflection is responsible for the elevated levels of dynamic column forces (shear and moment) shown in Figure 10.25.

Amplification of the maximum column forces in case B3T4 demonstrates that dynamic effects such as inertia are inherently difficult to capture using static analysis procedures. Combinations of structural flexibility and transient (momentary) restraint associated with inertial resistance, as well as other dynamic phenomena, may produce dynamic member forces (e.g., column shears and moments) that substantially exceed the design forces predicted by static analysis under equivalent magnitude loads. The results presented here imply that the effects of both superstructure stiffness and mass (inertia) need to be included in structural analysis performed for the purpose of establishing design forces for pier elements such as columns. Failure to account for superstructure-generated restraint at the top of a pier may result in the determination of significantly unconservative design forces.

The displacement, pile force, and column force data presented in cases A through I above indicate that using static analysis procedures to assess pier response to barge collision loads may lead to a mixture of conservative and unconservative predictions. Whether statically predicted design forces are conservative or not depends on the structural characteristics of the pier, superstructure, soil characteristics, characteristics of the impacting vessel (e.g., kinetic energy), and the load levels prescribed by design specifications (e.g., the AASHTO barge impact provisions).

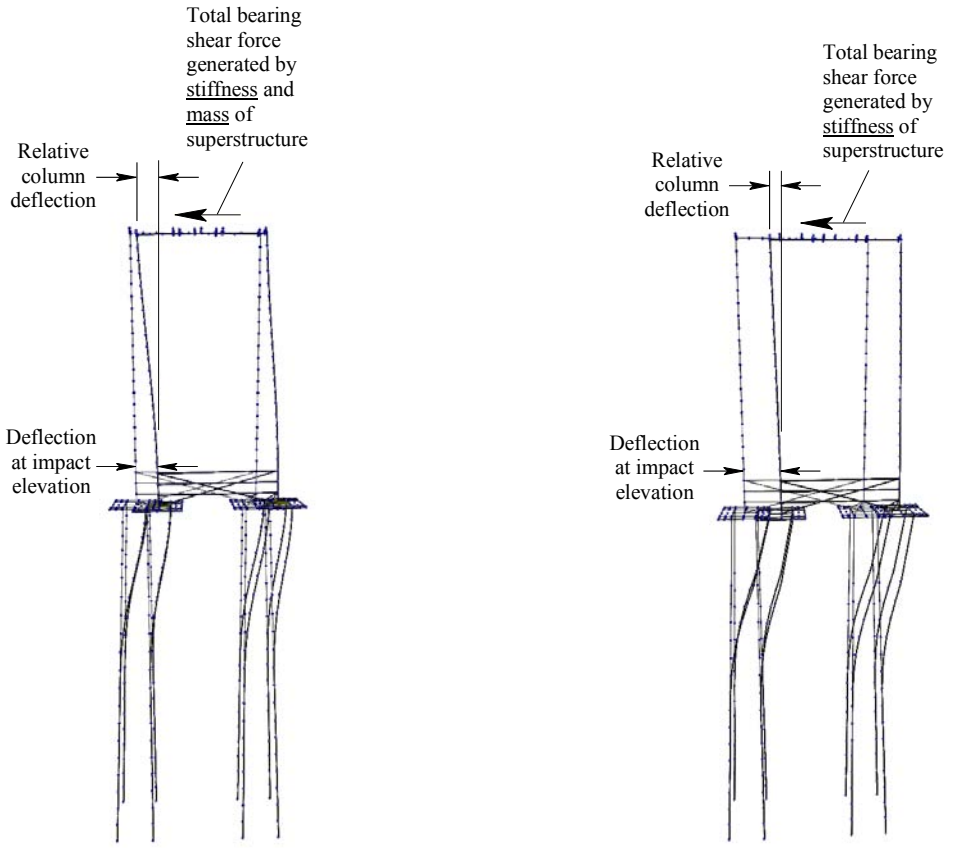

a) Dynamic analysis (case G)

b) Static analysis (case H)

Figure 10.26 Dynamic and static deflected shapes of Pier-3 under B3T4 loading condition

CHAPTER 11
CONCLUSIONS AND RECOMMENDATIONS

11.1 Conclusions

This study was undertaken for the purposes of quantifying impact loads that are imparted to bridge piers during barge-pier collision events, and quantifying the associated pier and soil responses. The study encompassed both experimental field testing and dynamic finite element analysis. Field testing included fifteen full-scale experimental barge impact tests conducted on two piers of the St. George Island Causeway Bridge in Florida. During each test, instrumentation systems (sensor networks) were used to quantify dynamic impact loads and resulting structure, soil, and barge responses. Subsequently, numerical finite element analysis techniques were employed to aid in interpretation of the experimental test data, and to enable an initial assessment of the level of accuracy that is present in the current AASHTO barge impact design provisions. Based on the data obtained, the following conclusions are drawn:

1. In moderate to high energy impact conditions (i.e., those capable of producing permanent inelastic barge deformation), the maximum impact loads that can be generated during a collision are limited principally by the load carrying capacity, and therefore the internal structural configuration, of barge bows.

2. The AASHTO barge width modification factor $R_B = \left(B_B / 35\right)$, where B_B is the barge width in ft., was found to be inconsistent in comparison to data measured experimentally. For the width of the barge used in this study, $R_B = 1.41$. However, better agreement between experimentally measured data—both loads and crush depths—and corresponding AASHTO-computed values resulted when the width correction procedure was omitted (i.e., $R_B = 1.0$ was used) than when $R_B = 1.41$ was used.

3. Substantial levels of impact resistance can be generated by soil forces acting directly on surfaces of buried foundation elements such as pile caps and tremie seals. In one impact test discussed in this study (test P1T7), soil forces acting on the buried cap and tremie seal were determined to be larger in magnitude than the sum of shear forces generated at the pile heads, and thus greater than the summation of all soil forces acting on the piles.

4. Under rapidly applied impact loads, dynamic components of total soil stiffness can be as large as, or larger than, static components. For the specific combinations of soil conditions and impact energies considered in this study, dynamic soil resistance was found to be primarily associated with soil particle velocities (i.e., dynamic increases of soil stiffness were found to be velocity-dependent).

5. Embedment of piles within thick concrete pile caps and tremie seals produces flexural restraint at the pile heads that can significantly shorten the flexible length of the piles. Alterations of flexible length can result in changes of lateral pier stiffness, and therefore dynamic response to applied impact load.

6. Inertia forces, which are proportional to mass and acceleration, can have a significant influence on pier response to barge impact loads. Inertia forces in an impacted pier are mobilized more rapidly than are displacement-dependent (stiffness) or velocity-dependent (damping) resistance forces, and constitute the primary form of resistance mobilized during the early part of a collision event. However, once an impacted pier has accelerated and reached the point of maximum velocity, inertia forces transition from being a source of resistance to being a source of effective loading.

7. Static design loads specified in the AASHTO barge impact provisions for moderate to high energy impacts—defined here as impacts having kinetic energies in excess of approximately 300 kip-ft.—on stiff piers were found to be substantially larger than corresponding impact loads measured experimentally. Detailed numerical studies of one collision of this type (test P1T7) confirmed that static pier analysis using AASHTO-specified loads produced foundation design forces that were substantially larger than those computed via experimentally-validated dynamic pier analysis.

8. Static design loads specified in the AASHTO barge impact provisions for low-speed, low-energy impacts—typical of the "drifting barge" impact condition—on flexible piers were found to be smaller than the impact loads measured experimentally. Detailed numerical studies of two collisions of this type (tests P3T3 and B3T4) revealed, however, that static pier analysis using AASHTO-specified loads produced foundation design forces that were only marginally smaller than those computed via experimentally-validated dynamic pier analysis.

9. During barge impact loading of multiple-pier bridge structures, a portion of load imparted to the impacted pier may be transferred ("shed") through the superstructure to adjacent piers. For the highest energy multiple-pier barge impact test conducted in this study (test B3T4), the applied collision load maximized at 328 kips. Using dynamic numerical analysis techniques, the peak load transferred from the pier to the superstructure through the bridge bearings was estimated to be 130 kips, or 40% of the applied load. However, as is the case for pier inertia forces, superstructure forces transition from being a source of resistance to being a source of loading once sufficient acceleration has occurred.

10. Superstructure resistance force acting at the top of an impacted pier is a combination of static displacement-dependent stiffness force and dynamic mass-dependent inertia force. Although the latter acts only momentarily, it can produce a short-term increase in superstructure-induced restraint at the top of the pier that can cause substantial dynamic amplifications of pier column design forces. Failure to account for the combination of static and dynamic superstructure restraint at the top of a pier may result in the determination of significantly unconservative column design forces.

11. If static design forces are to be used for vessel collision design of bridge components, as is typical in current design practice, then the effects of dynamic collision phenomena such as inertia, soil damping, and dynamic restraint require that the static loads stipulated by design specifications be set at sufficiently high levels so as to envelope dynamic force effects. Enveloping dynamic effects in this manner may, however, lead to non-uniformity in the level of safety that is present in various structural components of a pier.

11.2 Recommendations

11.2.1 Development of updated vessel-collision design provisions

1. Impact load data collected at St. George Island correspond to collision locations near the barge mid-bow. Stiffness characteristics of corner regions of barge bows should be investigated, using either experimental or numerical procedures, to determine if elevated impact forces would be generated by collisions at such locations.

2. A review of structural configurations typically used in the bow sections of barges should, if feasible, be conducted. Possible impediments to conducting such a review relate to the proprietary nature of most barge designs. Information of value from such a review would include representative spacings and structural stiffnesses of internal stiffening frames used in barge construction. These parameters directly influence the maximum impact loads that can be generated during a collision.

3. Data obtained from dynamic simulations involving varying types of barges colliding with bridge piers should be used to develop an updated expression for the barge width modification factor R_B presently contained in the AASHTO provisions. The new expression should be based, at least in part, on pier column cross-sectional geometry and typical internal stiffening frame spacings within barges.

4. The database of information generated in this study should be expanded by conducting a numerically-based parametric study in which a wider variety of pier configurations, barge types, and impact energies are considered. Updated vessel-collision bridge design provisions should then be developed by merging the parametric analysis results together with data collected in the present study and data available in the literature. It is recommended that the new provisions be structured in a multi-level format that permits designers to choose from one of the following approaches:

   Equivalent-static method (currently being developed using FDOT research funding)

   A static force approach similar in complexity to the current AASHTO provisions, but with updated expressions that produce improved-accuracy load predictions for a wider variety of impact conditions. Calculation of barge crush depth, an intermediate step in the current AASHTO provisions, should be considered for elimination. Instead, expressions predicting static design load directly from parameters such as barge kinetic energy or barge momentum should be developed. Static load levels should be established such that they produce member design forces equal to or greater than those produced by dynamic analysis of equivalent impact conditions.

   Applied-dynamic method (currently being developed using FDOT research funding)

   A dynamic time-history analysis approach in which design provisions would guide the engineer through the process of constructing a simplified (e.g., piecewise-linear) time-varying loading function. Dynamic analysis of the structure subjected to application of the simplified loading function would then be performed to quantify

member design forces. Parameters such as barge kinetic energy, momentum, pier stiffness, pier mass, etc. would be used to establish the specific form of the simplified loading function.

Coupled-dynamic method (currently being developed using FDOT research funding)

A dynamic time-history analysis approach in which a simplified dynamic barge flotilla model is coupled to a dynamic model of pier and soil behavior. Member design forces for pier elements would be computed based on a dynamic analysis of coupled interaction between barge, pier, and soil. Guidance regarding barge characteristics such as bow crushing stiffness would be included in the design provisions.

Alternative methods

Methods based on physical experimentation, advanced numerical modeling, or both, that are capable of matching or exceeding the accuracy levels associated with the methods cited above.

11.2.2 Bridge modeling and analysis

1. Software packages intended for use in vessel collision pier analysis (such as FB-MultiPier) should include features capable of representing static (displacement-dependent) and dynamic (velocity-dependent) soil resistance forces that act on buried pile caps and tremie seals. Such features should account for the fact that soil resistance forces do not act on pile nodes inside the cap and seal volume.

2. Software packages intended for use in vessel collision pier analysis should include features capable of representing the effects of pile cap and tremie seal thickness on pile stiffness and pier mass. Such features should account for fixity of pile elements within the cap and seal thickness, mass of concrete contained within the cap and seal, and absence of soil within the volume defined by the cap and seal boundaries.

3. Simplified and robust models of nonlinear barge crushing and dynamic barge-pier interaction (coupling) should be added to vessel collision pier analysis software packages to facilitate bridge pier design based on the “coupled-dynamic” analysis method proposed above.

11.2.3 Characterization of soil forces

1. Research targeted at experimentally quantifying soil coefficients for use in velocity-dependent models of soil damping force should be undertaken.

2. Research targeted at experimentally quantifying frictional and passive soil resistance forces that act on buried foundation elements should be undertaken.

REFERENCES

AASHTO (1991), *Guide Specification and Commentary for Vessel Collision Design of Highway Bridges*, American Association of State Highway and Transportation Officials, Washington, D.C.

AASHTO (1994), *LRFD Bridge Design Specifications and Commentary*, American Association of State Highway and Transportation Officials, Washington, D.C.

Brown, D.A., O'Neill, M.W., Hoit, M., McVay, M.C., El Naggar, M.H., Chakraborty, S. (2001), *Static and Dynamic Lateral Loading of Pile Groups*, NCHRP Report No. 461, Washington D.C.

Arroyo, J.R., Ebeling R.M., and Barker B.C. (2003), Analysis of Impact Loads from Full-Scale Low-Velocity, Controlled Barge Impact Experiments, December 1998. ERDC/ITL TR-03-3, US Army Corps of Engineers, 2003.

Consolazio, G.R., and D.R. Cowan (2003), "Nonlinear Analysis of Barge Crush Behavior and Its Relationship to Impact Resistant Bridge Design", *Computers and Structures*, Vol. 81, Nos. 8-11, pp. 547-557.

Consolazio, G.R., and D.R. Cowan (2005), "Numerically Efficient Dynamic Analysis of Barge Collisions with Bridge Piers", *ASCE Journal of Structural Engineering*, ASCE, Vol. 131, No. 8, pp. 1256-1266.

FB-MultiPier (2005), *FB-MultiPier User's Manual*. Florida Bridge Software Institute, University of Florida, Gainesville, Florida.

Goble G., Schulz J., and Commander B. (1990), *Lock and Dam #26 Field Test Report for The Army Corps of Engineers*, Bridge Diagnostics Inc., Boulder, CO.

Knott, M., Prucz, Z. (2000), Vessel Collision Design of Bridges: Bridge Engineering Handbook, CRC Press LLC.

Larsen, O.D. (1993), Ship Collision with Bridges: The Interaction between Vessel Traffic and Bridge Structures, IABSE Structural Engineering Document 4, IASBE-AIPC-IVBH, Zurich, Switzerland.

LS-DYNA (2003), *LS-DYNA Keyword User's Manual: Version 970*, Livermore Software Technology Corporation, Livermore, CA.

McVay, M.C., O'Brien, M., Townsend, F.C., Bloomquist, D.G., and Caliendo, J.A. (1989), "Numerical Analysis of Vertically Loaded Pile Groups", ASCE, Foundation Engineering Congress, Northwestern University, Illinois, July, 1989, pp. 675-690.

McVay, M.C., Wasman, S.J., Bullock, P.J. (2005), St. George Geotechnical Investigation of Vessel Pier Impact, Engineering and Industrial Experiment Station, University of Florida, Gainesville, Florida.

Meier-Dörnberg, K.E. (1983), *Ship Collisions, Safety Zones, and Loading Assumptions for Structures in Inland Waterways*, Verein Deutscher Ingenieure (Association of German Engineers) Report No. 496, 1983, pp. 1-9.

Minorsky, V.U. (1959), "An Analysis of Ship Collisions with Reference to Protection of Nuclear Power Plants", *Journal of Ship Research*, Vol. 3, pp. 1-4.

Mokwa, R.L. (1999), *Investigation of the Resistance of Pile Caps to Lateral Loading*, Ph.D. Dissertation, Virginia Polytechnic Institute and State University, Blacksburg, Virginia.

Patev, R.C. and Barker, B.C. (2003). Prototype Barge Impact Experiments, Allegheny Lock and Dam 2, Pittsburgh, Pennsylvania. ERDC/ITL TR-03-2, US Army Corps of Engineers.

Woisin, G. "The Collision Tests of the GKSS." *Jahrbuch der Schiffbautechnischen Gesellschaft*, Vol. 70, pp. 465-487, Berlin.

APPENDIX A
MEASURED IMPACT LOADS

Concrete impact blocks and bi-axial clevis-pin load cells were used to measure the impact loads imparted to the test piers during the barge impact tests. On the following pages, time histories of the experimentally recorded horizontal and vertical impact loads are presented. The sign convention used in the time-history load plots is indicated in Figure A.1. All data have been time-shifted such that the origin of the time axis (t = 0 sec.) corresponds to the time at which initial contact between the barge and pier occurred.

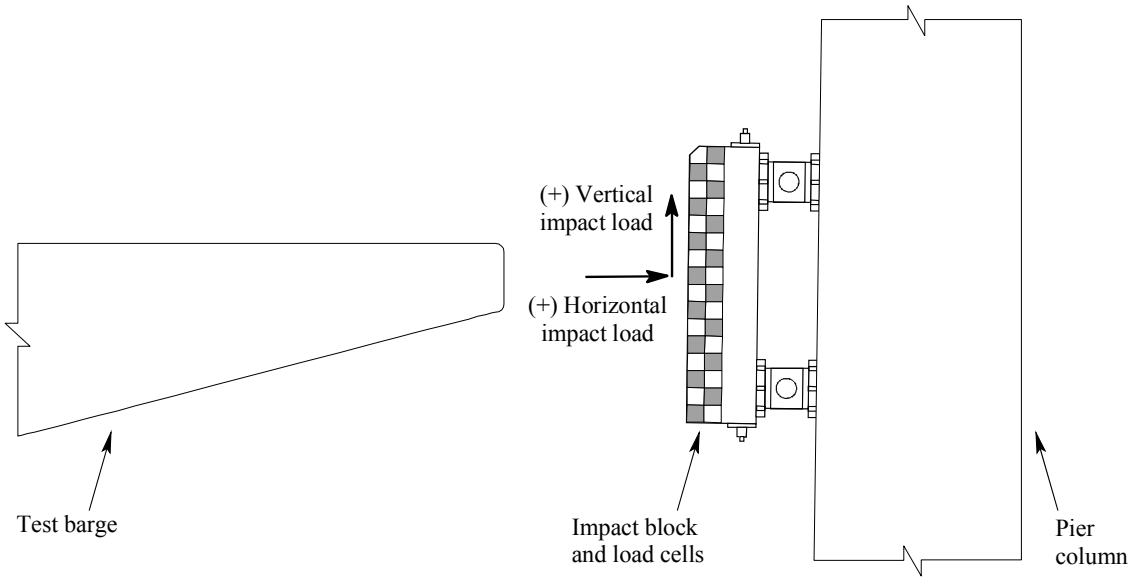

Figure A.1. Sign convention for horizontal and vertical impact loads

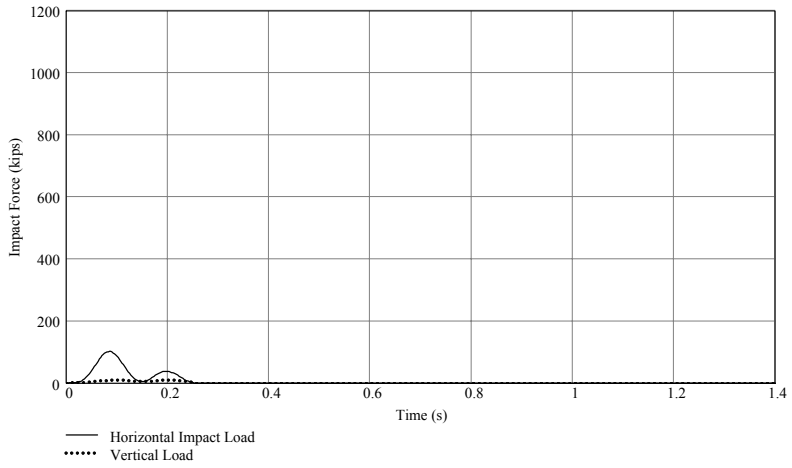

Figure A.2. Experiment P1T1

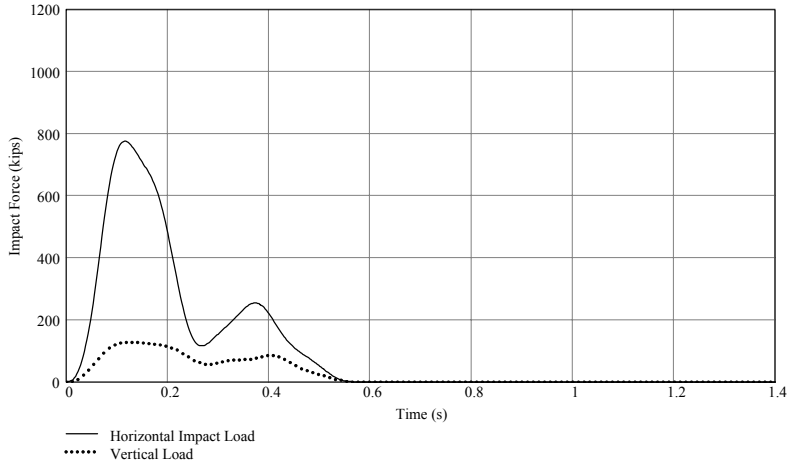

Figure A.3. Experiment P1T3

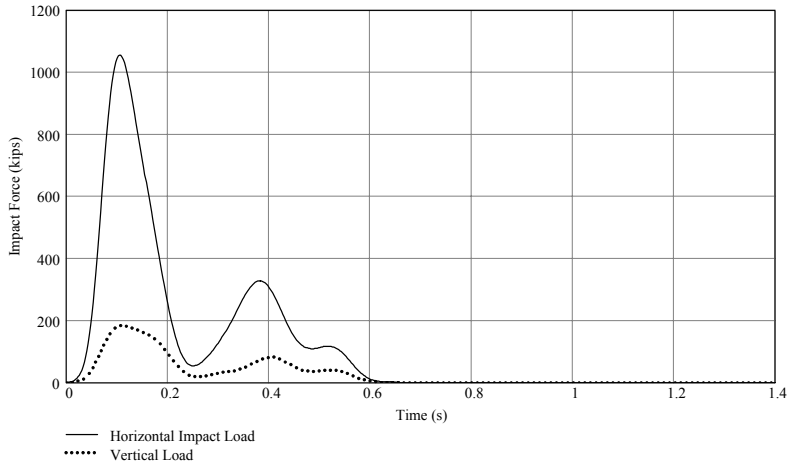

Figure A.4. Experiment P1T4

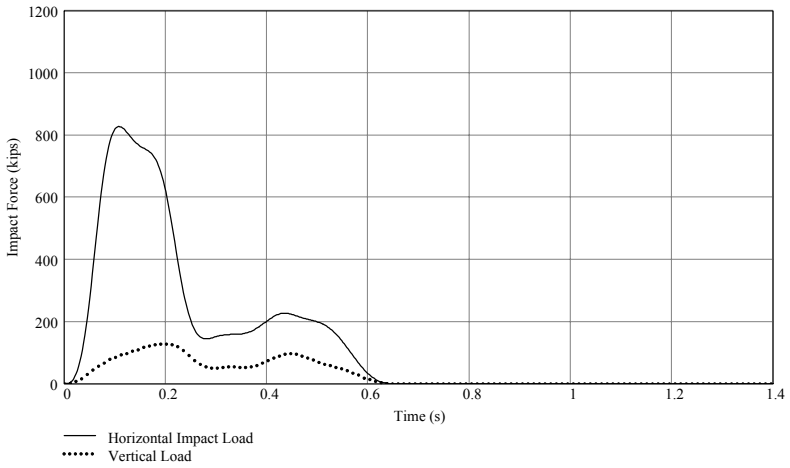

Figure A.5. Experiment P1T5

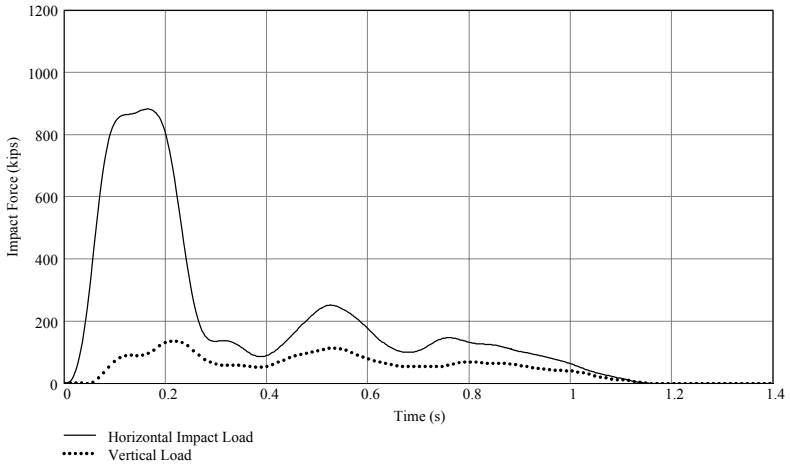

Figure A.6. Experiment P1T6

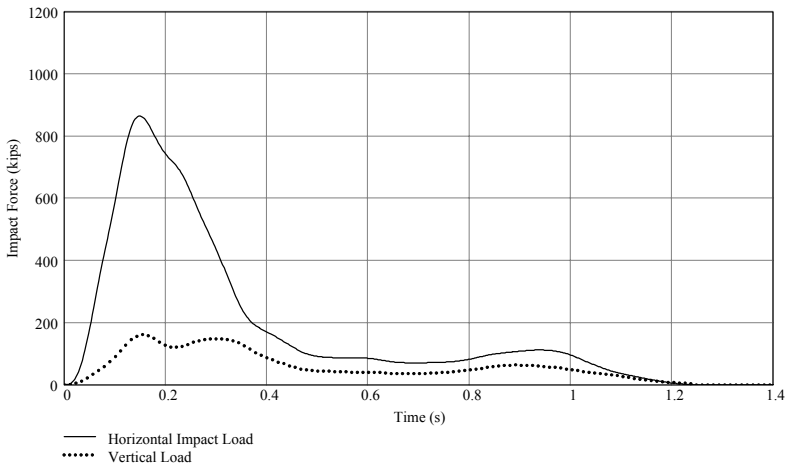

Figure A.7. Experiment P1T7

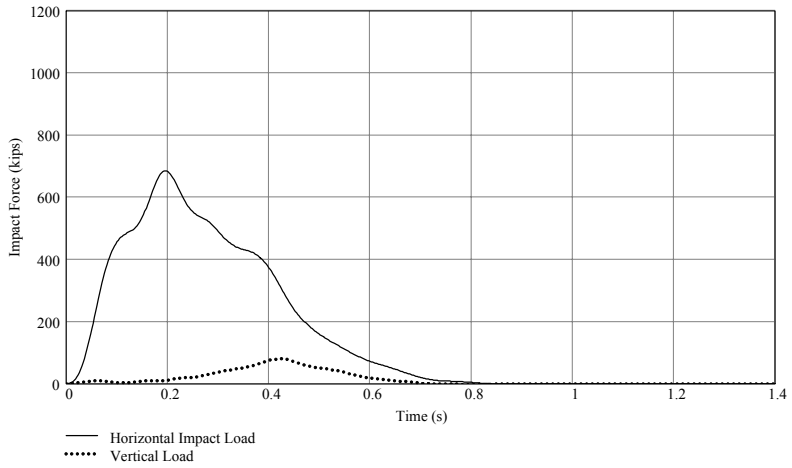

Figure A.8. Experiment P1T8

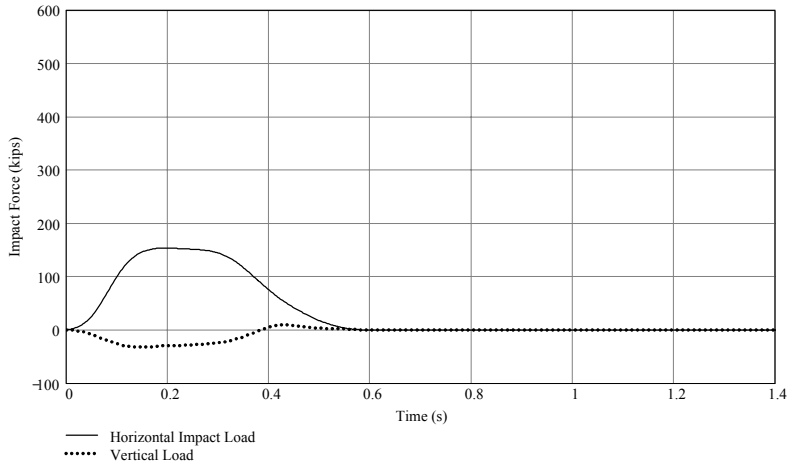

Figure A.9. Experiment B3T1

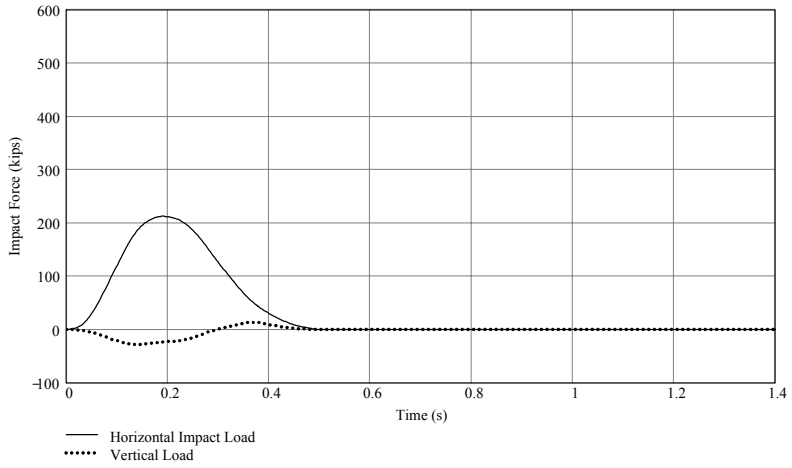

Figure A.10. Experiment B3T2

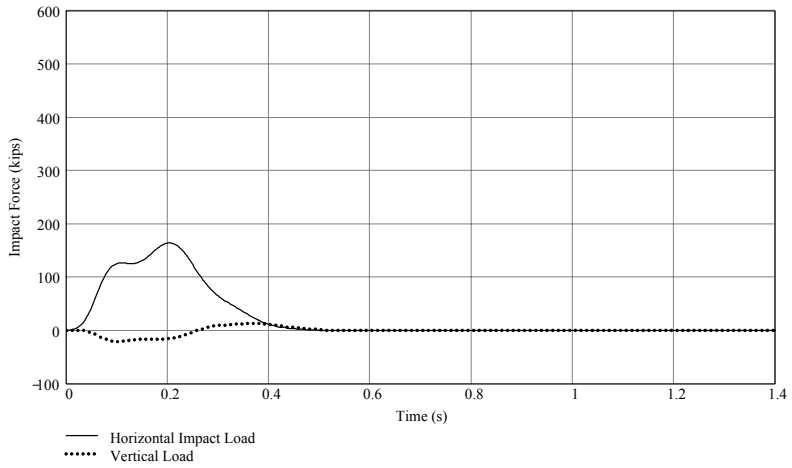

Figure A.11. Experiment B3T3

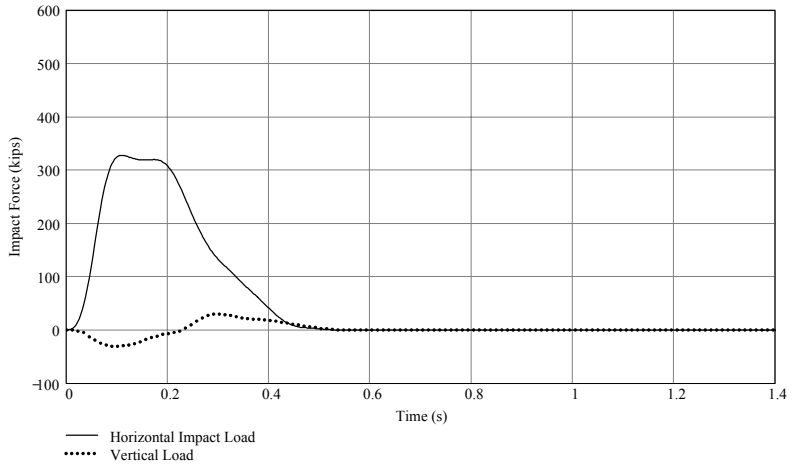

Figure A.12. Experiment B3T4

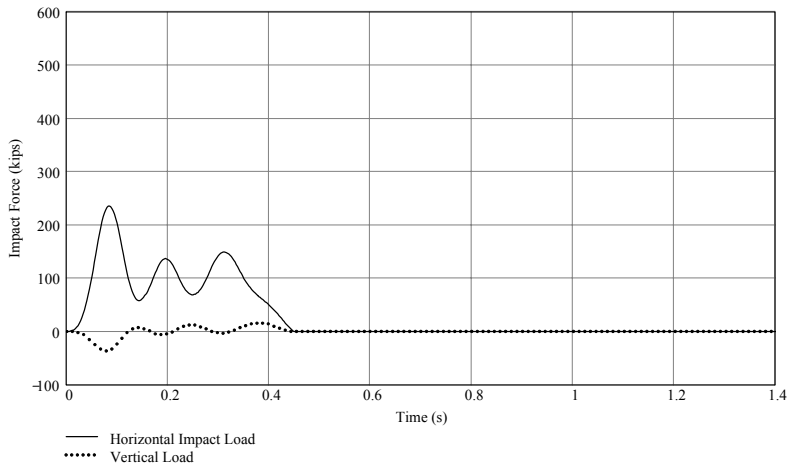

Figure A.13. Experiment P3T1

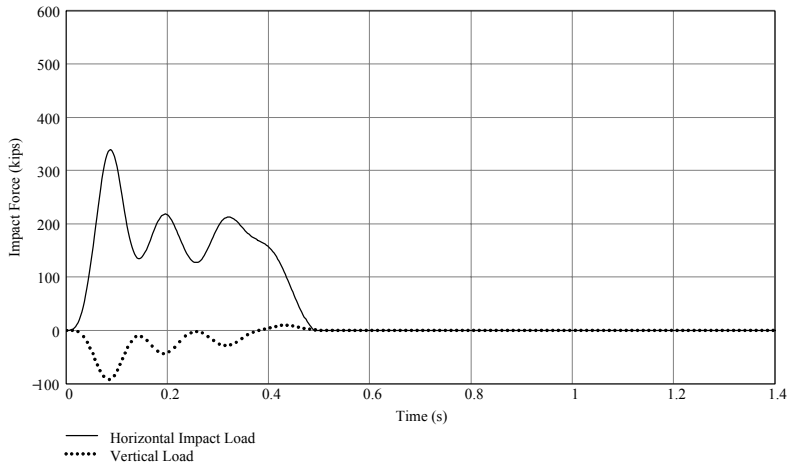

Figure A.14. Experiment P3T2

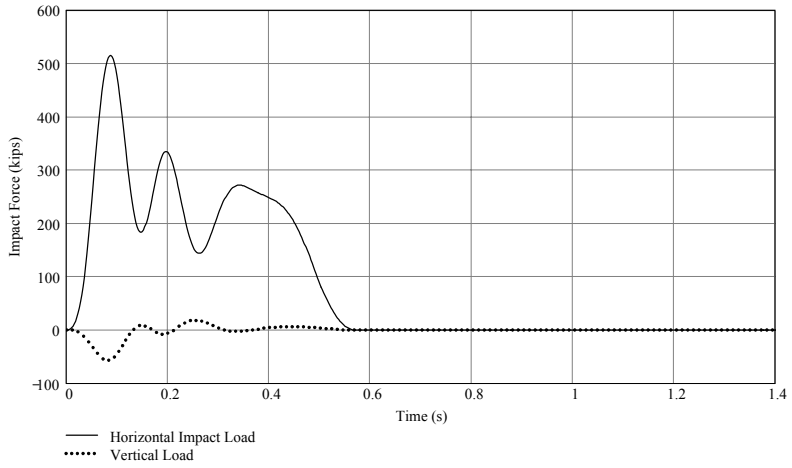

Figure A.15. Experiment P3T3

APPENDIX B
MEASURED PIER ACCELERATIONS

Uniaxial accelerometers were installed at multiple locations on the test piers to record accelerations in global X, Y, and Z directions (Figure B.1) during the impact tests. On the following pages, time histories of X, Y, and Z accelerations are presented. All data have been time-shifted such that the origin of the time axis (t = 0 sec.) corresponds to the time at which initial contact between the barge and pier occurred. During the experimental tests, accelerations were collected at a sampling rate of 2000 Hz. For purposes of presenting the results here, a low-pass 60 Hz noise removal filter has been applied to the data.

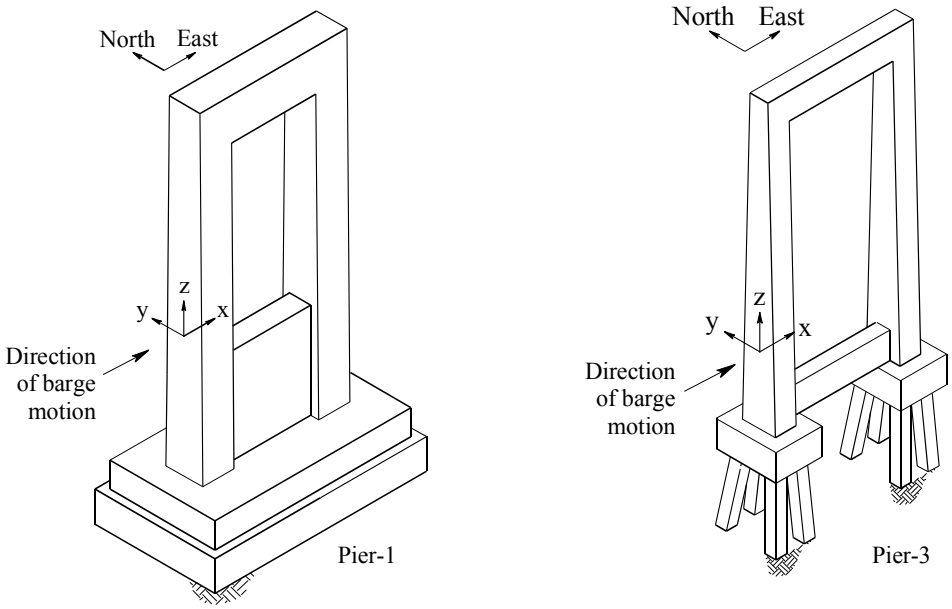

Figure B.1. Global X, Y, and Z directions for Pier-1 and Pier-3

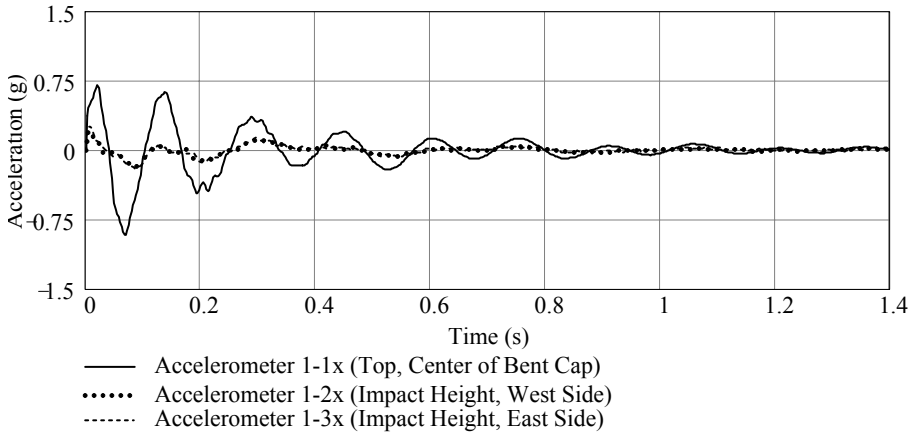

Figure B.2. Experiment P1T1, X-direction

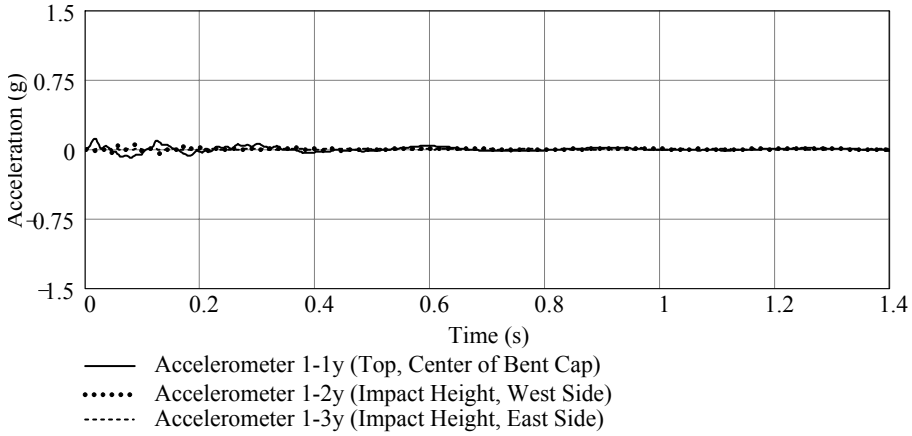

Figure B.3. Experiment P1T1, Y-direction

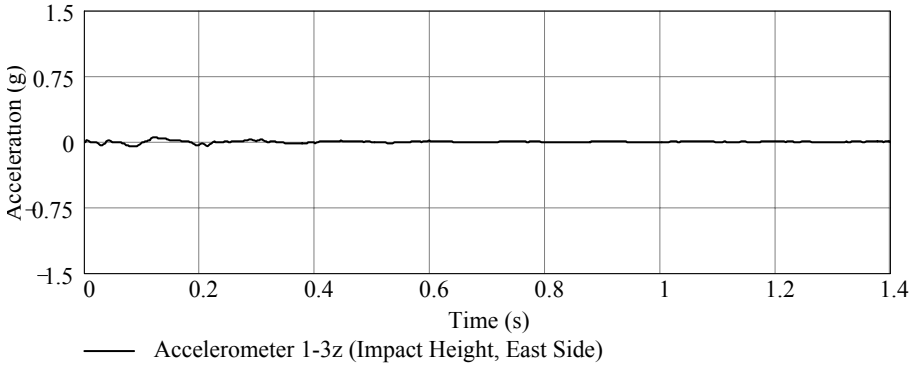

Figure B.4. Experiment P1T1, Z-direction

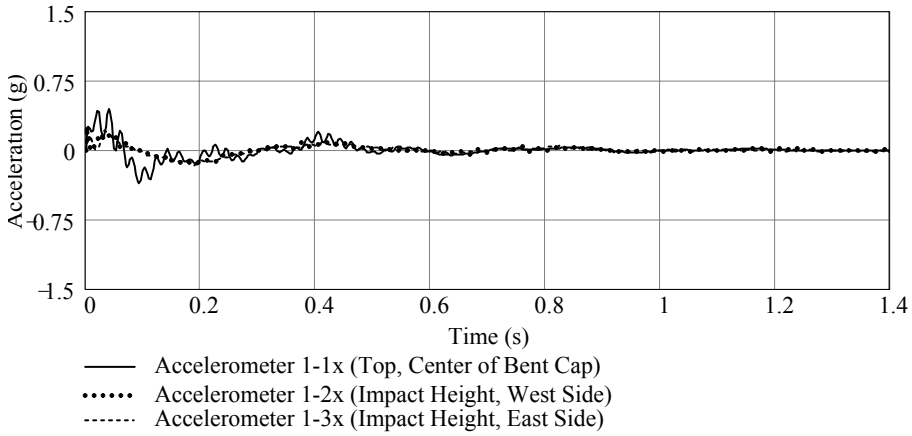

Figure B.5. Experiment P1T3, X-direction

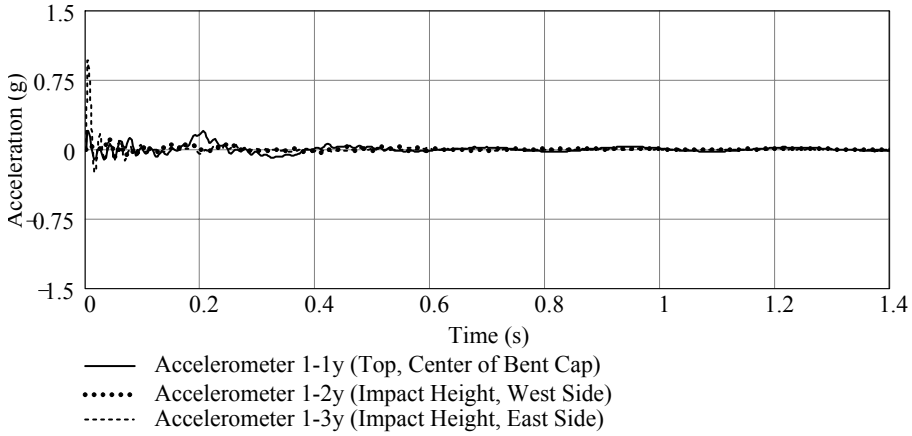

Figure B.6. Experiment P1T3, Y-direction

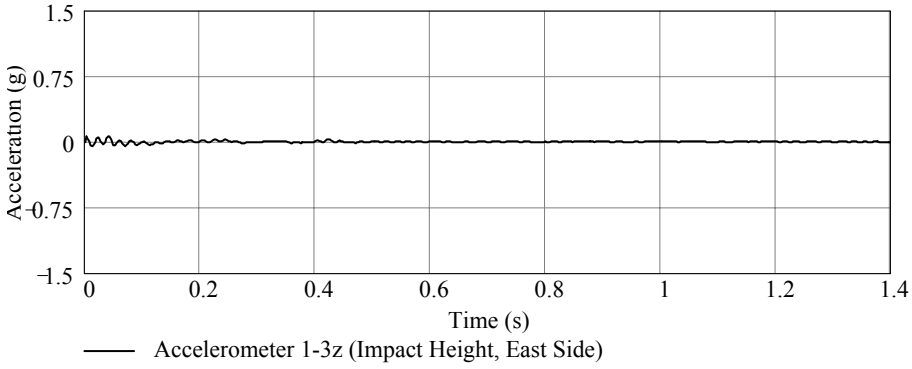

Figure B.7. Experiment P1T3, Z-direction

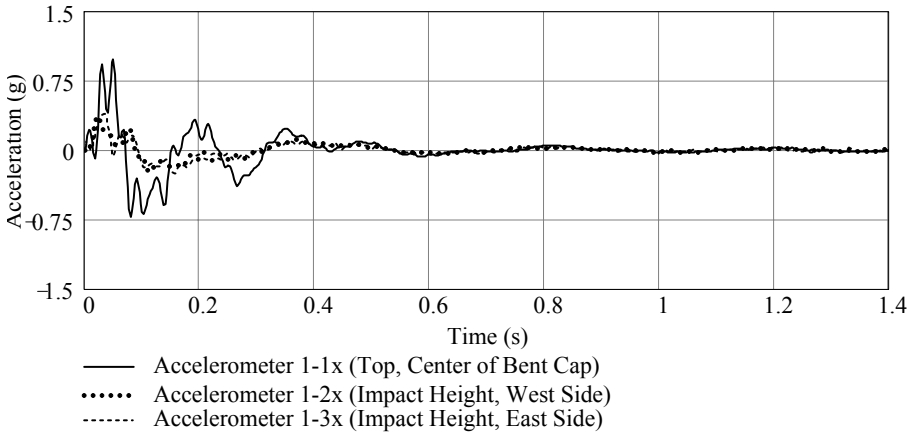

Figure B.8. Experiment P1T4, X-direction

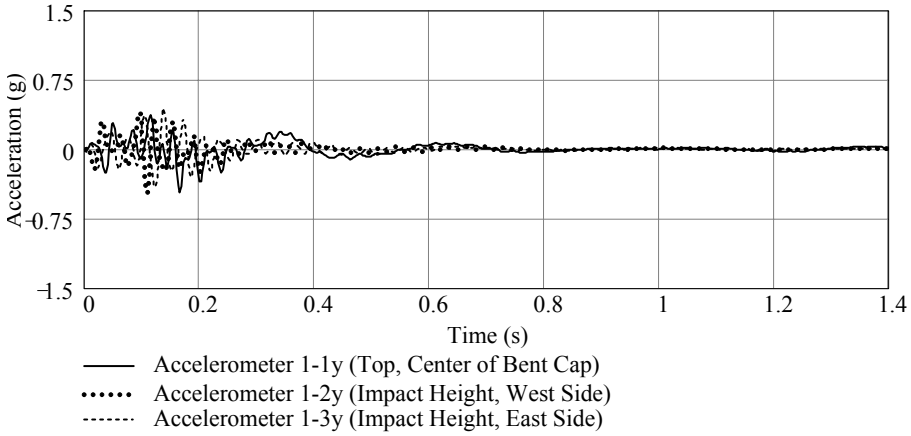

Figure B.9. Experiment P1T4, Y-direction

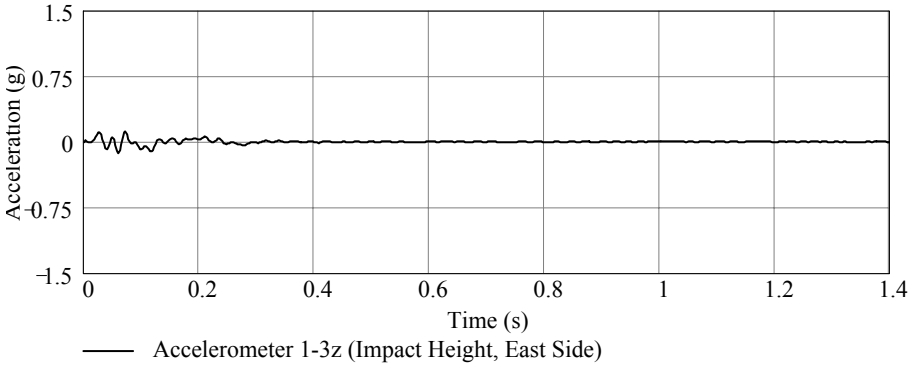

Figure B.10. Experiment P1T4, Z-direction

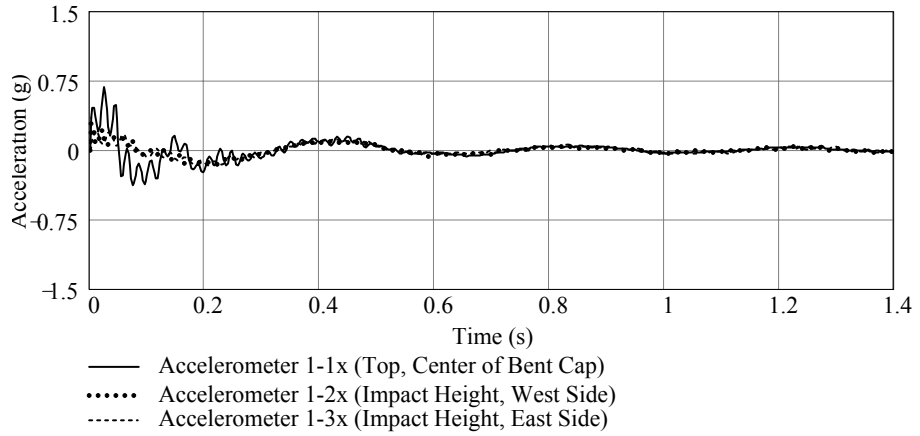

Figure B.11. Experiment P1T5, X-direction

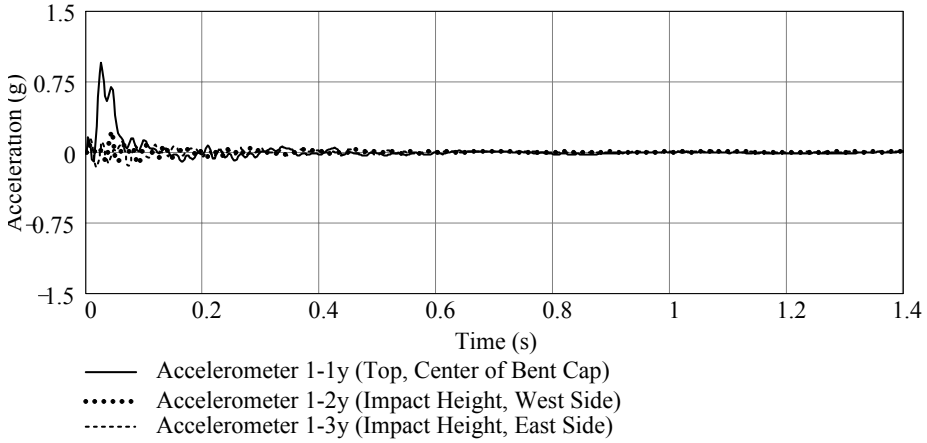

Figure B.12. Experiment P1T5, Y-direction

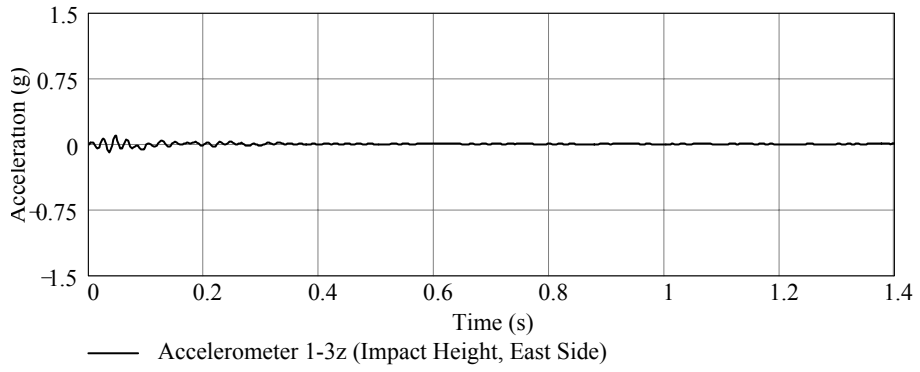

Figure B.13. Experiment P1T5, Z-direction

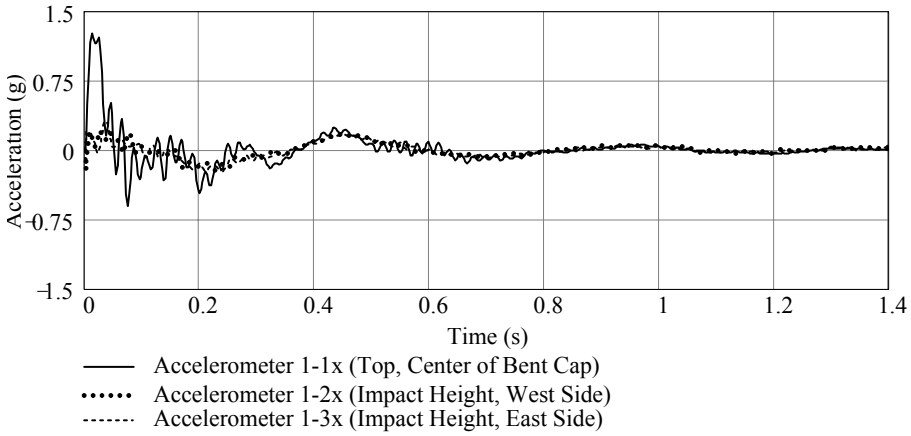

Figure B.14. Experiment P1T6, X-direction

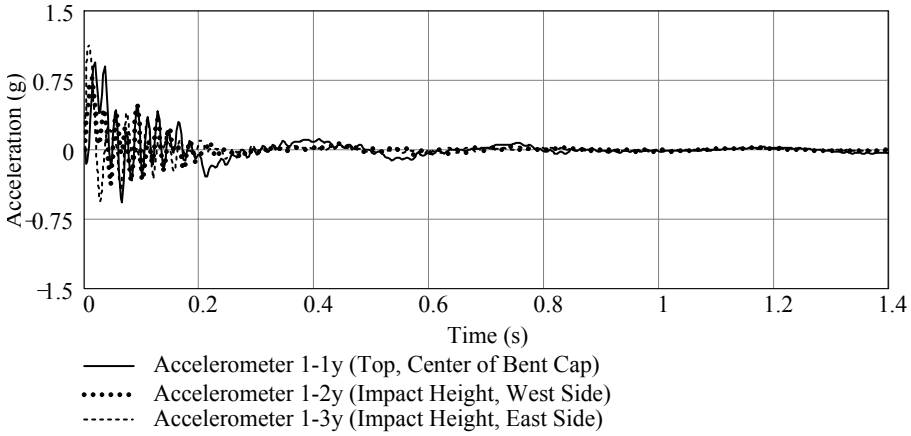

Figure B.15. Experiment P1T6, Y-direction

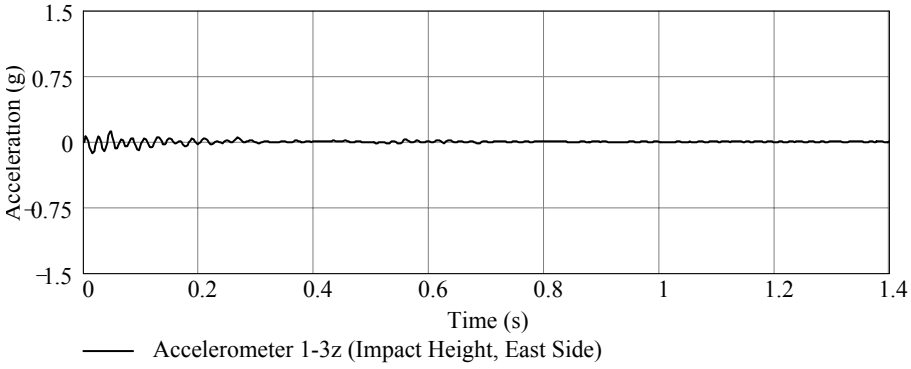

Figure B.16. Experiment P1T6, Z-direction

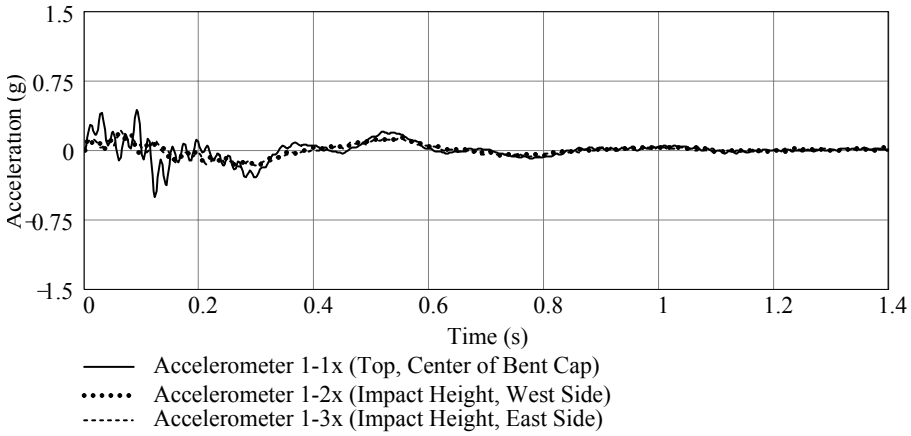

Figure B.17. Experiment P1T7, X-direction

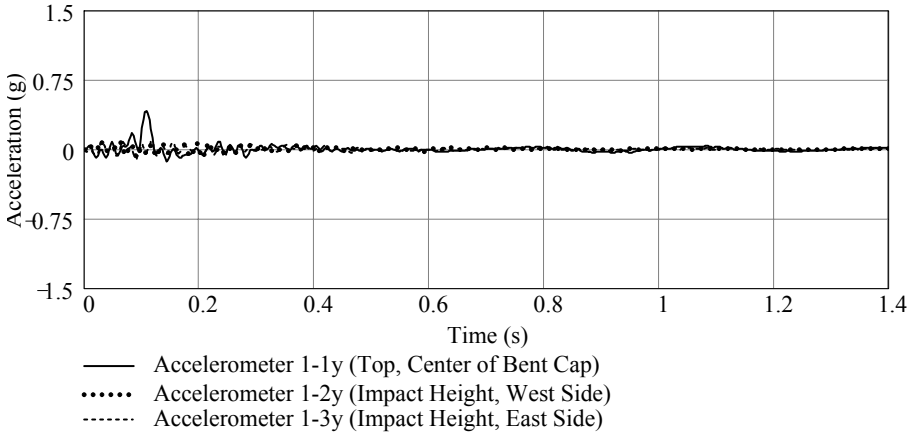

Figure B.18. Experiment P1T7, Y-direction

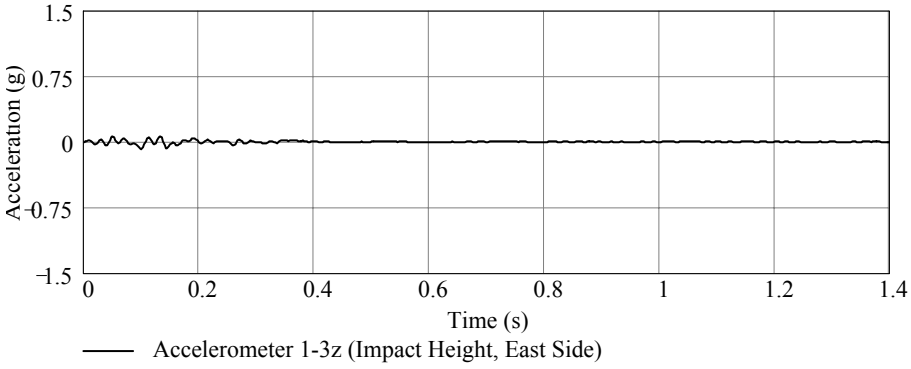

Figure B.19. Experiment P1T7, Z-direction

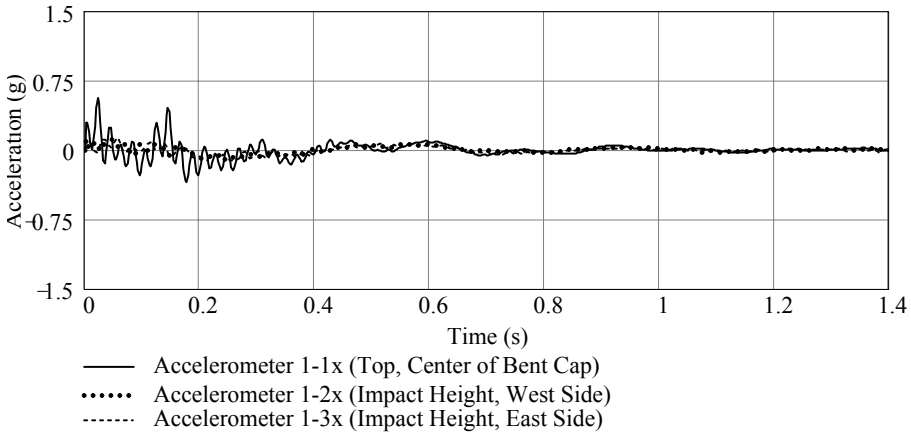

Figure B.20. Experiment P1T8, X-direction

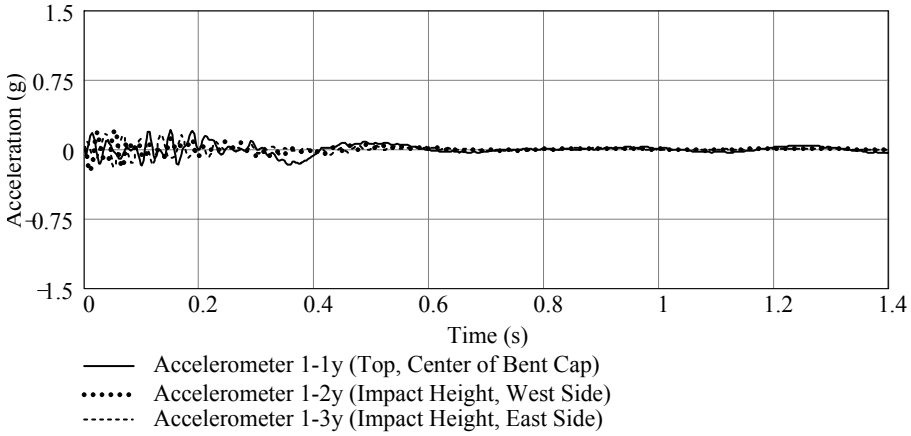

Figure B.21. Experiment P1T8, Y-direction

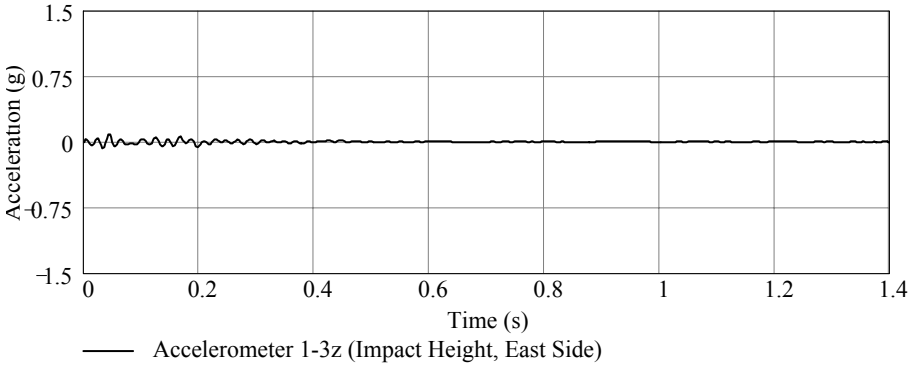

Figure B.22. Experiment P1T8, Z-direction

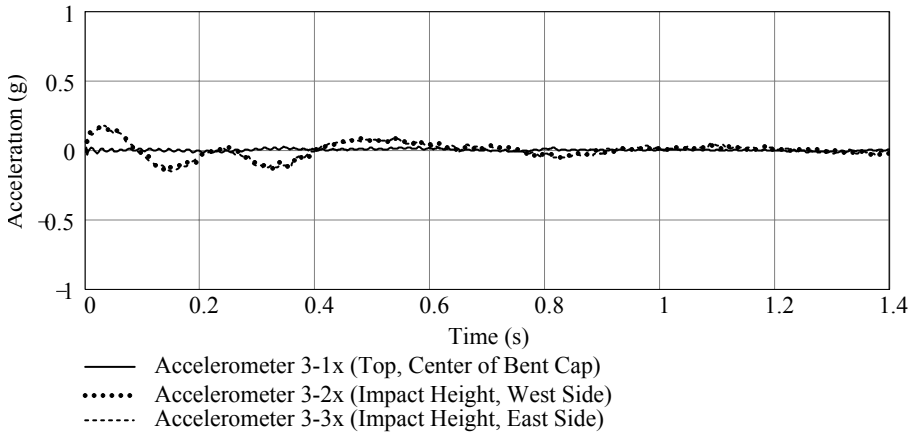

Figure B.23. Experiment B3T1, X-direction

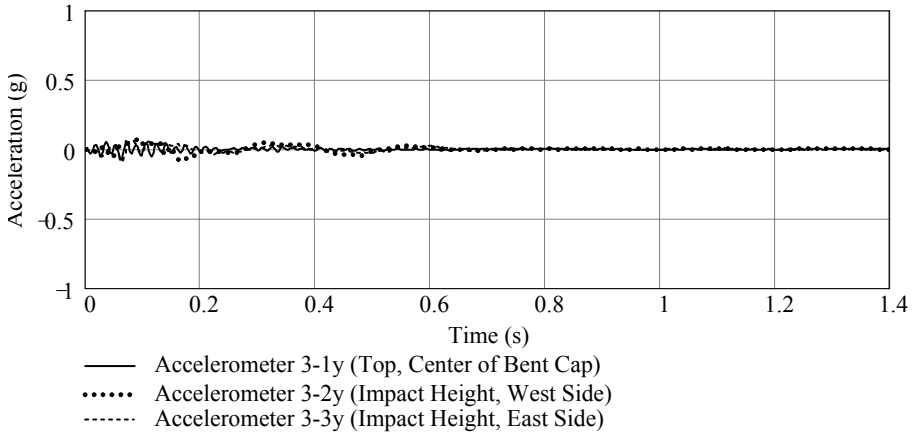

Figure B.24. Experiment B3T1, Y-direction

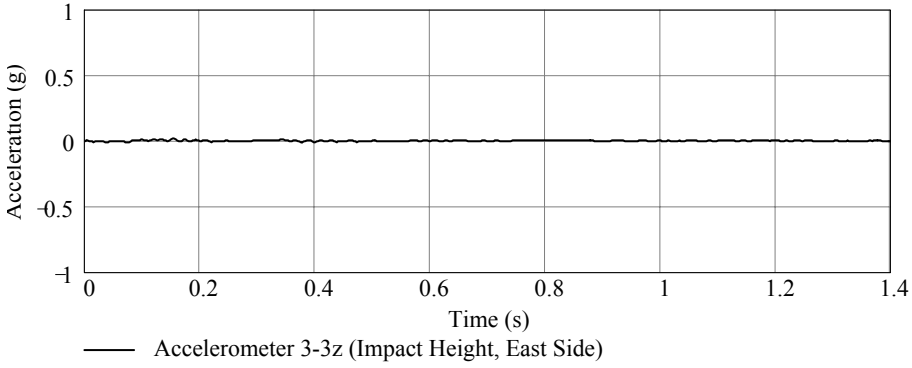

Figure B.25. Experiment B3T1, Z-direction

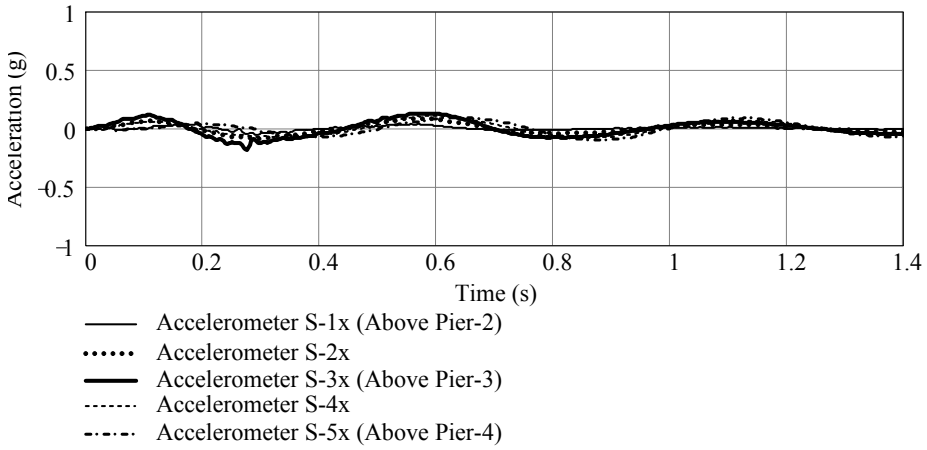

Figure B.26. Experiment B3T1, X-direction, superstructure

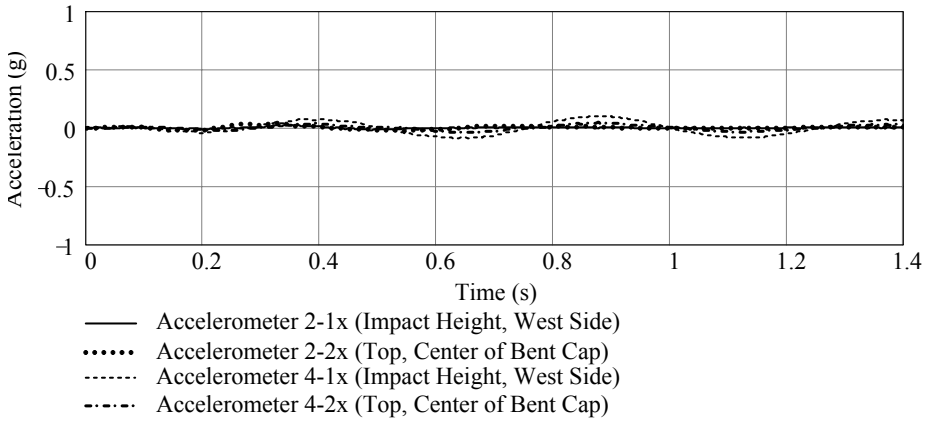

Figure B.27. Experiment B3T1, X-direction, Pier-2 and Pier-4

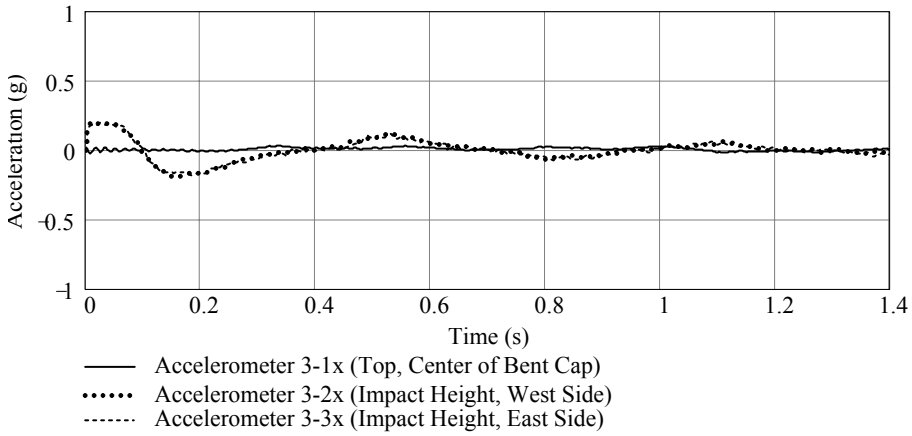

Figure B.28. Experiment B3T2, X-direction

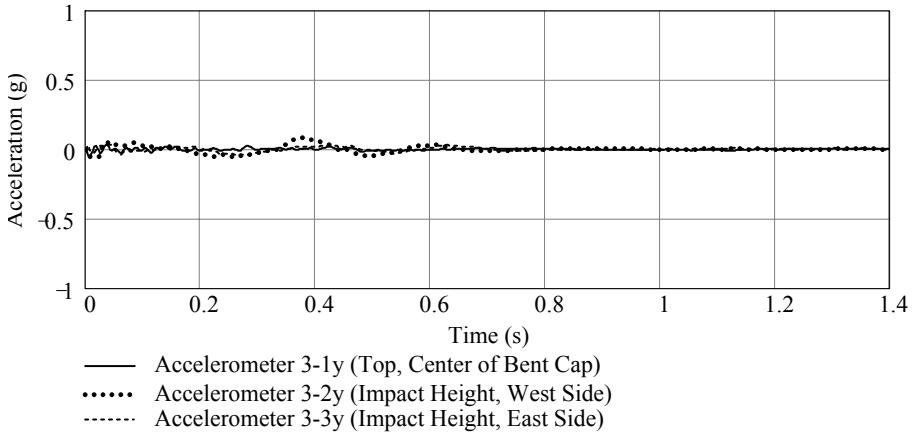

Figure B.29. Experiment B3T2, Y-direction

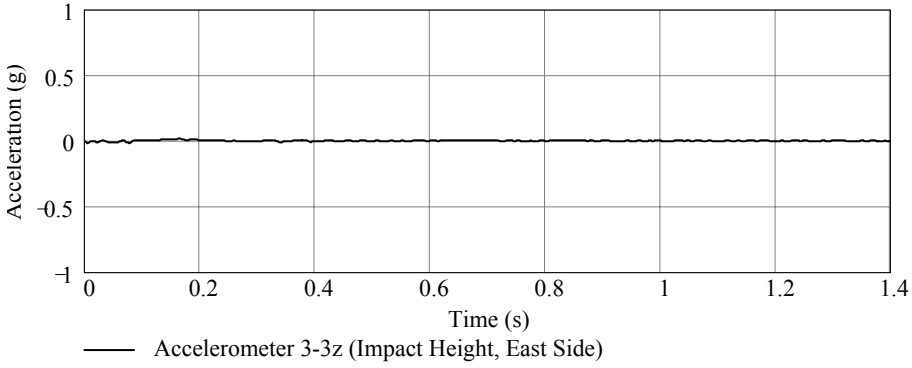

Figure B.30. Experiment B3T2, Z-direction

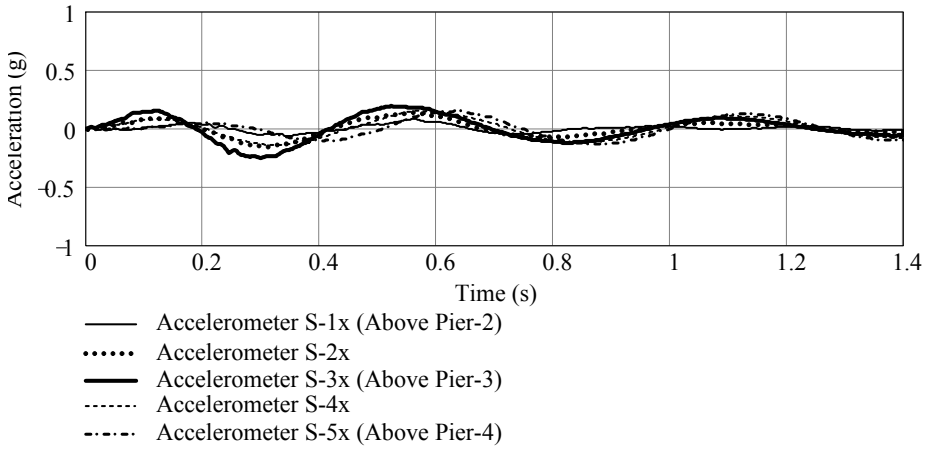

Figure B.31. Experiment B3T2, X-direction, superstructure

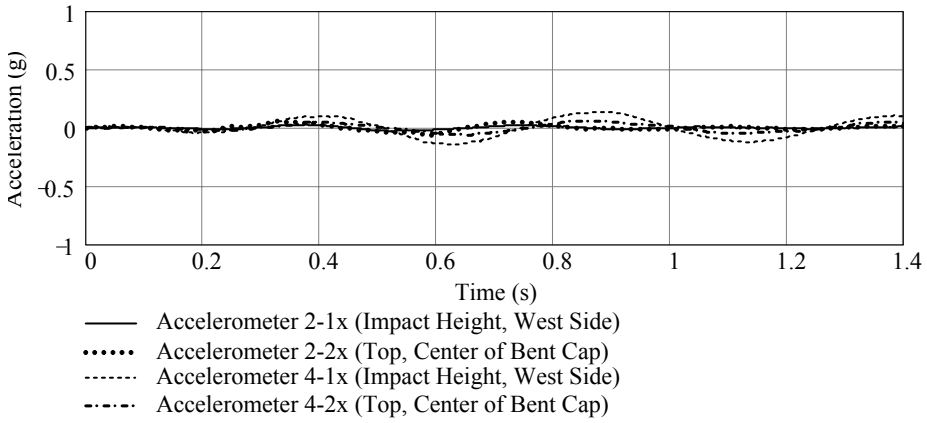

Figure B.32. Experiment B3T2, X-direction, Pier-2 and Pier-4

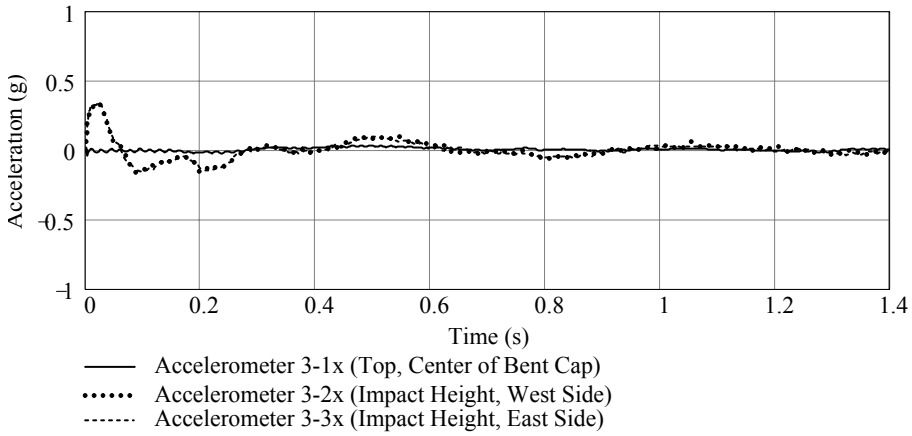

Figure B.33. Experiment B3T3, X-direction

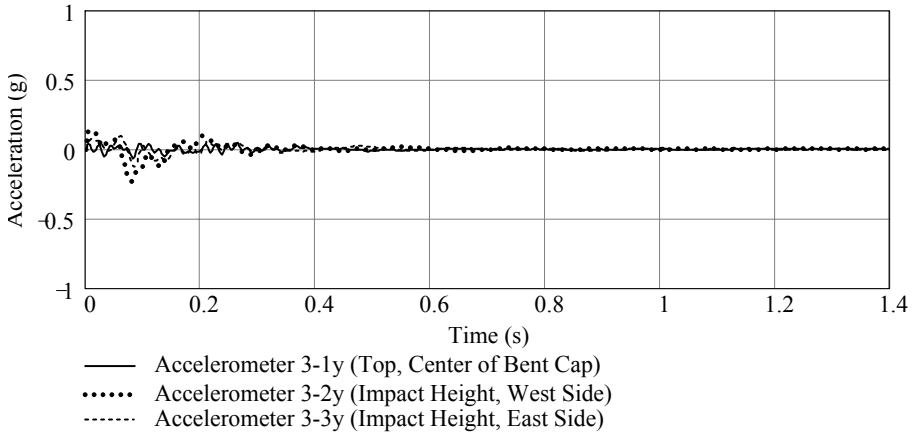

Figure B.34. Experiment B3T3, Y-direction

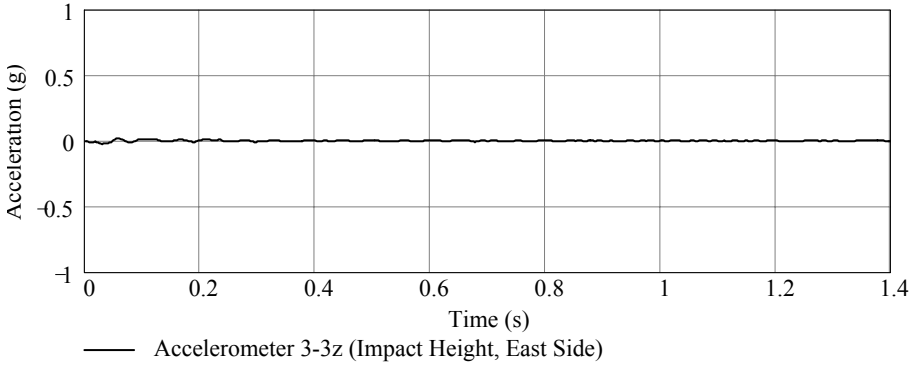

Figure B.35. Experiment B3T3, Z-direction

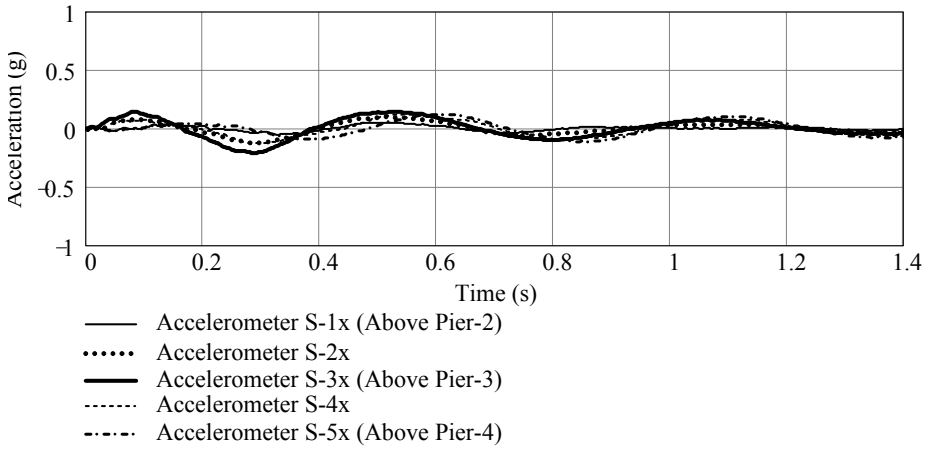

Figure B.36. Experiment B3T3, X-direction, superstructure

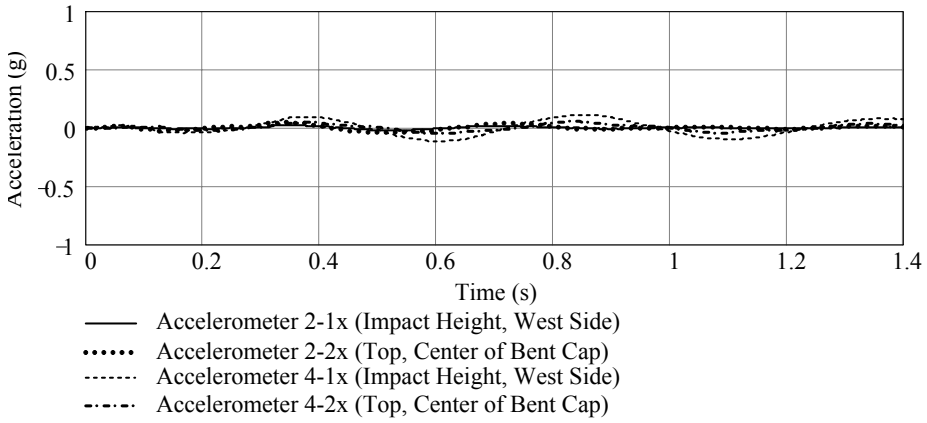

Figure B.37. Experiment B3T3, X-direction, Pier-2 and Pier-4

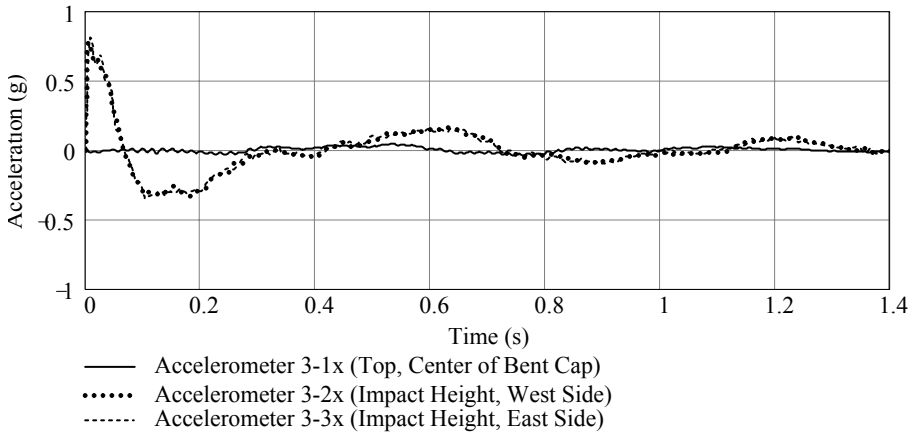

Figure B.38. Experiment B3T4, X-direction

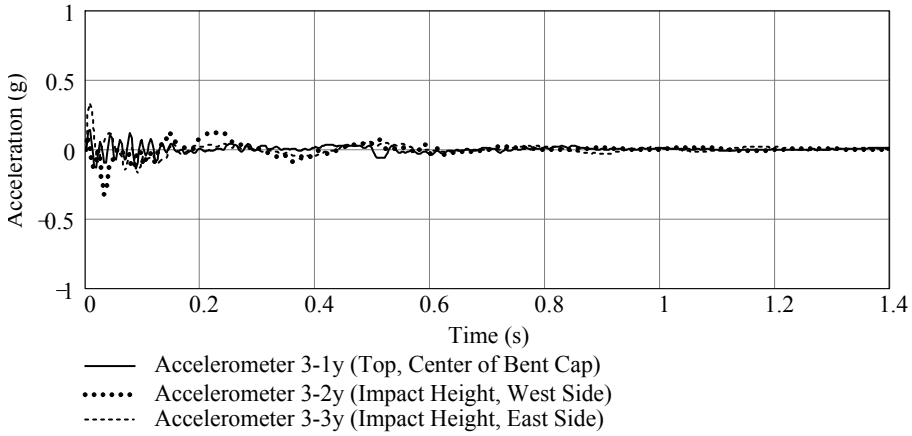

Figure B.39. Experiment B3T4, Y-direction

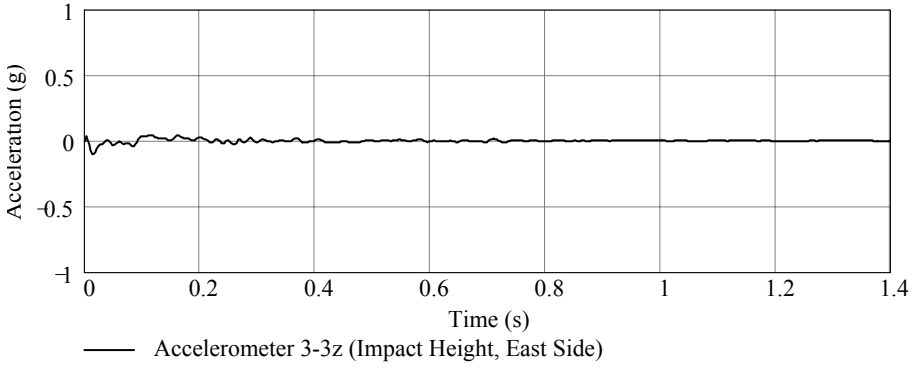

Figure B.40. Experiment B3T4, Z-direction

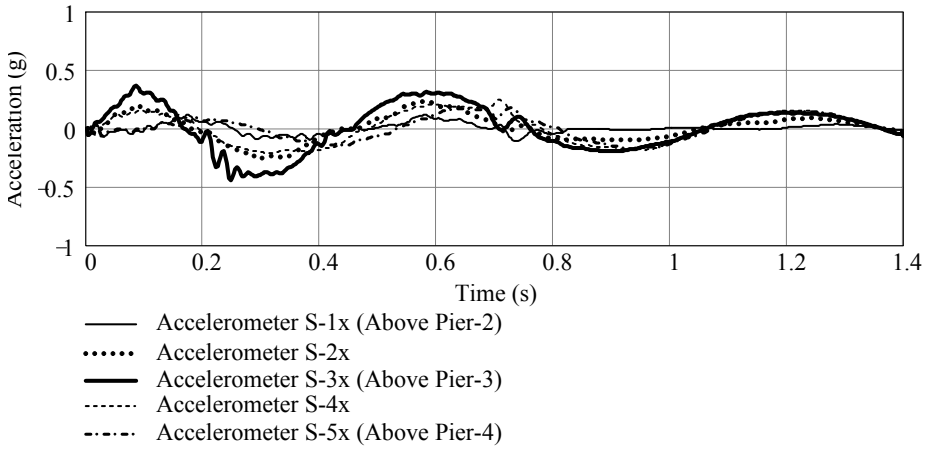

Figure B.41. Experiment B3T4, X-direction, superstructure

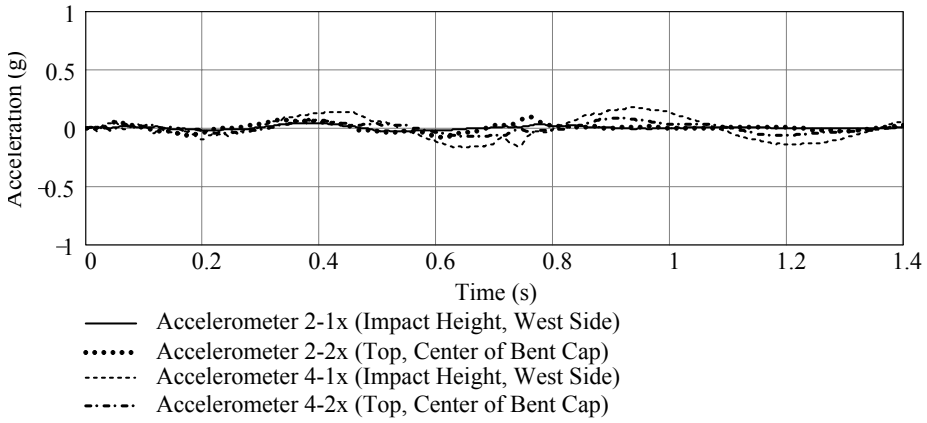

Figure B.42. Experiment B3T4, X-direction, Pier-2 and Pier-4

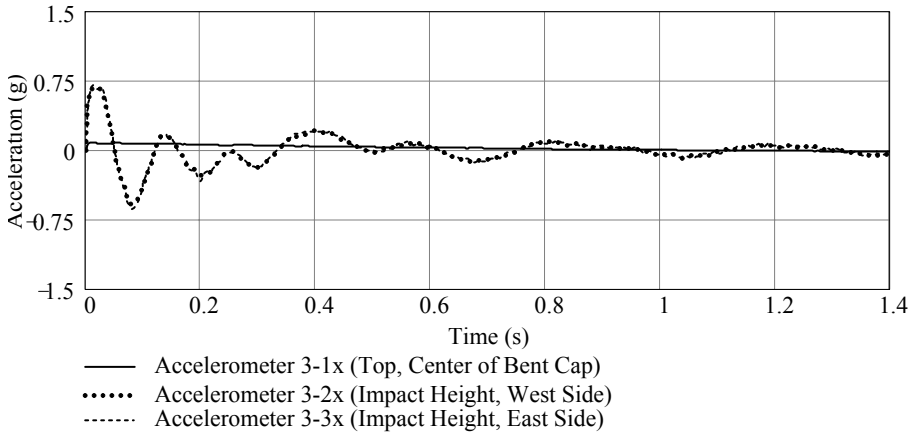

Figure B.43. Experiment P3T1, X-direction

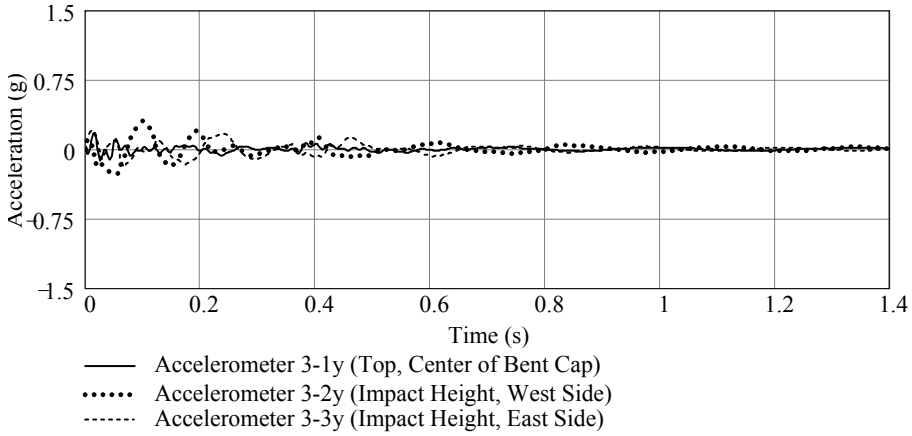

Figure B.44. Experiment P3T1, Y-direction

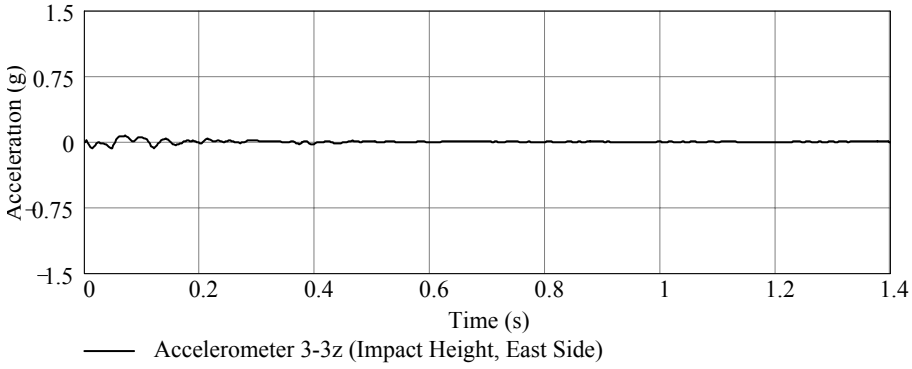

Figure B.45. Experiment P3T1, Z-direction

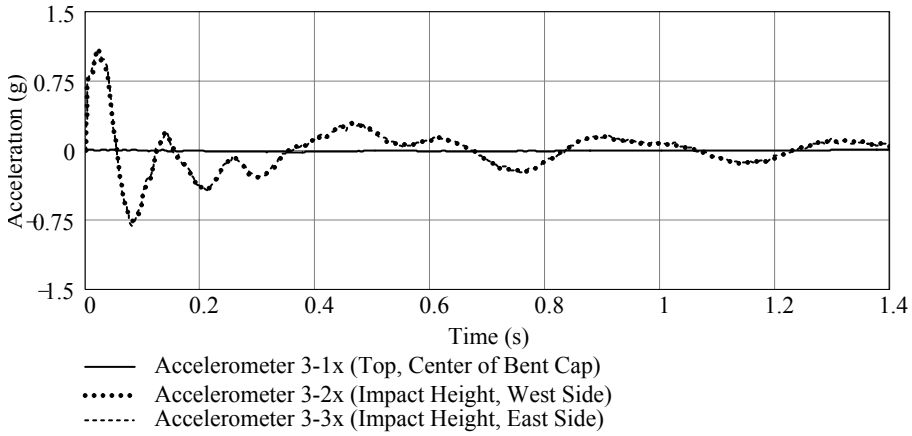

Figure B.46. Experiment P3T2, X-direction

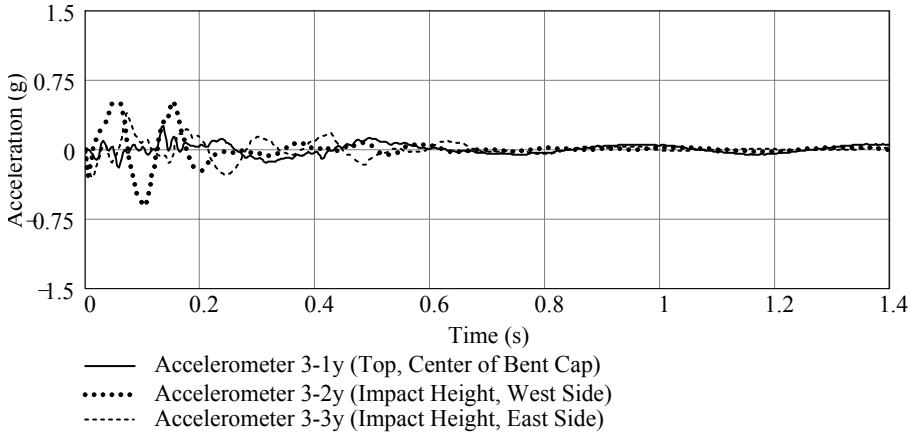

Figure B.47. Experiment P3T2, Y-direction

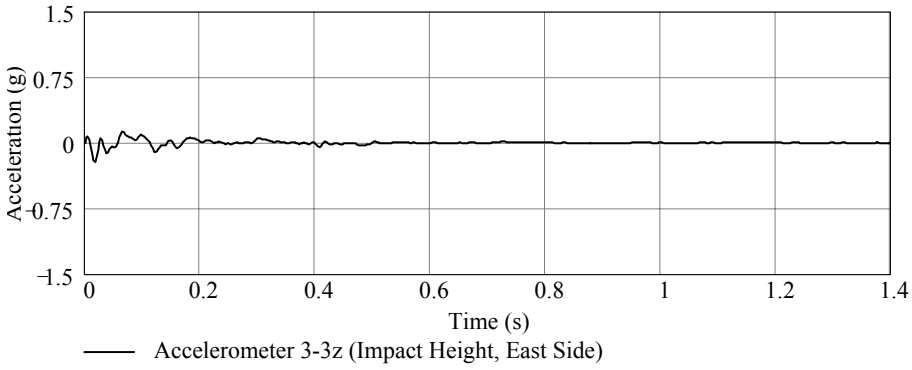

Figure B.48. Experiment P3T2, Z-direction

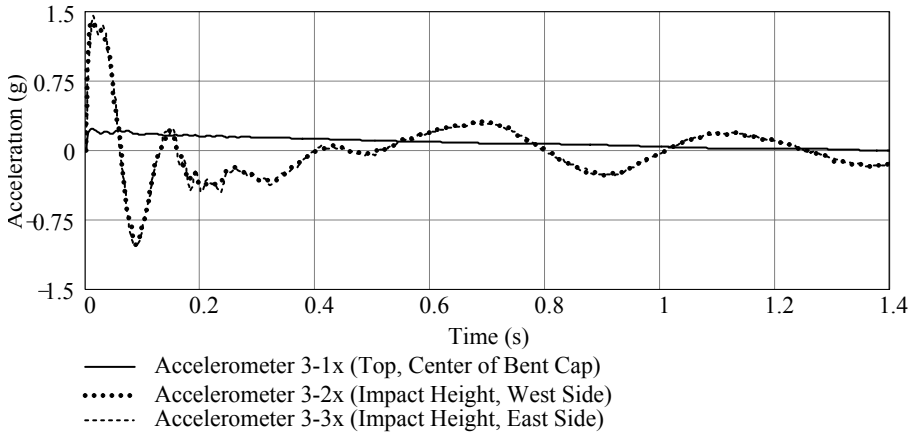

Figure B.49. Experiment P3T3, X-direction

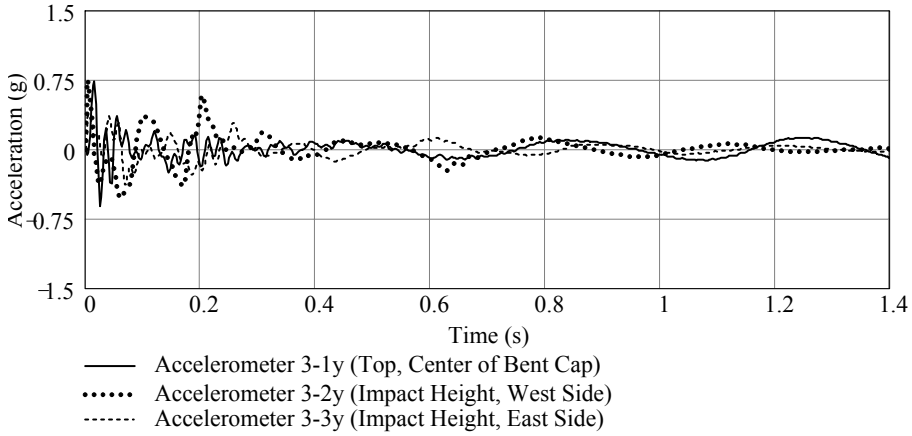

Figure B.50. Experiment P3T3, Y-direction

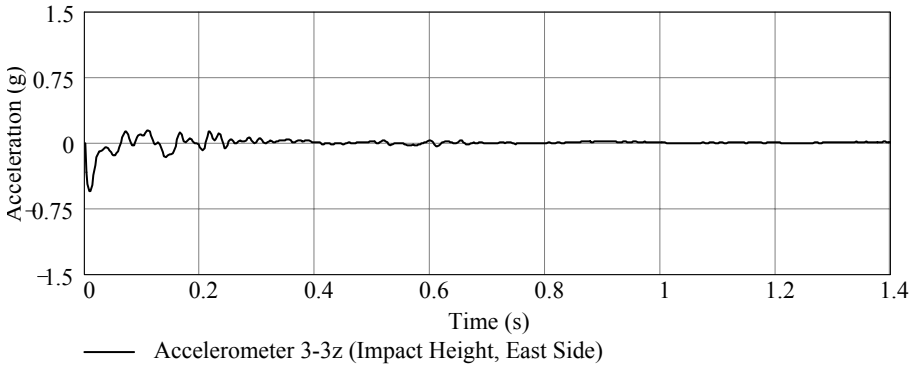

Figure B.51. Experiment P3T3, Z-direction

APPENDIX C
MEASURED BARGE ACCELERATIONS

Uniaxial accelerometers were installed at multiple locations on the test barge to record accelerations in the global X, Y, and Z directions (Figure C.1) during the impact tests. On the following pages, time histories of X, Y, and Z accelerations are presented. During test series P1, excessive signal noise was unfortunately introduced into the data acquisitions system, thus rendering the measured barge accelerations unreliable. This issue was resolved before conducting test series B3 and P3. Therefore, data presented on the following pages correspond to test series B3 and P3, but not P1.

All data presented here have been time-shifted such that the origin of the time axis (t = 0 sec.) corresponds to the time at which initial contact between the barge and pier occurred. During the experimental tests, accelerations were collected at a sampling rate of 2000 Hz. For purposes of presenting the results here, a low-pass 60 Hz noise removal filter has been applied to the data.

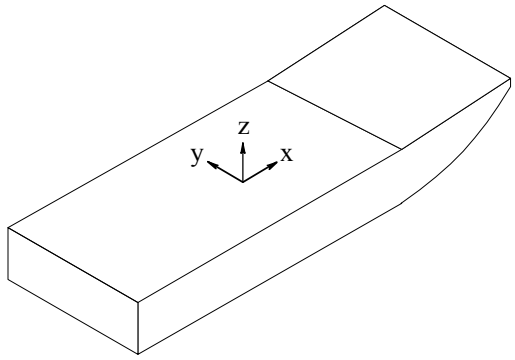

Figure C.1. X, Y, and Z directions for test barge

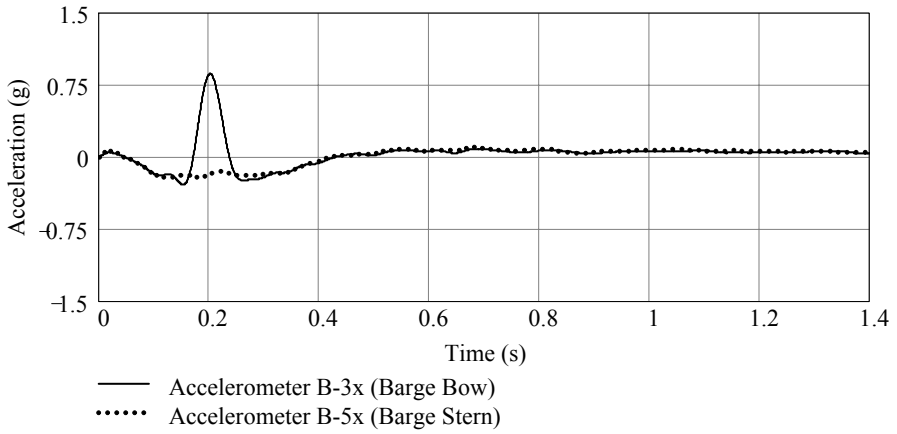

Figure C.2. Experiment B3T1, X-direction

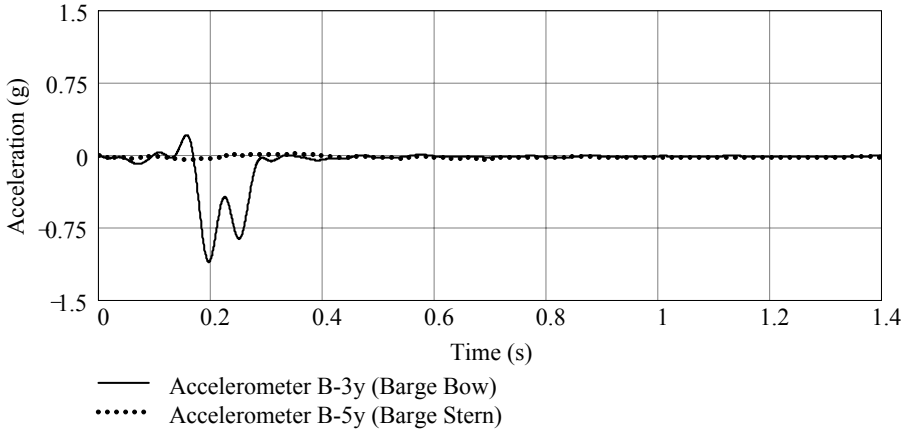

Figure C.3. Experiment B3T1, Y-direction

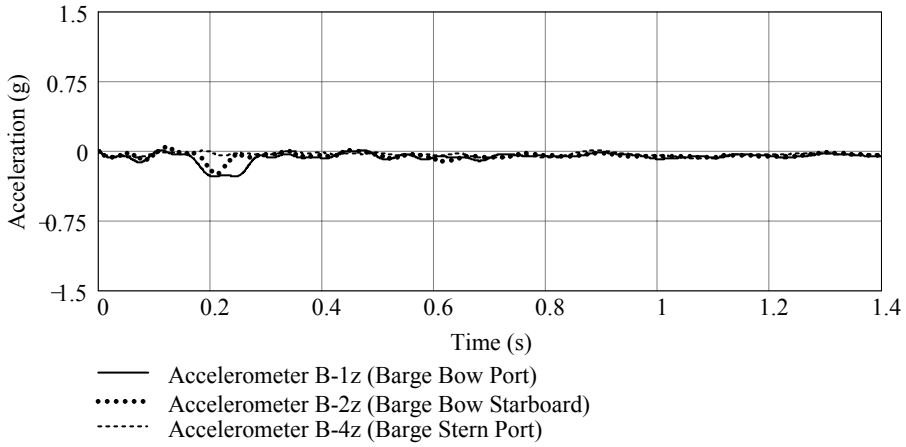

Figure C.4. Experiment B3T1, Z-direction

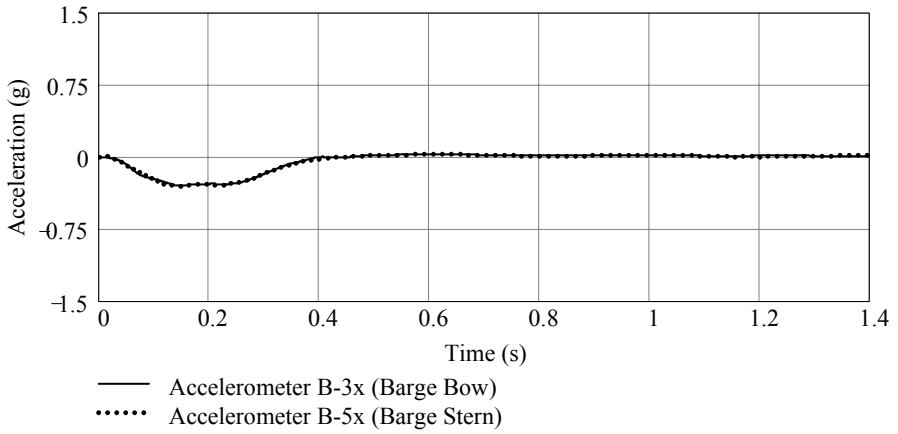

Figure C.5. Experiment B3T2, X-direction

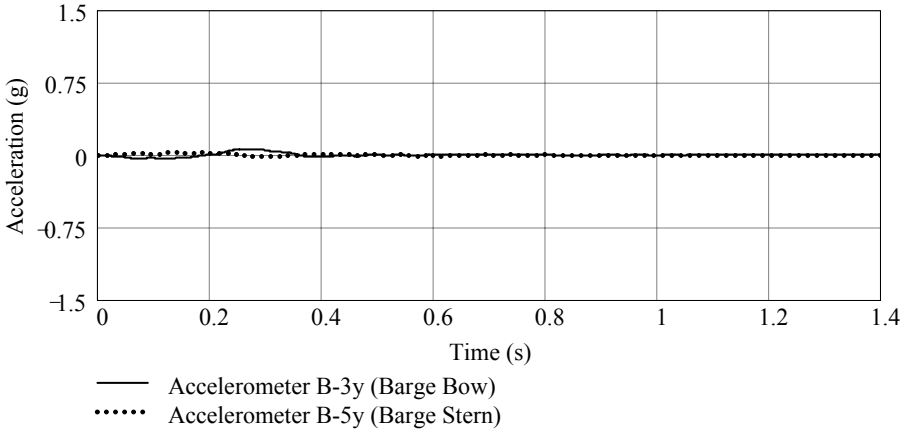

Figure C.6. Experiment B3T2, Y-direction

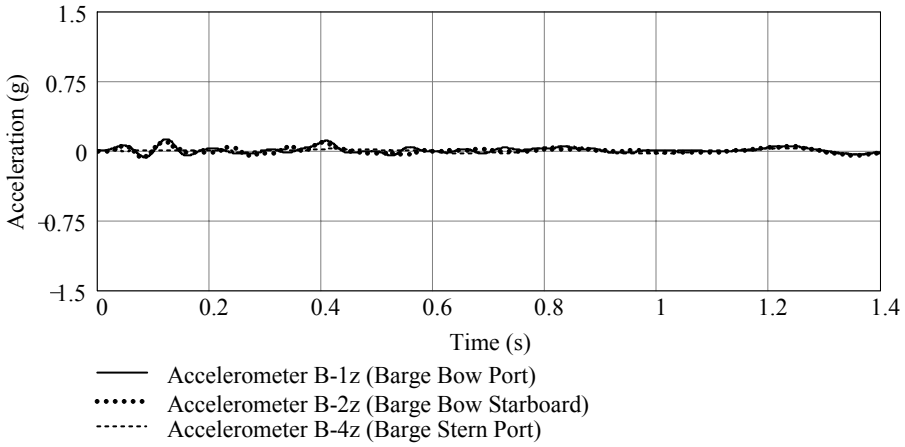

Figure C.7. Experiment B3T2, Z-direction

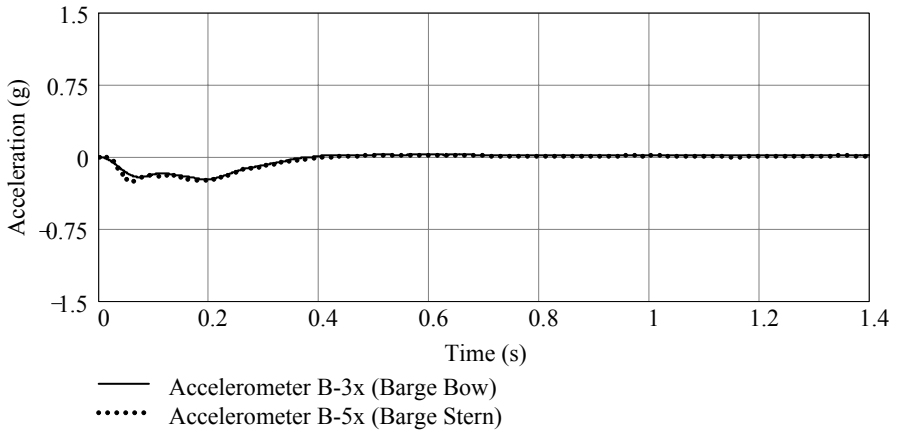

Figure C.8. Experiment B3T3, X-direction

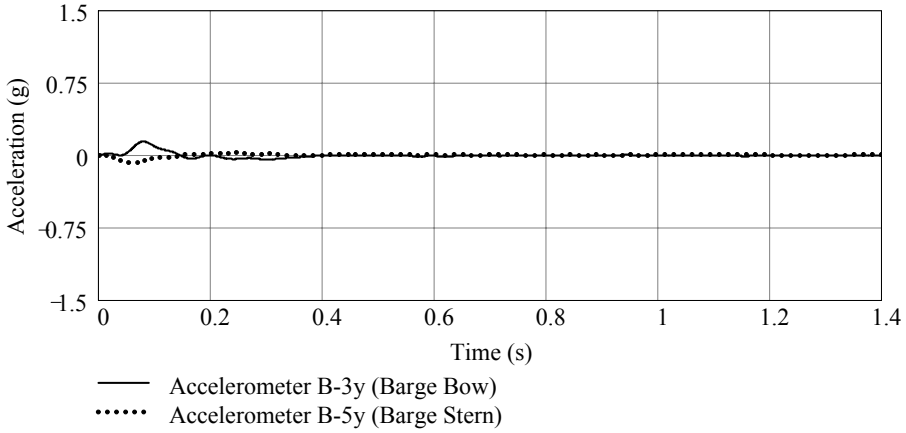

Figure C.9. Experiment B3T3, Y-direction

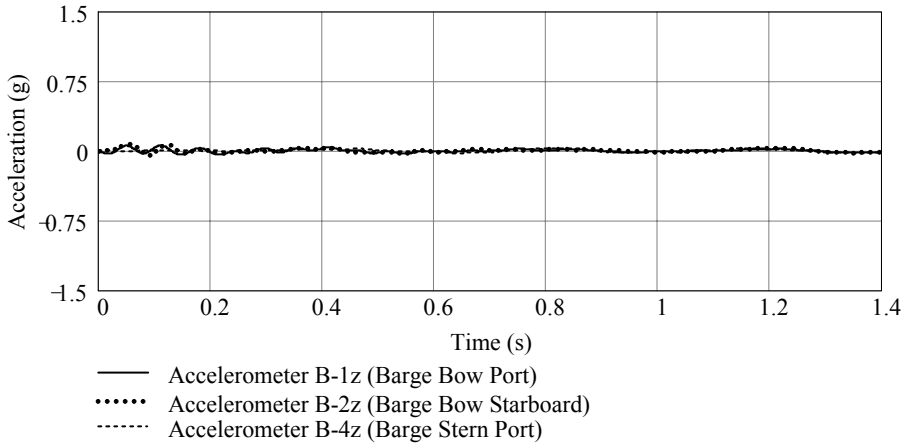

Figure C.10. Experiment B3T3, Z-direction

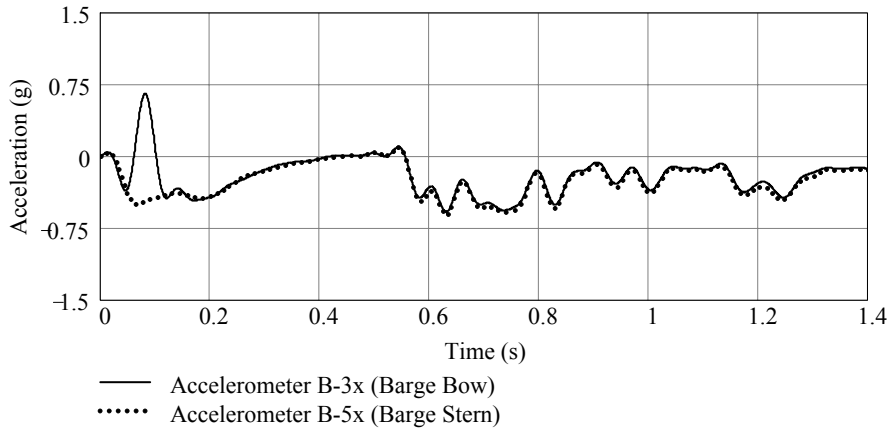

Figure C.11. Experiment B3T4, X-direction

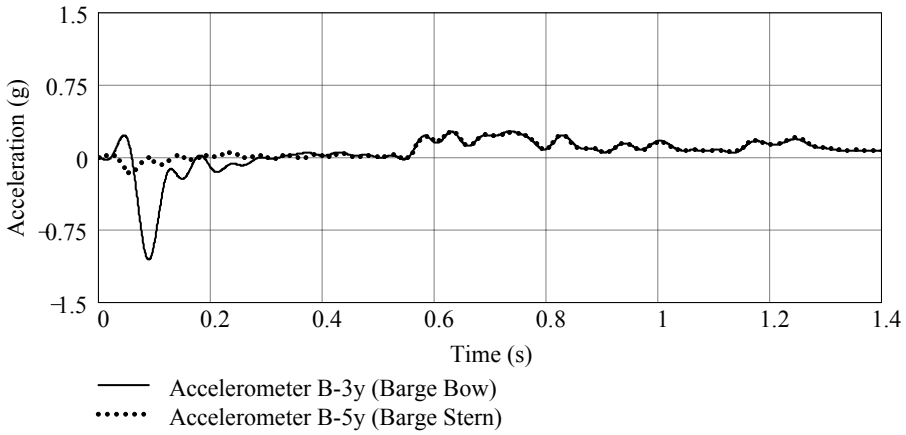

Figure C.12. Experiment B3T4, Y-direction

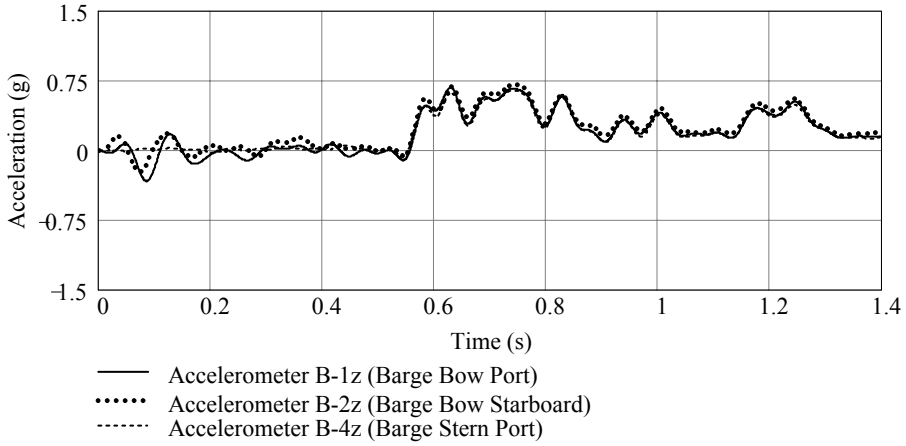

Figure C.13. Experiment B3T4, Z-direction

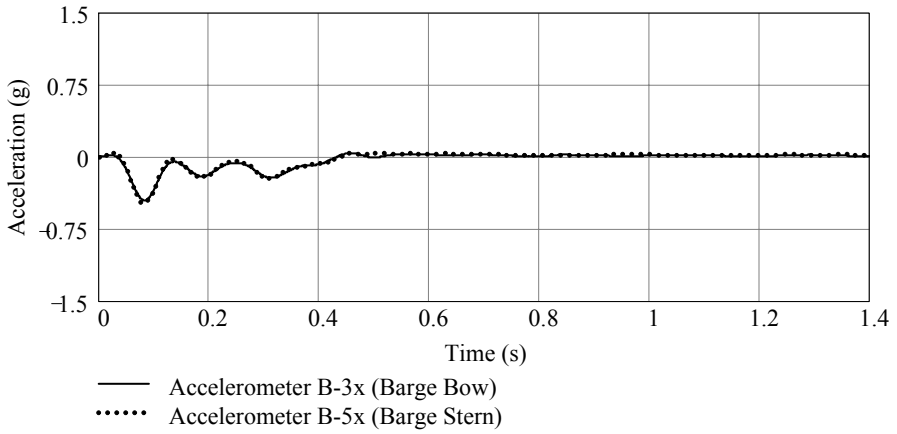

Figure C.14. Experiment P3T1, X-direction

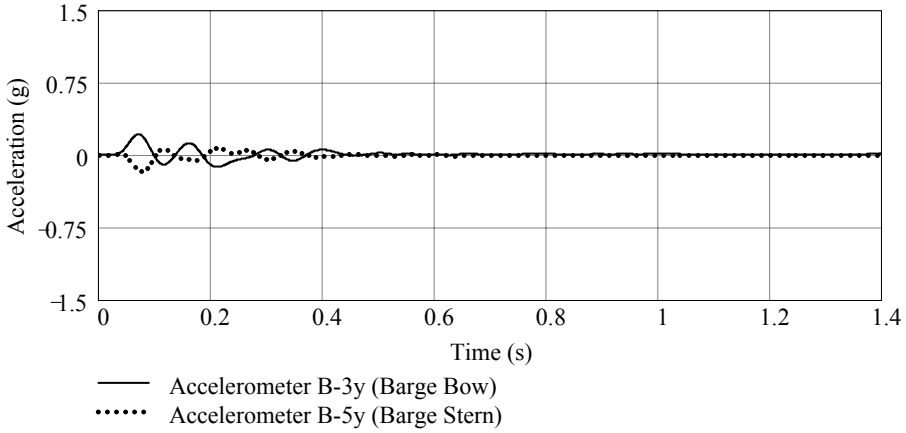

Figure C.15. Experiment P3T1, Y-direction

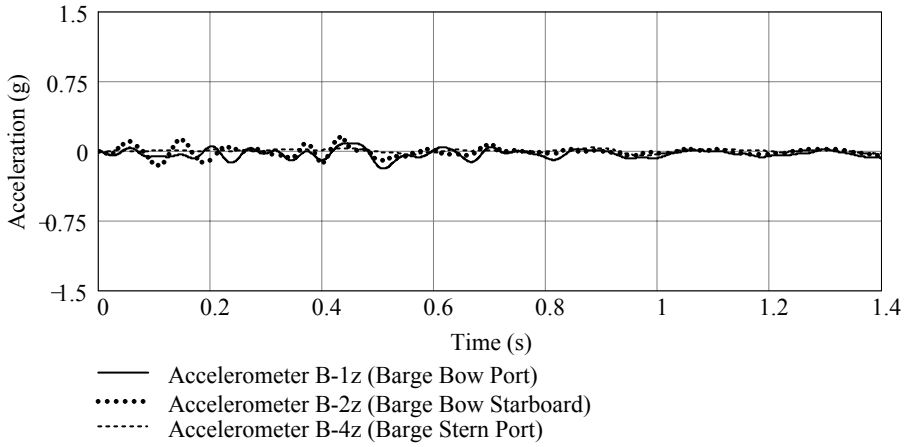

Figure C.16. Experiment P3T1, Z-direction

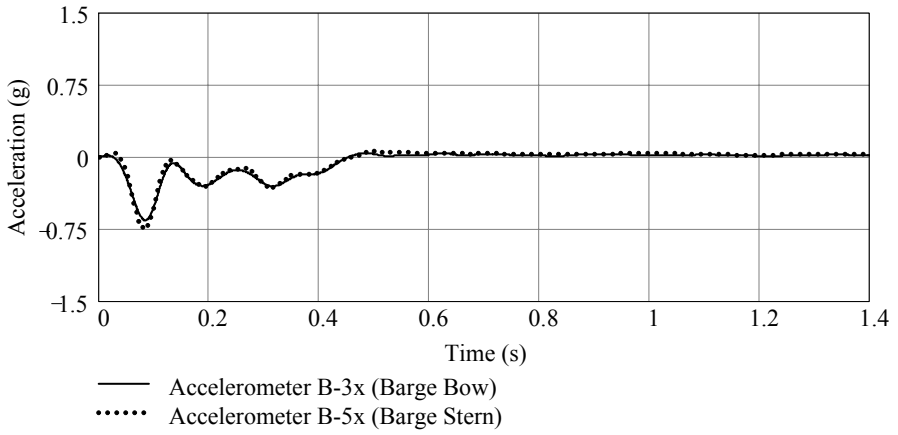

Figure C.17. Experiment P3T2, X-direction

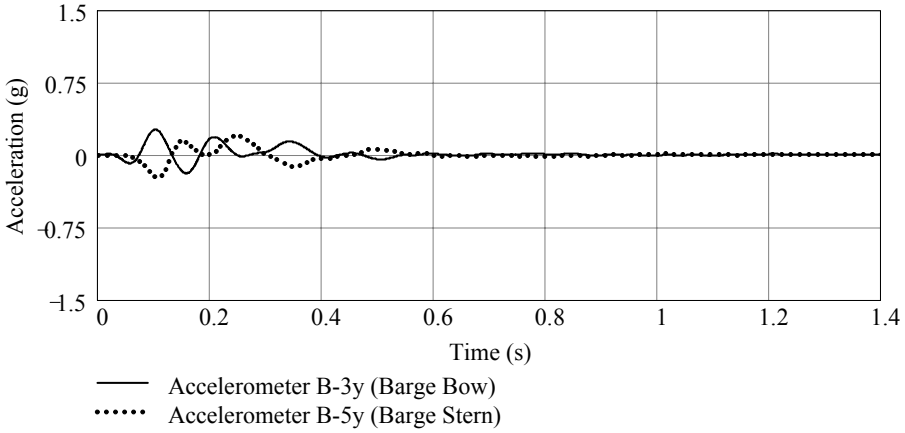

Figure C.18. Experiment P3T2, Y-direction

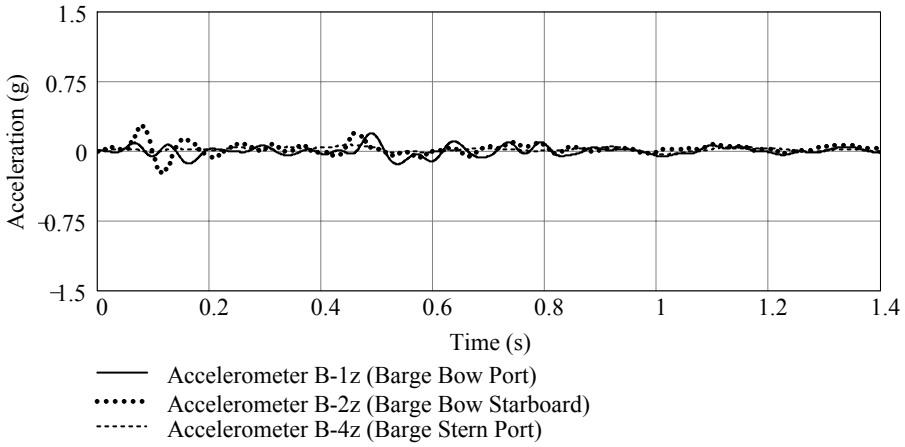

Figure C.19. Experiment P3T2, Z-direction

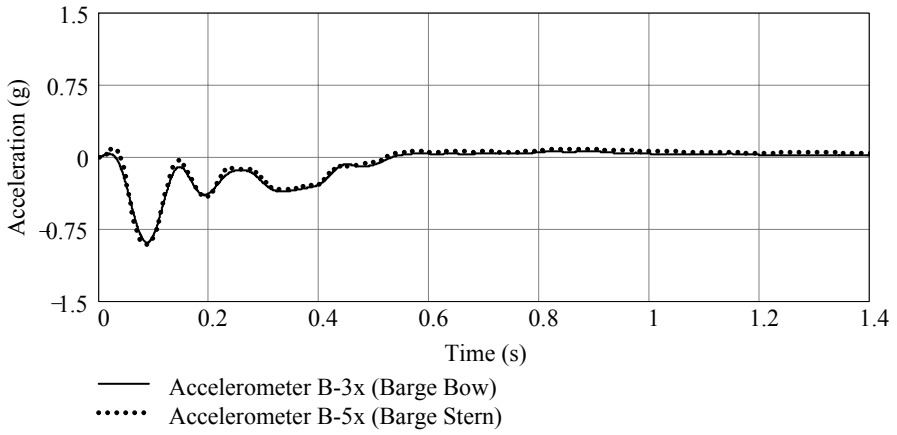

Figure C.20. Experiment P3T3, X-direction

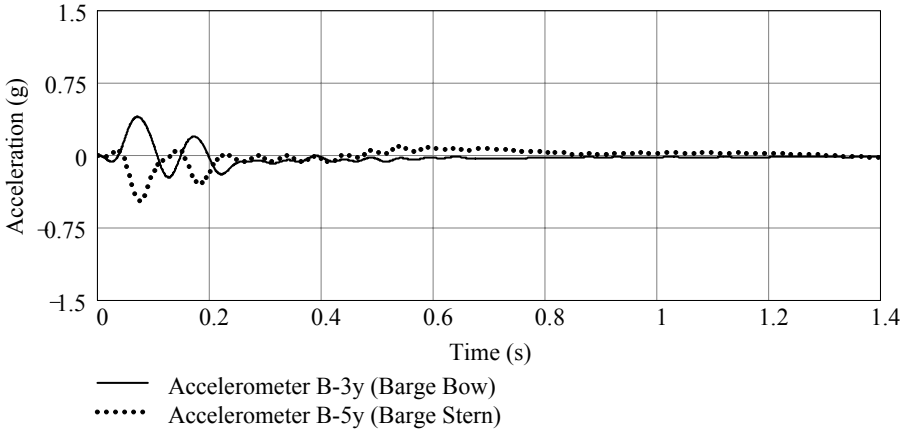

Figure C.21. Experiment P3T3, Y-direction

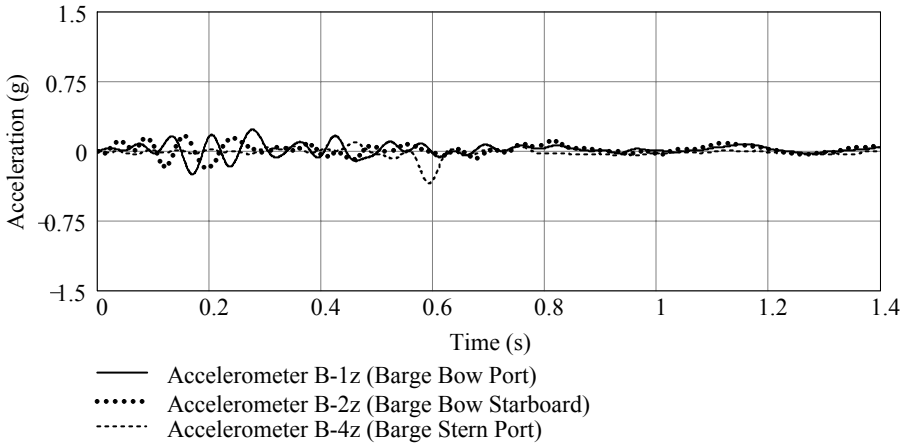

Figure C.22. Experiment P3T3, Z-direction

APPENDIX D
MEASURED PIER DISPLACEMENTS

Displacement transducers were installed at two locations on each test pier to record pier displacements during the impact tests. On the following pages, time histories of the experimentally recorded pier displacements are presented. All data have been time-shifted such that the origin of the time axis (t = 0 sec.) corresponds to the time at which initial contact between the barge and pier occurred. During the experimental tests, displacements were collected at a sampling rate of 2000 Hz. For purposes of presenting the results here, a low-pass 1000 Hz noise removal filter has been applied to the data.

Data are presented for test series B3 and P3, but not for series P1. Examination of data obtained from series P1 revealed that the timber-pile platform that was installed to anchor the displacement transducers was unfortunately within the soil-zone-of-influence of Pier-1. Alternately stated, due to the large footprint of Pier-1, pressure waves were generated during the impacts that traveled from the pile cap/seal, through the soil, and into the timber-pile platform. As a result, the timber-pile platform did not remain stationary during the series P1 tests, and the displacement transducers thus measured the relative motion between the pier and platform rather than the motion of the pier relative to a stationary anchorage point. Because the motions of the anchorage platform are unknown, it is not possible to recover the pier displacements for Pier-1 from the displacement transducer data. Instead, displacement time histories for Pier-1 are computed (in Appendix I) based on double time-integration of measured pier accelerations. In the cases of the B3 and P3 test series, the timber-pile platform was outside the soil-zone-of-influence of Pier-3, and therefore the displacement transducer data obtained from these tests are valid.

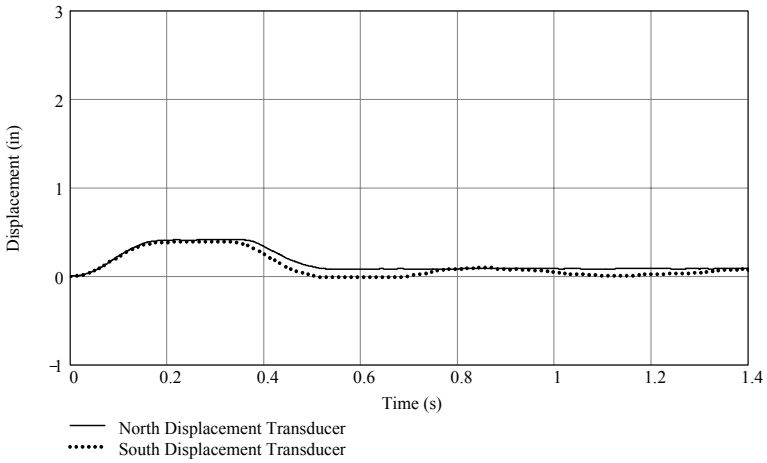

Figure D.1. Experiment B3T1

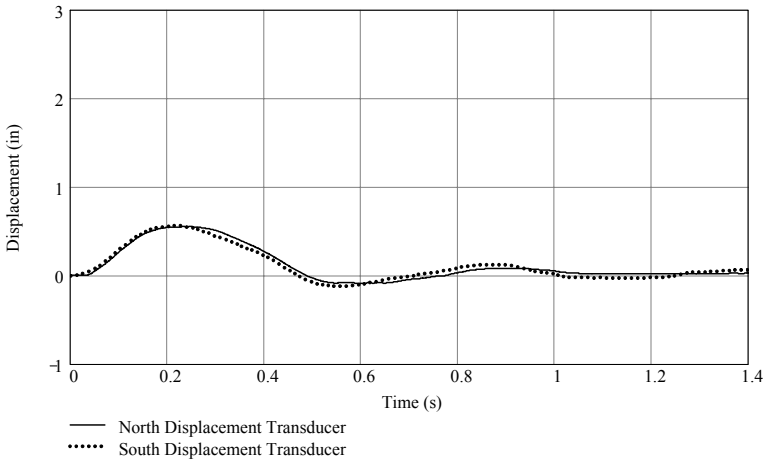

Figure D.2. Experiment B3T2

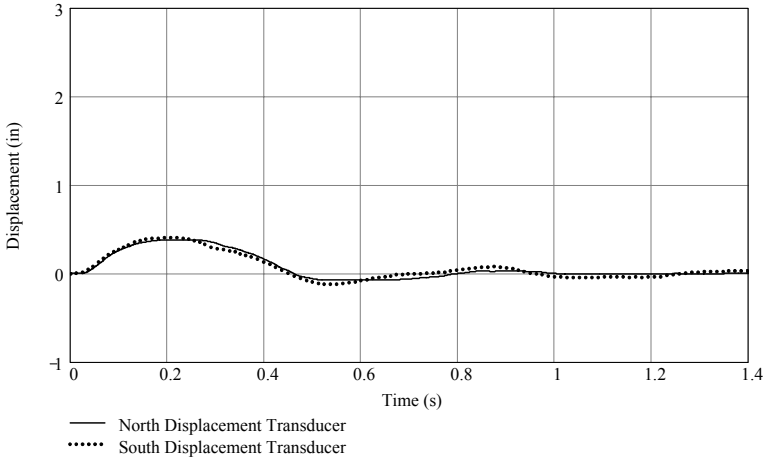

Figure D.3. Experiment B3T3

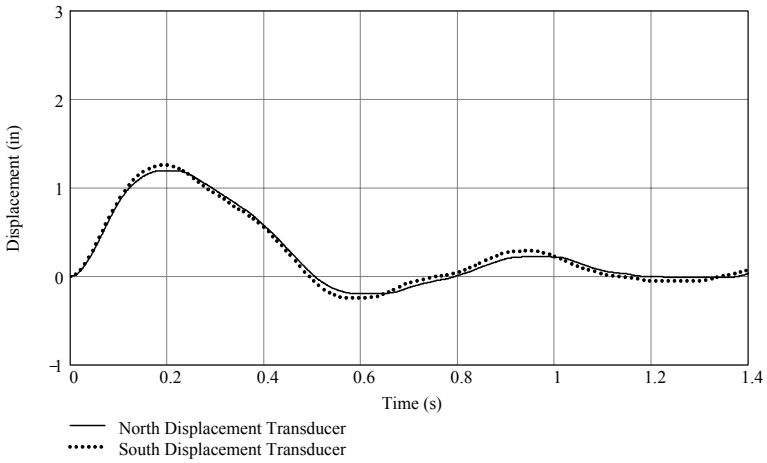

Figure D.4. Experiment B3T4

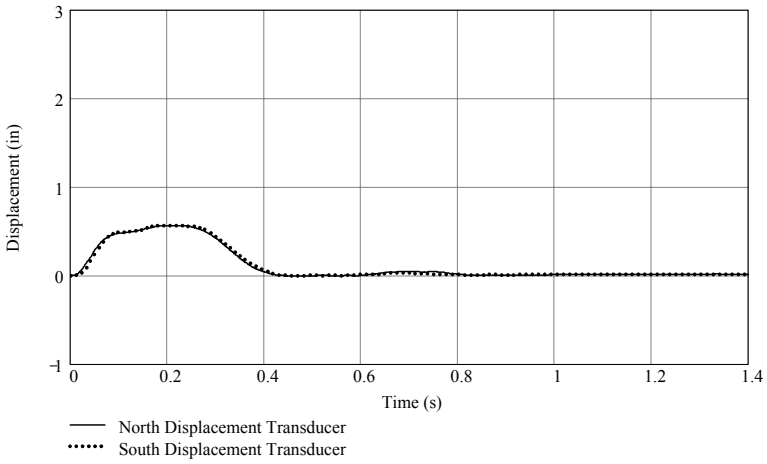

Figure D.5. Experiment P3T1

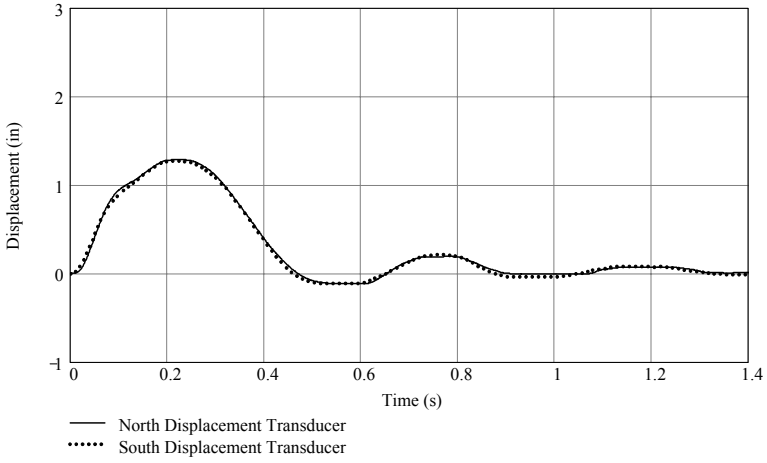

Figure D.6. Experiment P3T2

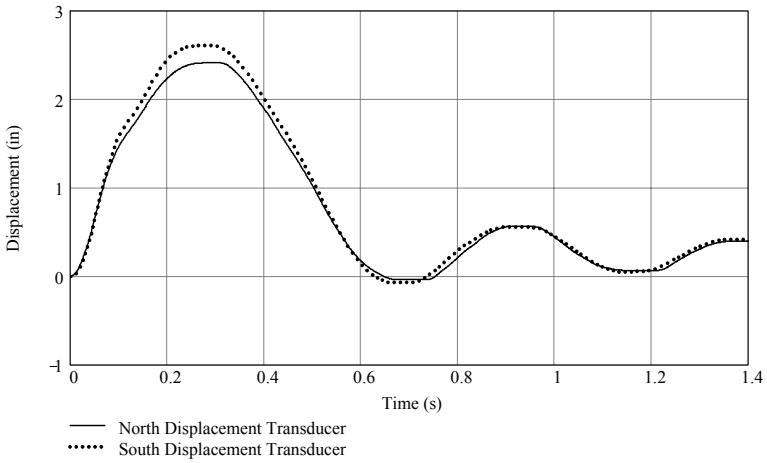

Figure D.7. Experiment P3T3

APPENDIX E
MEASURED WATER PRESSURES

During test series P1, a pressure transducer was submerged below water level on the east (non-impact) side of Pier-1 to record water pressure variations during the impact tests. On the following pages, time histories of the experimentally recorded water pressure changes are presented. All data have been time-shifted such that the origin of the time axis (t = 0 sec.) corresponds to the time at which initial contact between the barge and pier occurred. Pressure changes were computed by subtracting the absolute water pressure measured at time t = 0 sec. from the absolute water pressures measured throughout the remainder of the tests. Pressure data were experimentally collected at a sampling rate of 2000 Hz. For purposes of presenting the results here, a low-pass 1000 Hz noise removal filter has been applied to the data. Water pressure data were not recorded during test series B3 or P3 due to the much smaller submerged surface area of Pier-3 (in comparison to that of Pier-1).

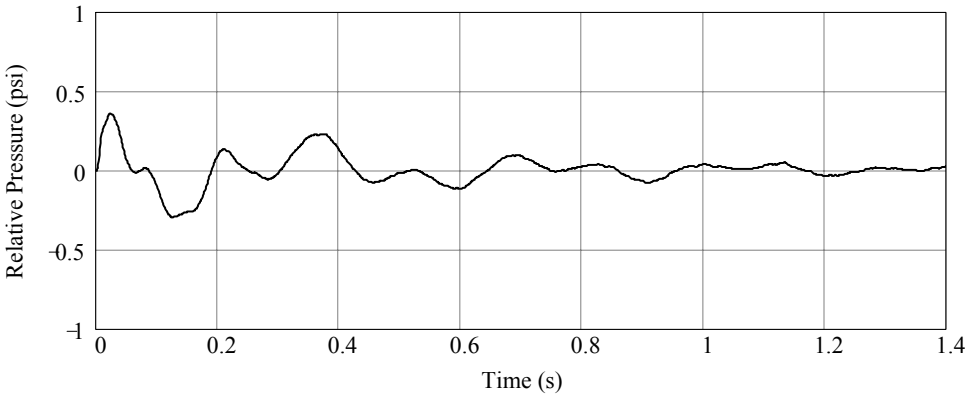

Figure E.1. Experiment P1T1, pressure change relative to initial pressure

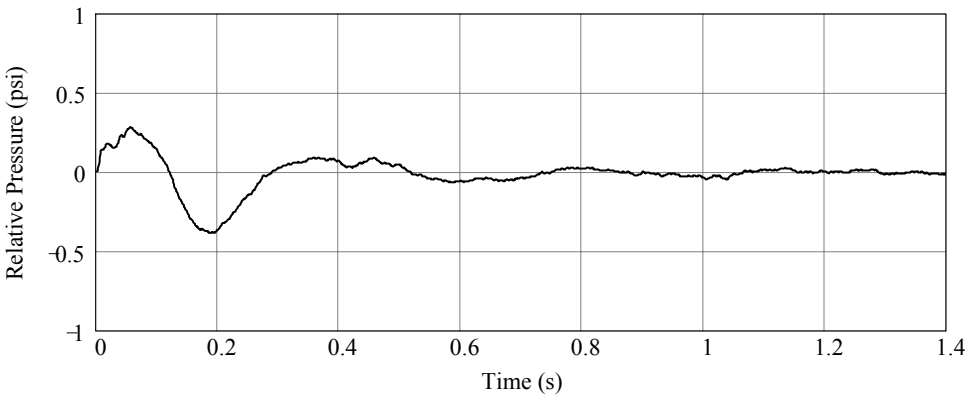

Figure E.2. Experiment P1T3, pressure change relative to initial pressure

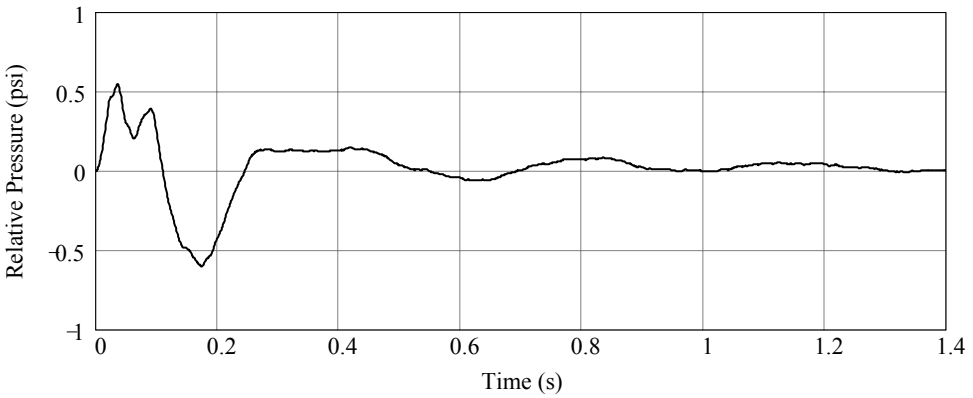

Figure E.3. Experiment P1T4, pressure change relative to initial pressure

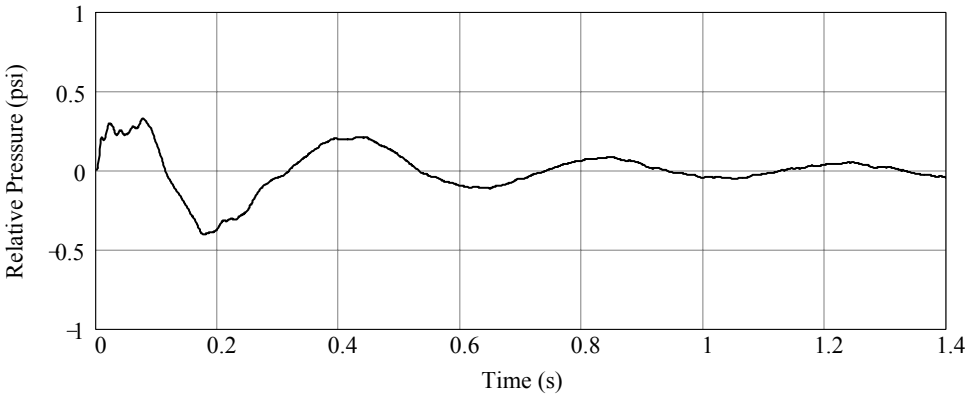

Figure E.4. Experiment P1T5, pressure change relative to initial pressure

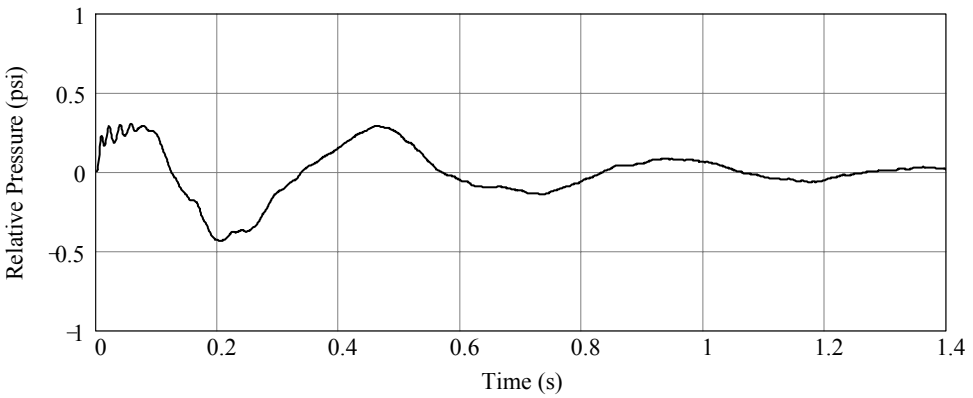

Figure E.5. Experiment P1T6, pressure change relative to initial pressure

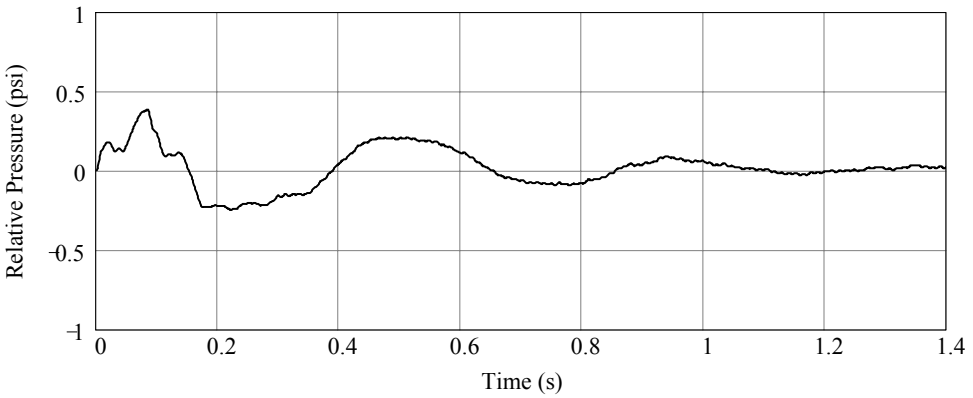

Figure E.6. Experiment P1T7, pressure change relative to initial pressure

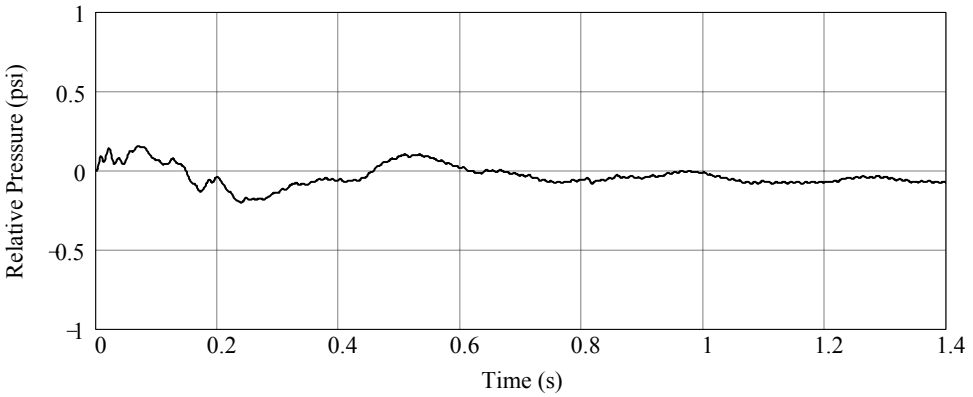

Figure E.7. Experiment P1T8, pressure change relative to initial pressure

APPENDIX F
MEASURED PILE STRAINS

Strain rings (strain measurement sensors) were used to measure surface strains on the piles of Pier-3 during impact test series B3 and P3. On the following pages, time histories of the experimentally recorded strain data are presented. Pile identification numbers used in the time-history strain plots are given in Figure F.1. All data have been time-shifted such that the origin of the time axis (t = 0 sec.) corresponds to the time at which initial contact between the barge and pier occurred.

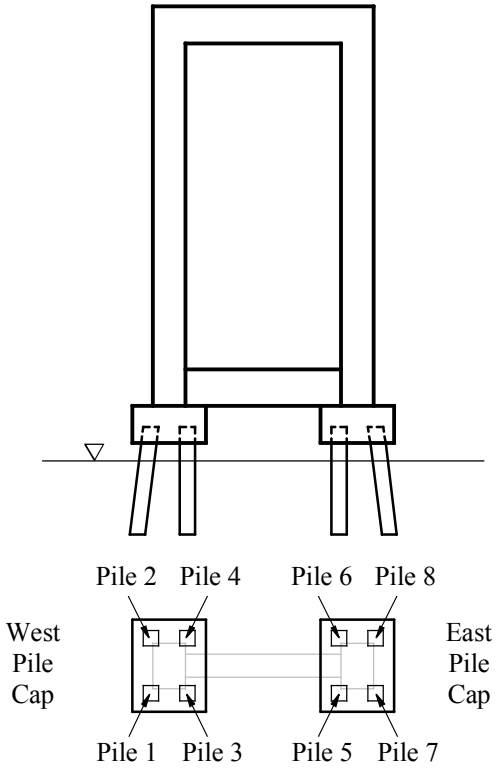

Figure F.1. Pile identification numbers for interpretation of strain measurements

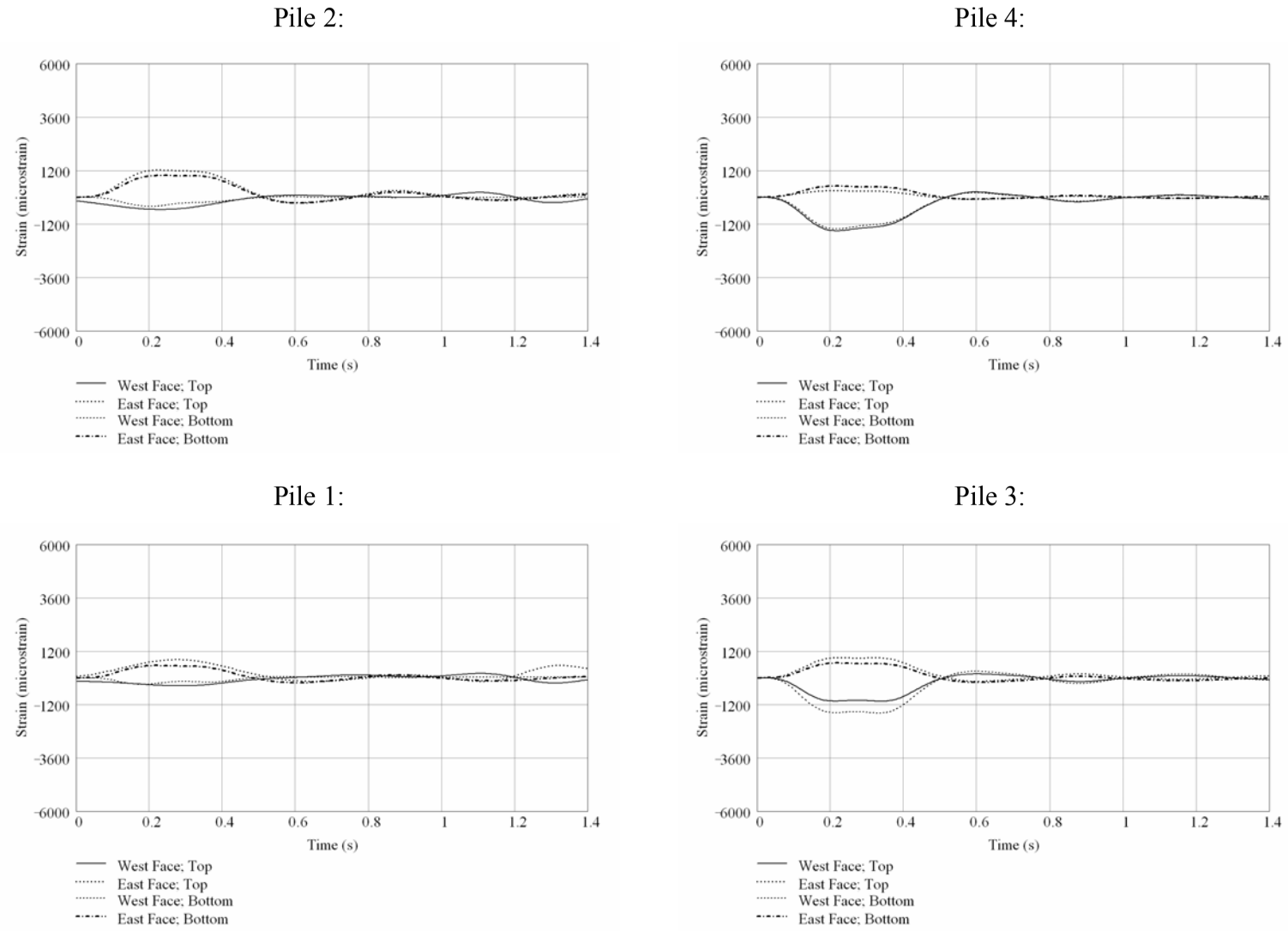

Figure F.2. Experiment B3T1 pile strains, Pier-3 West pile-cap

Pile 6:

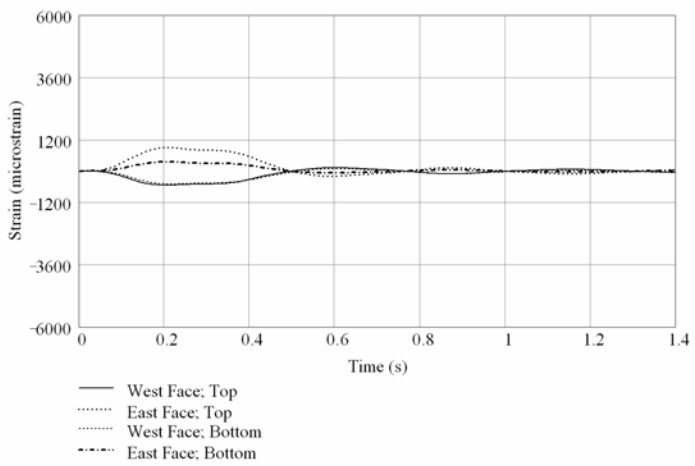

Pile 8:

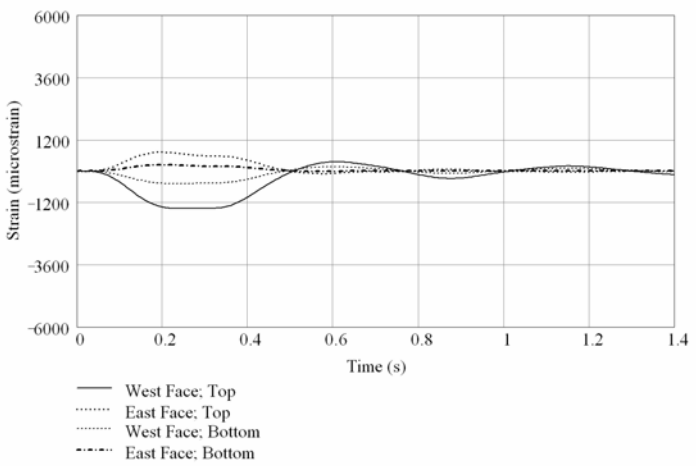

Pile 5:

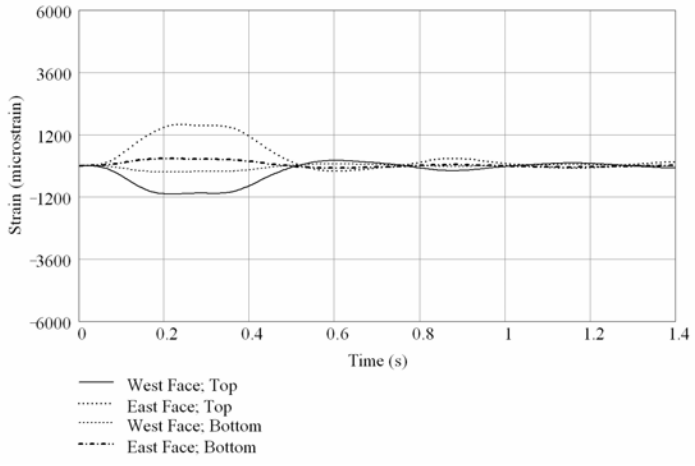

Pile 7:

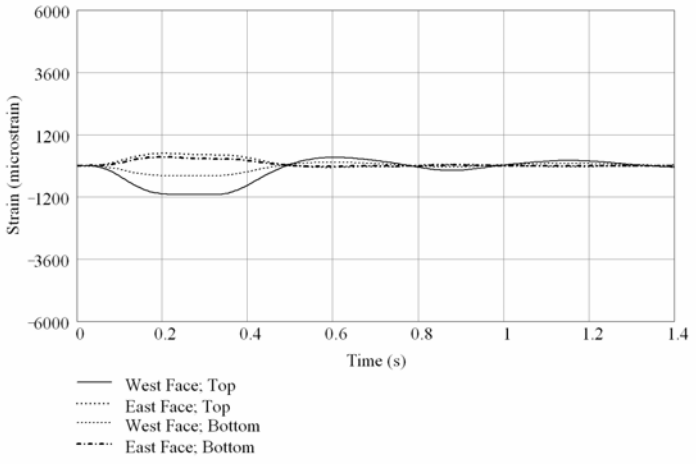

Figure F.3. Experiment B3T1 pile strains, Pier-3 East pile-cap

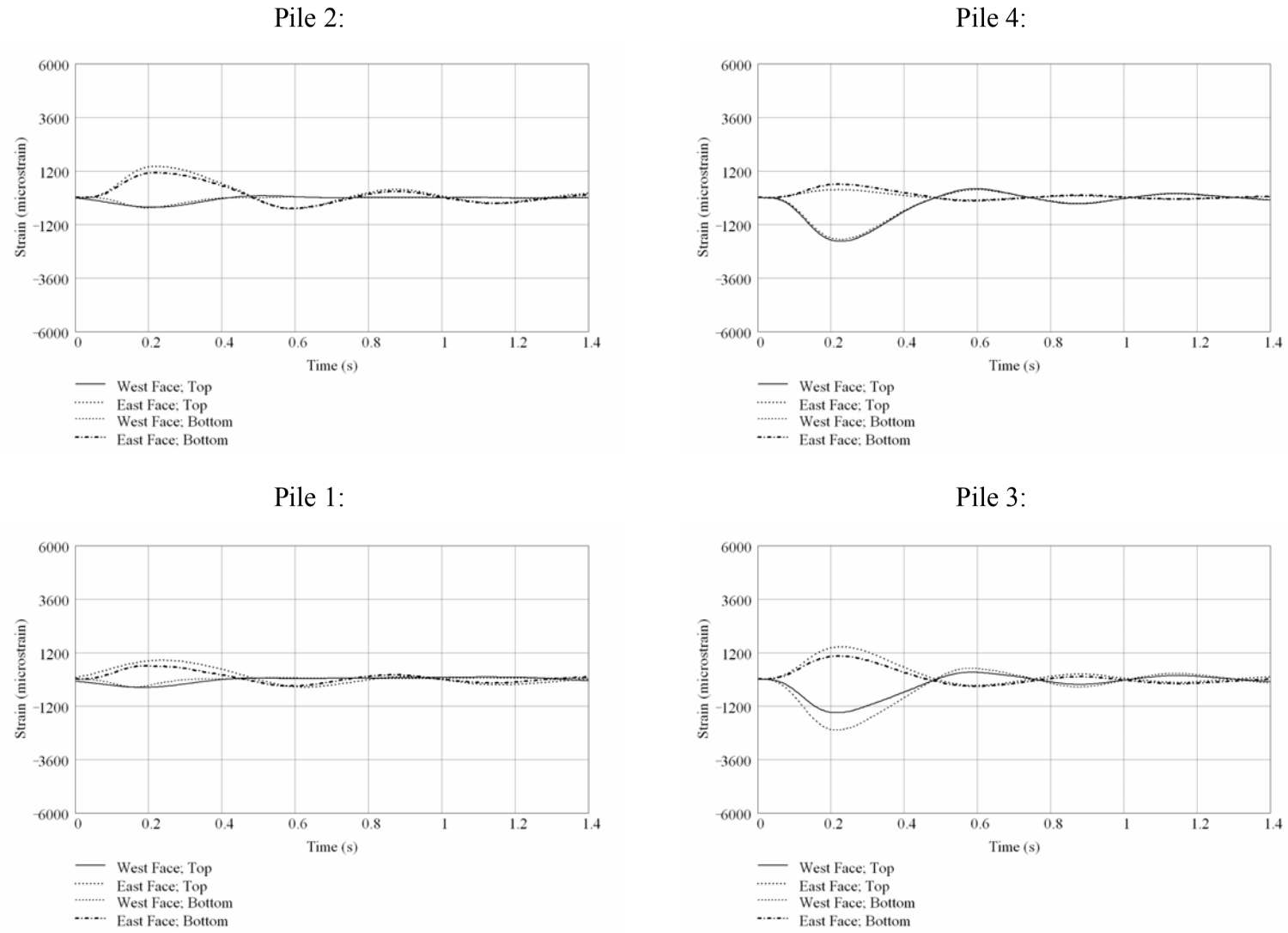

Figure F.4. Experiment B3T2 pile strains, Pier-3 West pile-cap

Pile 6:

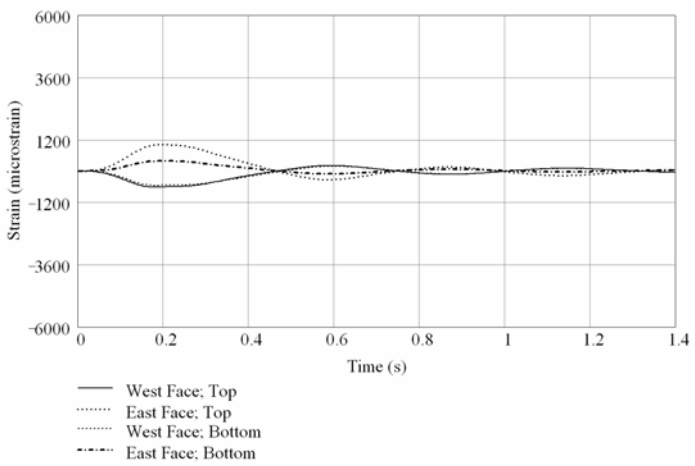

Pile 8:

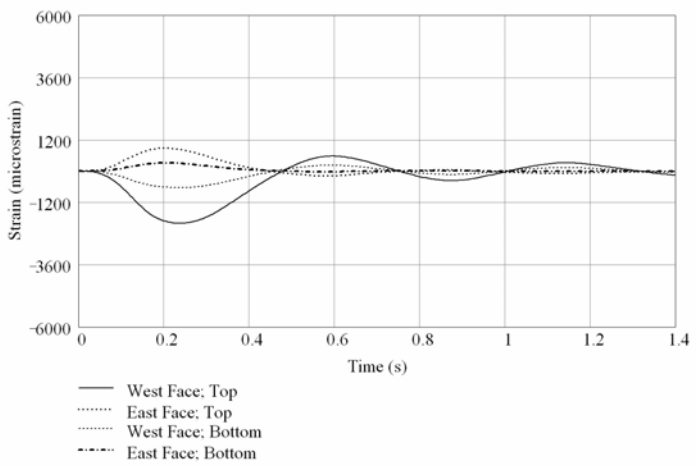

Pile 5:

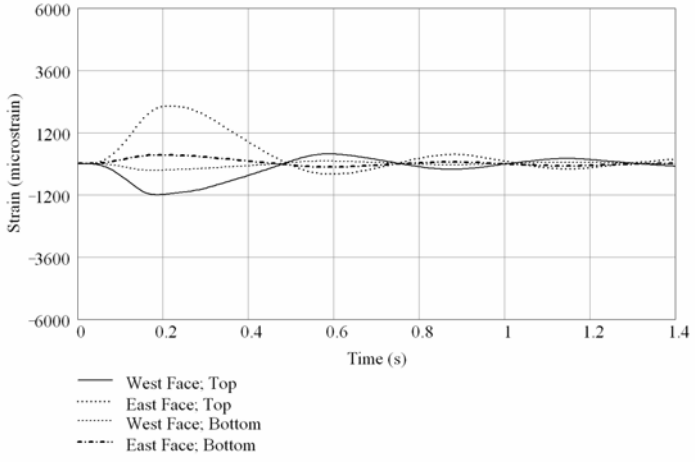

Pile 7:

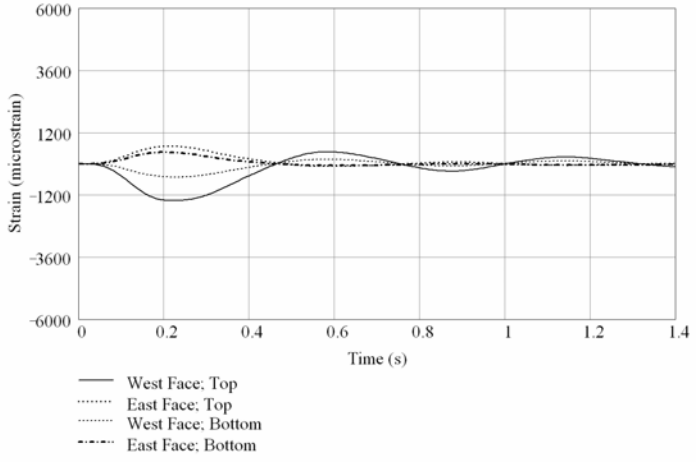

Figure F.5. Experiment B3T2 pile strains, Pier-3 East pile-cap

Pile 2:

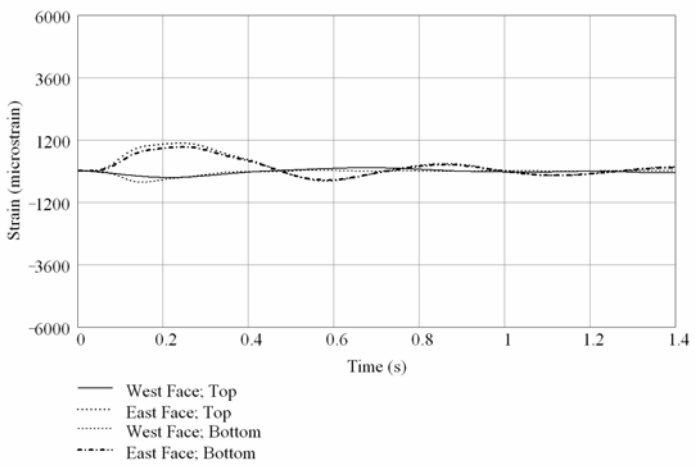

Pile 4:

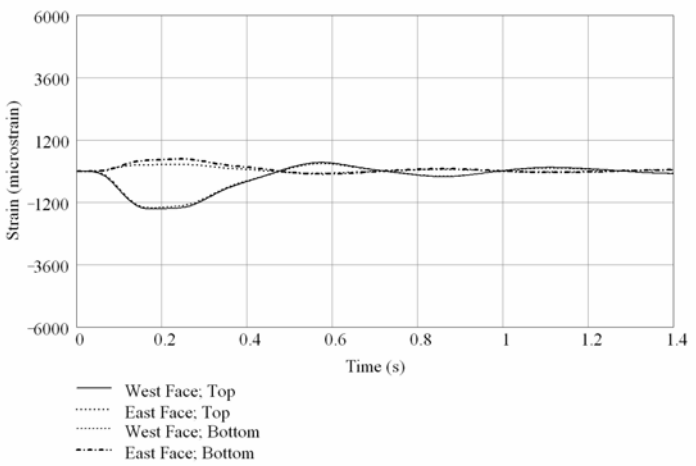

Pile 1:

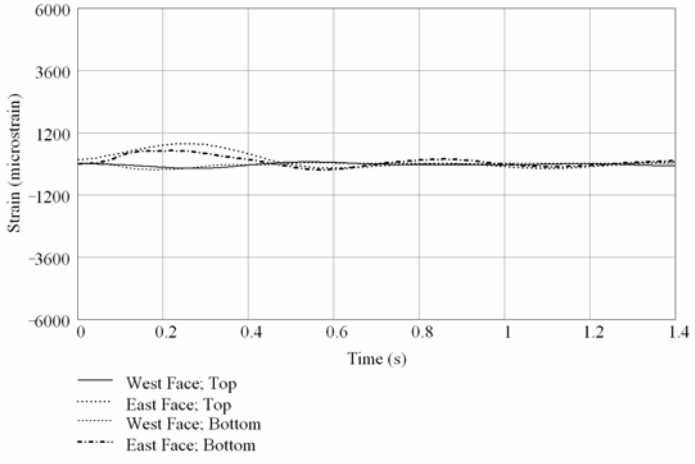

Pile 3:

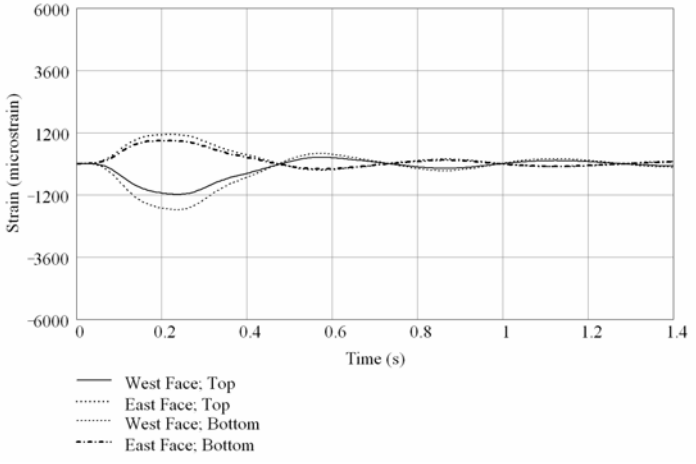

Figure F.6. Experiment B3T3 pile strains, Pier-3 West pile-cap

Pile 6:

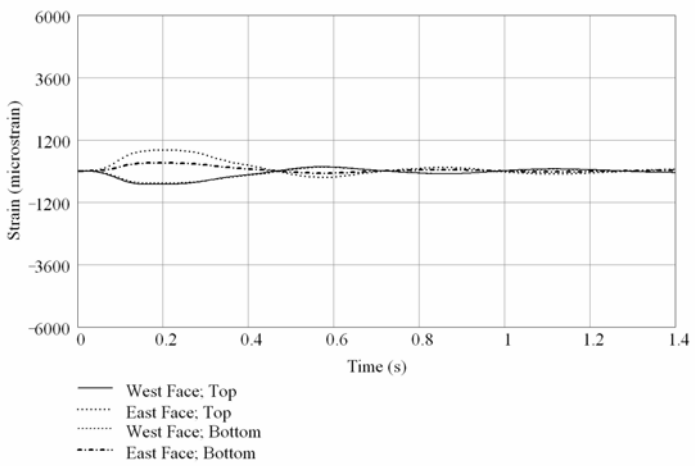

Pile 8:

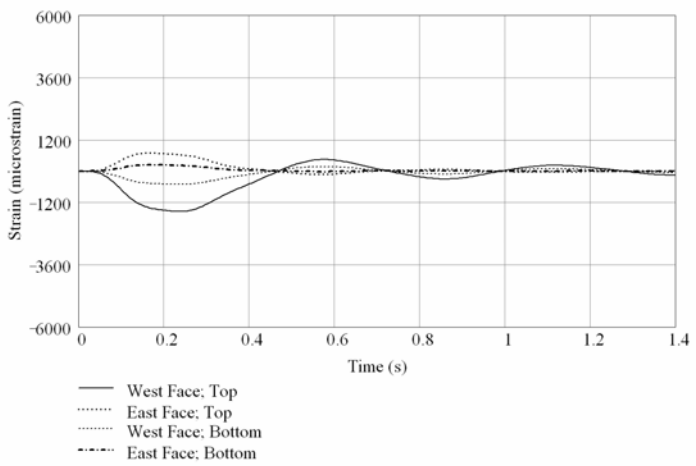

Pile 5:

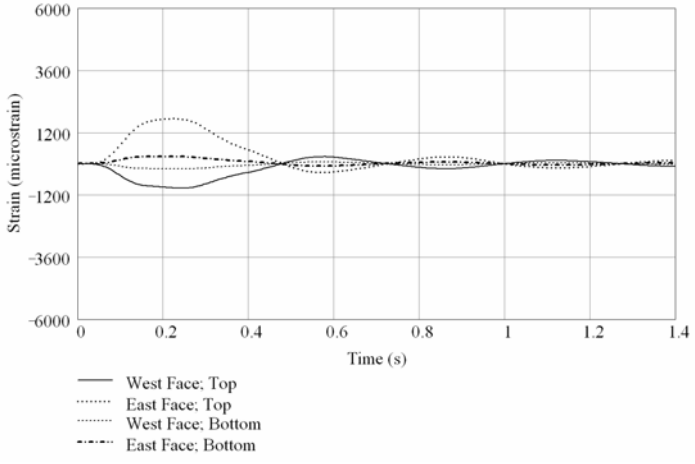

Pile 7:

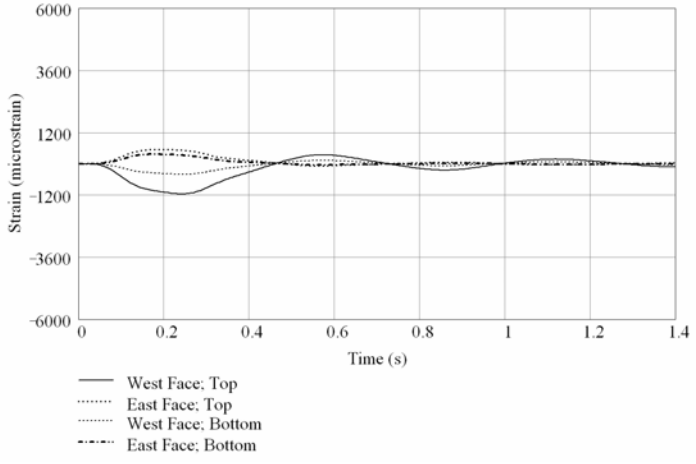

Figure F.7. Experiment B3T3 pile strains, Pier-3 East pile-cap

Pile 2:

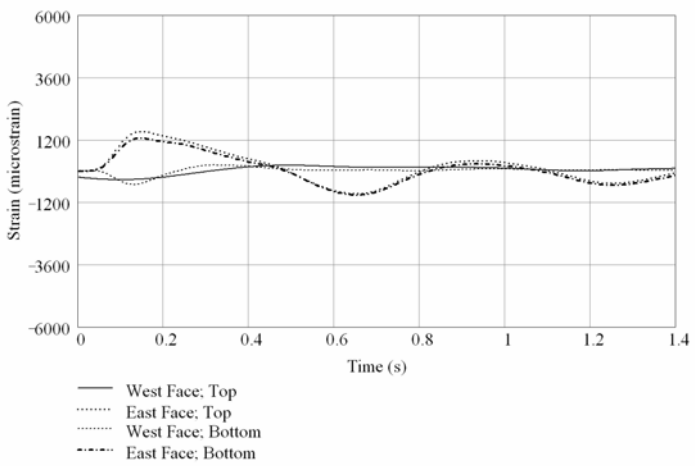

Pile 4:

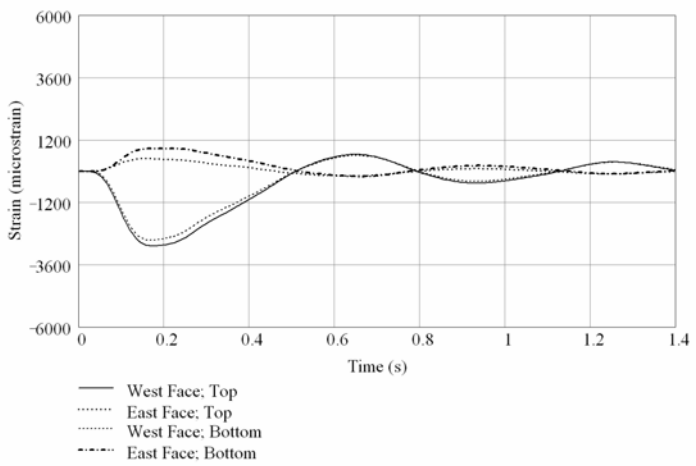

Pile 1:

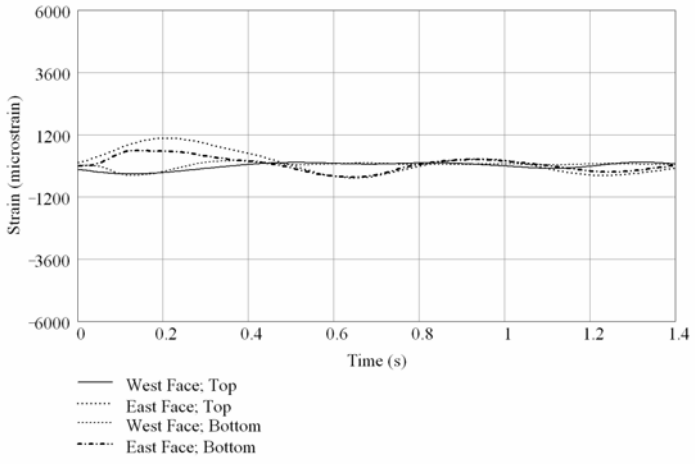

Pile 3:

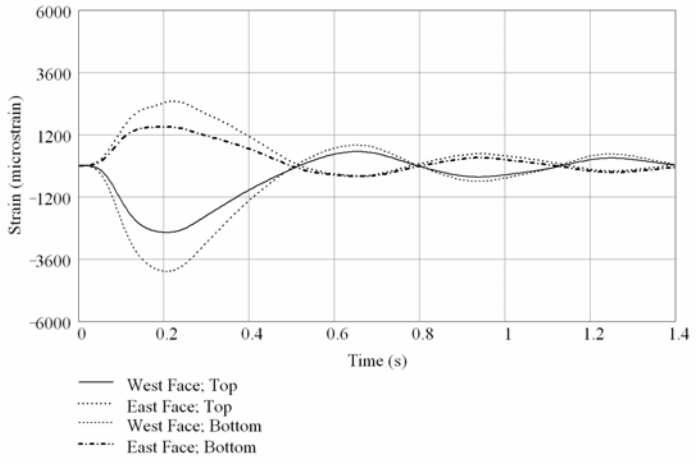

Figure F.8. Experiment B3T4 pile strains, Pier-3 West pile-cap

Pile 6:

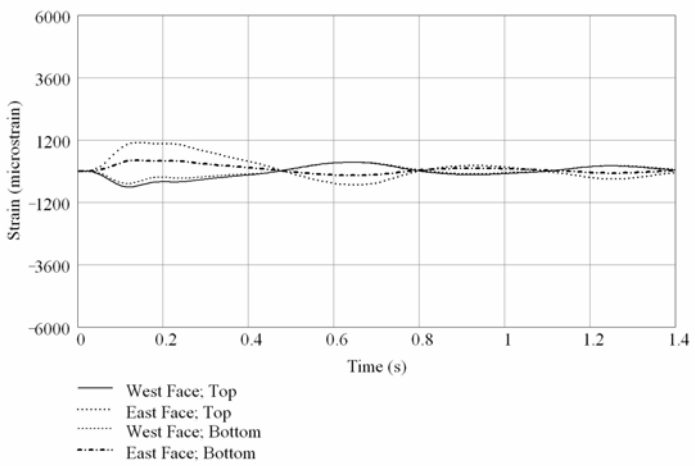

Pile 8:

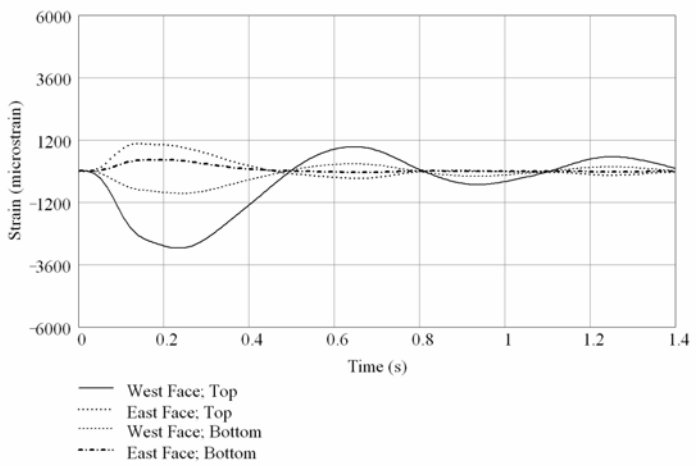

Pile 5:

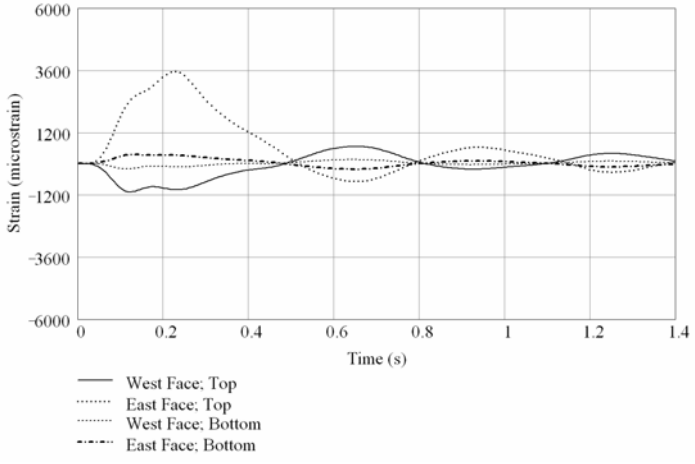

Pile 7:

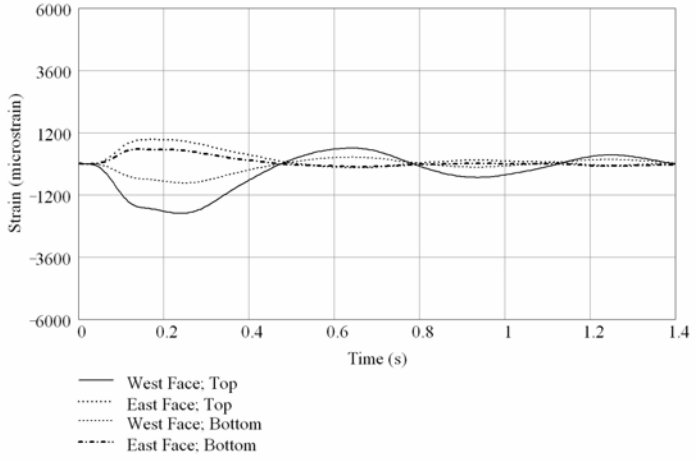

Figure F.9. Experiment B3T4 pile strains, Pier-3 East pile-cap

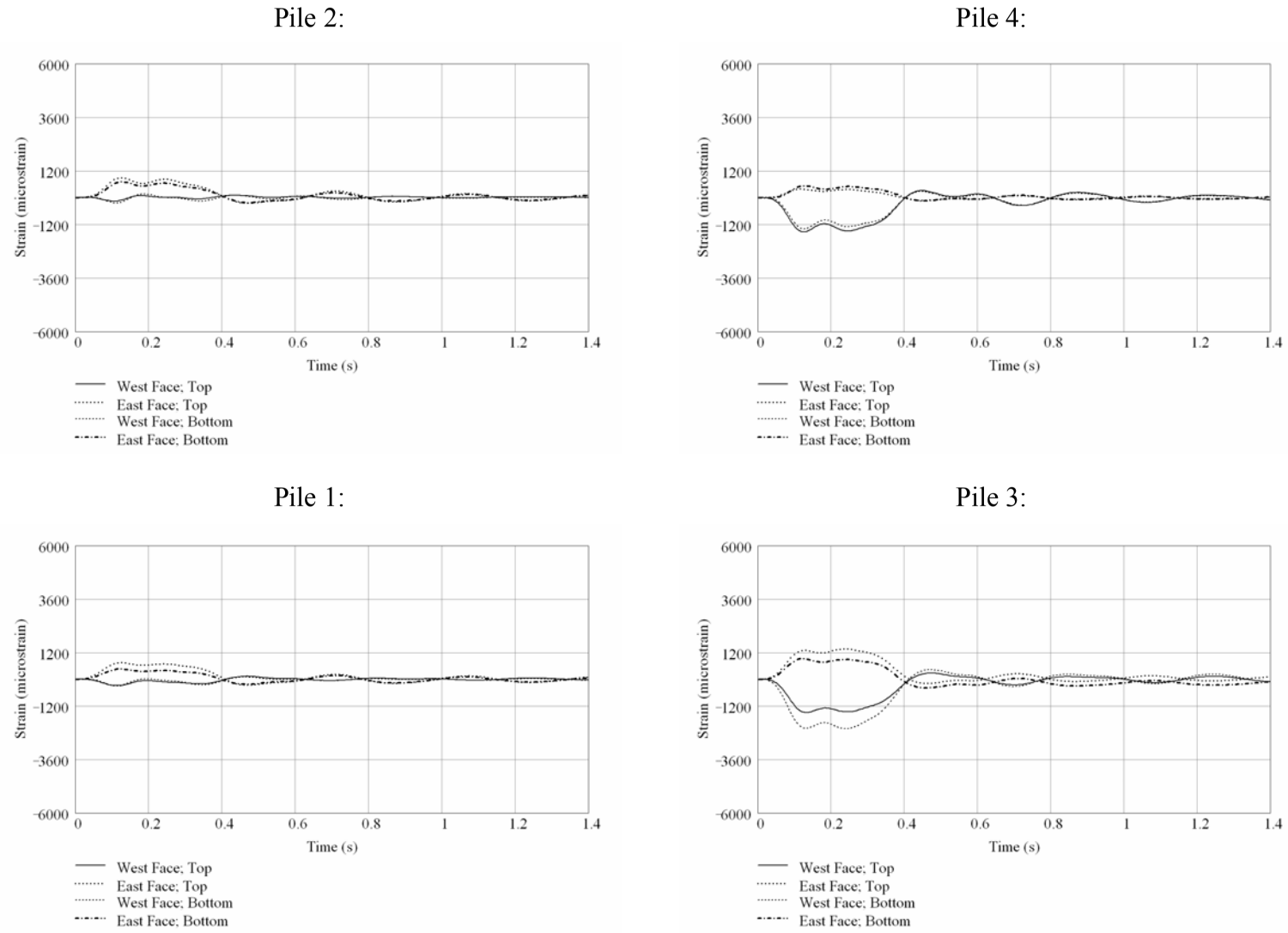

Figure F.10. Experiment P3T1 pile strains, Pier-3 West pile-cap

Pile 6:

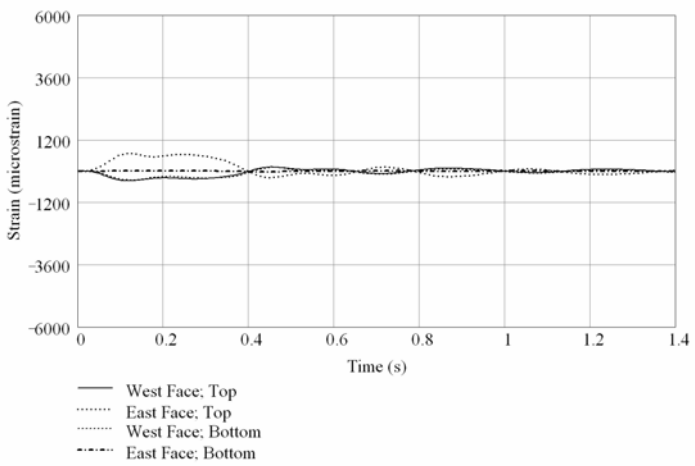

Pile 8:

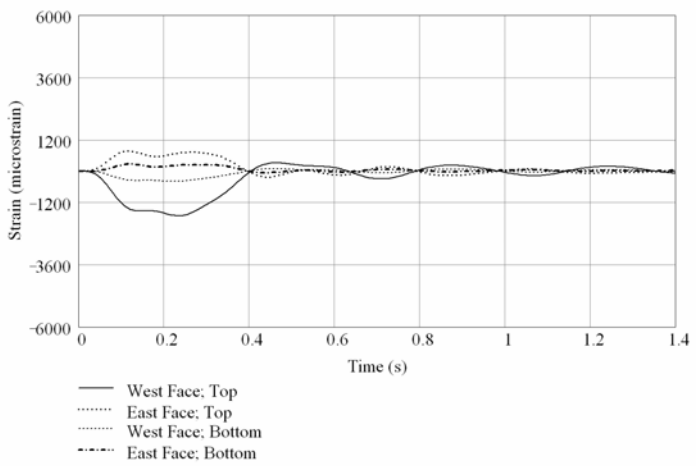

Pile 5:

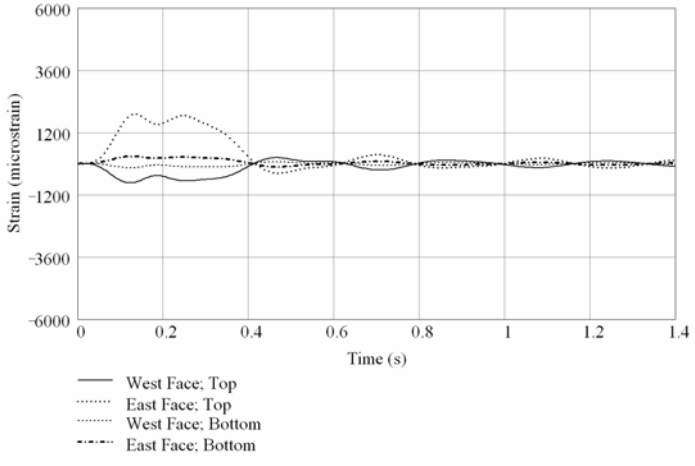

Pile 7:

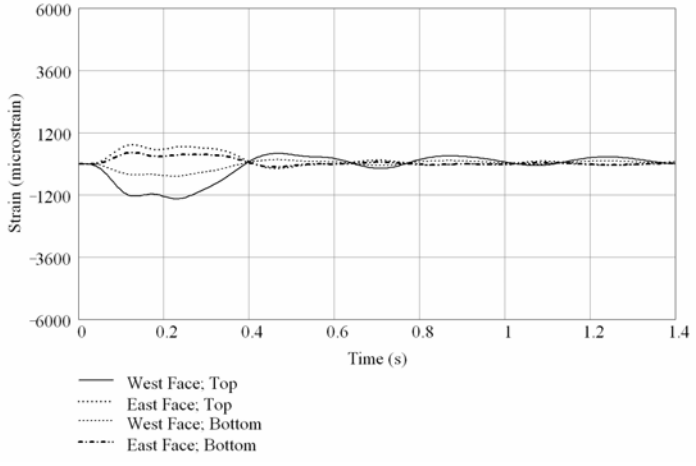

Figure F.11. Experiment P3T1 pile strains, Pier-3 East pile-cap

Pile 2:

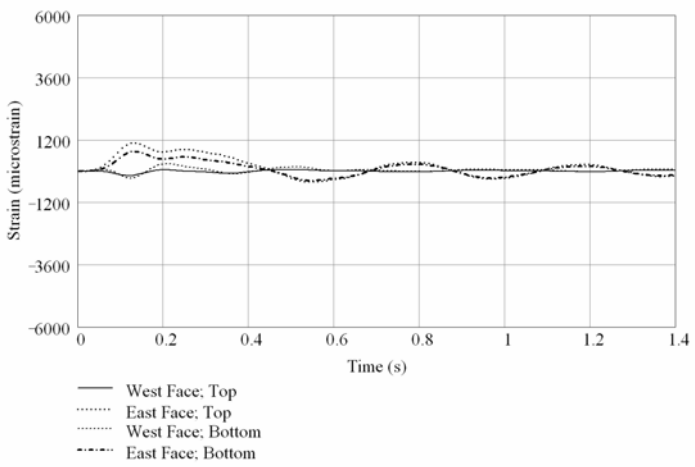

Pile 4:

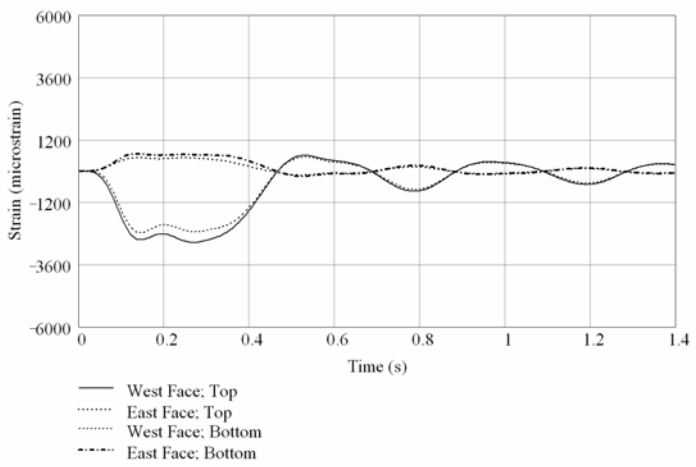

Pile 1:

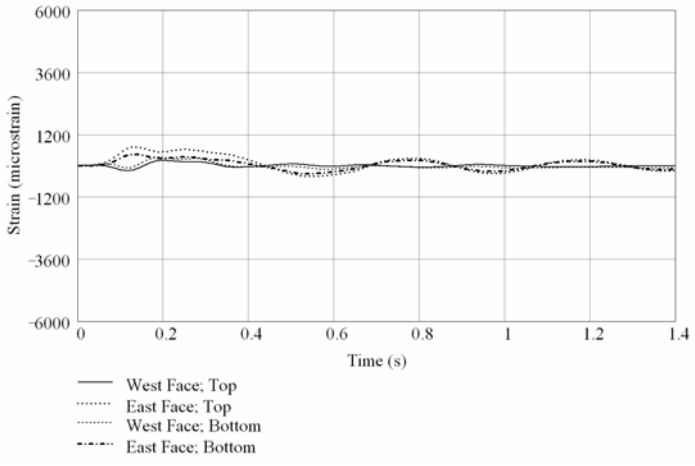

Pile 3:

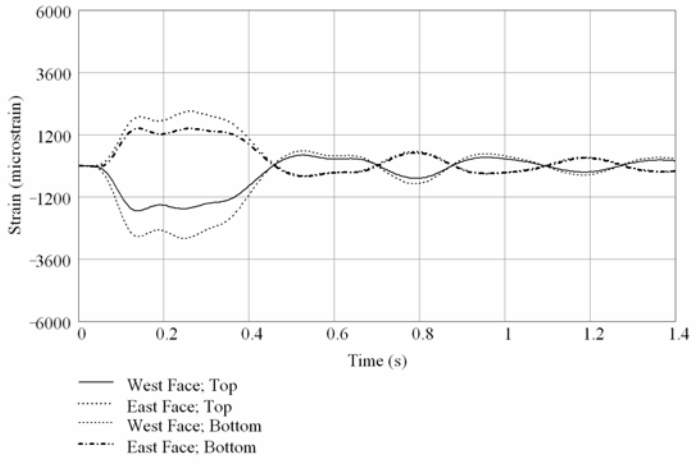

Figure F.12. Experiment P3T2 pile strains, Pier-3 West pile-cap

Pile 6:

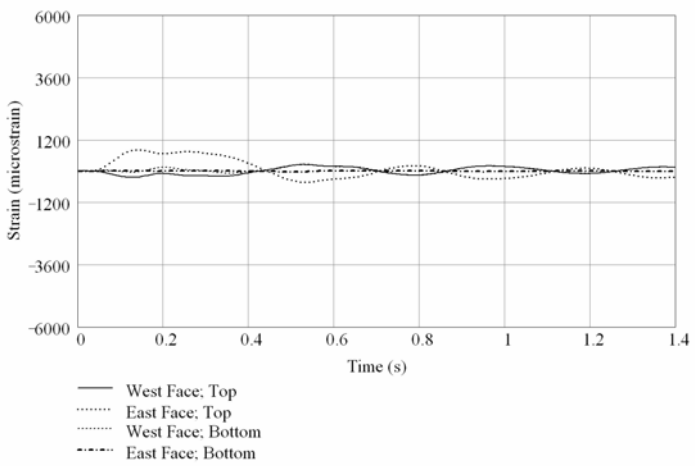

Pile 8:

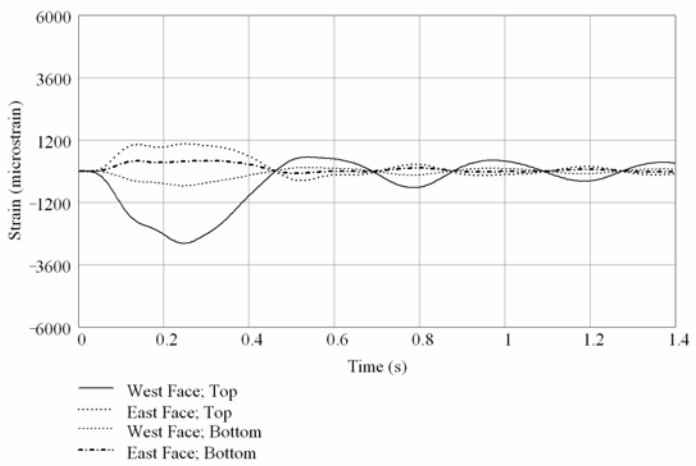

Pile 5:

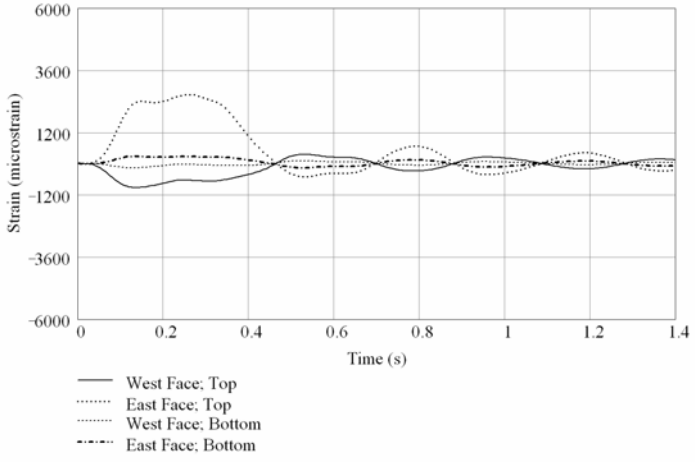

Pile 7:

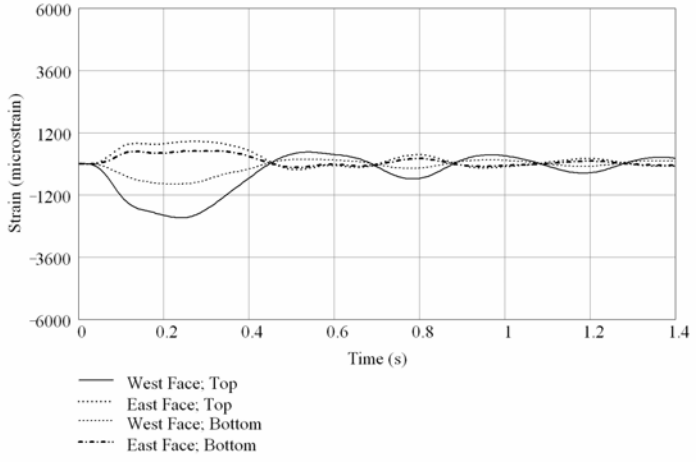

Figure F.13. Experiment P3T2 pile strains, Pier-3 East pile-cap

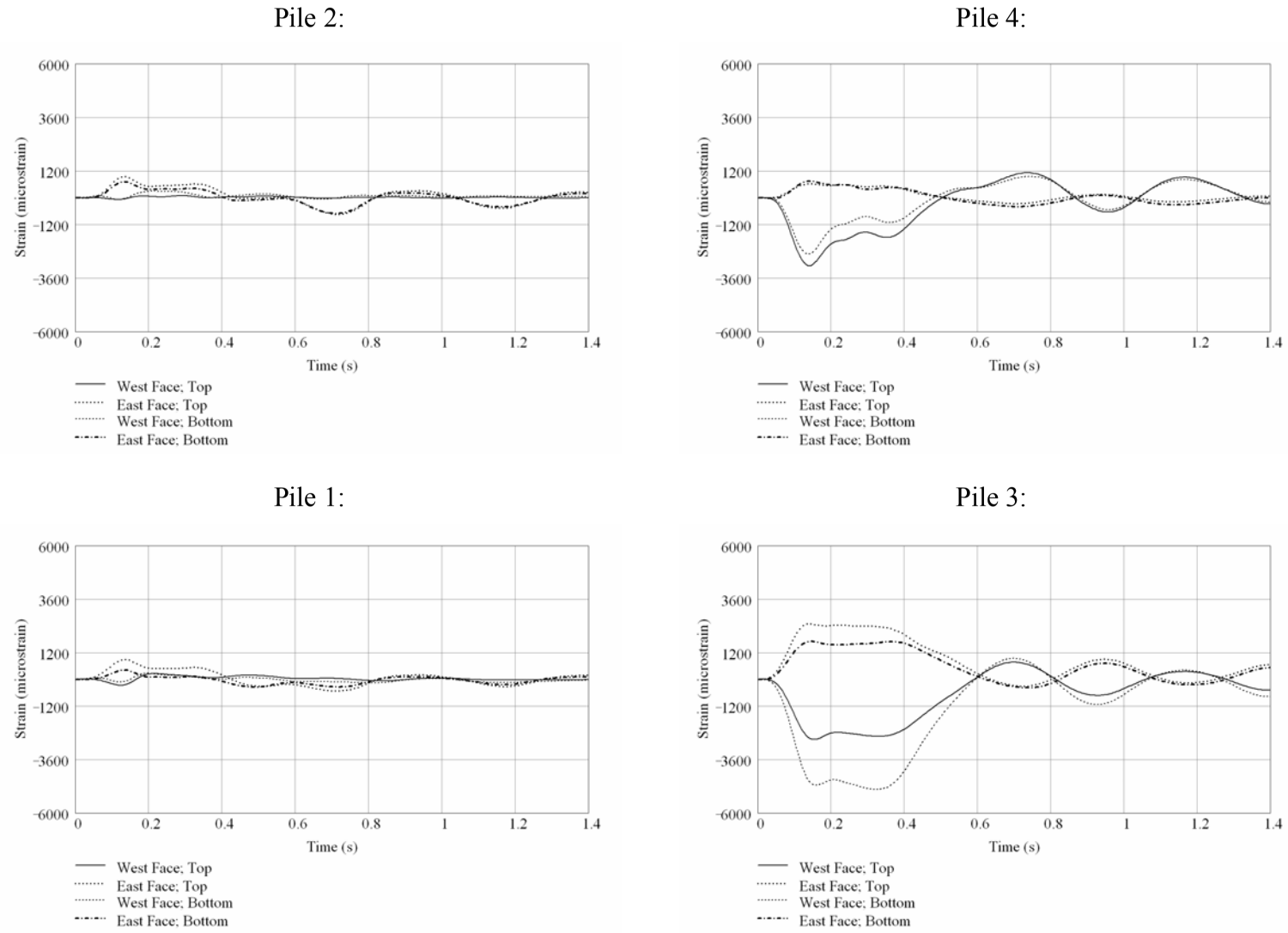

Figure F.14. Experiment P3T3 pile strains, Pier-3 West pile-cap

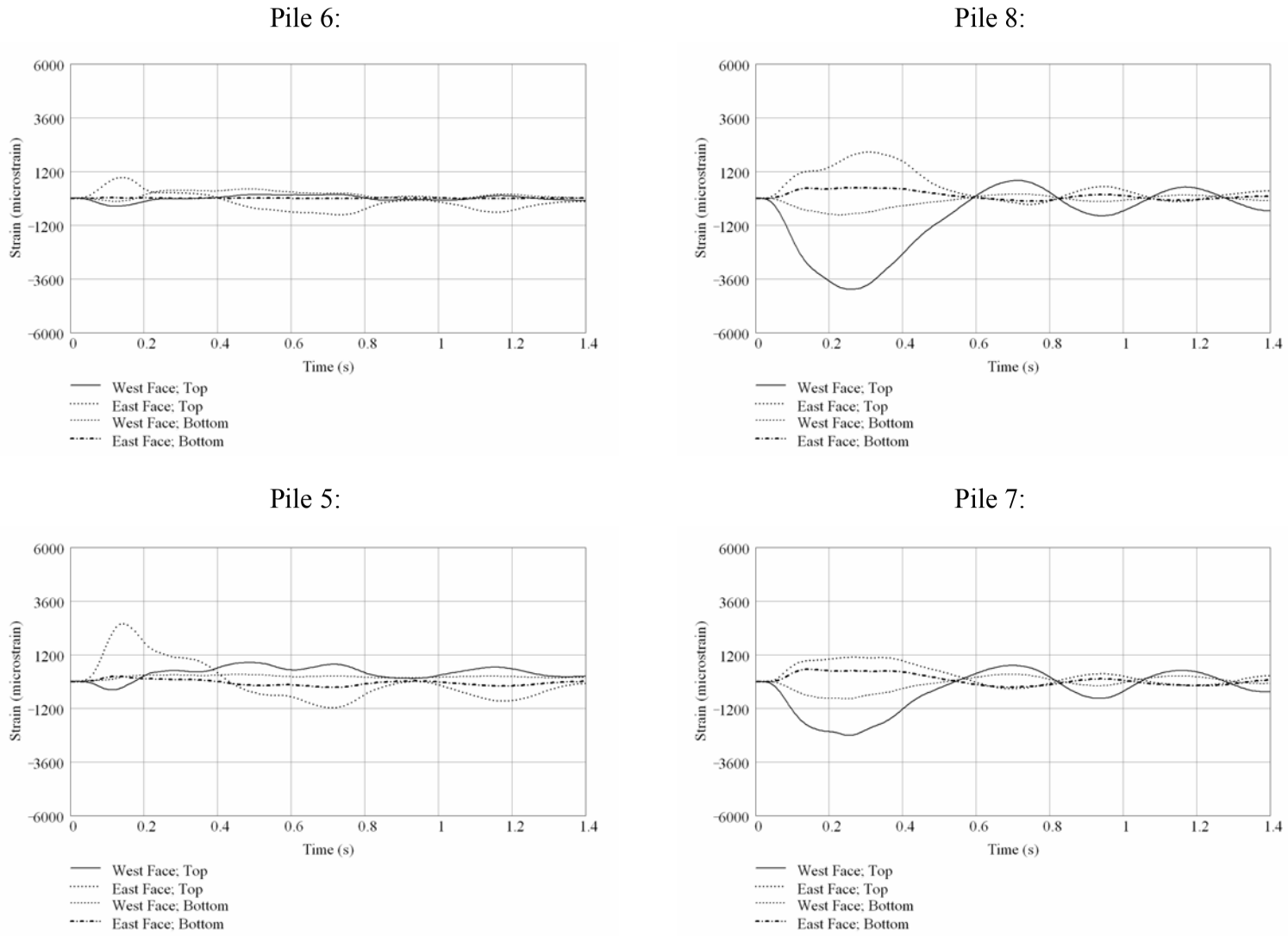

Figure F.15. Experiment P3T3 pile strains, Pier-3 East pile-cap

APPENDIX G
MEASURED BARGE CRUSH DEPTHS

Permanent barge deformations caused by collisions in the series P1 impact tests were quantified by measuring and recording barge-bow crush depths at multiple lateral positions (Figure G.1) after each impact test. The collection of crush measurements recorded after each test constitutes a barge bow damage profile. Several of the collision tests conducted involved impacts on previously damaged areas of the barge bow. Thus, in general, the damage profiles measured after each test were cumulative in nature including both the damage from the test just conducted as well as damage associated with earlier impacts. Incremental damage profiles, representing the increment of damage caused by a particular impact test and its associated energy, were then computed by taking differences between measured damage profiles from successive tests. On the following pages, both cumulative and incremental damage profiles are presented. Crush measurements were made for each test in series P1 except test P1T1 which was a low-energy diagnostic impact test that produced no measurable permanent barge deformation. In test series B3 and P3, the flexibility of Pier-3 and the lower impact speeds resulted in no measurable barge deformation being observed. Thus damage data are presented on the pages that follow only for tests P1T2 through P1T8.

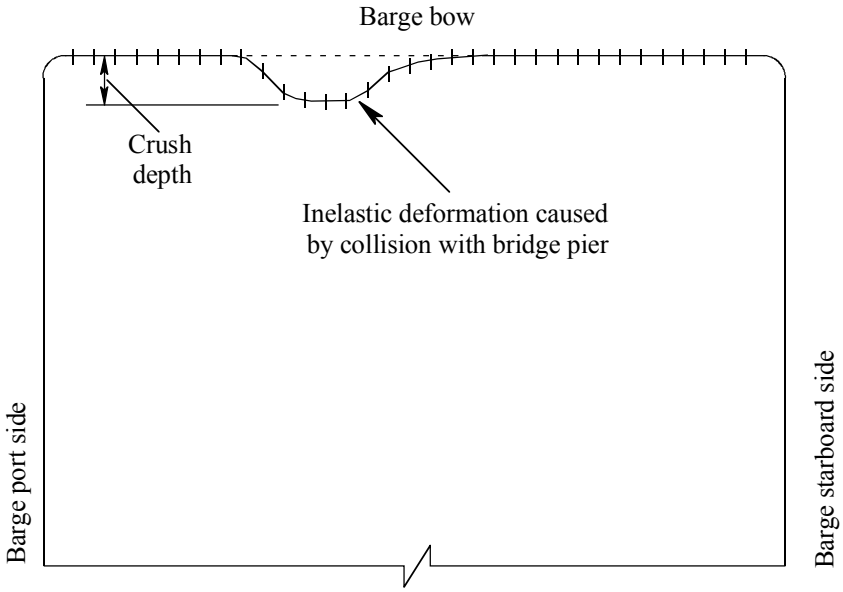

Figure G.1. Measurement of permanent barge deformation

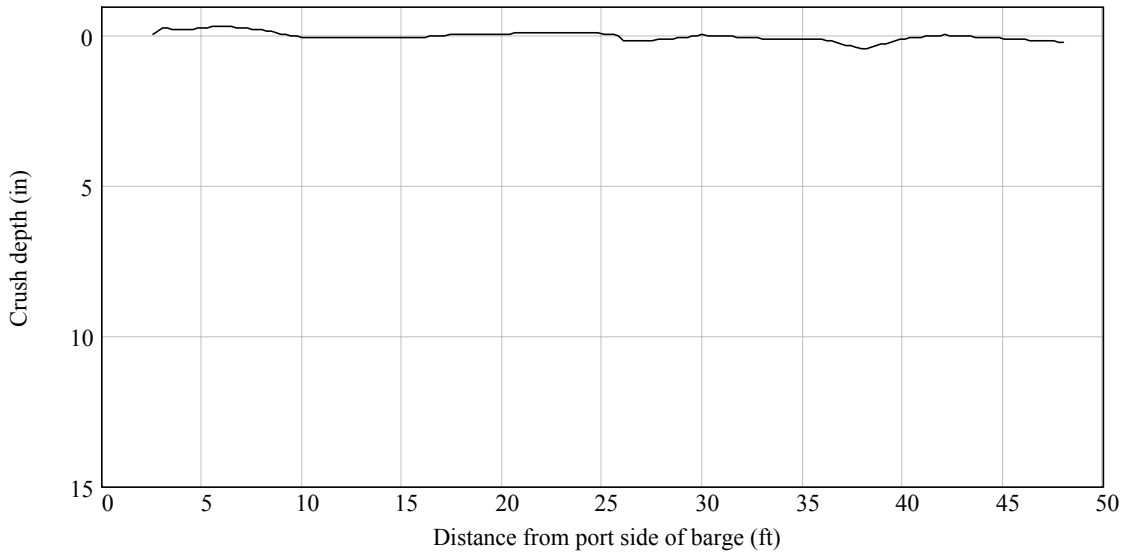

Figure G.2. Initial profile of barge bow prior to impact testing

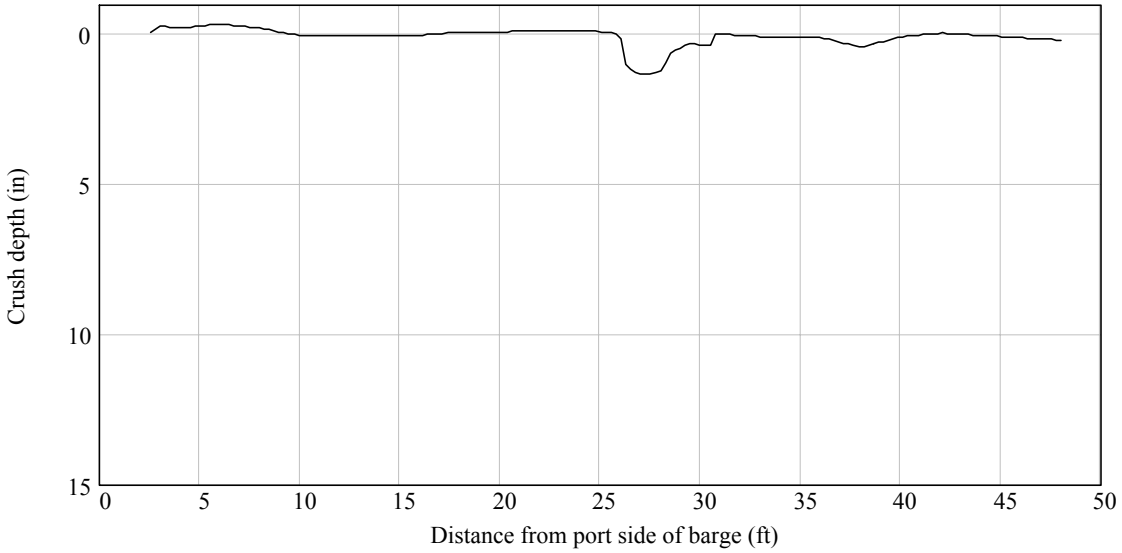

Figure G.3. Measured cumulative crush depth after Experiment P1T2

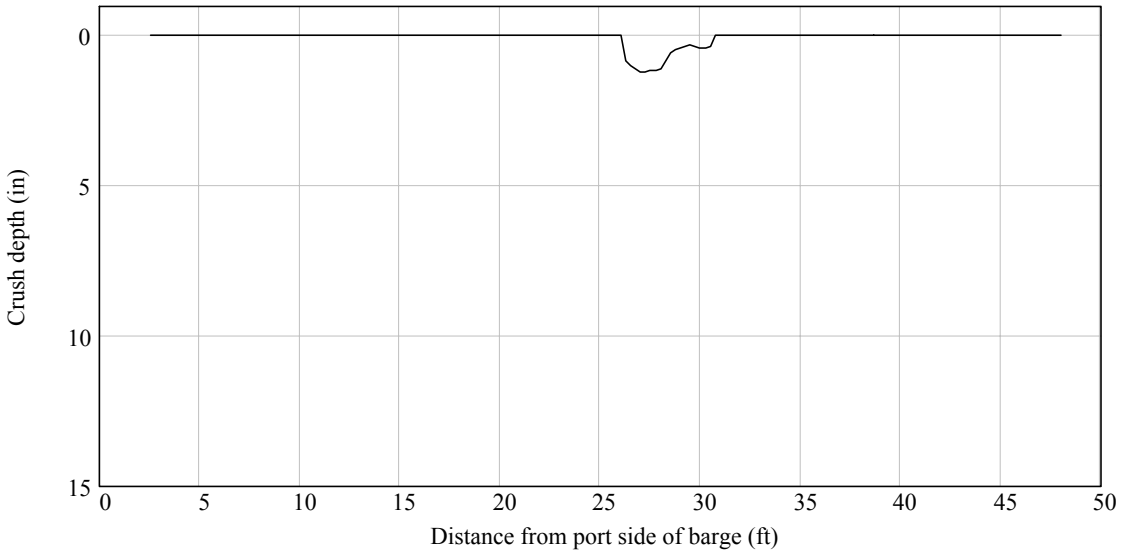

Figure G.4. Computed incremental crush depth after Experiment P1T2

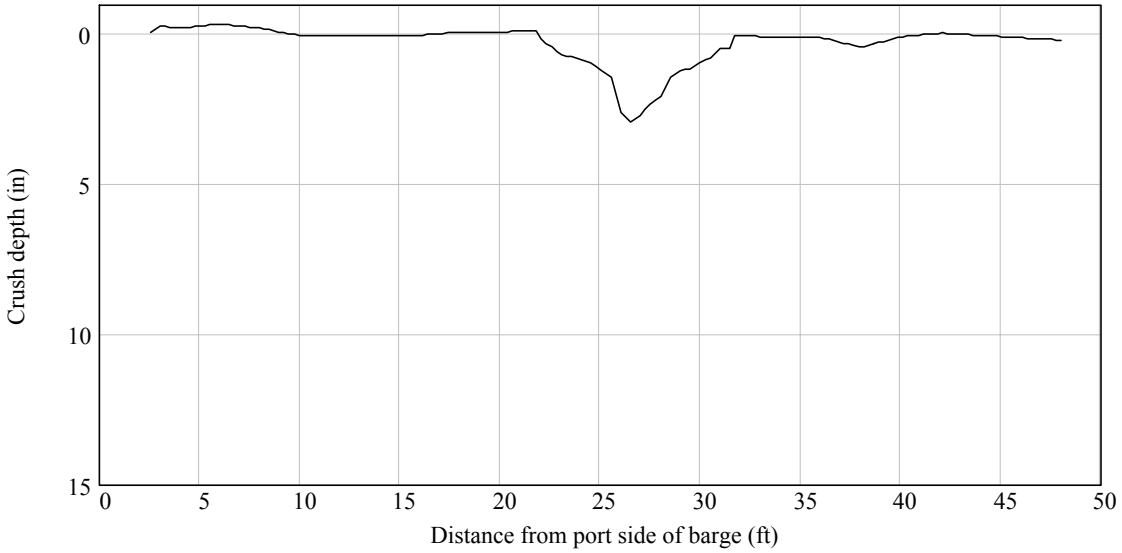

Figure G.5. Measured cumulative crush depth after Experiment P1T3

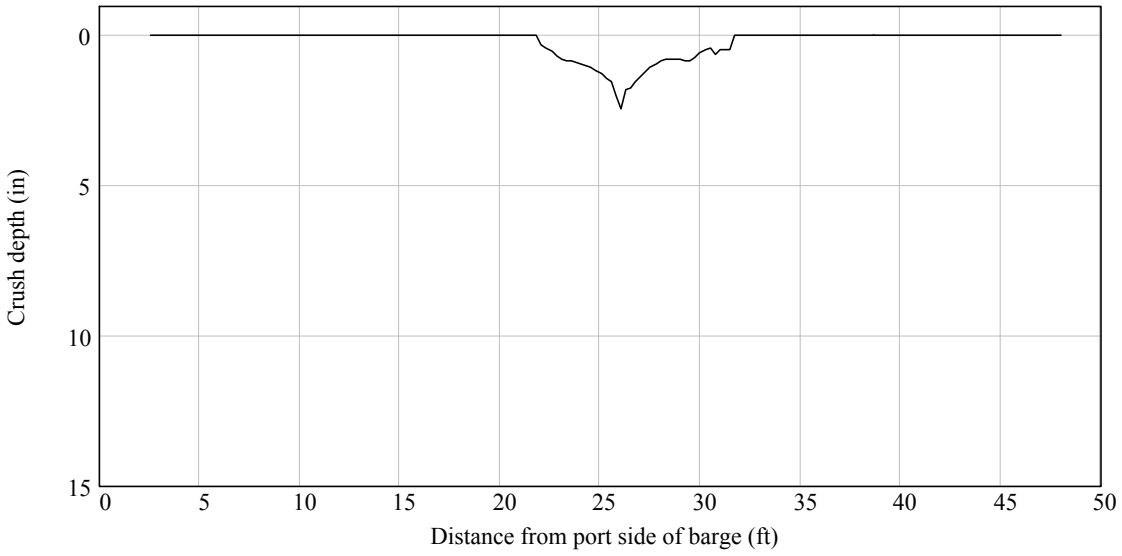

Figure G.6. Computed incremental crush depth after Experiment P1T3

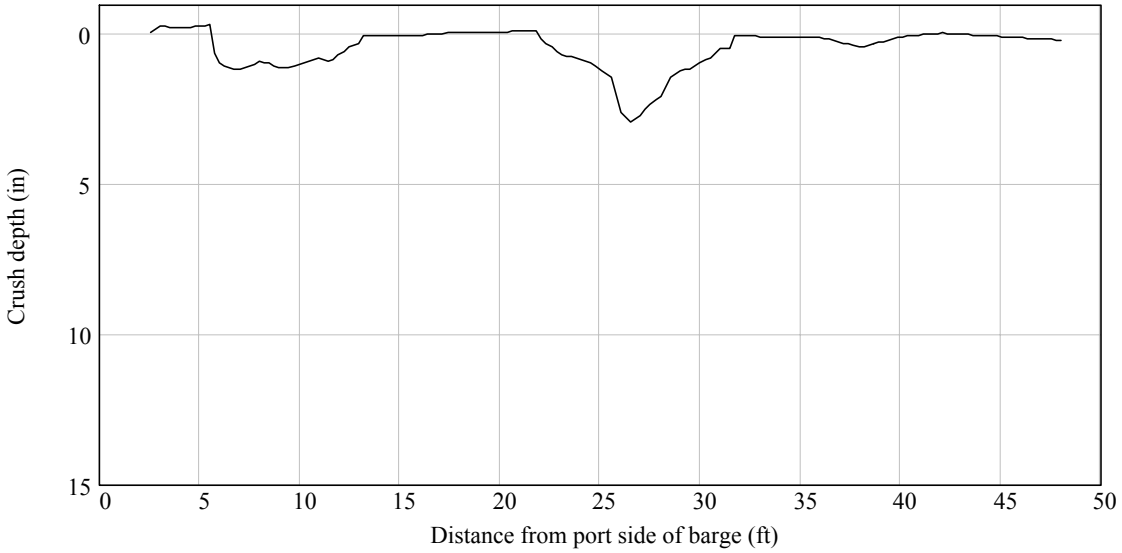

Figure G.7. Measured cumulative crush depth after Experiment P1T4

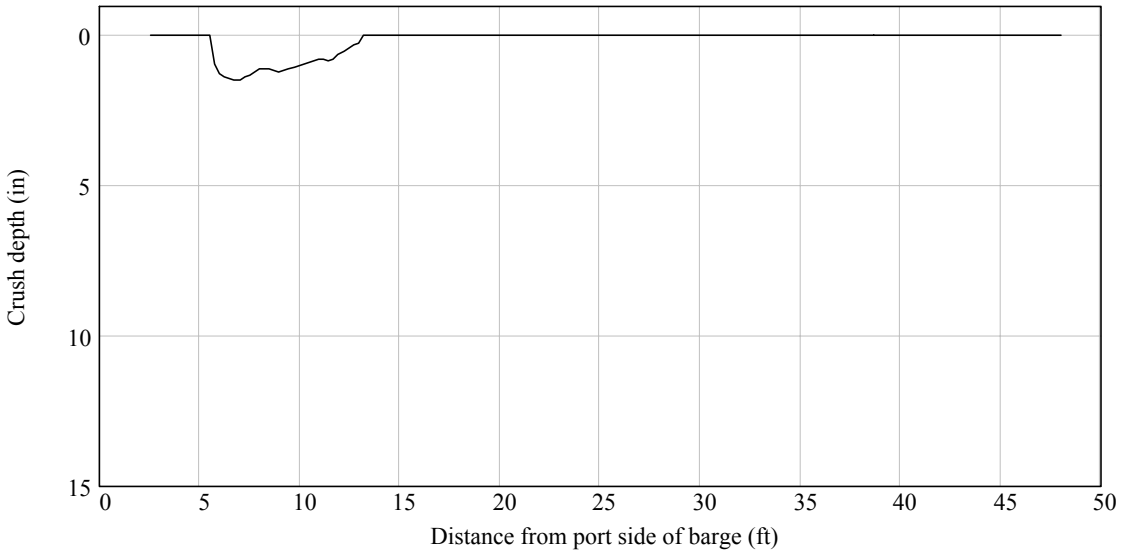

Figure G.8. Computed incremental crush depth after Experiment P1T4

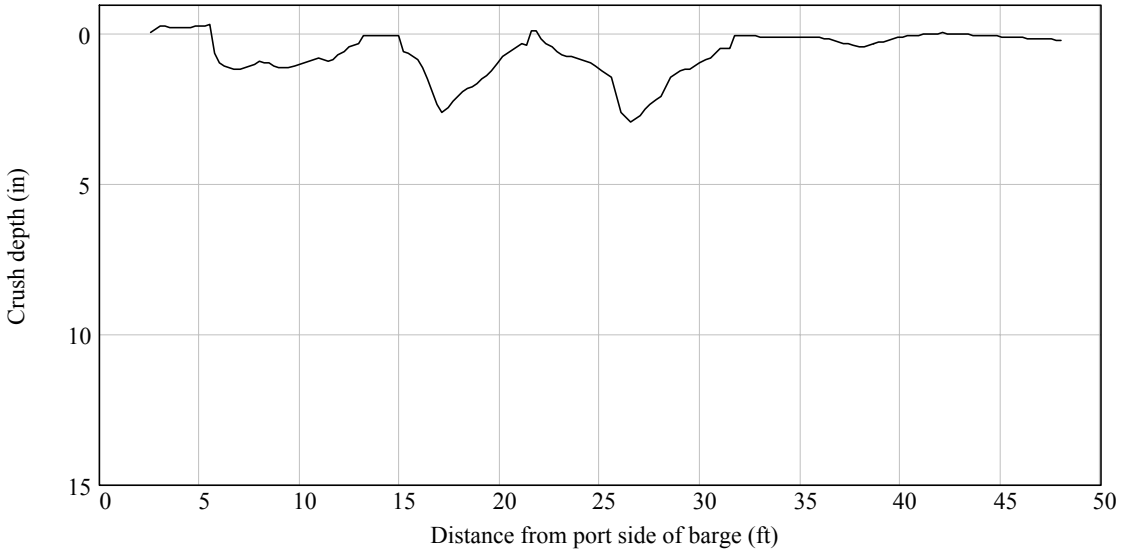

Figure G.9. Measured cumulative crush depth after Experiment P1T5

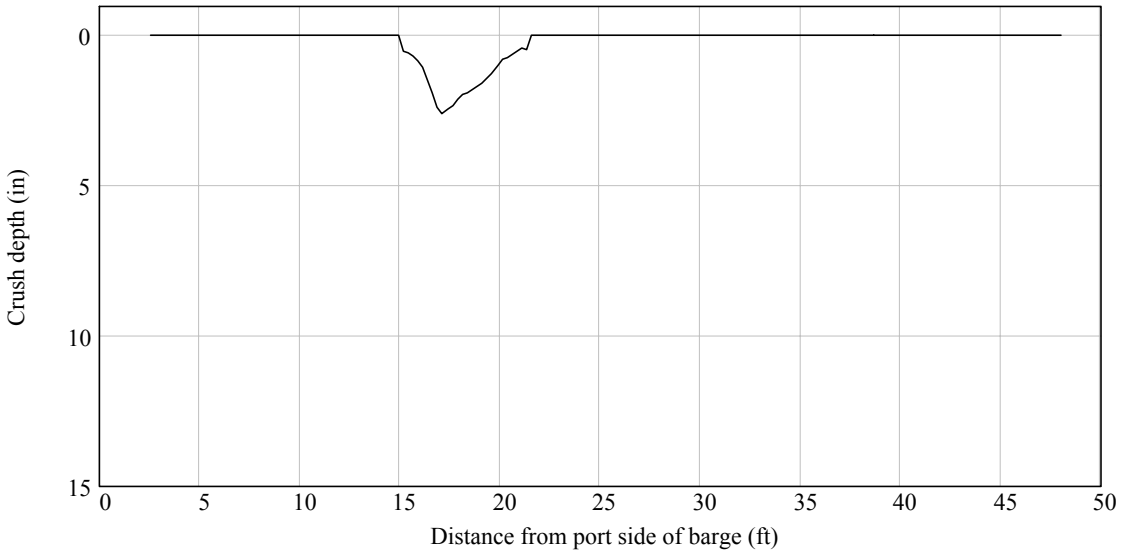

Figure G.10. Computed incremental crush depth after Experiment P1T5

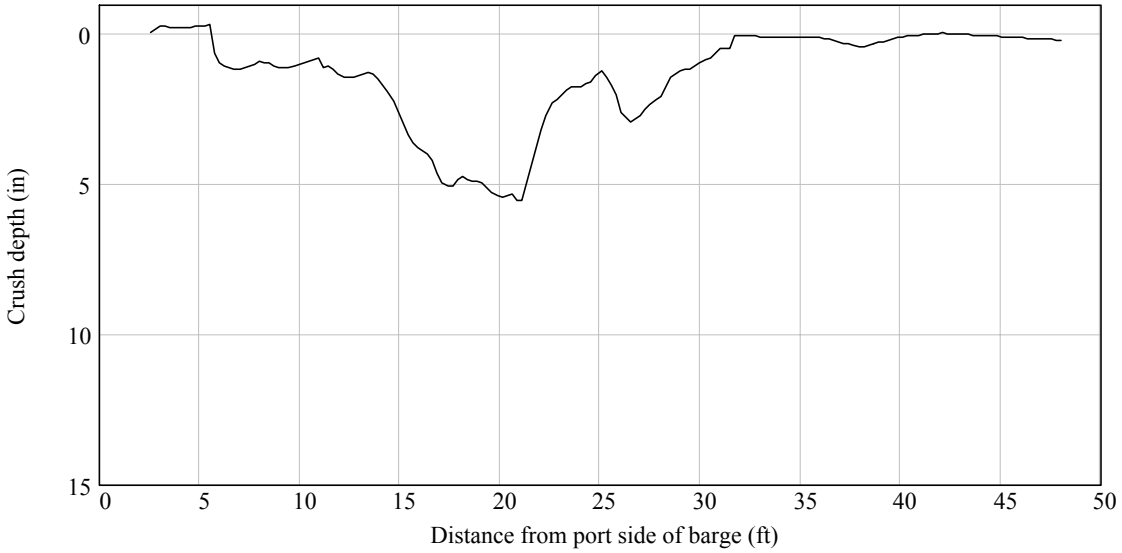

Figure G.11. Measured cumulative crush depth after Experiment P1T6

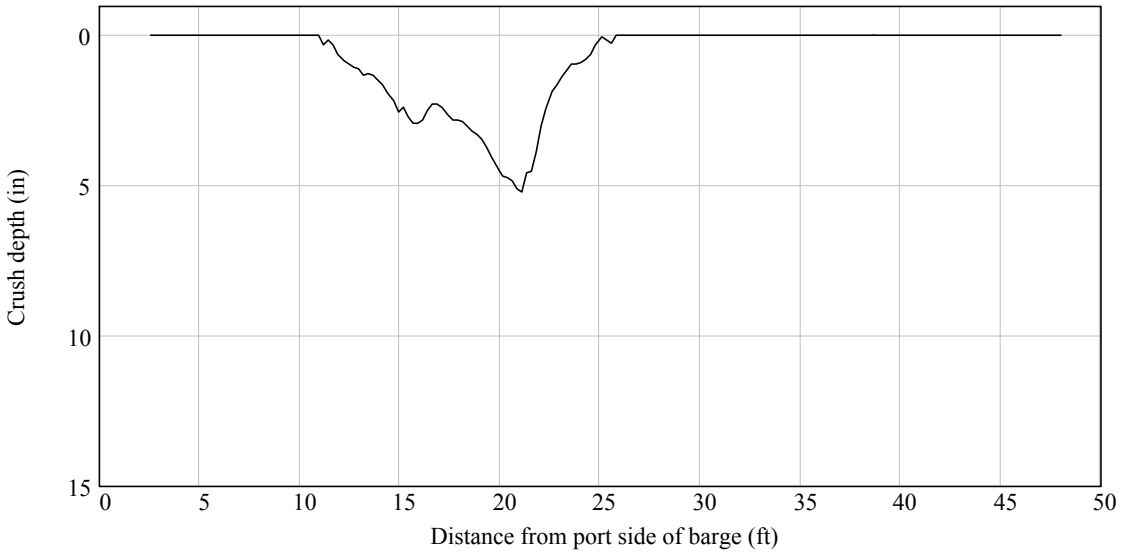

Figure G.12. Computed incremental crush depth after Experiment P1T6

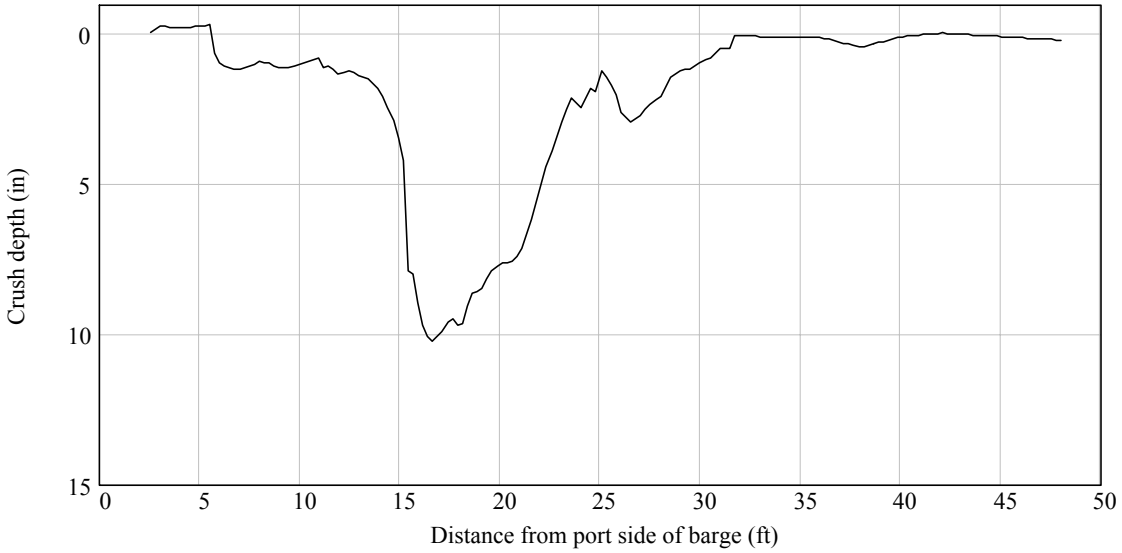

Figure G.13. Measured cumulative crush depth after Experiment P1T7

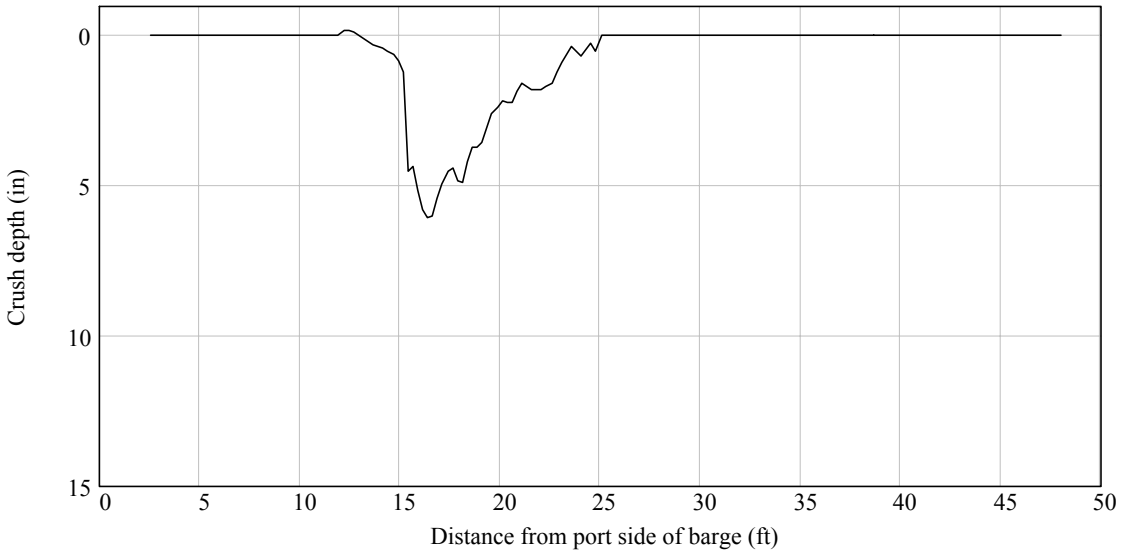

Figure G.14. Computed incremental crush depth after Experiment P1T7

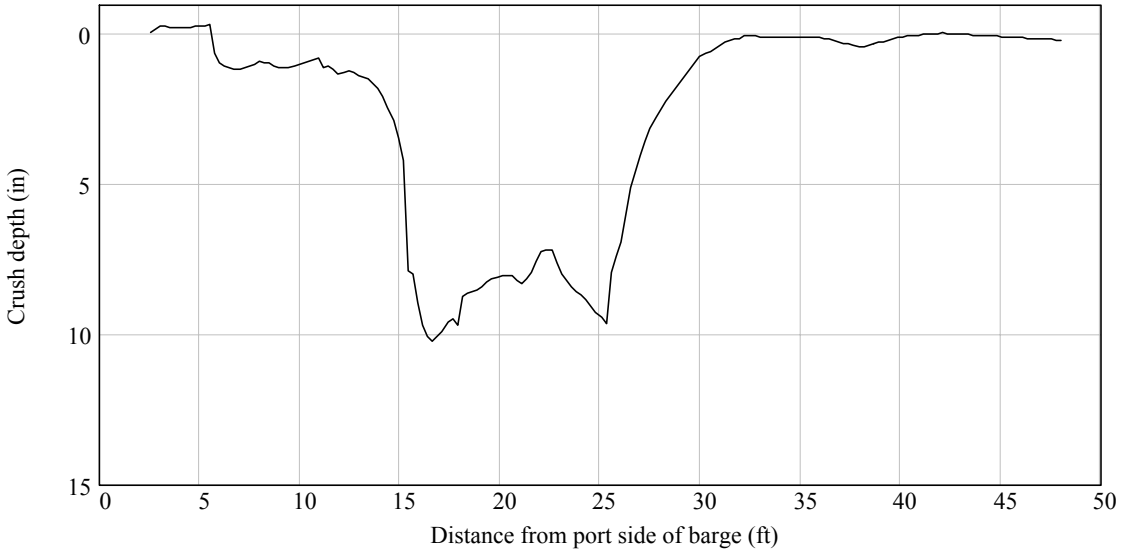

Figure G.15. Measured cumulative crush depth after Experiment P1T8

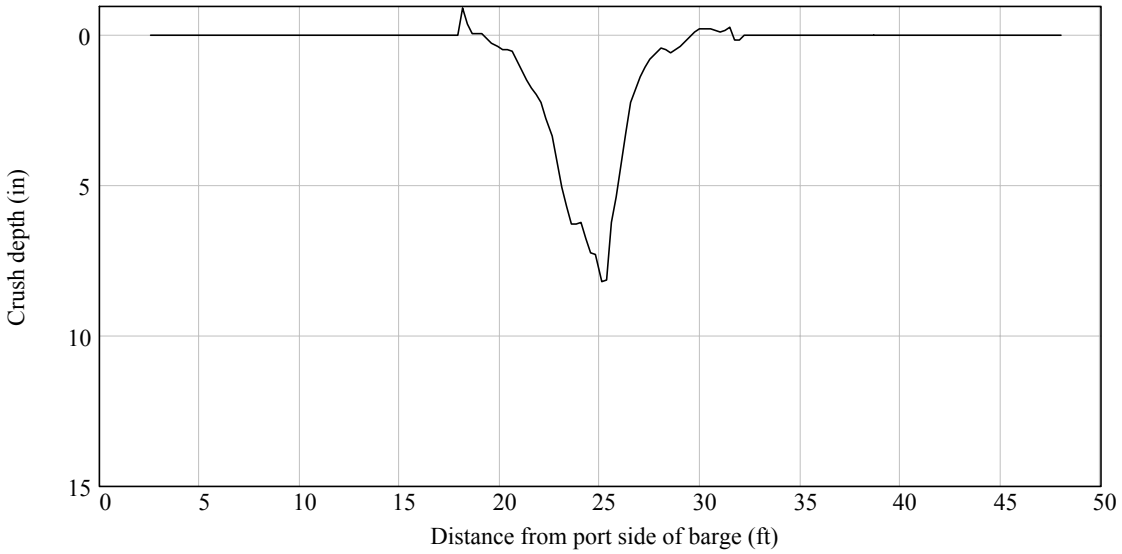

Figure G.16. Computed incremental crush depth after Experiment P1T8

APPENDIX H
CALCULATION OF IMPACT FORCES FROM MEASURED BARGE ACCELERATIONS

Indirectly determined time-varying impact loads are calculated in this appendix using measured barge accelerations so that comparisons to the directly measured impact loads presented earlier in Appendix A may be made. Barge acceleration data measured during impact test series B3 and P3 were previously presented in Appendix C. During each test, as the barge impacted the test pier and was brought to an abrupt stop, it underwent a time-varying deceleration (negative acceleration) in the x-direction. Estimation of the impact forces acting on the barge that produced the measured decelerations can be made using the expression $P_b = m_b \ddot{u}_b$ where m_b is the mass of the barge, $\ddot{u}_b$ is the measured acceleration (deceleration) of the barge, and P_b is the estimated impact force. This calculation is not valid for test series P1 due to energy dissipation that occurred as a result of inelastic crushing of the barge bow. Results are therefore presented on the following pages only for test series B3 and P3.

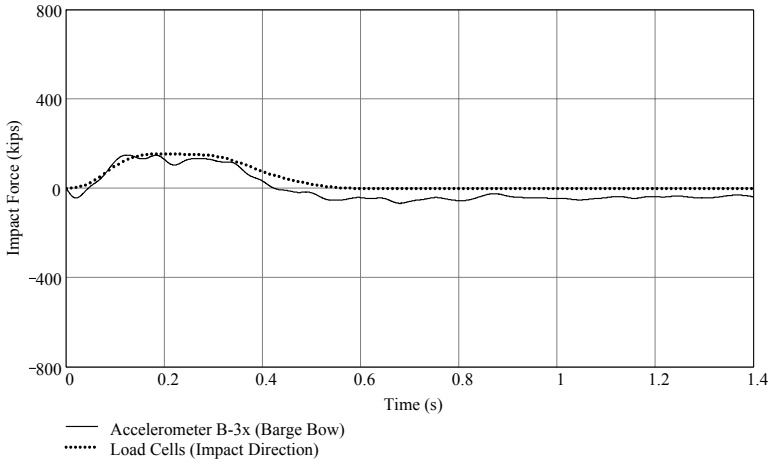

Figure H.1. Experiment B3T1

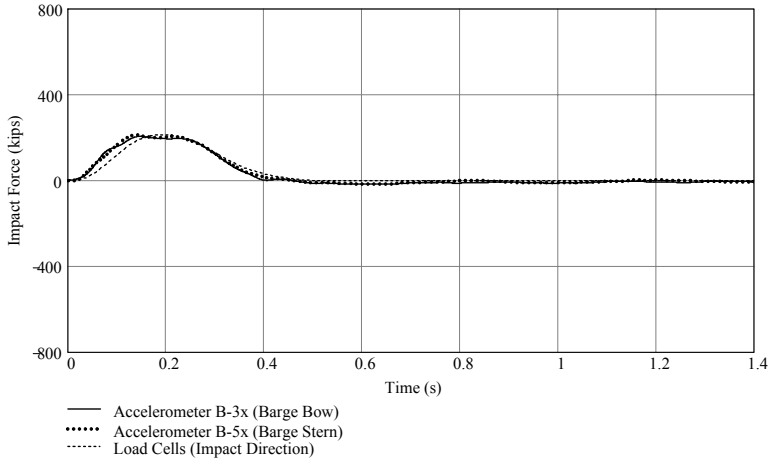

Figure H.2. Experiment B3T2

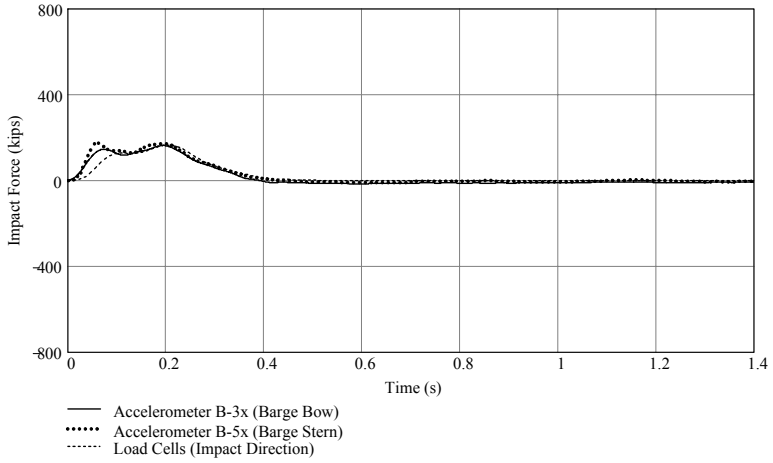

Figure H.3. Experiment B3T3

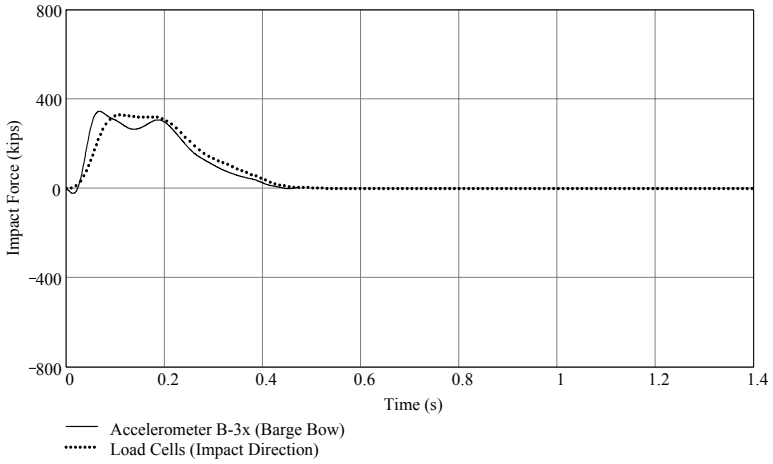

Figure H.4. Experiment B3T4

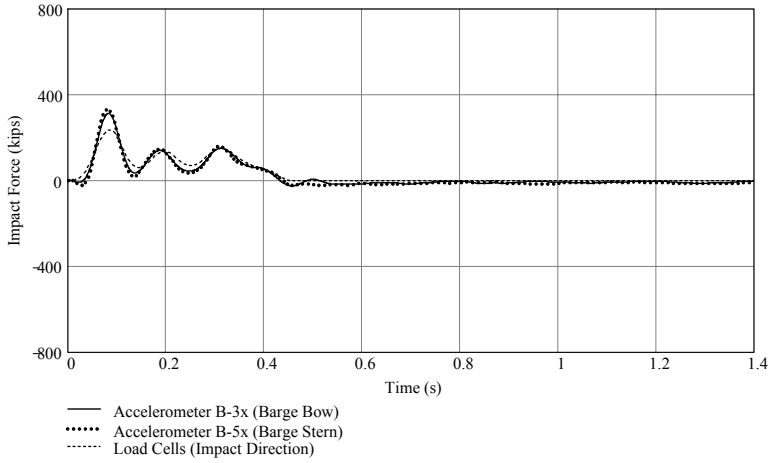

Figure H.5. Experiment P3T1

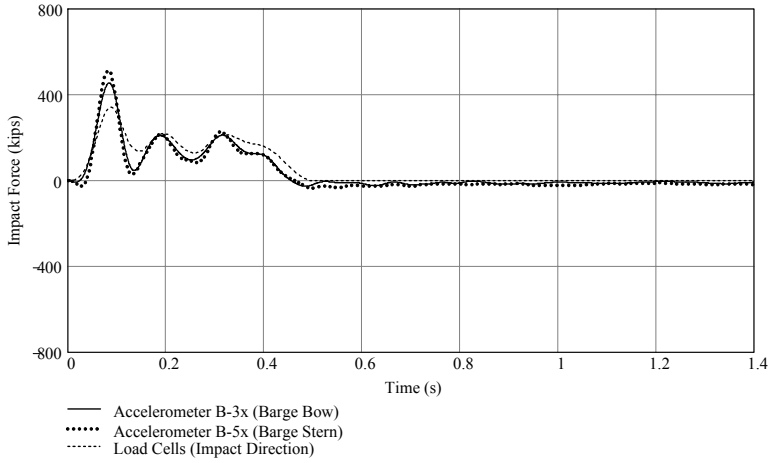

Figure H.6. Experiment P3T2

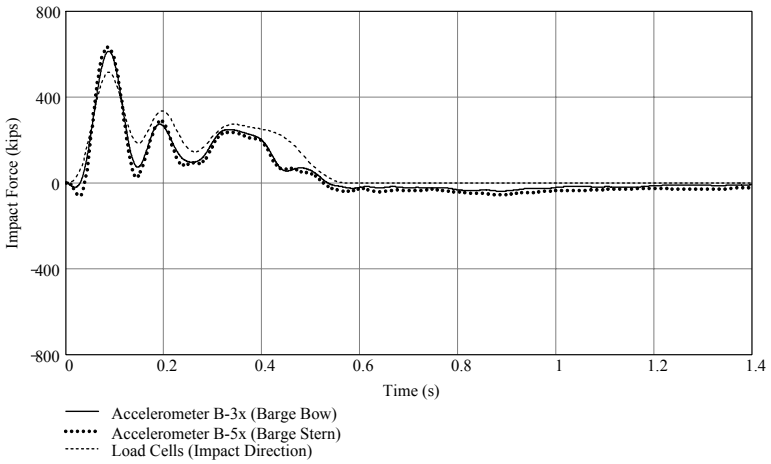

Figure H.7. Experiment P3T3

APPENDIX I
CALCULATION OF PIER DISPLACEMENTS FROM MEASURED PIER ACCELERATIONS

Indirectly determined time-varying pier displacements are calculated in this appendix using measured pier accelerations. In Appendix B, time histories of pier acceleration were presented for test series P1, B3, and P3. Displacements may be theoretically computed by numerically double time integrating the measured accelerations as $u(t) = \iint \ddot{u}(t)\, dt$ where $u(t)$ are the time-varying displacements and $\ddot{u}(t)$ are the experimentally measured pier accelerations. Due to the presence of noise in the measured acceleration data, additional data processing steps were required to prevent drift of the computed displacements.

A low-pass 60 Hz filter was applied to the raw acceleration data to remove frequency content above that which was required to adequately recover the translational motions of the pier. In addition, following each of the two numerical integration stages, the data were de-trended to remove drift. An assumption made in the de-trending process was that the piers did not sustain permanent (residual) lateral displacement as a result of the applied impact loads. In test series B3 and P3, examination of pier displacements directly measured using displacement transducers corroborated the fact that Pier-3 did not sustain permanent displacements as a result of impact. In test series P1, data recorded by the displacement transducers were not deemed sufficiently reliable (see Appendix D for additional details) for the purpose of evaluating whether residual displacements occurred or not.

However, for three of the series P1 tests—P1T1, P1T6, and P1T7—supplementary geotechnical data were available (McVay et al. 2005) to facilitate calculation of pier displacements after impact. In the case of P1T1, the residual pier displacement was sufficiently small as to be considered zero. In tests P1T6 and P1T7, the residual displacements were approximately an order of magnitude less than the peak dynamic pier displacements. Therefore, on the pages that follow, the assumption of zero residual displacement has been made for all tests. In the main body of this report, however, where experimentally determined data and numerically predicted data are compared in detail for test P1T7, the de-trending steps used in the double time integration procedure noted above were additionally modified to incorporate the residual pier displacement determined from the geotechnical data.

Data presented on the following pages for test series P1 have been computed indirectly through numerical time integration as described above. For test series B3 and P3, both indirectly computed and directly measured displacement data are presented and compared.

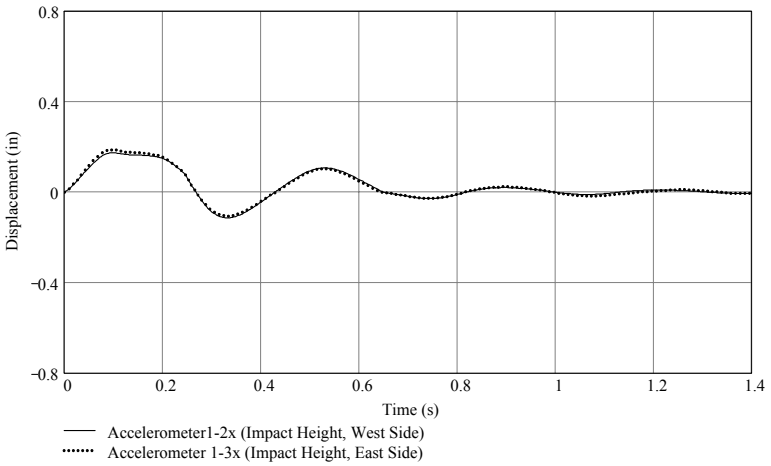

Figure I.1. Experiment P1T1

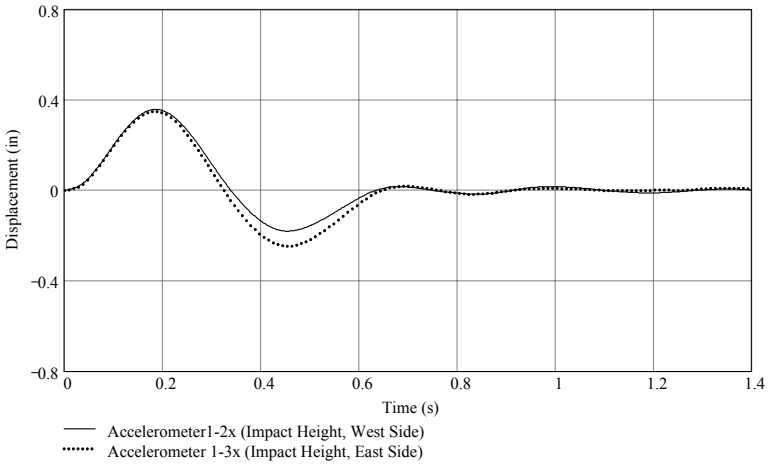

Figure I.2. Experiment P1T3

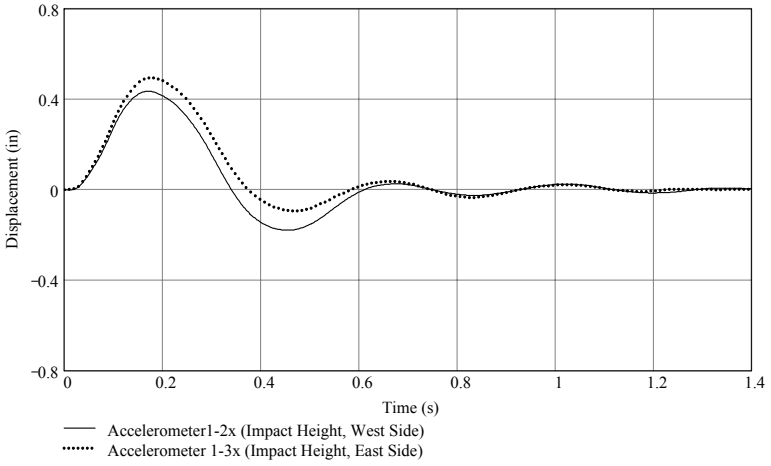

Figure I.3. Experiment P1T4

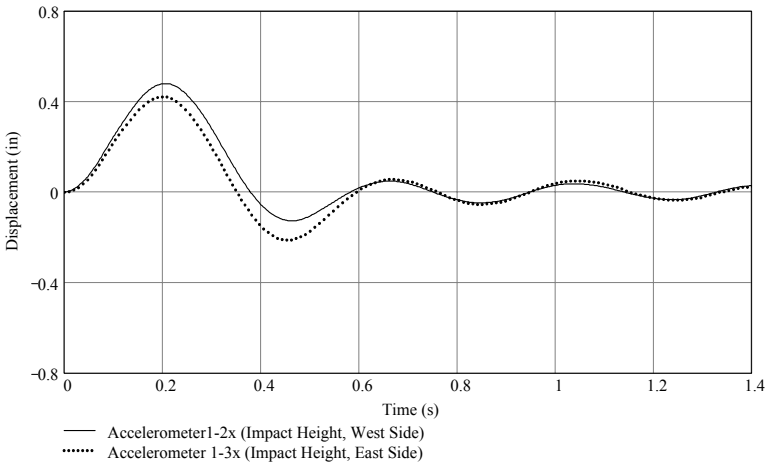

Figure I.4. Experiment P1T5

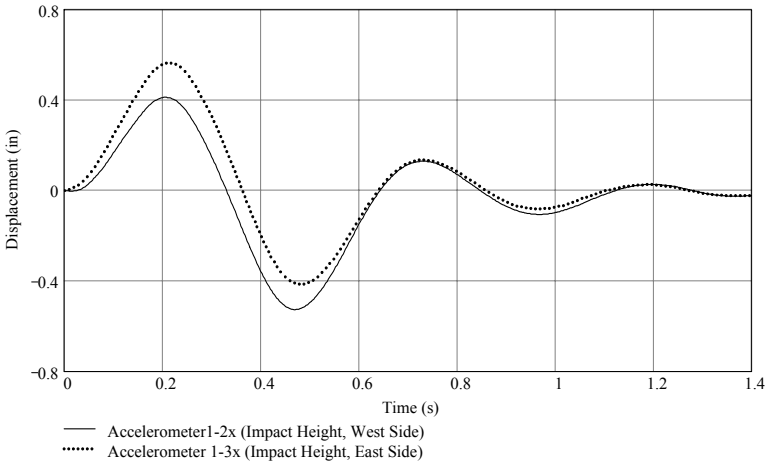

Figure I.5. Experiment P1T6

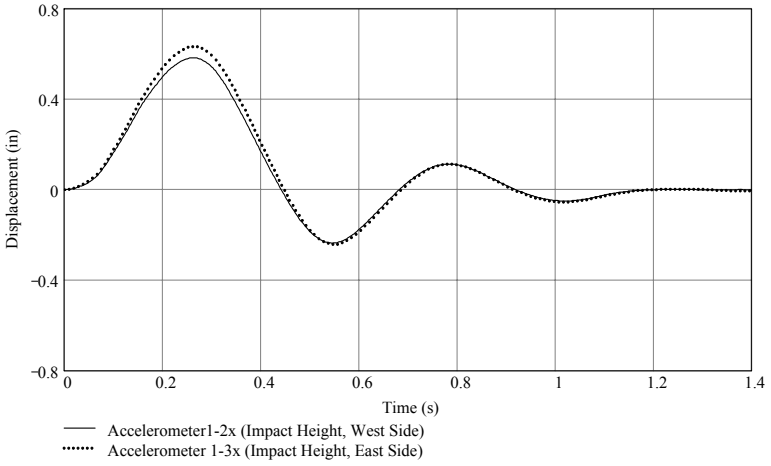

Figure I.6. Experiment P1T7

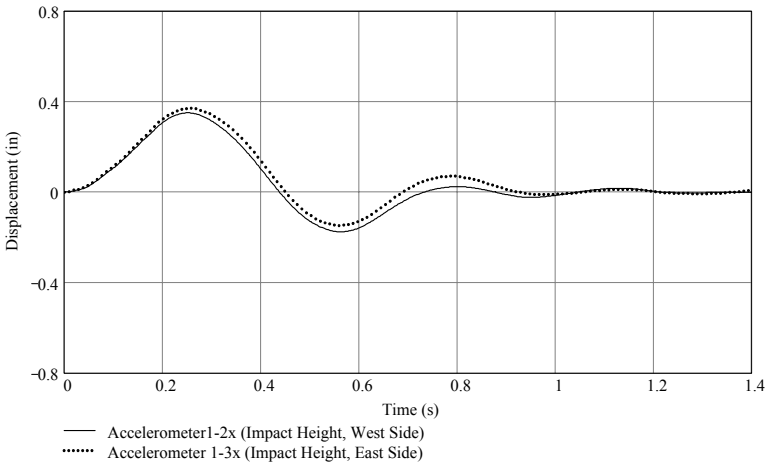

Figure I.7. Experiment P1T8

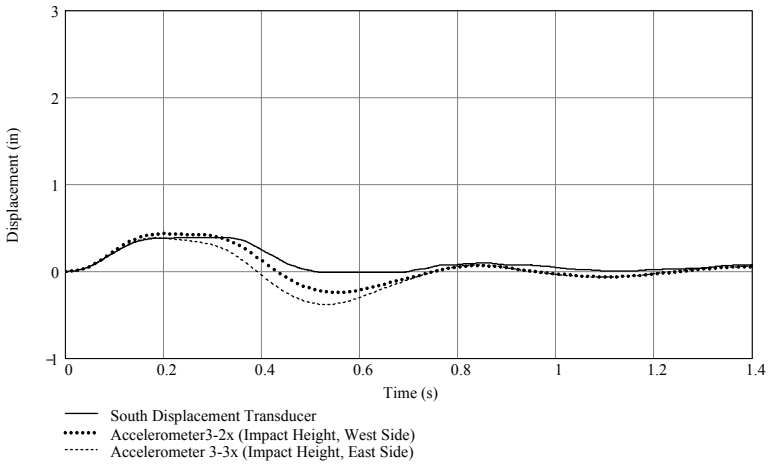

Figure I.8. Experiment B3T1

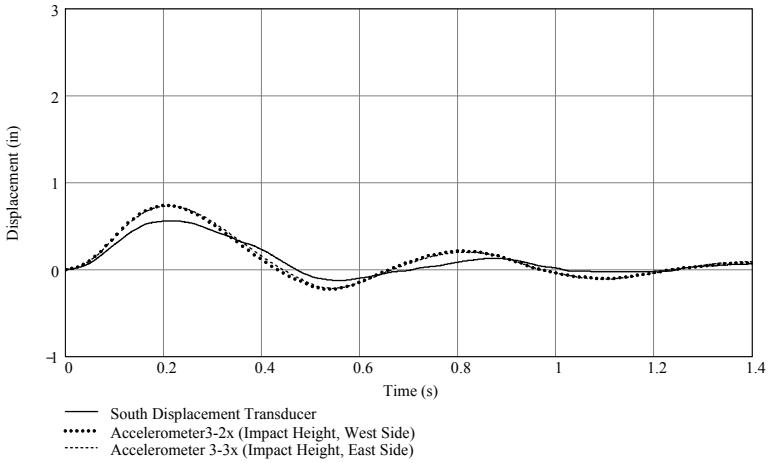

Figure I.9. Experiment B3T2

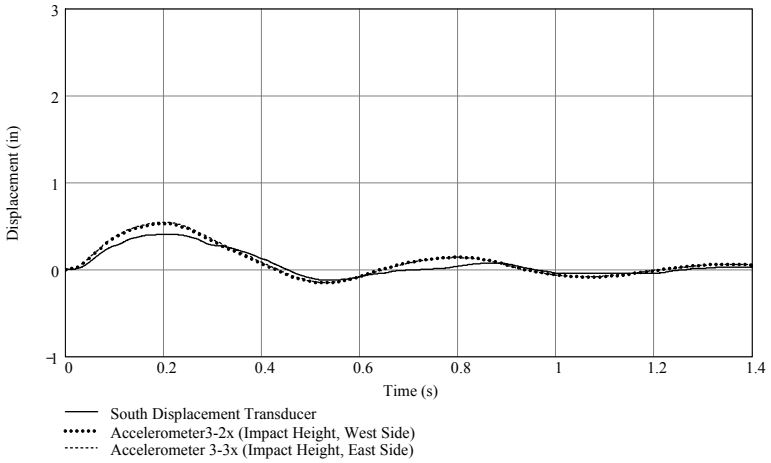

Figure I.10. Experiment B3T3

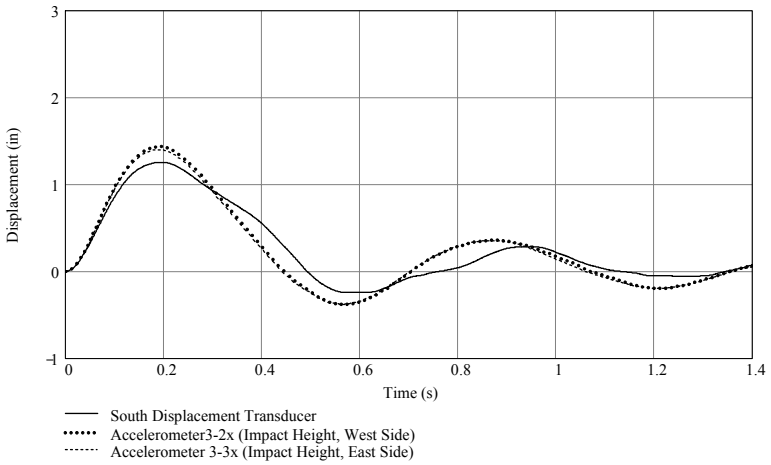

Figure I.11. Experiment B3T4

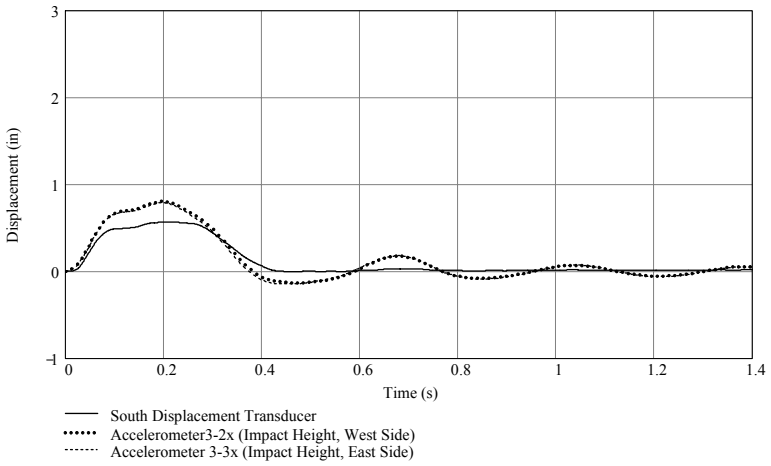

Figure I.12. Experiment P3T1

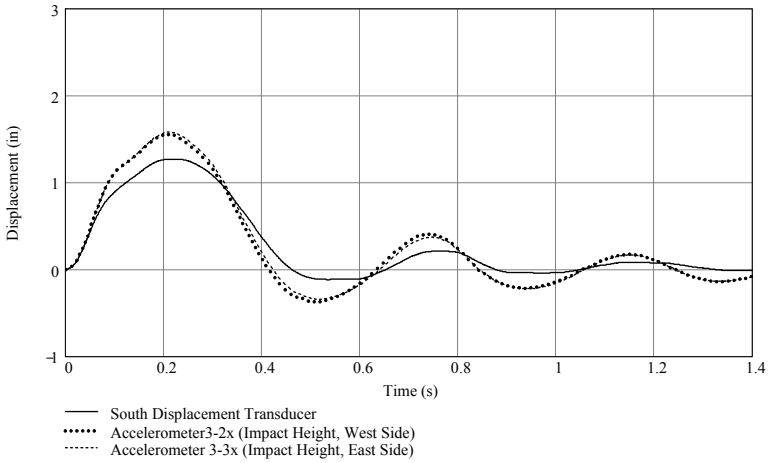

Figure I.13. Experiment P3T2

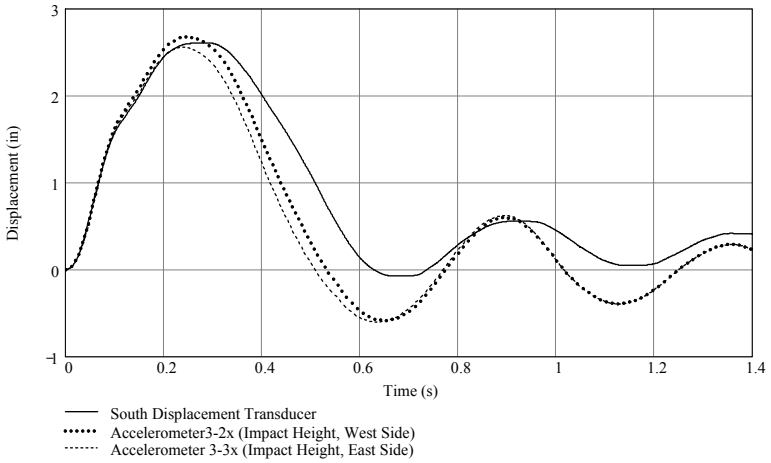

Figure I.14. Experiment P3T3